Catarina Isabel Cabral de Carvalho e Melo Simões Barbosa

Mestre em Engenharia Química e Bioquímica

Carbon Dioxide Hydrogenation Towards Methane with Ruthenium Nanoparticles in Ionic Liquid Media

Dissertação para obtenção do Grau de Doutor em Química Sustentável

Orientador:	Dr.ª Ewa Bogel-Łukasik, Investigadora Auxiliar, FCT-UNL
Co-orientador:	Prof. Dr. Manuel Nunes da Ponte, Professor Catedrático, FCT-UNL

Júri:

Presidente:	Prof. Doutor José Paulo Barbosa Mota
Arguentes:	Prof. Doutor Carlos Manuel Faria de Barros Henriques
	Prof. Doutora Lúcia Raquel Brandão Moreira
Vogais:	Prof. Doutor Luís Alexandre Almeida Fernandes Cobra Branco
	Prof. Doutora Ana Maria Staack Reis Machado
	Prof. Doutora Ewa Bogel-Łukasik

FACULDADE DE CIÊNCIAS E TECNOLOGIA
UNIVERSIDADE NOVA DE LISBOA

Julho 2018

Catarina Isabel Cabral de Carvalho e Melo Simões Barbosa

Mestre em Engenharia Química e Bioquímica

Carbon Dioxide Hydrogenation Towards Methane with Ruthenium Nanoparticles in Ionic Liquid Media

Dissertação para obtenção do Grau de Doutor em
Química Sustentável

Orientador:	Dr.ª Ewa Bogel-Łukasik, Investigadora Auxiliar, FCT-UNL
Co-orientador:	Prof. Dr. Manuel Nunes da Ponte, Professor Catedrático, FCT-UNL

Júri:

Presidente:	Prof. Doutor José Paulo Barbosa Mota
Arguentes:	Prof. Doutor Carlos Manuel Faria de Barros Henriques
	Prof. Doutora Lúcia Raquel Brandão Moreira
Vogais:	Prof. Doutor Luís Alexandre Almeida Fernandes Cobra Branco
	Prof. Doutora Ana Maria Staack Reis Machado
	Prof. Doutora Ewa Bogel-Łukasik

FCT FACULDADE DE
CIÊNCIAS E TECNOLOGIA
UNIVERSIDADE NOVA DE LISBOA

Julho 2018

Carbon Dioxide Hydrogenation Towards Methane with Ruthenium Nanoparticles in Ionic Liquid Media

In loving memory of my mother
and grandmother

ACKNOWLEDGMENTS

RESUMO

O dióxido de carbono (CO_2) é um gás de estufa de grande impacto ambiental cujas emissões continuam a subir a cada ano. Imensa investigação é feita para desenvolver métodos de captura e utilização deste composto. No âmbito da utilização, a aplicação de CO_2 na produção de combustíveis é uma estratégia bastante atrativa.

Este trabalho focou-se no desenvolvimento de um processo onde líquidos iónicos são utilizados na síntese e estabilização de nanopartículas metálicas, que, num meio bifásico de CO_2+H_2/LI, vão catalisar a hidrogenação de CO_2 em metano.

Durante este trabalho sintetizaram-se de uma forma simples e *in situ* nanopartículas de ruténio com um diâmetro médio entre os 1,6-2,9 nm capazes de converter CO_2 em metano com uma seletividade de 100%. Estas reações foram realizadas a 150℃, temperaturas bastante baixas neste tipo de processo. O desempenho das reações foi avaliado a partir dos seus rendimentos. O estudo dividiu-se nas seguintes partes:

Otimização, onde diferentes condições de reação foram testadas, tais como: o tipo de precursor e a sua quantidade; temperatura e duração de reação e a proporção dos reagentes.

Estudo do efeito de vários líquidos iónicos diferentes, na sua maioria fluorados de base imidazólica, onde se verificou que o desempenho da reação dependia principalmente da estabilização das nanopartículas. Esta foi favorecida pela presença de longas cadeias alquílicas no catião e de cadeias fluoradas laterais no anião. O nonaflato de 1-octil-3-metilimidazólio, [C_8mim][NfO], apresentou o melhor desempenho com 84,4% de rendimento. Ao utilizar aniões de baixo volume molar, a forte coordenação destes levou a uma mudança da seletividade, formando-se monóxido de carbono.

Estudo da reciclabilidade, onde foi possível reutilizar o sistema, havendo uma pequena desativação no fim de cada reutilização causada pela agregação de NPs e acumulação de água no sistema. No geral esta reação apresenta potencial parar ser implementada num processo em contínuo.

Palavras-chave: Dióxido de Carbono, Hidrogenação, Líquidos Iónicos, Metano, Nanopartículas, Ruténio.

x

ABSTRACT

Carbon dioxide (CO_2) is a greenhouse gas of major environmental impact whose emissions continue to rise each year. Extensive research is being done to develop methods of capturing and utilization. Regarding CO_2 utilization, its application towards fuel production is a very attractive strategy.

This work focuses on the development of a chemical process that converts CO_2 into methane. This process aims at using ionic liquids in the synthesis and stabilization of metal nanoparticles that catalyse CO_2 hydrogenation in a biphasic CO_2+H_2/IL medium.

In this work ruthenium nanoparticles with a mean size between 1.6-2.9 nm were synthesized in-situ through a simple and straightforward process. These nanoparticles can convert CO_2 into methane with a selectivity of 100%. These reactions were carried out at temperatures of 150℃ and below, a very low value for this kind of process. Reaction performance was assessed though its yield. The study was divided into three main parts:

Optimization, where different reaction conditions were tested such as: type and quantity of precursor; temperature and duration of reaction; and reactant ratio.

Study on the effect of several ILs, mostly imidazolium based with fluorinated anions, where it was observed that reaction performance depended mainly on nanoparticle stabilization. This was favoured by the presence of long alkyl chains in the cation and fluoride chains in the anion. 1-Octyl-3-methylimidazolium nonaflate, [C_8min][NfO], presented the best results with 84.4% yield. When using low molar volume anions, their strong coordination led to a change of selectivity, towards the formation of carbon monoxide.

Recyclability study, where it was possible to reuse the system, although the catalyst slightly deactivated after each reuse due to nanoparticle aggregation and water accumulation in the system. Overall, this reaction reveals potential for implementation in a continuous process.

Keywords: Carbon Dioxide, Hydrogenation, Ionic Liquids, Methane, Nanoparticles, Ruthenium.

TABLE OF CONTENTS

LIST OF FIGURES

xviii

xxii

LIST OF TABLES

LIST OF SYMBOLS AND ABBREVIATIONS

Cations:

[C_2C_1py]	1-ethyl-3-methylpyridinium
[C_2mim]	1-ethyl-3-methylimidazolium
[$C_4(3)pz$]	1-Butil-2,3,5-trimethylpyrazolium
[C_4mim]	1-butyl-3-methylimidazolium
[C_4dmim]	1-butyl-2,3-dimethylimidazolium
[C_8mim]	1-methul-3-octylimidazolium
[$C_{10}mim$]	1-decyl-3-methylimidazolium

Anions:

[Cl]	Chloride
[CTf_3]	tris(trifluoromethanesulfonyl]methide/ triflide
[BF_4]	tetrafluoroborate
[$MeSO_3$]	methanesulfonate/mesylate
[NfO]	nonafluoro-1-butanesulfonate / nonaflate
[NTf_2]	bis(trifluoromethylsulfonyl)imide
[OTf]	trifluoromethanesulfonate/triflate
[PF_6]	hexafluorophosphate
[PFO]	perfluorooctanoate
[TFA]	trifluoroacetate

Other Abbreviations:

Al_2O_3	alumina
Ar	argon
CCD	charged-coupled device
CCU	carbon capture and utilization
$CDCl_3$	deuterated chloroform
CDU	carbon dioxide utilization
CH_4	methane
CO	carbon monoxide
CO_2	carbon dioxide
DCM	dichloromethane
DLS	dynamic light scattering
DSC	differential scanning calorimetry
EDS	energy dispersive spectroscopy
GC	gas chromatography
H_2	hydrogen
$HClO_4$	perchloric acid
IL/ILs	ionic liquid/ ionic liquids
MeOH	methanol
M-NPs	metal nanoparticles
NMR	nuclear magnetic resonance
NPs	nanoparticles
Pc	critical pressure

PPh$_3$	triphenylphosphine
R	ideal gas constant
RuCl$_3$	ruthenium chloride
Ru(acac)$_3$	ruthenium(III) acetylacetonate
[Ru(cod)Cl$_2$]$_n$	dichloro(1,5-cyclooctadiene)ruthenium(II), polymer
[Ru(ρ-cymene)Cl$_2$]$_2$	dichloro(p-cymene)ruthenium(II) dimer
Ru(cod)methylally$_2$	bis(2-methylallyl)(1,5-cyclooctadiene)ruthenium(II)
SDS	sodium dodecyl sulphate
Tc	critical temperature
TCA	trichloroanisole
TCD	thermal conductivity detector
TEM	transmission electron microscopy
TSIL	task-specific ionic liquids
UV-vis	ultraviolet-visible
ρ	density (mol/cm^{-3})

Chapter 1 – SCOPE OF THE THESIS AND GENERAL INTRODUCTION

1.1 SCOPE OF THE THESIS

In this project we intend to explore the use of CO_2 as a renewable source of carbon and we aim to convert it into fuels, preferably methane.

The reaction process was based in a continuous-flow hydrogenation of CO_2 concept [1]. In our process CO_2 hydrogenation reactions take place in the ionic liquid-rich phase on a biphasic IL+CO_2/H_2 system. The IL acts as a stationary phase where the catalyst is immobilized, and the reaction occurs. At high pressure, high-density CO_2 facilitates H_2 diffusion into the IL. The ILs negligible vapor pressure allows gas phase to dissolve in the liquid phase, while preventing liquid evaporation. The high thermal stability allows the use of ionic liquids at high reaction temperature without degradation. Furthermore, the implementation of ionic liquids in this process emulates a novel reactor concept that uses a liquid phase with high heat capacity for temperature control. The heat produced during the reaction is removed allowing the process to occur in isothermal conditions [2].

In the first stage of the work, commercial heterogeneous catalysts and Ru homogeneous were tested. Later we used a straightforward process where Ru(0) nanoparticles are formed and stabilized in-situ due to the steric and electrotactic properties of the IL to catalyse CO_2 hydrogenation towards CH_4. According to literature a similar process has been used for formic acid synthesis [3,4].

Reactions selectivity and activity were studied, and conditions of reaction optimized. We attempted to study nanoparticles properties and compare them with reactions outcome. ILs properties were also studied, in order to understand how they can promote or inhibit the reaction results and also how can they influence nanoparticle formation. The possibility of converting this reaction into continuous process was also studied.

Overall, this work aims to develop new techniques of CO_2 conversion into methane that can be later applied as CCU technologies. Together with Power to gas concept of using surplus renewable energy, this method can be "greener" and sustainable process to (almost) continuous recycle carbon.
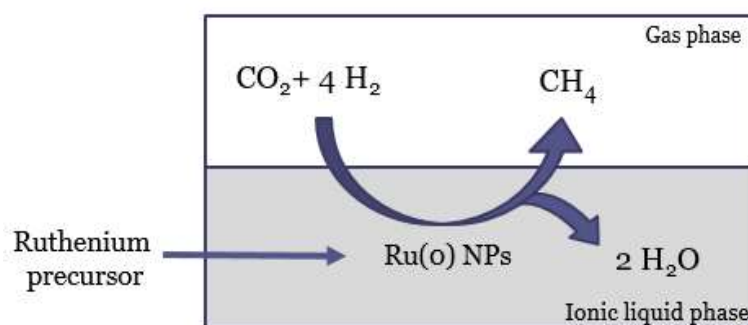
Figure 1.1. Scheme of CO_2 methanation

For the duration of this thesis, a total of four supervised students collaborated with the experimental work. Joana Afonso (Master student), assembled part the apparatus and preliminary tests, **section 3.7**. Patricia Marques (Bachelor student) followed initial reactor calibration and UV-Vis tests **section 3.3.1**. Anna Szczepańska (Erasmus student) contributed with part of optimizations tests, **section 3.2**, and finally Duarte Rente (Master student) participated in some IL tests (including IL synthesis) and the catalysts recycling study, **sections 3.5 and 3.6**. From this work resulted one peer reviewed article in ChemSusChem [5], two oral communications in international scientific symposia, and a second article is currently in preparation for submission.

1.2 CO_2 EMISSIONS

Carbon dioxide (CO_2) is widely known as one of the most significant greenhouse gases leading to global warming. Since industrial revolution, the concentration of this gas in the atmosphere has kept rising, mainly due to the combustion of fossil-fuels for energy [6]. Nowadays the sector of transportation (24%) and the sector of electricity and heat generation (42%) combined are one third of the world total from fossil-fuel combustion [7]. The production of cement, metals, and bioethanol as well as the refinery and petrochemical industries also greatly contribute to the formation of CO_2 [8]. Although CO_2 emissions produced by human action are smaller when compared with natural sources, natural emissions are mostly balanced by natural absorptions while anthropogenic CO_2 remains in the atmosphere. Despite social awareness, regarding global warming, the concentrations of atmospheric CO_2 keep steadily increasing from year to year. CO_2 concentrations kept constantly rising since the start of industrial revolution (280 ppm) and have

in 2015 reached the alarming 400 ppm [9]. Nowadays (2018) concentrations surpassed 410 ppm [10].
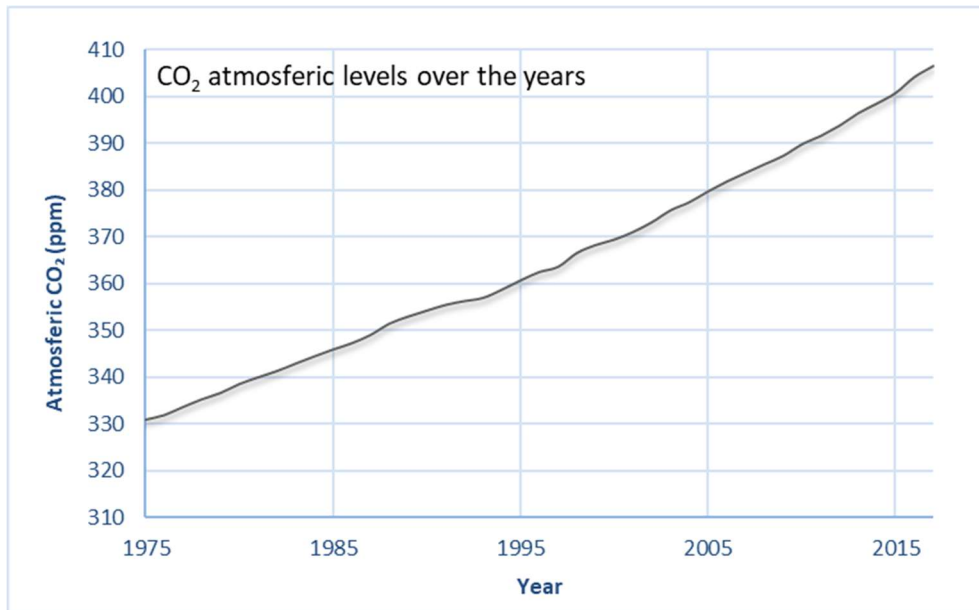
Figure 1.2. Annual mean of CO_2 atmospheric levels collected by NOAA-ESRL at the Mauna Loa observatory, Hawaii. CO_2 concentrations are expressed in mole fraction in dry air, abbreviated as ppm [10].

1.3 CO_2 MITIGATION

Lately, several efforts are being taken in account to mitigate CO_2 emission. The United Nations Paris agreement [11] is a global action climate deal between 195 countries that strives for limiting global warming to well 2°C.

Technically, there are three main strategies for reducing the CO_2 build-up in the atmosphere: reduction of the amount of CO_2 produced; storage of CO_2; and utilization of CO_2 [12].

Reduction strategy consists simply in using the energy in a more efficient way and promoting energy conservation; resource to energy sources with low carbon fuels (natural gas instead of coal) or switching to non-fossil fuels such as hydrogen or renewable energies.

Carbon Capture and Sequestration (CCS) is a method that plays a significant role in CO_2 mitigation. The main idea of this process is to capture the atmospheric CO_2 from exhausting sources where this gas concentration is higher (e.g. large power plants or cement factories), separate it from other gases and store it deep underground, in adequate geological structures [13].

3

CCS methods can be classified as: pre-combustion capture, oxy-fuel process, and post-combustion capture [14].

In Pre-combustion capture, the fuel is pre-treated with oxygen before combustion to create syngas (CO and H_2 mixture). The syngas will undergo water gas shift reaction with steam producing more H_2 and CO_2. The CO_2 is later separated by cryogenic distillation or chemical absorption process [15].

In oxy-fuel combustion, nearly pure oxygen is used for combustion instead of ambient air, and this results in a flue gas that is mainly CO_2 and H_2O, which are separated by water condensation [16].

In Post-combustion capture the removal of CO_2 is made from the flue gas produced after fuel combustion has taken place. This flue gas is usually at 1 atm, contains 10–15% of CO_2 concentration by volume and inert gases [12]. It is primarily used in pulverized coal power plants and natural gas combined cycle power plants and it is considered the most important, since it is the most preferred. It is a more mature technology, and can easily retrofit into existing plants [17]. All this capture technologies are available in the market but are costly in general, and contribute to around 70–80% of the total cost of full CCS system including capture, transport and storage [18].

Commonly, CO_2 separation is made through adsorption with a liquid solvent. Most traditional sorbents used are monoethanolamine (MEA), diethanolamine (DEA) and potassium carbonate. MEA aqueous solutions are found to be most efficient, with absorption that can reach over 90%[17]. However the process of amine regeneration after capture requires an immense amount of energy due to the use of high temperature (100-140ºC) [19]. Amine-based scrubbing systems indicate a parasitic power requirements of 22-30% of power plants output [20]. MEA corrosiveness, solvent degradation in the presence of oxygen and volatility of solvent contribute for environmental pollution [19]. Nowadays, solutions are intensively being researched and developed. Among several strategies we can enumerate the following: changing solvent concentration, the use of corrosion inhibitors, or using alternative sorbents like alternative alkanolamines, amino acid salts, sodium carbonate solutions, ammonia, blended solvents [18] the use of ionic liquids [19] and IL based compounds [21,22]. Calcium looping process is an emerging and low-cost process that may allow capture from atmospheric air based on carbonation/calcination of CaO [23].

Independently of the solution found in the future, the CCS process is already being implemented; CCS optimization process will result in the increase of the amount of pure CO_2 that will be later

4

transported in pipelines and injected at high pressure in underground geological formations. The main concerns about geo-sequestration are the environmental impact associated with the possibility of leakage and ocean acidification [14]. Furthermore, when stored in underground reservoirs CO_2 plays nothing else more than the role of a waste.

These requests an alternative or at least complementing option, which send us to the third strategy mentioned previously, CO_2 utilization.

1.4 CO_2 UTILIZATION

Carbon Dioxide Utilization (CDU), is a set of strategies that aims to use CO_2 as a chemical feedstock in different applications as a means of helping to address climate change. CO_2 can be used as solvent or working fluid. Supercritical CO_2 is nowadays used industrially in processes such as decaffeination of tea or coffee beans or extraction of trichloroanisole (TCA) from cork. As a technological fluid it can also be used to enhance oil recovery or, as air conditioning coolant, dry washing, food preservation and in beverage industries [24,25]. All these processes are of direct use and require no CO_2 conversion.

CO_2 can also take the part of starting material, as a carbon building block to produce valuable-added compounds that can be applied in the chemical industry. It is a desirable source of C_1 due to its abundancy, low price, nontoxicity and non-flammability. There are several methods used in CO_2 conversion namely chemical, biochemical, photochemical and electrochemical conversion [24]. In this study we will focus on catalytic chemical synthesis. Nowadays, the most common use of CO_2 as a chemical feedstock is in the formation of urea, which is found in around 90% of the world's fertilisers. Other compounds include carbamates, carbonates carboxylates, and biodegradable polymers [13,24]. However, it is obvious that conversion of CO_2 into chemical products will not be the final answer for greenhouse effect, after all, even if CO_2 was the starting material of all chemical compounds that could possibly be produced with it, only a small fraction of anthropogenic CO_2 would be consumed. A total of 110 million tons of CO_2 are used to produce chemicals, which corresponds to only 1% of the net annual anthropogenic release of CO_2 (13000 million tons) [26].

Another interesting product from CO2 conversion is formic acid (HCOOH). It is a chemical used in the process of tanning and dyeing leather and other textiles. It can also be used as a food preservative [27]. It is the simplest carboxylic acid and has been considered a promising way of

storing hydrogen in a liquid form [28]. Formic acid can be obtained through CO_2 hydrogenation, see equation 1. Synthesis of formic acid is one of the CO_2 hydrogenation reactions that require less consumption of H_2 and milder reaction conditions.

$$CO_2 + H_2 \leftrightarrow HCOOH \tag{1}$$

Currently it is still industrially produced by the carbonylation of methanol with carbon monoxide to methyl formate and the following hydration of the ester with water [29]. Recently, much research is made on CO_2 conversion into formic acid using both heterogeneous and homogeneous catalysts [4,30–32].

1.4.1 CO₂ CONVERSION INTO FUEL

Alternatively demand of the energy sector always high and keeps rising. Converting CO_2 back into fuels that can be reused in this sector could be the solution. This will not only reintegrate the CO_2 captured back into the carbon cycle but also lower the use of fossil fuel. CO_2 can be the starting material for potential fuels such as methanol, dimethyl ether, methane, and higher chain hydrocarbons. These products, however, would require great investment in infrastructures that would allow them to be stored and distributed in large scale.

Nowadays, methanol is mainly used as feedstock for a variety of chemicals. Noble prize winner, George Olah, proposed the "methanol economy" by defending methanol as best alternative to fossil fuels. He stated that hydrogen can be stored by CO_2 conversion to MeOH, "a convenient liquid fuel and raw material for synthetic hydrocarbons and their products" [33]. Also mentions that it is an excellent fuel due to its capacity to be blended with gasoline, although it has half the volumetric energy density relative to gasoline or diesel. However, before being able to be used pure as fuel, issues like metal corrosion and/or cold engine start, still need to be solved [34].

Through CO_2 hydrogenation, MeOH is most commonly obtained using catalysts that contain Cu and Zn as the main components together with different modifiers. Among noble-based catalyst, Pd is the most commonly used, exhibiting considerate activity and selectivity [35].

$$CO_2 + 3H_2 \leftrightarrow CH_3OH + H_2O \tag{2}$$

CO_2 hydrogenation to methanol with heterogeneous often requires high temperature (>200°C) and/or high pressure (>50 bar). Homogeneous catalysts have been studied because they can operate at lower temperatures. Also hydrogenation reaction is entropically unfavourable, performing it at lower temperature would improve the overall theoretical yield [36].

Dimethyl ether (DME) is also an emergent chemical that can be used as fuels. It is considered a good alternative to diesel since it has high centane number, produces smoke-free combustion and quickly vaporizes in the engine [34]. It can be synthesised by the reaction of methanol produced by CO_2 reduction [28]. This reaction is exothermic, is not affected by pressure. It is favoured at low temperatures.

$$2\ CH_3OH \leftrightarrow CH_3OCH_3 + H_2O \tag{3}$$

1.5 POWER TO GAS TECHNOLOGY

One of the methods of CO_2 conversion into fuels that employs renewable energy is Power-to-Gas (PtG). Although well established, renewable energies such as solar energy and wind energy are dependent on intermittent and floating sources and it is necessary to balance them to stabilize the energy network. PtG is a process that uses the surplus energy from renewable sources, and that otherwise would go to waste, and converts it into synthetic natural gas that can be injected in the gas grid and later used when energy demand is higher than renewables can supply. Methane can also be applied in transportation sector and heat production. The method uses the excess electricity in the electrolysis of water to generate H_2. This H_2 is used to reduce CO_2 producing a gas mixture that mainly contains CH_4 and H_2O, that after treatment into a gas-rich gas can be added to the natural gas grid. [2,37,38].
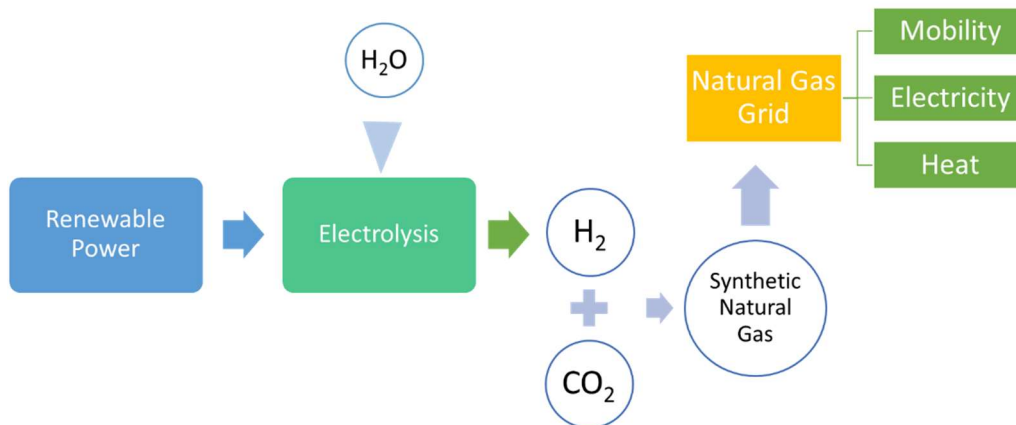
Figure 1.3. Schematics of Power-to-Gas process.

The development and implementation of this type of technologies is becoming increasingly necessary. As an example, in March 2018, for the first time in decades Portugal's renewable energy production exceeded demand on mainland (103.6%) [39]. However, due to the lack of a robust connected energy grid and/or storage solutions capable of satisfying the energy needs, the country was still dependent on fossil fuels and energy imports to balance supply energy [40].

1.6 CO_2 METHANATION

Methane is the main component of natural gas and it seems to be one of the most feasible options of CO_2 conversion since it can be fed into the existing infrastructures of natural gas without any further investment.

Methane can be obtained through the complete reduction of CO_2. This reaction is called CO_2 methanation or Sabatier reaction since it was first discovered by Sabatier and Sanders [41].

$$CO_2 + 4\,H_2 \leftrightarrow CH_4 + 2\,H_2O \qquad \Delta H_{298K} = 165 Kj.mol^{-1} \qquad (4)$$

CO_2 methanation is a reversible reaction, highly exothermic and thermodynamically favourable [42], however, there are several kinetic limitations involved with the eight-electron process to reduce the fully oxidized carbon into methane [38,43,44].

Typically, temperature of reaction range between 200-450 °C depending on catalyst, support and reaction conditions [45]. Reaction temperature is a critical factor due to the exothermic nature of the reaction, a lower value improves the selectivity of the process towards methane production.

Despite the studies carried out on CO_2 methanation, the exact reaction mechanism is not yet fully known. Two mechanisms have been proposed for the reaction. The first mechanism involves the formation of CO as an intermediate product through RWGS reaction, which is later converted into methane. The second mechanism involves the direct reaction of CO_2 with H_2 to form methane [42,46,47].

Industrially this process uses Nickel catalysts at high temperatures, due to this catalyst low cost and considerate activity [45]. However, Ni based catalyst can be deactivated even at low temperatures due to nickel particles sintering [42]. This contributed to the development of new metals catalyst.

A wide variety of other noble and non-noble metals have been widely studied as catalyst, such as Fe, Co, Cu, Pd, Rh, Ru, Pt, Mo, Re, Ag and Au. Among these, Ru reveals to be one of the most active and stable metals requiring lower reaction temperatures [43],[48].

Supported Ru and Rh catalysts are known to be more efficient that those based on Ni, but they are also increase the price of the process.

Research on CO_2 methanation with Ru mainly focus on the catalyst support since catalytic activity greatly depends on the metal dispersion and support material [45]. Ceria is one of the materials that has been widely used, improving reaction rate at 250°C when added to Ru/Al_2O_3 catalyst [49]. Methanation of CO_2 with $Ce_{0.96}Ru_{0.04}O_2$ and $Ce_{0.95}Ru_{0.05}O_2$ catalyst reached a conversion of 55% and 99% selectivity at 450 °C reaction temperature [50]. Zamani et al. [51] optimized $Ru/Mn/Cu-Al_2O_3$ preparation (10.9 wt.% of metal loading, 1035 °C calcination temperature and 5 wt.g of catalyst loading) for CO_2 methanation at 220°C, obtaining a CO_2 conversion value of 98.8%.

1.7 HIGH PRESSURE CO_2

A fluid is defined as supercritical when its temperature and its pressure are higher than the critical values [52]. While working with CO_2 at high pressure conditions it can easily become a supercritical fluid due to its low critical point (Pc = 73.8 bar, Tc = 304.2 K), see Figure 1.4. At

this state the interface between gas and liquid disappears and the density of the both phases becomes identical varying rapidly with temperature and pressure. The fluid exhibits gas-like transport properties (viscosities), liquid-like densities and diffusivities intermediate to that of a liquid and a gas. Furthermore, the capacity to dissolve organic compounds like a nonpolar solvent makes this kind of fluids a great alternative solvent for many applications.
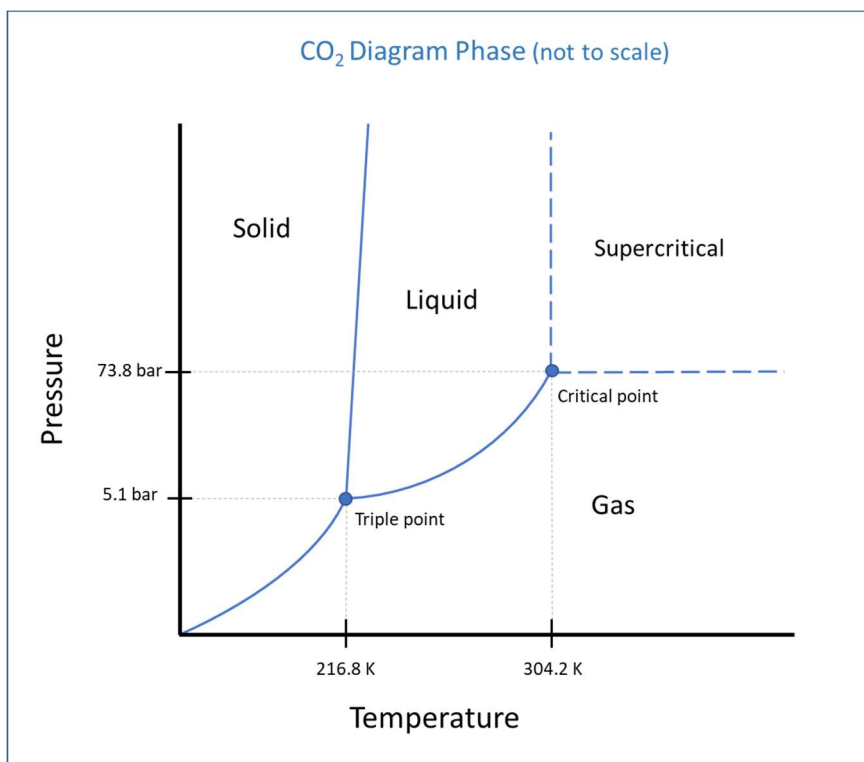
Figure 1.4. Phase diagram of CO_2.

Supercritical CO_2 (scCO_2) is the most widely used SCF due to its non-toxicity, relative inertness and nonflammability, while remaining abundant and inexpensive [54]. The solvent power of scCO_2 can be easily tuned by small changes in both temperature and pressure. Due to these properties, CO_2 is commonly considered as a "green solvent". It has been widely studied as solvent for extraction and purification, chemical reactions, polymerizations, materials processing and particle formation [55].

High pressure CO2 has been widely applied in hydrogenation reactions because it can improve the reaction rate and/or the product selectivity. Due to its ability to dissolve in reactive gases like H_2, scCO_2 improves the solubility of H_2 in the reaction mixture and eliminates mass transfer limitations [56–58].

1.8 IONIC LIQUIDS

Ionic liquids (ILs) are commonly defined as salts that are liquid at temperatures below 100ºC. Unlike common salts that are composed by inorganic ions, like chloride (Cl-) or fluoride (F-) and sodium (Na+) or potassium (K+) cations, ILs are generally composed of an organic cation and either an organic or an inorganic anion [59,60]. Those bulky organic ions usually possess a delocalized charge that causes disruption of crystal packing and reduction of the crystal lattice energy [61]. The weak interactions between these low-coordinated ions results in a reduction of melting point that can go low enough to make this kind of compounds liquid at room temperature (RTILs). Figure 1.5 illustrates some examples of the most common cations and anions constituents of ILs.
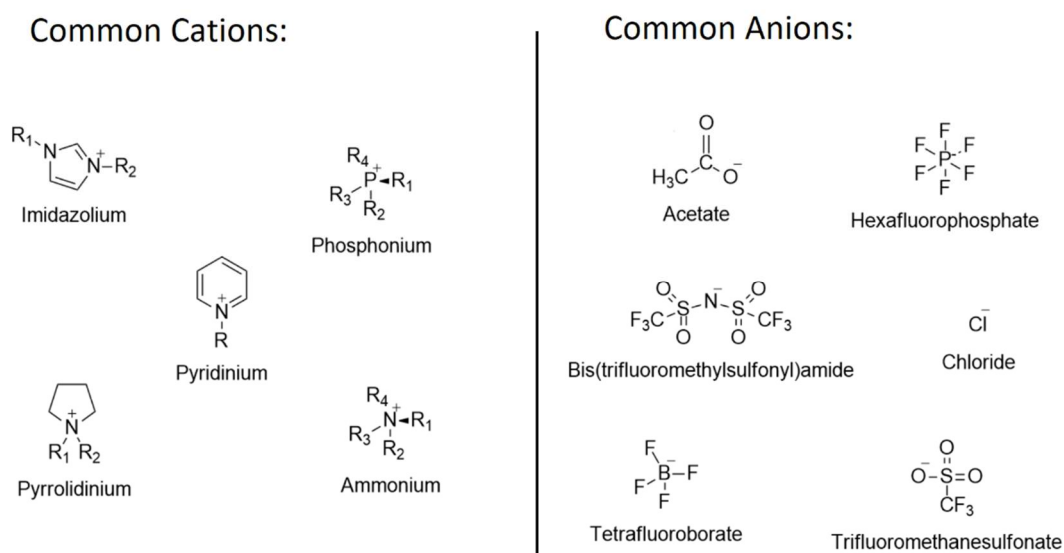
Figure 1.5. Common cations and anions of ionic liquids.

ILs are considered a "green" alternative to traditional organic solvents by many due to their unique properties. Their negligible vapour pressure and thermal stability is an advantage to volatile organic solvents in many chemical processes that require the use of high temperatures. Furthermore a very low vapour pressure reduces the risk of explosion [62]. Their density is usually is greater than that of water [63]. Most physicochemical properties of ILs can be tuned through the appropriate combination of anion and cation. A very interesting property of ILs that can be tuned is solubility. ILs are miscible with substances having very wide range of polarities

and can simultaneously dissolve organic and inorganic substances [63]. For these reasons they have been widely used as solvents for separation processes and chemical reactions. Nowadays ILs have already been tested as catalysts [64], reaction media [65], battery electrolytes, lubricants [66] and stabilizing media [67].

Solubility of CO_2 can be significantly higher in ILs than in conventional organic liquids, even in the case of physical absorption. Furthermore, the low volatility of ILs allows a great dissolution of CO_2 in the IL phase with no transference at all the IL in the gas phase.

As mention earlier, ILs have been recently tested as CCS solvents. The interest on CO_2 capture from flue gases of power stations or from natural gas sources has promoted the study of task-specific ionic liquids with high absorption capacity of that gas [68,69] and highly selective solubility in relation to other gases, like nitrogen or methane [70]. The advantage of IL over the amines that are currently used for CO_2 absorption is that they are much more amenable to in situ transformations, avoiding the high energy losses involved in the absorption-desorption cycles from amines. Research for CO_2 capture involving ILs include the use the task specific ILs, IL-based solvents, membranes and polymers [22,71].

Mixtures of high pressure carbon dioxide and ILs were first used for green processing by Brennecke and collaborators [72]. Their initial works with imidazolium based ILs, a common kind of cation, allowed to understand that CO_2 interaction with the anion is the main factor in which solubility depends on. In this study, the anions that presented stronger connection were the ones with fluoroalkyl groups in their structure, namely [OTf], [NTf$_2$], and [CTf$_3$]. The increase of the chain length of the cation also increases CO_2 solubility; however, it is a much minor effect.

Thermal stability is also primarily related to the nature of the anion, accordingly with Papaiconomou at al [73] for every cation they studied the thermal stability follows the trend: [NTf$_2$] > [NfO] > [OTf] > [DCA].

When applying CO_2 in hydrogenation reactions and IL and a catalyst immobilizer the process will have two phases, the gas phase and the liquid phase. Maybe even a third phase in case the catalyst is in solid phase. Different outcomes may occur. The viscosity of the IL may increase the diffusional limitations, since reagents need to travel from the gas phase, to the liquid to the catalyst, which will inhibit the reaction. The high solubility of CO_2 in the IL will make it drag the H_2 with it when it is mixed with the liquid phase, does increasing the amount of H_2 dissolved in this phase promoting the reaction. Moreover, IL+CO_2 mixture also proved to drive selectivity of hydrogenation towards different products[74]. Tumas et al.[75] reported a pioneer work on

12

reactions in biphasic ionic liquid + supercritical CO_2 mixtures. In their work, IL 1-butyl-3-methylimidazolium hexafluorophosphate was applied in for hydrogenation of alkenes and CO_2.

1.9 NANOPARTICLES

Nanoparticles (NPs) are defined as any material with at least one dimension within 1-100 nm range size [76]. Due to their catalytic, optical, magnetic and electronic properties, fine metal particles in the nanometre size range have numerous applications in different fields such as chemical processes, medicine, biology, micro and nanoelectronics [77,78].

There are several methods of nanoparticle synthesis, however these can be classified into two main categories: top-down and bottom-up. In the top-down approach, the nanoparticles are formed by size reduction (usually through grinding) of metallic aggregates, this method being associated with high costs of synthesis and is limited to the formation of MNP's with 100 nm [77]. On the other hand, bottom-up approaches aim at the use of a molecular precursor as starting point, such as reduction of metal salts or the photolytic, sonolytic, or thermal decomposition of metal–organic precursors [79].

Nanoparticles have properties intermediate between bulk and single particles. One of the main advantages to use nanoparticles as catalysts is related with their high catalytic activity. However, these nanoparticles need to be stabilized against aggregation into larger particles and eventually bulk aggregates, in order to retain their catalytic activity. Aggregation occurs due to their extensively large surface area and the main means of their stabilization in solution utilizes electrostatic or steric protection.

It is recognized that ILs are suitable media for stabilization of metal nanoparticles (NPs) and excellent alternatives to surfactants or solid supports. Additionally, ILs are an effective media for the synthesis of different metal nanoparticles [80], metal oxide and complexes nanoparticles [81] and alloys nanoparticles with control of morphology, size, size distribution and other properties. It was found that several ILs can be used as solvent and stabilizer to efficiently tune the particle growth and prevent undesired nanoparticle aggregations. Also, metal NPs can be synthesized in ILs media trough chemical reduction or decomposition, photochemical reduction or electro-reduction/electrodeposition of metal salts where the metal atom is in a formally positive oxidation state. Metal carbonyls $M_x(CO)_y$ or [Ru(COD)(COT)] can be decomposed to metal NPs in ILs by conventional heating, UV photolysis or microwave irradiation.[82]

Dupont et al reported [67] the use of alkylmethylimidazolium based ILs as suitable reaction media for the ruthenium nanoparticles production. Normally, imidazolium ILs reaction media provides both steric and electronic protection [83] to stabilize the Ru nanoparticles produced when the precursor is reduced by H_2. In his work he formed Ru(0) NPs using Ru (II) precursors such as Ru(cod)methylally$_2$ and ILs as well as mild conditions and was able to use them in hydrogenation reactions of arenes. In the case of Ru NPs, the size and shape is governed by the degree of self-organization of the imidazolium based IL in which they are generated: in general the more structured IL corresponds to smaller NPs [84].

Srivastava et all hydrogenated CO_2 with Ru nanoparticles stabilized in 1,3-di(N,N-dimethylaminoethyl)-2-methylimidazolium bis(trifluoromethylsulfonyl) imide [3]. With mild conditions of reaction (temperatures below 120°C and total pressures of 40 bar) he was able to obtain formic acid and a catalyst recyclability of at least 7 uses.

Chapter 2 – EXPERIMENTAL SECTION

This chapter contains a variety of information regarding the experimental work and is divided in tree main sections:

Section 2.1 describes in detail the apparatus that was designed and built from scratch for the execution of this work. All hydrogenating reactions (with one exception, see **section 2.3.3** and **3.4.1**) took place in this installation. Changes made to the apparatus during the work are also described in this section.

Section 2.2, named material and methods begins with the description of all compound and materials used for the work, giving a special emphasis to the ILs used. Among these ILs used, a total of 10 imidazolium ILs were synthesised. Their syntheses, NMRs and elemental analyses is also described in this section. After materials description, follows the protocols of different hydrogenation reactions executed in the installation described in **section 2.1**. These protocols are ordered chronologically. The final part of this section describes the analytical methods executed to the reaction samples during the work.

Section 2.3, named Reactor Calibration, describes all laboratory work and necessary calculations involved on the assessment of the reaction performance, most precisely, all work involved in the calculation the reactions yield. This work started with the simple determination of the apparatus volume. The second part contains all calculations and equations and methods that lead to the reaction's yield of methane using the initial amount of H_2 and the produced amount of CH_4. Later it's explained how the initial amount of H_2 and final amount of CH_4 are calculated. Since the final amount of CH_4 is dependent of CH_4 molar fraction and the initial amount of CO_2, this section is followed by an explanation on how GC data is converted into the required molar fraction of CH_4 and the two experimental methods used to find a correlation between experimental values and CO_2 initial amount. Methane was the main product of reaction, but not the only one, the next section describes the changes in the calculations in case CO is the reaction product.

Hydrogenation reaction used a Parr reactor once to test stirring effect, this reactor is described in **section 2.3.3**. All procedures required to calculate the yield are presented in this section including volume determination and the explanation of how the magnetic drive's dead volume changes CH_4 yield calculations.

Finally, the equations that were used to calculate reactions turnover time and CO_2 conversion are described in this section.

2.1 DESCRIPTION OF THE APPARATUS

A new high-pressure apparatus, where to carry out hydrogenations of carbon dioxide, was designed and built. This apparatus included the reactor and its feeding lines, as well as two additional sections, designed to obtain representative samples of the gaseous reaction products. The apparatus (Figure 2.1) was thus composed by tree main sections: (RZ) reaction zone, (EZ) expansion zone, (CZ) capture zone. All main parts and connections were made in stainless steel, and it was assembled inside a fume hood.
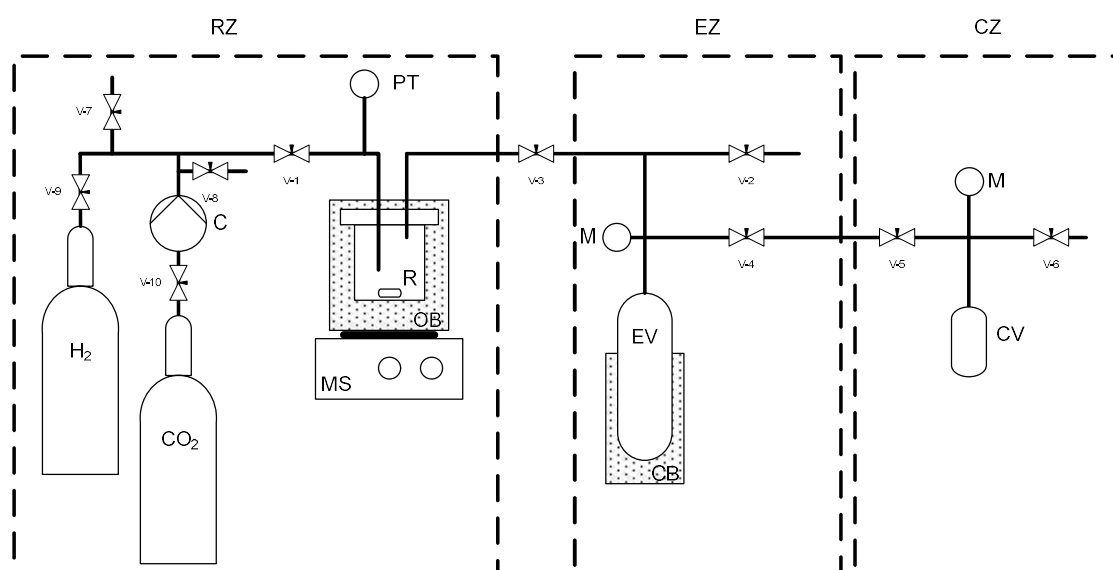
Figure 2.1. Schematics of the hydrogenation apparatus: (RZ) reaction zone, (EZ) expansion zone, (CZ) capture zone, (C) CO_2 compressor, (R) reactor, (OB) oil bath, (MS) magnetic stirrer, (PT) pressure transducer, (M) manometer, (EV) expansion vessel, (CB) cooling bath, (CV) capture vessel, (v-1 to v-10) valves.

The reaction zone is the part of the installation where CO_2 is hydrogenated. It is composed by a 30 cm^3 stainless steel vessel (Figure 2.2) – designated as reactor from now on, - with inlet and outlet tubing. The head of the reactor has an inlet tubing dip that allows the added gas to pass through any liquid solvent added to the reactor. The reactor's inlet is connected to a H_2 cylinder, and to the CO_2 supply through a gas compressor (C). Both cylinders are connected to valves (v-7 and v-8) that can be open to depressurize the system to atmosphere if necessary. The outlet of the reactor is attached to the expansion zone.

Figure 2.2. Picture of the reactor. From the right to the left: head of the reactor with a dip tube, cylinder, split ring closure rings with bolts, drop band.

The use of an oil bath to heat the reactor was adopted, due to the lower risk of deflagration with this method. Reactor heating was achieved by dipping it inside a Grant W6 Heated Water Bath Circulator filled with oil. Oil bath maximum temperature set is 150ºC. Stirring in the reactor was obtained using a magnetic stirrer (MS) below the oil bath and a magnetic stirring bar inside the autoclave (see Figure 2.1). The oil bath kept mixed by the circulator motor.

The expansion zone is composed by a large vessel (EV) connected to a manometer (M), a valve for pressure release (v-2), and a connection for the capture vessel (CV). The expansion vessel has is used to depressurize the system into a contained area, lowering the pressure inside the system and facilitate sampling.

The capture zone is composed by a capture vessel (CV), connected to a manometer, a valve (v-5) that connects the expansion to the capture zone, and a valve (v-6) for the admission of vacuum in the mentioned zones. The purpose of this zone is to be a portable vessel that after being filled with sample gas from the expansion zone can then be disconnected (v-5) and taken to the GC where the gas sample is analysed.

A picture of the apparatus is displayed below:

Figure 2.3. Picture of the reaction apparatus.

During the experimental work, some minor changes took place in the apparatus. The cooling bath of the expansion zone was removed. The size of the magnetic bars was changed.

At the final stage of the work, the sample capture method was changed, and the expansion zone and the capture zone were no longer used.

2.2 Materials and Methods

2.2.1 Reactants

Hydrogen and carbon dioxide were supplied by Air Liquid with a stated molar purity of 99.999% and 99.98% respectively.

2.2.2 Catalysts

Commercial heterogeneous catalysts: Palladium (0.5 wt.%) on alumina in 3.2 pellets, Rhodium (0.5 wt.%) on alumina in 3.2 pellets, Ruthenium (0.5 wt.%) on alumina in 3.2 pellets were supplied by Sigma-Aldrich.

Ruthenium catalytic Precursors: Dichloro(1,5-cyclooctadiene)ruthenium(II), polymer, 95%; Dichloro(p-cymene)ruthenium(II) dimer; Bis(2-methylallyl)(1,5-cyclooctadiene)ruthenium(II) and Ruthenium (III) chloride hydrate and Ruthenium(III) acetylacetonate, 97% were supplied by Aldrich.
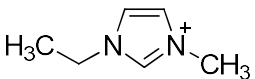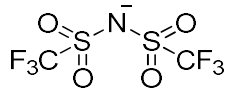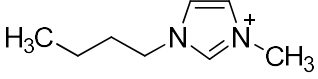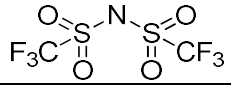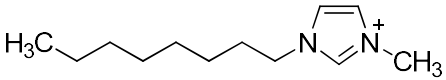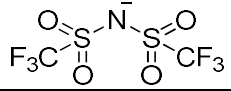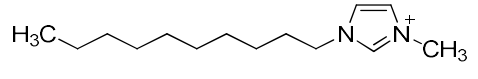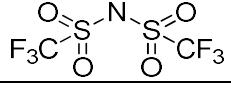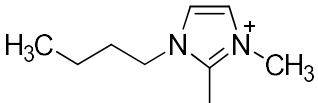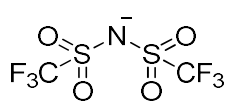
2.2.3 Solvents
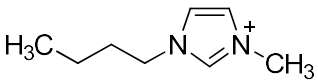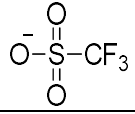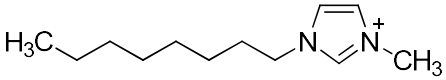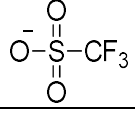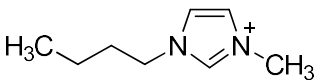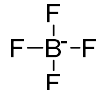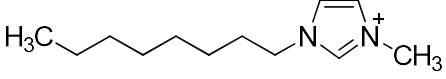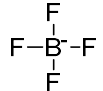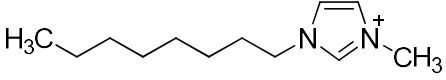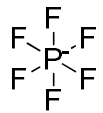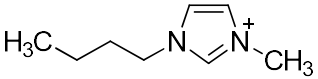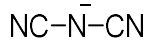
Acetone (≥99.8%) was supplied by Honeywell. Acetonitrile anhydrous (99.8%) was supplied by Sigma-Aldrich. Dichloromethane (≥99.9%) was supplied by Honeywell. Ethanol (96º) and ethanol absolute anhydrous (≥99.9%) were supplied by Carlo Erba. Isopropanol (≥99%) was supplied by Sigma. Methanol (≥99.8%) was supplied by Sigma-Aldrich; Toluene, ACS grade, (≥99.9%) was supplied by Sigma-Aldrich.

2.2.4 IONIC LIQUIDS

A list of all used ILs with some detailed information (structure, molecular weight, purity and supplier) can be found in tables Table 2.1, Table 2.2 and Table 2.3:

Table 2.1 List of commercial ILs used.

Name: 1-Ethyl-3-methylimidazolium bis(trifluoromethylsulfonyl)imide		
MW: 391.31 g.mol^{-1}	Supplier: Solchemar	Purity: ≥ 98%
[C₂mim][NTf₂]	**Cation structure**	**Anion structure**

Name: 1-Butyl-3-methylimidazolium bis(trifluoromethylsulfonyl)imide		
MW: 419.36 g.mol^{-1}	Supplier: Solchemar	Purity: ≥ 98%
[C₄mim][NTf₂]	**Cation structure**	**Anion structure**

Name: 1-Methyl-3-octylimidazolium bis(trifluoromethylsulfonyl)imide		
MW: 475.47g.mol^{-1}	Supplier: Io-li-tec	Purity: 99%
[C₈mim][NTf₂]	**Cation structure**	**Anion structure**

Name: 1-Decyl-3-Methylimidazolium bis(trifluoromethylsulfonyl)imide		
MW: 503.53 g.mol^{-1}	Supplier: Solchemar	Purity: >98%
[C₁₀mim][NTf₂]	**Cation structure**	**Anion structure**

Name: 1-Butyl-2,3-dimethylimidazolium bis(trifluoromethylsulfonyl)imide		
MW: 433.39 g.mol^{-1}	Supplier: Io-li-tec	Purity: 99%
[C₄dmim][NTf₂]	**Cation structure**	**Anion structure**

Name: 1-Butyl-3-methylimidazolium triflate		
MW: 288.29 g.mol⁻¹	**Supplier**: Io-li-tec	**Purity**: 99%

	Cation structure	Anion structure
[C₄mim][OTf]	H₃C—⟨imidazolium⟩N⁺–CH₃	O⁻–S(=O)(=O)–CF₃

Name: 1-Methyl-3-octylimidazolium triflate		
MW: 344.40 g.mol⁻¹	**Supplier**: Io-li-tec	**Purity**: 99%

	Cation structure	Anion structure
[C₈mim][OTf]	H₃C—(chain)—N⁺⟨imidazolium⟩N–CH₃	O⁻–S(=O)(=O)–CF₃

Name: 1-Butyl-3-methylimidazolium tetrafluoroborate		
MW: 226.02 g.mol⁻¹	**Supplier**: Solchemar	**Purity**: >98%

	Cation structure	Anion structure
[C₄mim][BF₄]	H₃C—(chain)—N⟨imidazolium⟩N⁺–CH₃	F–B⁻(F)(F)–F

Name: 1-Methyl-3-octylimidazolium tetrafluoroborate		
MW: 282.13 g.mol⁻¹	**Supplier**: Solchemar	**Purity**: >98%

	Cation structure	Anion structure
[C₈mim][BF₄]	H₃C—(chain)—N⟨imidazolium⟩N⁺–CH₃	F–B⁻(F)(F)–F

Name: 1-Methyl-3-octylimidazolium hexafluorophosphate		
MW: 340.29 g.mol⁻¹	**Supplier**: Solchemar	**Purity**: >98%

	Cation structure	Anion structure
[C₈mim][Pf₆]	H₃C—(chain)—N⟨imidazolium⟩N⁺–CH₃	P(F)(F)(F)(F)(F)F

Name: 1-Butyl-3-methylimidazolium dicyanoamide		
MW: 205.26 g.mol⁻¹	**Supplier**: Solchemar	**Purity**: >98%

	Cation structure	Anion structure
[C₄mim][DCA]	H₃C—(chain)—N⟨imidazolium⟩N⁺–CH₃	NC–N⁻–CN
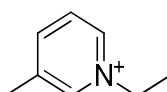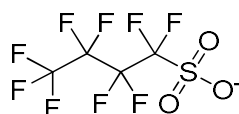
Name: 1-Ethyl-3-methylpyridinium perfluorobuanesulfonate		
MW: 421.28 g.mol⁻¹	**Supplier**: Merck	**Purity**: 98%
[C₂C₁py][NfO]	**Cation structure**	**Anion structure**

Table 2.2. List of commercial ILs used for synthesis of new ILs.
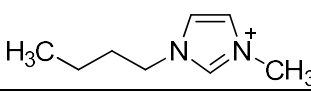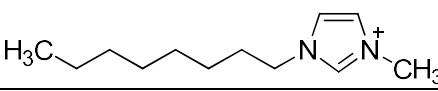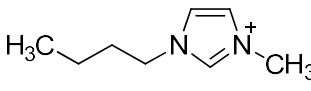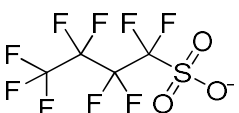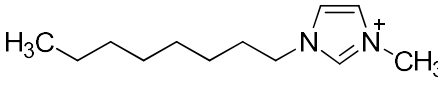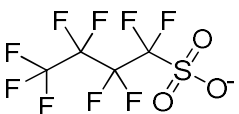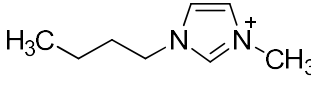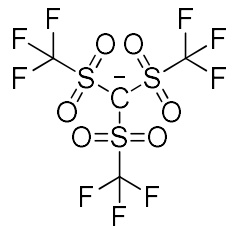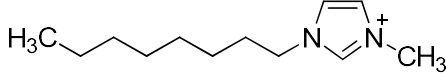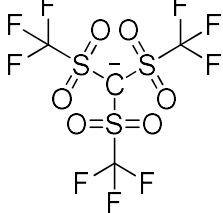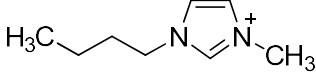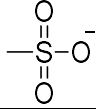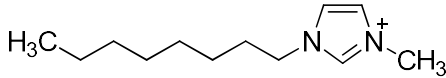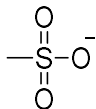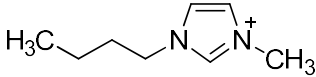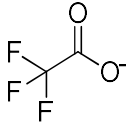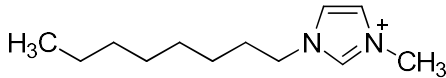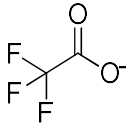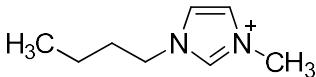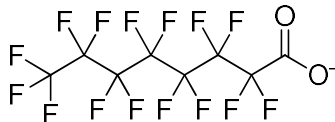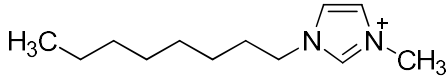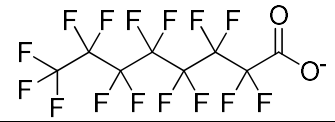
Name: 1-Butyl-3-methylimidazolium chloride		
MW: 174.67 g.mol⁻¹	**Supplier**: Solchemar	**Purity**: >98%
[C₄mim][Cl]	**Cation structure**	**Anion structure** $\overset{-}{Cl}$

Name: 1-Methyl-3-octylimidazolium chloride		
MW: 230.78 g.mol⁻¹	**Supplier**: Solchemar	**Purity**: >98%
[C₈mim][Cl]	**Cation structure**	**Anion structure** $\overset{-}{Cl}$

Table 2.3. List of synthesized ILs.

Name: 1-Butyl-3-methylimidazolium perfluorobuanesulfonate		**MW**: 438.31 g.mol⁻¹
[C₄mim][NfO]	**Cation structure**	**Anion structure**

Name: 1-Methyl-3-octylimidazolium perfluorobuanesulfonate		**MW**: 494.42 g.mol⁻¹
[C₈mim][NfO]	**Cation structure**	**Anion structure**

Name: 1-Butyl-3-methylimidazolium tris(trifluoromethanesulfonyl]methide		**MW**: 559.99 g.mol⁻¹
[C₄mim][CTf₃]	**Cation structure**	**Anion structure**

Name: 1-Methyl-3-octylimidazolium tris(trifluoromethanesulfonyl]methide		**MW**: 606.54 g.mol⁻¹
[C8mim][CTf3]	**Cation structure**	**Anion structure**

Name: 1-Butyl-3-methylimidazolium mesylate		**MW**: 234.32 g.mol⁻¹
[C4mim][MeSO3]	**Cation structure**	**Anion structure**

Name: 1-Methyl-3-octylimidazolium mesylate		**MW**: 290.42 g.mol⁻¹
[C8mim][MeSO3]	**Cation structure**	**Anion structure**

Name: 1-Butyl-3-methylimidazolium trifluoroacetate		**MW**: 252.23 g.mol⁻¹
[C4mim][TFA]	**Cation structure**	**Anion structure**

Name: 1-Methyl-3-octylimidazolium trifluoroacetate		**MW**: 308.34 g.mol⁻¹
[C8mim][TFA]	**Cation structure**	**Anion structure**

Name: 1-Butyl-3-methylimidazolium perfluorooctanoate		**MW**: 552.28 g.mol⁻¹
[C4mim][PFO]	**Cation structure**	**Anion structure**

Name: 1-Methyl-3-octylimidazolium perfluorooctanoate		**MW**: 608.38 g.mol⁻¹
[C8mim][PFO]	**Cation structure**	**Anion structure**

Syntheses of ionic liquids

The experimental methods applied to the syntheses of the ionic liquids used in this work that could not be bought from commercial suppliers are detailed below, NMR spectra can be found in Appendix A.

Synthesis of [C₄mim][NfO]: Potassium nonafluoro-1-butanesulfonate (1.2 equiv.) was added slowly to a stirred solution of [C$_4$mim][Cl] (3.17 g, 0.018 mol) in DCM (40 cm^3). The mixture was stirred overnight at room temperature. The precipitated salt was filtered off, and the solution was washed with water (3 x 20 cm^3). The organic layer was collected, dried with a rotary evaporator, and kept under vacuum for 24h. This IL was obtained in 82.3% yield and presented itself as a colourless liquid. ^{1}H NMR (400 MHz, CDCl$_3$): δ 9.07 (s, 1H), 7.37 (d, J=14.8 Hz, 2H), 4.5 (t, J = 7.4 Hz, 2H), 3.93 (s, 3H), 1.88 – 1.76 (m, 2H), 1.38 – 1.25 (m, 2H), 0.90 ppm (t, J = 7.3 Hz, 3H). ^{13}C NMR (101 MHz, CDCl$_3$): δ 137.02, 123.99, 122.52, 119.22, 116.35, 114.23, 111.10, 50.12, 36.56, 32.23, 19.61, 13.45 ppm. ^{19}F NMR (376 MHz, CDCl$_3$): δ -81.02 (t, J = 9.9 Hz, 3F), -114.69 – -115.16 (m, 2F), -121.55 – -121.92 (m, 2F), -125.80 – -126.28 ppm (m, 2F). Anal. Calc.: C, 32.88; H, 3.45; N, 6.39. Found: C, 32.71; H, 3.48, N, 6.25.

Synthesis of [C₈mim][NfO]: Potassium nonafluoro-1-butanesulfonate (1.2 equiv.) was added slowly to a stirred solution of [C$_8$mim][Cl] (3.05 g, 0.013 mol) in DCM (45 cm^3). The mixture was stirred overnight at room temperature. The precipitated salt was filtered off, and the solution was washed with water (3 x 20 cm^3). The organic layer was collected, dried with a rotary evaporator and kept under vacuum for 24 h. This IL was obtained in 67.9% yield as a white solid at room temperature. After reaching melting temperature (T$_m$ = 38.33°C) the IL presents itself as a colourless liquid. ^{1}H NMR (400 MHz, CDCl$_3$): δ 9.14 (s,1H), 7.37 (s,1H), 7.30 (s,1H), 4.17 (t, J = 7.3 Hz, 2H), 3.97 (s, 3H), 1.92 – 1.75 (m, 2H), 1.43 – 1.13 (m, 10H), 0.86 ppm (t, J = 6.4 Hz, 3H). ^{13}C NMR (101 MHz, CDCl$_3$): δ 136.93, 123.79, 122.19, 119.07, 116.93, 114.39, 114.05, 50.26, 36.44, 31.73, 30.26, 29.05, 28.94, 26.25, 22.70, 13.99 ppm. ^{19}F NMR (400 MHz, CDCl$_3$): δ -80.94 (t, J = 9.8 Hz, 3F), -114.81 – -114.98 (m, 2F), -121.62 – -121.82 (m, 2F), -125.93 – -126.13 ppm (m, 2F). Anal. Calc.: C, 38.87; H, 4.69; N, 5.67. Found: C, 38.81; H, 4.70; N, 5.62.

Synthesis of [C₄mim][CTf₃]: Potassium tris(trifluoromethanesulfonyl)methide (1.2 equiv.) was added slowly to a stirred solution of [C$_4$mim][Cl] (3.10 g, 0.018 mol) in ethanol (60 cm^3). The mixture was stirred overnight at room temperature. The precipitated salt was filtered off, and the solution was dried with a rotary evaporator, washed with water (3 x 2 cm^3), dried again by rotary evaporator and kept under vacuum for 24 h. This IL was obtained in 73.3% and presented itself as a colourless liquid. ^{1}H NMR (400 MHz, CDCl$_3$): δ 8.43 (s, 1H), 7.32 (s, 1H), 7.28 (s, 1H), 4.11

24

(t, J = 7.4 Hz, 2H), 3.86 (s, 3H), 1.90 – 1.97 (m, 2H), 1.37 – 1.27 (m, 2H), 0.92 ppm (t, J = 7.3 Hz, 3H). ^{19}F NMR (376 MHz, CDCl$_3$): δ -77.04 ppm (s,9F). Anal. Calc.: C, 34.80; H, 2.74; N, 5.07. Found: C, 26.14; H, 2.97; N, 4,83.

Synthesis of [C$_8$mim][CTf$_3$]: Potassium tris(trifluoromethanesulfonyl)methide (1.2 equiv.) was added slowly to a stirred solution of [C$_8$mim][Cl] (3.11g, 0.013 mol) in a 1:1 mixture of ethanol and DCM (40 cm^3). The mixture was stirred overnight at room temperature. The precipitated salt was filtered off, and the solution was in dried by rotary evaporator, washed with water (3 x 2 cm^3), dried again by rotary evaporator and kept under vacuum for 24 h. This IL was obtained in 86.4% yield and presented itself as a colourless liquid. ^{1}H NMR (400 MHz, CDCl$_3$): δ 8.54 (s, 1H), 7.28 (d, J = 10.2 Hz, 4H), 4.12 (t, J = 7.4 Hz, 2H), 3.90 (s, 3H), 1.91 – 1.76 (m, 2H), 1.38 – 1.19 (m, 10H), 0.85 (t, J = 6.9 Hz, 3H). ^{13}C NMR (101 MHz, CDCl$_3$): δ 135.82, 123.86, 122.40, 121.82, 118.64, 50.40, 36.41, 31.71, 30.15, 29.01, 28.88, 26.20, 22.64, 14.09 ppm. ^{19}F NMR (376 MHz, CDCl$_3$): δ = -76.71 ppm (s, 9F). Anal. Calc.: C, 31.68; H, 3.82; N, 4.62. Found: C, 31.60; H, 3.63; N, 3,42.

Synthesis of [C$_4$mim][MeSO$_3$]: Sodium mesylate was prepared by adding 25 cm^3 of a 0.5M sodium hydroxide solution to 10 cm^3 of a 1M methanesulfonic acid solution in methanol, and dried via rotary evaporator and vacuum.Sodium mesylate (1.2 equiv) was added slowly to a stirred aqueous solution (30 cm^3) of [C$_4$mim][Cl] (2.11 g, 0.012 mol). The mixture was stirred overnight at room temperature. Later all water was removed using a rotary evaporator followed by under vacuum heating. The dried sample was washed with ethanol, and the precipitated salt was filtered off, and the solution was again dried with a rotary evaporator and placed under vacuum. Later, the sample was washed with DCM, any remaining salt was filtered off, and the solution was again in dried by rotary evaporator and kept under vacuum for 24 h. This IL was obtained in 73.4% yield and presented itself as a colourless liquid. ^{1}H NMR (400 MHz, CDCl$_3$): δ 10.14 (s, 1H), 7.53 (s, 1H), 7.40 (s, 1H), 4.25 (t, J = 7.3 Hz, 2H), 4.02 (s, 3H), 2.90 (s, 3H), 1.89 – 1.72 (m, 2H), 1.39 – 1.22 (m, 2H), 0.89 ppm (t, J = 7.3 Hz, 3H). ^{13}C NMR (101 MHz, CDCl$_3$): δ 137.97, 123.35, 121.79, 49.61, 39.52, 36.36, 31.98, 19.30, 13.27 ppm. Anal. Calc.: C, 46.13; H, 7.74; N, 11.96. Found: C, 46.14; H, 7.54; N, 12.14.

Synthesis of [C$_8$mim][MeSO$_3$]: Sodium mesylate was prepared by adding 25 cm^3 of a 0.5M sodium hydroxide solution to 10 cm^3 of a 1M methanesulfonic acid solution in methanol, and dried via rotary evaporator and vacuum. Sodium mesylate (1.2 equiv.) was added slowly to a stirred aqueous solution (60 cm^3) of [C$_8$mim][Cl] (3.05 g, 0.013 mol). The mixture was stirred overnight at room temperature. Later all water was removed using a rotary evaporator followed by under vacuum heating. The dried sample was washed with ethanol, and the precipitated salt

was filtered off, and the solution was again dried with a rotary evaporator and placed under vacuum. Later, the sample was washed with DCM, any remaining salt was filtered off, and the solution was again in dried by rotary evaporator and kept under vacuum for 24 h. The obtained IL, 78.1% yield presented itself as a colourless liquid. ^{1}H NMR (400 MHz, CDCl$_3$): δ 10.08 (s, 1H), 7.48 (s, 1H), 7.33 (s, 1H), 4.23 (t, J = 7.4 Hz, 2H), 4.03 (s, 3H), 2.72 (s, 3H), 1.89 – 1.75 (m, 2H), 1.35 – 1.12 (m, J = 7.7 Hz, 10H), 0.82 ppm (t, J = 6.5 Hz, 3H). ^{13}C NMR (101 MHz, CDCl$_3$): δ 138.48, 123.88, 122.07, 50.45, 40.02, 36.91, 32.01, 30.65, 29.30, 26.61, 22.92, 18.85, 14.40 ppm. Anal. Calc.: C, 53.76; H, 9.02, N, 9.65. Found: C. 53.92; H, 9,17; N, 9.88.

Synthesis of [C$_4$mim][TFA]: Sodium trifluoroacetate (1.2 equiv) was added slowly to a stirred solution of [C$_4$mim][Cl] (2.89 g, 0.017 mol) in ethanol (35 cm^3). The mixture was stirred overnight at room temperature. The precipitated salt was filtered off, and the solution was dried with a rotary evaporator and placed under vacuum. Later, the sample was washed with DCM, any remaining salt was filtered off, and the solution was again dried by rotary evaporator and kept under vacuum for 24h. This IL was obtained in 68.9% and presented itself as a colourless liquid. ^{1}H NMR (400 MHz, CDCl$_3$): δ 9.99 (s, 1H), 7.37 (d, J = 25.5 Hz, 2H), 4.18 (t, J = 7.3 Hz, 2H), 3.95 (s, 3H), 1.87 – 1,71 (m, 2H), 1.38 – 1.22 (m, 2H), 0.89 ppm (t, J = 7.3 Hz, 3H). ^{13}C NMR (101 MHz, CDCl$_3$): δ 162.27, 139.17, 124.10, 122.55, 119.55, 116.60, 50.51, 37.00, 32.79, 20.12, 14.04 ppm. ^{19}F NMR (376 MHz, CDCl$_3$): δ -75.22 ppm (s,3F). Anal. Calc.: C, 47.62; H, 5.99; N, 11.11. Found: C, 47,39; H, 6,18; N, 10,99.

Synthesis of [C$_8$mim][TFA]: Sodium trifluoroacetate (1.2 equiv.) was added slowly to a stirred solution of [C$_8$mim][Cl] (2.79 g, 0.012 mol) in ethanol (40 cm^3). The mixture was stirred overnight at room temperature. The precipitated salt was filtered off, and the solution was in dried by rotary evaporator and placed under vacuum. Later, the sample was washed with DCM, any remaining salt was salt was filtered off, and the solution was again in dried by rotary evaporator and kept under vacuum for 24h. The obtained IL, 75.2% yield presented itself as a yellowish liquid. ^{1}H NMR (400 MHz, CDCl$_3$): δ 9.88 (s,1H), 7.30 (d, J = 32.0 Hz, 2H), 4.18 (t, J = 7.3 Hz, 2H), 3.95 (s, 3H), 1.90 – 1.74 (m, 2H), 1.35 – 1.14 (m, 10H), 0.85 ppm (t, J = 6.4 Hz, 3H). ^{13}C NMR (101 MHz, CDCl$_3$): δ 162.19, 161.86, 137.98, 123.94, 122.11, 118.89, 115.97, 50.34, 36.56, 32.05, 30.51, 29.36, 29.28, 26.53, 22.96, 14.41 ppm. ^{19}F NMR (376 MHz, CDCl$_3$): δ -75.64 (s, 3F). Anal. Calc.: C, 54.53; H, 7.52; N, 9.09. Found: C, 54.74; H, 7.63; N, 9.11.

Synthesis of [C$_4$mim][PFO]: Sodium perfluorooctanoate (1.2 equiv.) was added slowly to a stirred solution of [C$_4$mim][Cl] (0.72g, 0.004 mol) in acetone (50 cm^3). The mixture was stirred overnight at room temperature. The precipitated salt was filtered off, and the solution was dried with a rotary evaporator and placed under vacuum. Later, the sample was washed with DCM, any

26

remaining salt was filtered off, and the solution was again dried by rotary evaporator and kept under vacuum for 24h. This IL was obtained in 74.6% and presented itself as a colourless liquid. ^{1}H NMR (400 MHz, CDCl$_3$): δ 10.05 (s, 1H), 7.37 (d, J = 30.7 Hz, 2H), 4.19 (t, J = 7.3 Hz, 2H), 3.96 (s, 3H), 1.88 – 1.73 (m, 2H), 1.37 – 1.23 (m, 2H), 0.89 ppm (t, J = 7.3 Hz, 3H). ^{13}C NMR (101 MHz, CDCl$_3$): δ 161.18, 138.23, 123.55, 121.96, 118.64, 115.77, 108.29, 49.79, 36.24, 32.10, 19.38, 13.20 ppm. ^{19}F NMR (376 MHz, CDCl$_3$): δ -80.86 (t, J = 10.9 Hz, 3F), -116.57 (t, J = 12.4 Hz, 2F), -119.18 – -124.86 (m, 8F), -125.77 – -126.69 ppm (m, 2F). Anal. Calc.: C, 34.80; H, 2.74; N, 5.07. Found: C, 34.70; H, 2.78; N, 5,25.

Synthesis of [C$_8$mim][PFO]: Sodium perfluorooctanoate was added slowly to a stirred solution of [C$_8$mim][Cl] (1.06 g, 0.005 mol) in acetone (50 cm^3). The mixture was stirred overnight at room temperature. The precipitated salt was filtered off, and the solution was in dried by rotary evaporator and kept under vacuum for 24h. The sample was washed with DCM, any remaining salt was filtered off, and the solution was again in dried by rotary evaporator and kept under vacuum for 24h. This IL was obtained in 79.0% yield as a white solid at room temperature. After reaching melting temperature (T$_m$ = 50.54 °C) the IL presents itself as a colourless liquid. ^{1}H NMR (400 MHz, CDCl$_3$): δ 10.29 (s, 1H), 7.31 (s, 1H), 7.24 (s, 1H), 4.21 (t, J = 7.4 Hz, 2H), 4.00 (s, 3H), 1.94 – 1.75 (m, 2H), 1.36 – 1.13 (m, 10H), 0.84 ppm (t, J = 6.6 Hz, 3H). ^{13}C NMR (101 MHz, CDCl$_3$): δ 161.42, 138.76, 123.47, 121.72, 119.04, 115.86, 111.34, 109.75, 108.35, 50.17, 36.36, 31.59, 30.29, 29.05, 28.96, 26.26, 22.62, 14.03 ppm. ^{19}F NMR (376 MHz, CDCl$_3$): δ -80.85 (t, J = 10.6 Hz), -116.62 (t, J = 13.6 Hz), -118.71 – -124.72 (m, 8F), -126.02– -128.04 ppm (m, 2F). Anal. Calc.: C, 39.48; H, 3.81; N, 4.60. Found: C, 39.90; H, 4.09; N, 4,59.

2.2.5 OTHER MATERIALS AND COMPOUNDS

Baysilicone oil M350 for the heated bath was supplied from Laborspirit. Triphenylphosphine, 99.0%, was supplied by Merck.

Reactants for IL synthesis: potassium nonafluoro-1-butanesulfonate (98%) and methanesulfonic acid (≥99%) were purchased from Sigma-Aldrich; potassium tris(trifluoromethanesulfonyl)methide (98%) was purchased from SynQuest Laboratories; sodium trifluoroacetate, sodium perfluorooctanoate and sodium hydroxide (98%) were purchased from Alfa Aesar.

2.2.6 CO$_2$ HYDROGENATION PROTOCOLS

Screening catalytic tests

In a typical experiment, 21 pieces of catalyst (~ 1 g of catalyst, ~ 50 μmol of metal) are admitted in the autoclave, along with a small magnetic bar. The autoclave is sealed and submerged in the silicone oil bath at room temperature. The system is submitted to vacuum, and 20 bar of CO$_2$ are added to the reactor. Hydrogen is then added to the reactor up to a total pressure of 40 bar. CO$_2$ is again added to the reactor until the total pressure reaches 80 bar. The temperature is then raised to 140 ºC. Between every intake of gas or temperature change, it was necessary to wait for pressure to stabilize. After the last stabilization, reaction was started by initiating stirring.

After 24 hours the reaction was stopped by terminating heating and stirring and the apparatus was cooled until it reached room temperature. Vacuum was applied to the expansion and capture zone. The reactor then was depressurized to the expansion zone, and 2 bar of sample gas were admitted to the capture vessel. Gas sample were taken to another facility to be analysed by GC-TCD.

In cases where the pressure ratio of the reactant gases is 1:1, 40 bar of H$_2$ are added initially to the reaction followed by CO$_2$ until reactor pressure reaches 80 bar.

Catalyst Preparation : Pd/Al$_2$O$_3$ (0.5 wt.%), Rh/Al$_2$O$_3$ (0.5 wt.%) and Ru/Al$_2$O$_3$ (0.5 wt.%) pellets were impregnated with IL using a modification of the incipient wetness impregnation described by Bogel-Łukasik et al. [74] The supported catalyst was coated directly by [C$_4$mim][BF$_4$] IL. The IL was placed on the catalyst surface till the first non-adsorbed drop of the ionic liquid appeared. After coating, the catalyst was dried at 333.15K overnight.

CO$_2$ hydrogenation with homogeneous catalysts

In a typical experiment, 50 or 25 μmol Ru precursor and an equimolar amount of PPh$_3$ are added to 1 cm^3 of toluene. The mix is stirred for 10 min and 1 cm^3 of [C$_4$mim][NTf$_2$] is added to the mixture while stirring. Toluene is dried from the solution with a rotary evaporator. The solution is added to the reactor. The reaction follows the same protocol executed in the screening catalytic tests described above, with the exception that CO$_2$ was now added to the reactor at 40°C for gas quantification purposes.

CO₂ hydrogenation with Ru nanoparticles

Most of the hydrogenation procedures in ionic liquids with the formation of ruthenium nanoparticles followed the **Standard Reaction Conditions**, which were defined during the optimization process. In a typical experiment, 125 μmol of Ru(cod)methyallyl$_2$ (~ 0.04 g) were weighted into a glass vial that fits into the reactor autoclave. A small magnetic bar and 1 cm^3 of ionic liquid were added to the vial. The vial was inserted into the reactor vessel and the reactor was sealed.

The reactor was submersed in a 40 °C oil bath and submitted to vacuum. 10 bar of H$_2$ were admitted to the reactor and then purged. The reactor was again submitted to vacuum and 40 bar of H$_2$ were admitted to the system. CO$_2$ was then admitted to the reactor until the total pressure reached 80 bar, followed by setting temperature to 145 ºC. Between every intake of gas or temperature change, it was necessary to wait for pressure to stabilize. After the last stabilization, reaction was started by initiating stirring.

After 24 hours, the reaction was stopped by terminating heating and stirring and the apparatus was cooled until it reached 40°C, where it was kept for gas capture. Gas capture followed method 2 described in *Gas chromatography analysis*.

Nanoparticle synthesis

In a typical experiment, the desired amount of Ru(cod)methyallyl$_2$ was weighted in a glass vial that fits the reactor autoclave. A small magnetic bar and 1 cm^3 of ionic liquid were added to the vial. The vial was inserted into the reactor vessel and the reactor was sealed.

The reactor was submersed in a 50 °C oil bath and submitted to vacuum. 4 bar of H$_2$ were admitted to the reactor and purged. The reactor was again submitted to vacuum and 4 bar of H$_2$ were admitted again to the system. Stirring was turned on.

After 18h of reaction, stirring and heating were turned off, and the system was depressurized.

Catalyst recyclability study

Recyclability study follows the same procedure of a typical reaction of CO_2 hydrogenation with Ru nanoparticles using standard reaction conditions as described above. After the gas sample capture, all gas is released, and vacuum is submitted for 30 min and then closed. Oil bath in turned off. Until the next run the IL containing the catalyst is kept inside the reactor mixing at room temperature and below atmospheric pressure.

The following run follows the same procedure from the point where the reactor is already closed. This procedure was repeated for as many runs necessary.

2.2.7 ANALYTICAL METHODS

Gas chromatography analysis

Identification and quantification of the compounds found in the gas phase were performed by Gas Chromatography. In this work, two different methods of sample capture/CG analysis were performed. Both methods are described below.

Method 1: After reaction stopped and reactor cooled to room temperature, vacuum was applied to the expansion and capture zones. The reactor was then depressurized to the expansion zone, and 2 bar of sample gas were admitted to the capture vessel. The gas samples were then taken to another facility, where the vessel was connected to an Agilent Micro GC 3000 equipped with a backflush 1 µl injector and a TCD detector. Separation took place in two different columns. Column providing **Channel 1** identified inorganic compound and methane. It used an isothermal method (100º), a MolSieve 5A 10 m x 0.32 mm with Plot U 3 m x 0.32 mm pre-column, and argon as carrier gas. Column providing **Channel 2** identified CO_2 and heavier compounds. It used an isothermal method (60º), a Plot U 8 m x 0.32 mm column with a Plot Q 1 m x 0.32 mm pre-column and helium as carrier. For both columns injector was at 90ºC, sampling time was 10s, injection time was 200ms, runtime was 180s.

Method 2: After each reaction, gas from the reactor was flushed through a trap in order to equilibrate the gas with atmospheric pressure, and a sample was taken with a VICI A-2 series precision sampling gas syringe, and injected in a GC Thermo Trace GC Ultra, equipped with a 1 cm^3 liner in the injector (1/10 split) and a TCD detector. Gas separation was performed in a 30 m

30

x 0.32 mm 1010 PLOT Capillary CG Column. Helium was used as carrier gas, at a flow of 1 cm^3 min^{-1}. The injector was at 200ºC, the detector at 120ºC and the oven was kept isothermally at 35ºC during the runtime of 50 min.

Figure 2.4. Picture of the trap used to capture gas sample in method 2 of GC analysis.

Transmission electron microscopy analysis

Transmission electron microscopy, (TEM), was used for particle size and characterization. Observations were made in a Hithachi H8100 equipped with EDS light elements ThermoNoran detector and CCD camera for image acquisition. Size distribution was calculated from a count over 300 nanoparticles chosen arbitrarily from the micrograph using ImageJ software.

Samples NP08 and NP44 was prepared by placing directly a thin film of the reaction mixture on Formvar-carbon coated copper grid [85] .

Sample NP42 was diluted in isopropanol, exposed to an ultrasound bath for 10 min., centrifuged for 10 min., and the supernatant was retrieved and submitted again to the same treatment. The obtained supernatant was placed on a Formvar-carbon coated copper grid.

Samples NP36, NP46, NP34, NP50, NP52 and NP48 were exposed to ultrasound bath for 10 min, filtered out of ionic liquid with acetone in a porous plate funnel with 4 paper filters. The solid powder caught in the paper filters was placed on Formvar-carbon coated copper grid

Nuclear magnetic resonance

NMR of the IL was made in a Bruker Avance III 400MHz spectrometer using $CDCl_3$ as solvent.

UV-vis spectroscopy

UV-vis analyses were applied to the studies of Ru(0) nanoparticles characterization. Studies on Ru composition in reaction samples were performed by UV-visible spectroscopy on a Perkin Elmer Lambda 35 UV/vis spectrometer. Sample absorption was scanned from 200 to 800 nm. All samples were diluted in acetonitrile in a 1:200 ratio. IL and Ru were added to the samples in the same proportions as used in hydrogenation reaction.

Morphological analyses

The reaction sample was directly dropped on a glass slide and observed in a Malvern Instruments Morphologi G3S. The particle size observation range was 1 µm – 1000 µm, and the particle size distribution was analysed by Malvern Morphologi 8.21 software.

Karl-Fisher titration

The moisture content from the desired samples was determined using Karl Fischer coulometric titration. 1.5 mg of each sample was placed into the titration vessel and titrated with Karl Fischer reagent, Hydranal-Coulomat AG. The instrument was composed of a 831 KF Coulometer and a Colorometer Metrohm 728 stirrer.

Differential scanning calorimetry

DSC analysis was performed with a TA Instruments Q-series TM Q2000 DSC with a refrigerated cooling system. The sample was purged continuously with 50 $cm^3.min^{-1}$ nitrogen. About 10–20 mg of salt was crimped in an aluminium standard sample pan with a lid.

2.3 Reactor Calibration

During the main experimental work, secondary experiments and procedures were conducted with the reactor. These procedures were made with the purpose of obtaining data about the reactor necessary for the calculation of the main experimental data. We will call these procedures "reactor calibration" from now on, and, although some were made chronologically along with the main experimental work, they will be reported in full in this subchapter.

2.3.1 Determination of the Apparatus Volume

The first reactor calibration procedure was to determine the volume of the system. To do this, we used a vessel with a known volume as the calibration vessel, *CbV*. The calibration vessel was attached to the part which volume was to be determined, and the part was connected either to a line vacuum or an Argon bottle, depending on the step of the procedure.

Measurements were made in separate for the tree different areas of the system: (RZ) reaction zone, (EZ) expansion zone and (CZ) capture zone (see Figure 2.1). In the three cases, all valves were open (except for v-2), and vacuum was initially admitted to the calibration system through v-1, followed by Argon admittance. Pressure in DM2 was registered as P_1, valve v-5 was closed and vacuum was admitted again to the rest of the system. The calibration vessel was kept at pressure P_1, because valve v-5 was closed. After vacuum, valve v-1 was closed, valve v-5 was opened and the gas inside expanded to the whole system. After the pressure value in DM2 was stabilized, it was registered as P_2.

Schemes of these installations can be seen below. The areas inside the dashed frames are part of the calibration zone while the area outside represents the part that is being measured:
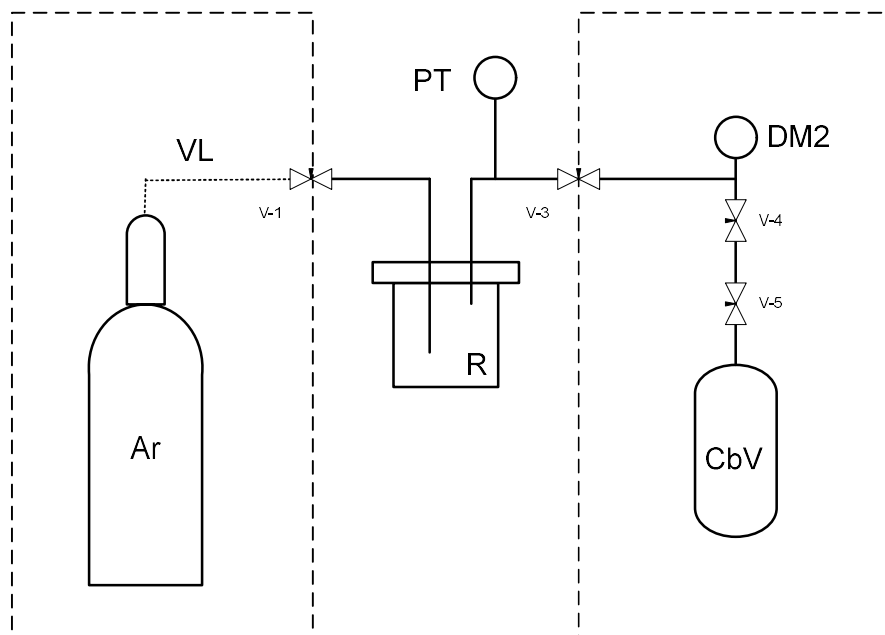
Figure 2.5. Schematics of the calibration of the reactor: (Ar) argon bottle, (VL) Argon inlet and vacuum line, (PT) pressure transducer, (R) reactor, (DM2) digital manometer, CbV calibration vessel, (v-1 to v-5) valves.
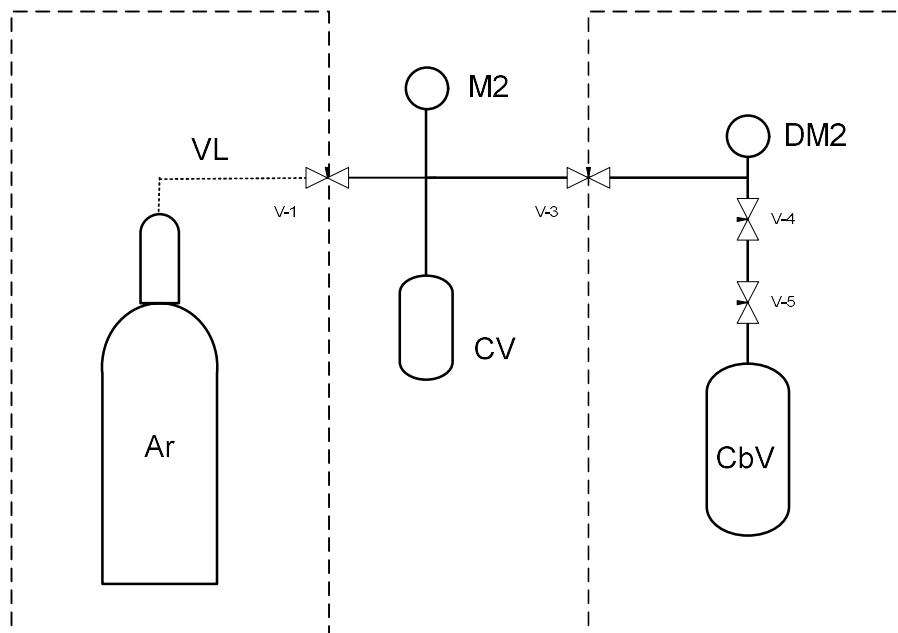
Figure 2.6. Schematics of the calibration of the capture vessel. (Ar) argon bottle, (VL) Argon inlet and vacuum line, (CV) capture vessel, (M2) manometer, (DM2) digital manometer, CbV calibration vessel, (v-1 to v-5) valves.
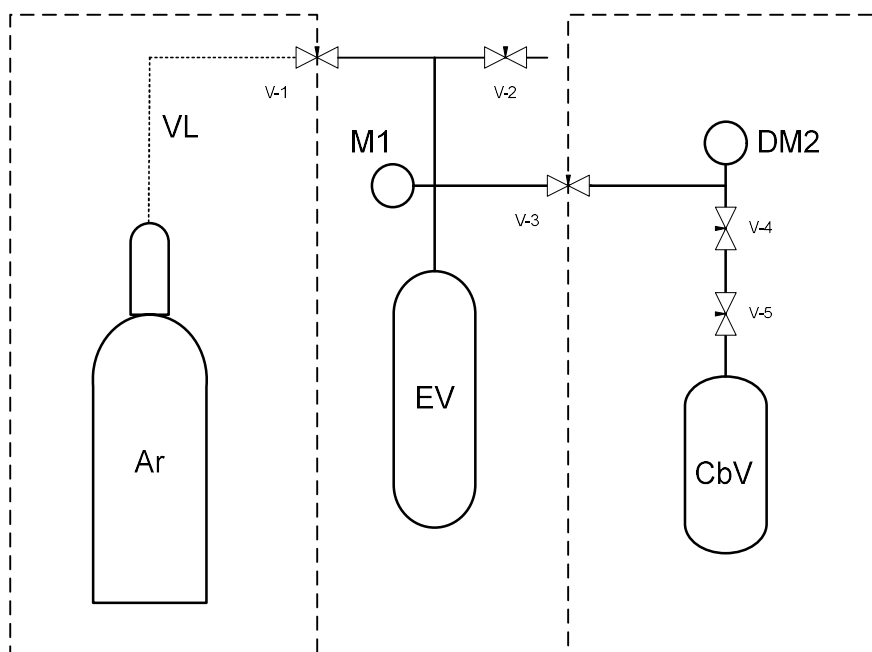
Figure 2.7. Schematics of the calibration of the expanse vessel. (Ar) argon bottle, (VL) Argon inlet and vacuum line, (M1) manometer, (EV) expansion vessel, (DM2) digital manometer, CbV calibration vessel, (v-1 to v-5) valves.

To calculate the volume of each zone the equation of the ideal gases law was applied.

Table 2.4. Calibration volumes.

Device	Volume (cm³)
Calibration vessel, CbV	1647.0
Tubing from v-3 to v-5, Vt	1.9
Reactor, R	32.2
Capture Vessel, CV	80.1
Expansion Vessel, EV	1015.1

2.3.2 REACTION YIELD

All hydrogenation reactions that took place had CO_2 used in excess. For this reason, reaction (%) yields were expressed in terms of methane production, and based on conversion of hydrogen:

$$(\%)yield\ CH_4 = \frac{real\ amout\ CH_4}{theoretical\ amout\ CH_4} \times 100 \qquad (5)$$

Taking in account the reaction stoichiometry (from equation 4) and the fact that H_2 is the limiting reactant, (%)yield CH_4 can be calculated as:

$$(\%)yield\ CH_4 = \frac{n_{CH_{4f}}}{n_{H_2i}/4} \times 100 \qquad (6)$$

Where, $n_{CH_{4f}}$ is the produced amount of CH_4 and n_{H_2i} is the initial amount of H_2 in the reactor.

Calculation of the amount of hydrogen loaded into the reactor, n_{H_2i}

The initial amount of H_2 introduced in the reactor, n_{H_2i} (mol), can be obtained by multiplying density of H_2 (mol.cm^{-3}) by the reactor's useful volume, V_{Ru} (cm^{-3}). The density of H_2 was calculated, at the input of temperature and pressure, using the NIST website [86], which based their calculations on the equation of state by Leachman et. al. [87].

$$n_{H_2i} = \rho_{H_2} \times V_{Ru} \qquad (7)$$

The reactor's useful volume, V_{Ru}, was the actual volume of the reactor that was occupied with the gas phase. Many of the reactions required a liquid phase to be added to the reactor, most of the times this liquid phase was added in the reactor in a glass vial that remained inside the reactor during reaction allowing for an easier recover of the reactional mixture after reaction. These volumes must be subtracted to the volume of the reactor for accurate calculation of V_{Ru}. The volume of the liquid phase, $V_{Lp} = 1$ cm^{-3} unless stated otherwise. The volume occupied by the glass vials was calculated through the density (g cm^{-3}) of glass and their mass (g). The mass was calculated as the average of the weight of random samples of 12 random glass vials, $m_{gv} = 6.61$g ± 0.06.

Table 2.5 Mass (g) of 12 random glass vials used in hydrogenation reaction.

Entry	Mass (g)	Entry	Mass (g)
1	6.58	7	6.60
2	6.59	8	6.66
3	6.54	9	6.63
4	6.71	10	6.63
5	6.63	11	6.55
6	6.55	12	6.69

Average mass = 6.61 g

From the density of glass, $\rho_g = 2.6 \; g.cm^{-3}$, taken from literature [88], the average volume occupied by the glass vial was calculated was $V_{gv} = 2.54 \; cm^{-3}$. Assuming the liquid phase occupies the useful volume of the reactor is:

$$V_{Ru} = V_R - V_{gv} - V_{Lp} \Leftrightarrow$$
$$V_{Ru} = 32.20 \; cm^{-3} - 2.54 \; cm^{-3} - 1 \; cm^{-3} = 28.66 \; cm^{-3}$$

(8)

Calculation of the amount of methane formed in the in the reactor, $n_{CH_{4f}}$

To find the total amount of methane produced in the reactor, $n_{CH_{4f}}$, (mol), equation 9 was used:

$$n_{CH_{4f}} = y_{CH_{4f}} \cdot n_{Totalf}$$

(9)

where: $y_{CH_{4f}}$ is the mole fraction of methane in the gas phase and n_{Totalf} is the total amount of gas. This equation was rearranged taking in account the reaction stoichiometry (see equation 4) it to make $n_{CH_{4f}}$ dependent of known values such as: $y_{CH_{4f}}$, $n_{H_2 i}$ and the initial amount of CO_2. ($n_{CO_2 i}$).

The total amount of gas is the sum of the total amounts of each gas after reaction, (water is not considered since is not detected in the GC).

$$n_{Totalf} = n_{CO_2 f} + n_{H_2 f} + n_{CH_4 f}$$

(10)

final amounts can be rearranged in the following way:

$$n_{CO_2f} = n_{CO_2i} - n_{CH_4f} \tag{11}$$

$$n_{H_2f} = n_{H_2i} - 4n_{CH_4f} \tag{12}$$

Equation 9 can be arranged as:

$$y_{CH_4f} = \frac{n_{CH_4f}}{\left(n_{CO_2i} - n_{CH_4f}\right) + \left(n_{H_2i} - 4n_{CH_4f}\right) + n_{CH_4f} + 0} \tag{13}$$

Finally, equation 13 be rearranged and used to calculate n_{CH_4f}.

$$n_{CH_4f} = \frac{y_{CH_4f} \cdot \left(n_{CO_2i} + n_{H_2i}\right)}{(1 + 4y_{CH_4f})} \tag{14}$$

Calculation of the mole fraction of CH₄ in the gas mixture, y_{CH_4f}

The value of the mole fraction in the gas mixture was obtained by gas chromatography analysis. As mentioned before in "Analytical methods" of this chapter, two different GC methods were used, for each method the approach to find methane molar fraction was different:

Method 1: The amount of CH₄ in the reaction samples was calculated using a calibration gas sample with known concentration of different gases, including CH₄. Appendix B provides the calibration certified of the gas mixture used to calibrate the GC and the concentration of each gas in ppm. In case of CH₄, the gas mixture contained 2482.1 ppm. Before samples injection in the GC a sample of the calibration mixture is injected. Mole fraction is obtained from a simple "rule of tree" between areas and calibration concentration.

The gas chromatograph used in method one was more sensitive than the second GC. Method one was initially used to detect smaller amounts of methane. Due to the sensitivity of this method, H_2 and CO_2 peaks were always saturated impeding their quantification.

Method 2: The second GC used had calibration curves of the gases of interest previously made with a total of 5 different gas standards. The provided calibration curves for H_2, O_2, N_2, CH₄ and CO_2 can be found in Appendix C. We obtain y_{CH_4f} value with the following calculation:

$$y_{CH_4f} = \frac{n_{CH_4gc}}{n_{CO_2gc} + n_{H_2gc} + n_{CH_4gc}} \tag{15}$$

where: n_{CH_4gc}, n_{CO_2gc} and n_{H_2gc} tare the amounts (mole) of each gas in the injected GC sample.

N_2 and O_2, due to contamination in the sampling process, were always identified, but only in traces amounts, and for calculations their presence in the sample was not considered.

Calculation of the amount of CO₂ loaded in the reactor

Carbon dioxide behaviour greatly deviates from the ideal gas. Due to its compressibility, it is expected that a pressure ratio of 1:1 of a H_2:CO_2 binary mixture will contain more CO_2 than H_2. During this work two calculation methods where used for the quantification of the CO_2 amount introduced in the reactor. The first method was developed in earlier state of the work for pressure ratios (H_2:CO_2) of 1:1 and 3:1. Since working pressure and temperature conditions are close to the CO_2 critical point, it was more difficult than expected to quantify CO_2 in the reactor. Later, while working at 1:1 ratios and changing the GC analysis method, a relevant degree of error was detected. A different approach was then used for this ratio and verified to be more accurate. This method was also applied to recalculate previous results, whenever possible. Below follow both methods:

CO₂ quantification, method 1: A series of tests were performed that consisted in filling the reactor with gases the same way as for a reaction preparation. However, instead of using the CO_2 compressor to pressurize the gas into the reactor, a screw injector with a known capacity was used. A manual HIP screw injector of 30 cm³ capacity and a manometer were connected to the apparatus system. Figure 2.8 presents a scheme of how the screw injector was connected to the installation.

In a typical experiment, the reactor was filled with 40bar of H_2, for a 1:1 ratio, or 60 bar, for a 3:1 ratio. The reactor was placed in a 40°C bath. A screw injector with a calibrated volume was cooled to 0°C and filled with CO_2 up, and pressure was brought to the desired final pressure in the reactor (for example: 80 bar). Valves to the reactor were open, releasing the CO_2 from the screw injector into the reactor where it mixed with H_2. Pressure value in the screw injector manometer decreased. The paddles of the screw injector were turned, decreasing its volume and increasing the total pressure until the manometer reached again the desired final pressure, as determined in the beginning of the experiment (80 bar in this example). The number of turns made with the paddles was recorded, each turn corresponds by calibration to 0.356 cm³. CO_2 density at data can be retrieved from NIST website[86] which is based on a fundamental equation of state by Span et

all. [89] Knowing temperature and pressure inside the screw injector it is possible to calculate the amount of CO_2 introduced by each turn.
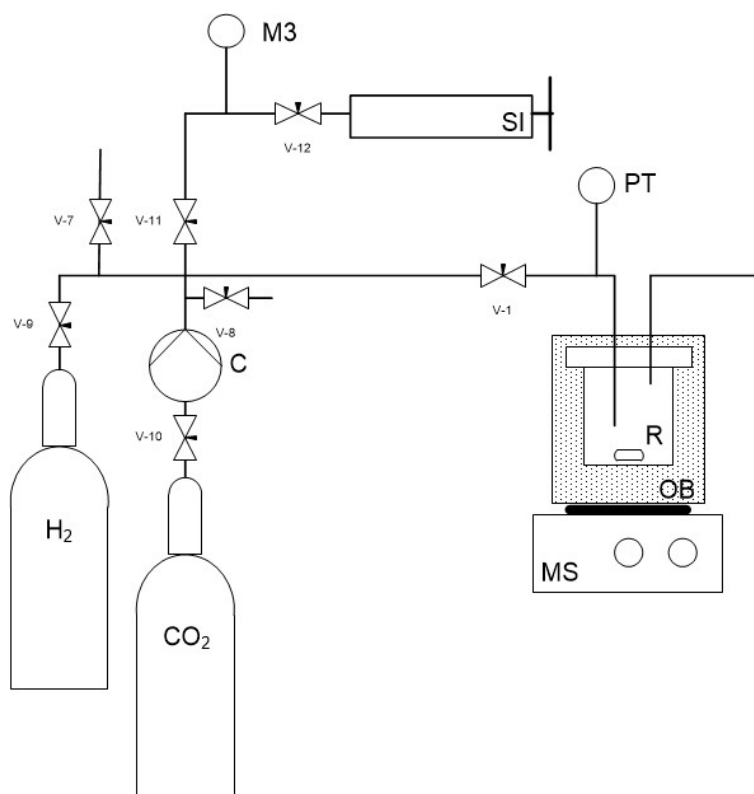
Figure 2.8. Schematics of reaction zone, where the screw injector is assembled to the apparatus: (C) CO_2 compressor, (R) reactor, (OB) oil bath, (MS) magnetic stirrer, (PT) pressure transducer, (M3) manometer, (SI) screw injector, (v-1, v-7 to v-12) valves.

Figure 2.9. Picture of the screw injector assembled to the apparatus.

40

The pressure in the reactor was registered for two different temperature sets, 40°C, the standard temperature of reactants admission, and 140°C, the standard reaction temperature at the time. From several experimental points it was possible to plot pressure vs CO_2 amount and generate a trendline. The trendline can be used to find an equation that allows to estimate the amount of CO_2 inside the reactor depending of reactor pressure.
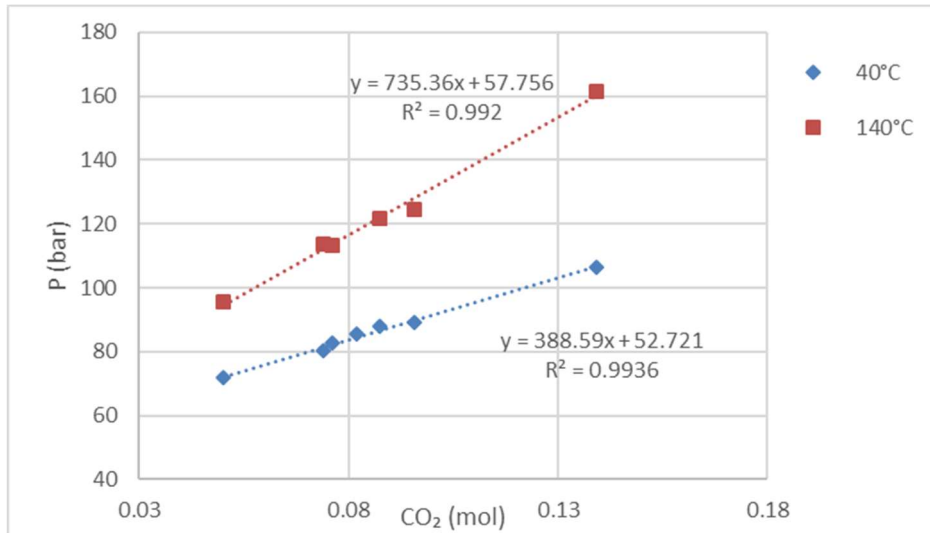
Figure 2.10. Pressure (bar) vs amount of CO_2 (mol) for the system where initially 40 bar of H_2 were introduced in the reactor. (◆), data values with the reactor in a 40°C bath; (■), data values with the reactor in a 140 °C bath.
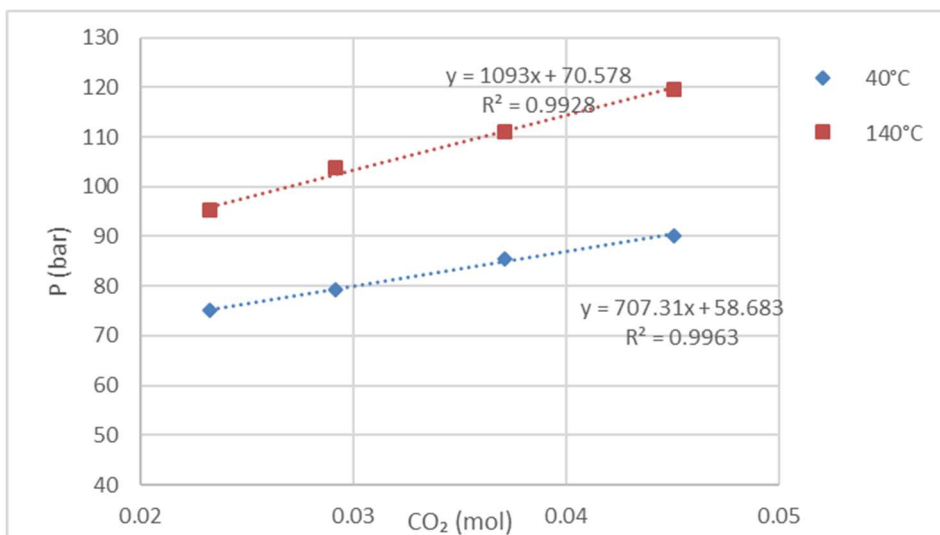
Figure 2.11. Pressure (bar) vs amount of CO_2 (mol) for the system where initially 60 bar of H_2 were introduced in the reactor. (◆), data values with the reactor in a 40°C bath; (■), data values with the reactor in a 140°C bath

Both cases present a R^2 value higher with 40°C experimental values. For the system where the initial pressure of CO_2 is 40 bar, H_2:CO_2 pressure ratio is 1:1, the equation found was the following:

$$n_{CO_2} = \frac{P_{40°c} - 52.721}{388.59}$$ (16)

For the system where the initial pressure of CO_2 is 60 bar, H_2:CO_2 pressure ratio is 3:1, the equation found was the following:

$$n_{CO_2} = \frac{P_{140°c} - 58.683}{707.31}$$ (17)

CO_2 quantification, method 2: A series of tests were performed that consisted in preparing the reactor the same way as for a reaction, except without catalyst. After preparation, when H_2 and CO_2 are stabilized in the reactor at 40°C a gas sample is taken for GC analysis the same way as described in method 2 of "Gas chromatography analysis, "Analytical methods" of this chapter. GC analysis provides the molar fraction of this binary mixture, y_{H_2} and y_{CO_2}.

During graphical analysis studies of the obtained data, we observed that, at the conditions of reaction preparation, the values of y_{CO_2} greatly deviate with small pressure variations of both gases. When working with lower or higher values of total pressure this wasn't verified. Partial pressure of CO_2, P'_{CO_2} and the theoretical value of CO_2 molar fraction if the binary mixture would behave like an ideal gas mixture, y'_{CO_2} were calculated for the experimental data. Plotting a graphical representation of $y_{CO_2}.P'_{CO_2}$ vs $y'_{CO_2}.P'_{CO_2}$ revealed to be the best approach to make the experimental data correlate with a trendline.

Table 2.6. Experimental data output for CO_2 quantification tests.

Entry	P_{H_2} (bar)	P_{Total} (bar)	P'_{CO_2} (bar)	y_{CO_2}	y'_{CO_2}	$y'_{CO_2}.P'_{CO_2}$	$y_{CO_2}.P'_{CO_2}$
1	41.92	76.60	34.68	0.48	0.45	15.70	16.67
2	42.95	83.98	41.02	0.51	0.49	20.04	20.76
3	42.68	85.01	41.02	0.54	0.50	21.08	22.73
4	41.99	85.49	43.51	0.56	0.51	22.14	24.15
5	41.85	85.63	43.78	0.52	0.51	22.38	22.91
6	42.40	106.87	64.47	0.67	0.60	38.89	43.47
Literature [90]	41.51	84.53	43.02	0.57	0.51	21.90	24.41
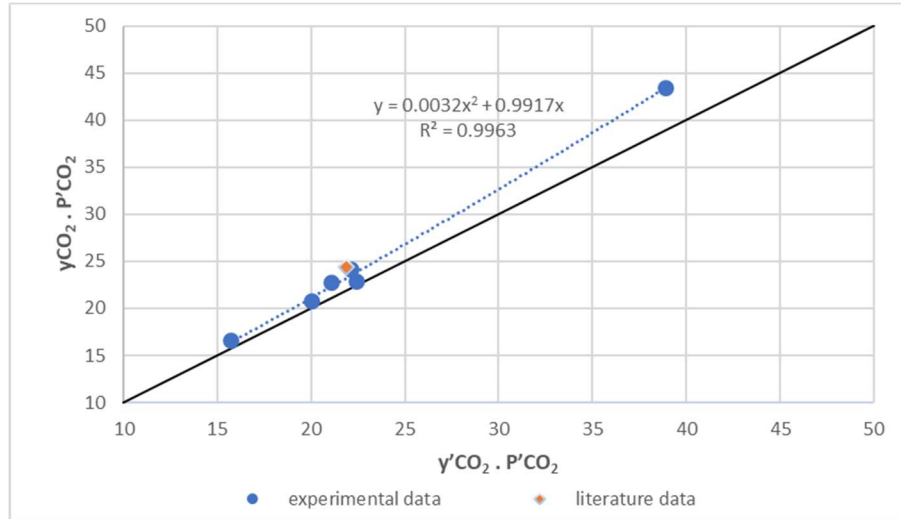
Figure 2.12. Graphic representing $y_{CO_2} \cdot P'_{CO_2}$ vs $y'_{CO_2} \cdot P'_{CO_2}$. ($\bullet$) values calculated from experimental data ($\blacklozenge$) value calculated from literature data [90].

The same calculations were applied to a literature data point from the work of Ababio et all [90]. The literature data point can be observed in the graphical representation and its position is very close to the generated trendline. From this trendline it is possible generate the equation that can estimate the molar fraction of CO_2 in the gas phase.

$$y_{CO_2} = \frac{3.2 \cdot 10^{-3} \cdot \left(y'_{CO_2} \cdot P'_{CO_2}\right)^2 + 0.9917 \cdot y'_{CO_2} \cdot P'_{CO_2}}{P'_{CO_2}} \qquad (18)$$

Beside the gas phase, the reactor contains also ionic liquid. At high pressure the amount of CO_2 dissolved in the IL is considerable and must be taken in account. A correction factor must be added to previous calculations.

Therefore, the amount of CO_2 dissolved in the IL phase was calculated. Literature data of [C$_8$mim][NTf$_2$] was used for calculations. According to literature at 40°C and 42.95 bar, CO_2 molar fraction, x_{CO_2}, in [C$_8$mim][NTf$_2$] is 0.575 [91]; IL density, ρ_{IL}, is 1.325 g.cm^3 [92]. From these values it is possible to calculate that the amount of IL in the reactor is 0.002787 mol, and the amount of CO_2 dissolved in in IL is 0.0037 mol. The amount of CO_2 dissolved in the IL, $n_{CO_2 \, dissolved}$, was added to the amount of CO_2 in the gas phased.

$n_{CO_2 \, gas \, phas}$ was calculated from equation (18) for a standard reaction where conditions of $Pi_{H_2} = 40$ bar and $P'_{CO_2} = 40$ bar and equation (19).

43

$$n_{CO_2} = \frac{x_{CO_2} \cdot n_{H_2}}{x_{H_2}} \tag{19}$$

Table 2.7. Amount of gas calculated in the gas phase for Pi_{H_2} = 40 bar and P'_{CO_2} = 40 bar at 40 °C.

	H$_2$	CO$_2$
P (bar)	40	40
Y	0.480	0.520
n (mol)	0.045	0.048

The total amount of CO$_2$ in the reactor was calculated for the standard conditions:

$$n_{CO_2 Total} = n_{CO_2 \, dissolved} + n_{CO_2 \, gas \, phase} = 0.052 \text{ mol} \tag{20}$$

This value was reconverted to a new value of molar fraction, and the difference between molar fractions is the correction factor, CF.

$$x_{CO_2 corrected} = \frac{n_{CO_2 Total}}{n_{CO_2 Total} + n_{H_2}} \tag{21}$$

$$CF = x_{CO_2 corrected} - y_{CO_2} = 0.051981 - 0.52015 = 0.0188 \tag{22}$$

The correlation factor was then added to the previously calculated experimental data and the molar fraction of CO$_2$ in the reactor was recalculated.

$$x_{TCO_2} = y_{CO_2} + CF \tag{23}$$

Follows the recalculations applied to the experimental data:

Table 2.8. Data for CO$_2$ quantification, $y_{CO_2}.P'_{CO_2}$ and $x_{TC\,2}.P'_{CO_2}$ values after implementing of the correction factor.

Entry	y'CO$_2$. P'CO$_2$	xTCO$_2$. P'CO$_2$
1	15.70	17.33
2	20.04	21.53
3	21.08	23.52
4	22.14	24.97
5	22.38	23.73
6	38.89	44.68

44
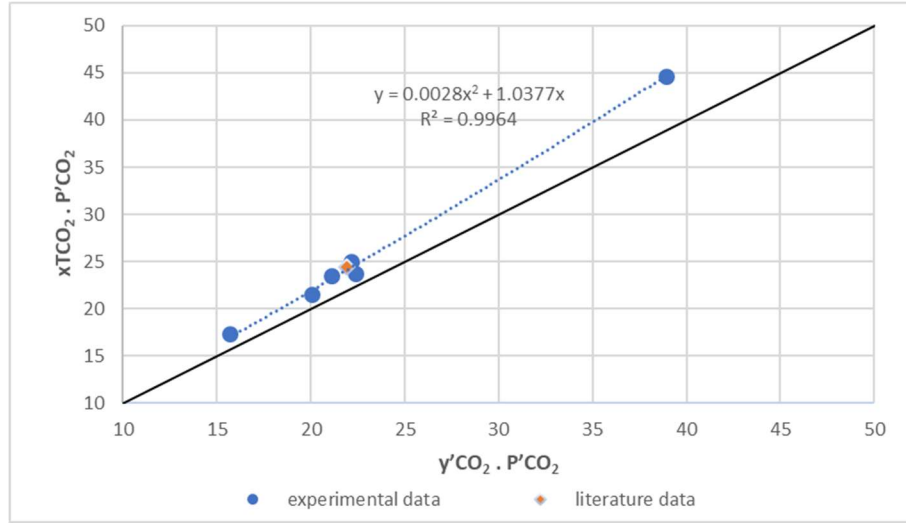
Figure 2.13. Graphic representing corrected values of $x_{TCO_2} \cdot P'_{CO_2}$ vs $y'_{CO_2} \cdot P'_{CO_2}$. ($\bullet$) values calculated from experimental data ($\blacklozenge$) value calculated from literature data [90]

It is possible to see that the data from literature is more adjusted to the new graphical representation. From the obtained trendline, it is possible to obtain an equation able to estimate the actual CO_2 mole fraction in the reactor:

$$x_{TCO_2} = \frac{2.8 \cdot 10^{-3} \cdot \left(y'_{CO_2} \cdot P'_{CO_2}\right)^2 + 1.0377 \cdot y'_{CO_2} \cdot P'_{CO_2}}{P'_{CO_2}} \tag{24}$$

The initial amount of CO_2, $n_{CO_2 i}$, in the reactor can be calculated applying x_{TCO_2} on equation 19:

$$n_{CO_2 i} = \frac{x_{TCO_2} \cdot n_{H_2}}{x_{H_2}} \tag{25}$$

Calculation of the amount of CO formed in the in the reactor, n_{CO_f}

Under some conditions, reaction selectivity shifted towards carbon monoxide formation instead of CH_4, equation (26).

$$CO_2 + H_2 \leftrightarrow CO + H_2O \tag{26}$$

The total amount of CO produced in the reactor, n_{CO_f}, can be calculated in an equivalent way made to find $n_{CH_4 f}$ from equation 9.

In this case, n_{CO_f}, in mole, can be calculated by equation (27):

$$n_{CO_f} = y_{CO_f} \cdot n_{Totalf} \tag{27}$$

Where: y_{CO_f} is the molar fraction of methane in the gas phase; n_{Totalf} is the total amount of gas in the reactor after reaction (mol), now given by the following equation:

$$n_{Totalf} = n_{CO_{2f}} + n_{H_{2f}} + n_{CO_f} + n_{H_2O_f} \tag{28}$$

Equation (27) can be rearranged as:

$$y_{CO_f} = \frac{n_{CO_f}}{n_{CO_{2f}} + n_{H_{2f}} + n_{CO_f}} \tag{29}$$

Assuming the stoichiometry of methanation reaction, equation (26), final amounts can be rearranged in the following way:

$$n_{CO_{2f}} = n_{CO_2i} - n_{CO_f} \tag{30}$$

$$n_{H_{2f}} = n_{H_2i} - n_{CO_f} \tag{31}$$

Equation (29) can be rearranged as follows:

$$y_{CO_f} = \frac{n_{CO_f}}{\left(n_{CO_2i} - n_{CO_f}\right) + \left(n_{H_2i} - n_{CO_f}\right) + n_{CO_f}} \tag{32}$$

$$\Leftrightarrow n_{CO_f} = \frac{y_{CO_f} \cdot \left(n_{CO_2i} + n_{H_2i}\right)}{\left(1 + y_{CO_f}\right)} \tag{33}$$

2.3.3 REACTOR WITH STRONG STIRRING SYSTEM

In order to verify whether stirring of reactants in our reactor could affect the observed yields, some reactions were carried out with a different stirring method, in a 25 mL stainless steel Parr reactor − Series 4591 Micro Reactor Systems equipped with a removable head with general purpose magnetic drive, split-ring closure with 6 bolts, heating jacket, fixed thermocouple,

46

manometer, and an addition pressure transducer, PDM model. An image of the reactor can be found below, in Figure 2.14.

Inside the reactor, the stirring mixer has a gas entrainment impeller (see right side of Figure 2.4) allowing better dispersion inside the reaction mixture. The stirring shaft is hollow, while mixing the speed of the stirrer creates a vacuum at the top, the gas phase enters through the top holes in the shaft and exit in the bottom mixing with the liquid phase and gas is continuously recirculated into the bottom through the impeller.

Figure 2.14. Photograph of the series 4591 micro Parr reactor installation on the left; picture of the stirring mixer.

To determine the reaction yield for this reaction system, the same calculations as before were applied. However, the volume of the reactor is different, and it had to be determined. Figure 2.15 shows a schematic of the calibration system.
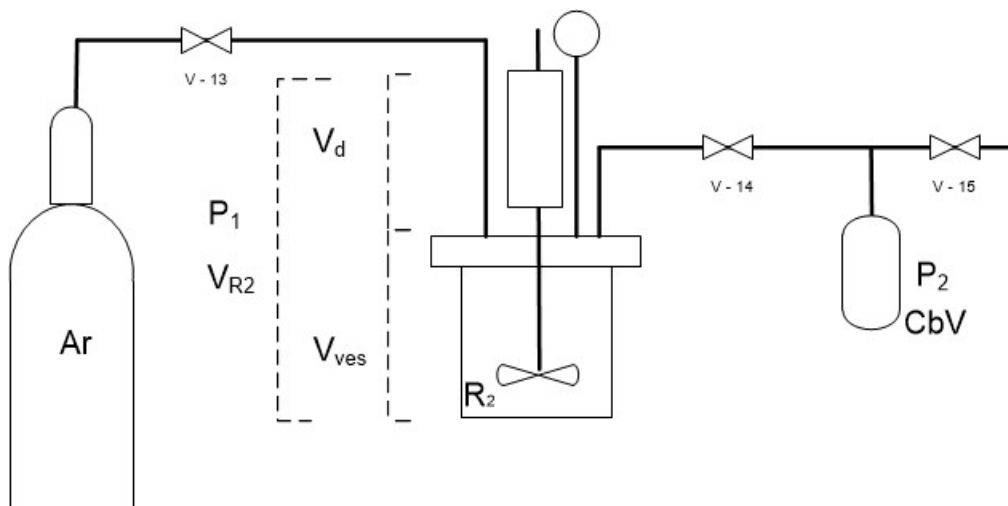
Figure 2.15. Scheme of the calibration installation of the 4591 micro Parr reactor. (Ar) argon bottle, (R_2) Parr reactor, (PT) pressure transducer, (CbV) calibration vessel, (v-11 to v-13) HIP valves, (V_{R2}) volume of the reactor, (Vves) Volume of the vessel, (Vd) volume inside the drive, (P1) Pressure inside the reactor, (P2) pressure inside the calibration vessel.

To calculate the total volume of the reactor (V_{R2}), a calibration flask, (CbV) with the known volume of 80.1 cm³ was connected to the reactor. After subjecting the system to vacuum, argon was added only to the reactor, and pressure was measured, P_1. The valve was opened between the reactor and the calibration flask and a new pressure value, P_2, was measured. This procedure was repeated three times, the measured values can be found in Table 2.9.

Knowing P_1, P_2 and that the amount of argon in the reactor remains the same, we will use equation (35) to determine the V_{R2}:

$$P_1 V_{R2} = P_2(V_{R2} + 80.1) \tag{34}$$

$$V_{R2} = \frac{P_2 * 80.1}{(P_1 - P_2)} \tag{35}$$

Table 2.9. Experimental values for P1 and P2. Calculated values for V_{R2}.

Entry	P₁ (bar)	P₂ (bar)	V_R2 (cm³)
1	86.8	31.6	45.85
2	57.2	20.7	45.43
3	37.9	13.5	44.32

The final value of $V_{R2} = 45.2$ cm³ is the mean of the three experimental values.

48

It is possible to see in that scheme that the total volume of the reactor (Vtotal) is composed by the sum of the vessel volume (Vves) and the volume inside the magnetic drive (Vd).

Vves (24.12 cm³) was calculated from the volume of a cylinder using the values of the internal height (5.050 cm) and the diameter (2.466 cm) of the vessel measured with a calliper.

The volume of the magnetic drive (Vd = 21.08 cm³) is considered a dead volume. Due to the high density of gas and narrow size of the connection between the vessel and motor there are diffusional limitations that restrict the access to the vessel. It is assumed that, after admission of the reactants and during reaction, the gas inside this chamber will not flow to the vessel and will not react, maintaining its initial composition in H_2 and CO_2.

GC analysis does not consider the gas inside the dead volume giving only the mole fraction inside the vessel. To calculate the yield of reaction, it is necessary to know the mole fraction inside the totality of the reactor.

For this we calculate the volume occupied by each gas in the totality of the reactor with the following equations:

$$V_{H_2} = y_{H_2 i} * V_d + y_{H_2 f} * V_{ves} \tag{36}$$

$$V_{CO_2} = y_{CO_2 i} * V_d + y_{CO_2 f} * V_{ves} \tag{37}$$

$$V_{CH_4} = y_{CH_4 f} * V_{ves} \tag{38}$$

Where: V_{H_2}, V_{CO_2} and V_{CH_4} are the volumes occupied by H_2, CO_2 and CH_4 respectively; $y_{H_2 i}$ and $y_{CO_2 i}$ are the molar fractions of H_2 and CO_2 after admission in the reactor; $y_{H_2 f}$, $y_{CO_2 f}$ and $y_{CH_4 f}$ are the molar fraction values of H_2, CO_2 and CH_4 respectively obtained from GC analysis after reaction. The molar fraction inside the totality of the reactor can be calculated with the following equations:

$$y_{H_2 R2} = \frac{V_{H_2}}{V_{R2}} \tag{39}$$

$$y_{CO_2 R2} = \frac{V_{CO_2}}{V_{R2}} \tag{40}$$

$$y_{CH_4 R2} = \frac{V_{CH_4}}{V_{R2}} \qquad (41)$$

Where: $y_{H_2 R2}$, $y_{CO_2 R2}$ and $y_{CH_4 R2}$ are the corrected molar fractions inside the Parr reactor for each gas. Reaction yield can then, be later calculated with these corrected values.

2.3.4 TURN OVER NUMBER

Turn over number was calculated by the following equation:

$$TON = \frac{n_{CH_4 f}}{n_{catalyst}} \qquad (42)$$

2.3.5 CARBON DIOXIDE CONVERSION

Carbon dioxide conversion presented in percentage was calculated by the following equation:

$$CO_2\ conversion = \frac{n_{CH_4 f}}{n_{CO_2 i}} \cdot 100 \qquad (43)$$

Chapter 3 – RESULTS AND DISCUSSION

3.1 INTRODUCTORY WORK

The goal of this thesis was to reduce CO_2 with hydrogen to produce compounds that might be used as fuels. The work described here was inspired by, on one hand, two publications by Wesselbaum et al. [1,93], and, on the other hand, an on-going work in our laboratory on electrochemical reduction of carbon dioxide [94]. The main idea was to use ILs to immobilize catalysts, using the high solubility of CO_2 in ILs to facilitate access of reactants to the catalytic centres, and to improve separation of products.

The experimental work of Wesselbaum et al., originating from the groups of Walter Leitner and Jürgen Klankermayer, of the University of Aachen, went in two directions:

(1) Continuous-flow hydrogenation of CO_2 into formic acid, where a Rh/Ru homogeneous catalyst was immobilized in an ionic liquid that worked as a non-volatile stationary phase, and products where extracted by $scCO_2$, which worked as a mobile phase. Monosulfonated triphenylphosphine-based compound were used as ligands [1].

(2) CO_2 conversion into methanol achieved in a 24 h reaction, at 140°C, with a homogeneous Ru complex as catalyst composed by [Ru(acac)$_3$] and a tridentate phosphine ligand, thriphos. THF was used as reaction solvent [93].

On the other hand, the on-going electrochemical work in our laboratory routinely analysed CO_2 reduction products to check for methane, carbon monoxide, hydrogen, and carbon dioxide.

Experimentally, we begun reactions testing two Ru organometallic compounds as catalyst precursors, Ru(cod)methylallyl$_2$ and [Ru(cod)Cl$_2$]$_n$, , and PPh$_3$ as ligand, entry **HC02** and **HC03** respectively. Ru complex was formed in toluene and added to IL to perform the reaction. Also, a blank test took place, with Ru(cod)methylallyl$_2$, the most reactive of these precursors and no ligand, entry **HC01**. Reaction conditions were based on literature mentioned above, except for the temperature of the blank test. The initial idea was to make several of these tests with increasing temperature, this however, ended up being studied later in this work (see **section 3.2.2**).

Table 3.1. CO_2 hydrogenation with homogeneous catalysts, initial reactions.[a]

Entry	Catalyst	Ionic liquid	Ligand	$H_2:CO_2$ ratio	Temp.
HC01	Ru(cod)methylallyl$_2$	[C$_4$mim][BF$_4$]	-	1:3	50°C
HC02	Ru(cod)methylallyl$_2$	[C$_4$mim][NTf$_2$]	PPh$_3$	1:3	140°C
HC03	[Ru(cod)Cl$_2$]$_n$	[C$_4$mim][NTf$_2$]	PPh$_3$	1:3	140°C

[a] *Conditions: 1 cm^3 of IL, 50 μmol catalyst, 1 equiv. ligand, time = 24 h. Pt = 80 bar at room temp.*

After reaction, the **HC01** sample presented a pitch-black appearance, GC and NMR analyses revealed that no CO_2 conversion took place.

From GC analysis we verified that no methane was produced from reactions **HC02** and **HC03**. ^{1}H NMR of sample **HC02** revealed a peak at δ 2.38 and at δ 3.42 ppm. Literature on NMR shifts of common impurities [95] states that: toluene ^{1}H NMR spectrum presents a singlet at δ 2.36 and a multiplet at 7.17 or 7.25. depending on isomeric orientation; methanol ^{1}H NMR spectrum presents a singlet at δ 3.49 and a singlet at δ 1.09 (not always identified). In conclusion, sample **HC02** peak at δ 2.38 corresponds to traces of toluene in the sample and peak δ 3.42 corresponds to methanol produced from the reaction. To confirm the presence of methanol, ^{1}H NMR of methanol was executed in our equipment. The results can be seen in Figure 3.1 and confirms methanol production.
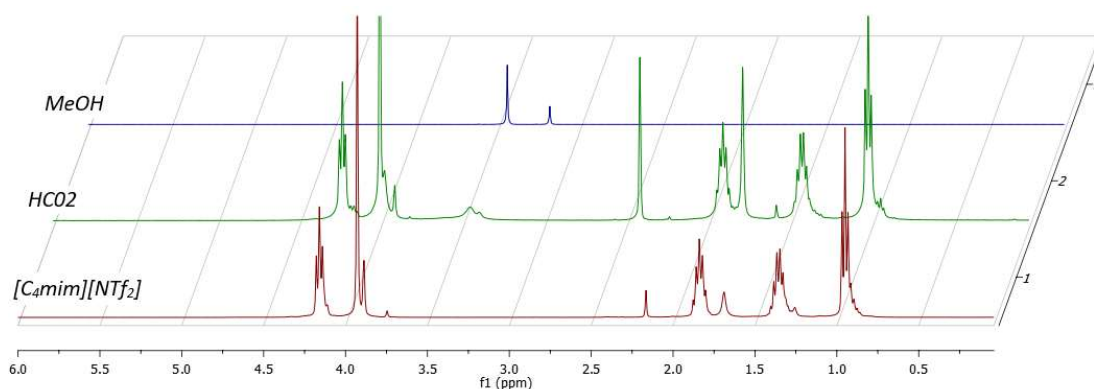
Figure 3.1. ^{1}H NMR (400 MHz, CDCl$_3$) spectrum of reaction mixture of **HC02** liquid sample compared with the ionic liquid before reaction and methanol spectra.

After reaction **HC02** produced methanol more experiments took place with the precursor Ru(cod)methylallyl$_2$ and ligand PPh$_3$. Table 3.2 features the conditions and results of each experiment.

Table 3.2. CO$_2$ hydrogenation with Ru(cod)methylallyl$_2$ precursor and PPh$_3$ ligand.[a]

Entry	Solvent	Ligand	H$_2$:CO$_2$ ratio	Product detected
HC04	[C$_4$mim][NTf$_2$]	PPh$_3$	1:3	-
HC05	[C$_4$mim][NTf$_2$]	PPh$_3$	1:1	Methane
HC06	Toluene	PPh$_3$	1:3	-
HC07	Toluene	PPh$_3$	1:1	-
HC08	[C$_4$mim][NTf$_2$] - Toluene	PPh$_3$	1:1	Methanol
HC09	[C$_4$mim][NTf$_2$] – DCM	PPh$_3$	1:1	-
HC10	[C$_8$mim][NTf$_2$]	PPh$_3$	1:1	Methane
HC11	[C$_4$mim][NTf$_2$]	-	1:3	Methane

[a] *Conditions: 1 cm^3 of solvent; 25 µmol catalyst; 1 equiv. ligand; time = 24 h; Pt = 80 bar at room temp.*

Entry **HC04**: Precursor and ligand were added directly to the IL without initially dissolution on toluene. No products were formed. Reactional mixture showed a yellow liquid with a black powder on the bottom.

Entry **HC05**: The same reaction as **HC04**, however, gas ratio was 1:1 instead of 1:3 (H$_2$:CO$_2$). Methane was formed, GC presented a peak with an area of 480. Reaction mixture presented a black coloration. It was possible to calculate yield of CH$_4$ as 0.6 %.
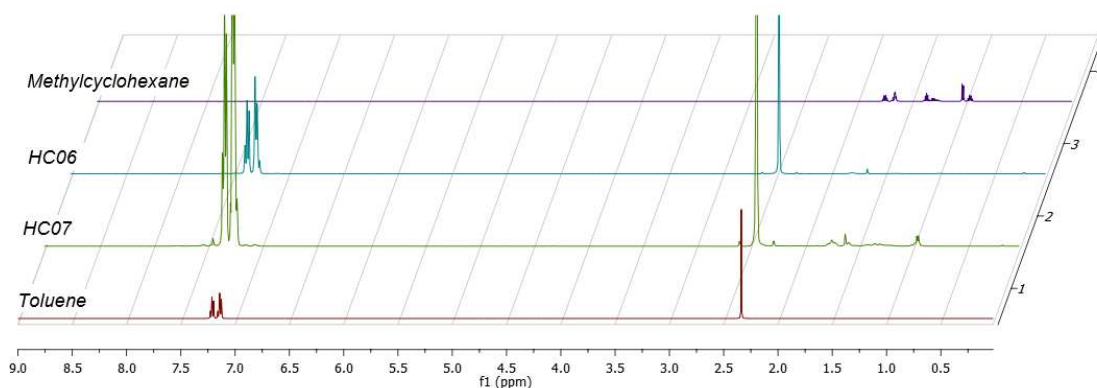
Figure 3.2. ^{1}H NMR (400 MHz, CDCl$_3$) spectra of reaction mixtures **HC06** and **HC07** liquid sample compared with toluene and methylcyclohexane spectra.

Entries **HC06** and **HC07**: Toluene was used as solvent instead of ionic liquid. In entry **HC07** gas ratio was 1:1 instead of 1:3 ($H_2:CO_2$). No CO_2 conversion detected in both cases. ^{1}H NMR detected toluene hydrogenation into methylcyclohexane in trace amount. Traces of methylcyclohexane are higher at **HC07**.
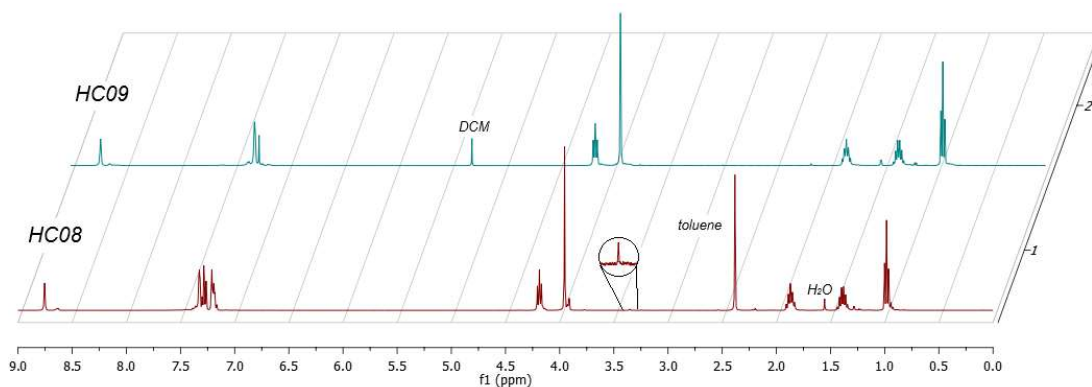
Figure 3.3. ^{1}H NMR (400 MHz, CDCl$_3$) spectra of reaction mixtures **HC08** and **HC09**.

Entries **HC08** and **HC09**: Reaction mixture was composed by 0.2 cm^3 of toluene or DCM, respectively, (where the compounds were dissolved) and 1 cm^3 of IL. Traces of methanol were detected in sample on sample **HC08.** Sample **HC08** presented a yellowish dark brown colour and **HC09** presented a strong yellow colour.

Entry **HC10**: The same reaction as **HC05**, however, [C$_8$mim][NTf$_2$] was used instead of [C$_4$mim][NTf$_2$]. Methane was formed, GC presented a peak of 729 of area. Reaction mixture presented a black coloration. It was possible to calculate CH_4 yield of 0.8%.

Entry **HC11**: The same reaction as **HC04** but without adding PPh$_3$. Traces of methane were detected by GC analysis. Reaction mixture presented a pitch-black coloration. No other products were detected.

54
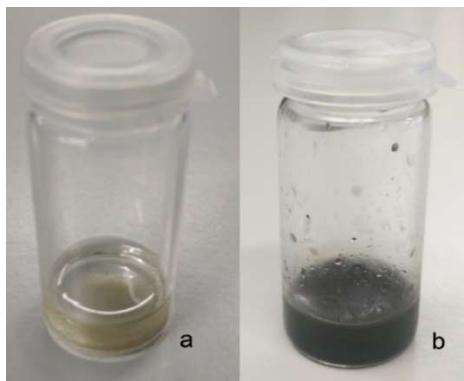
Figure 3.4. Picture of a generic reaction sample containing only Ru(cod)methylallyl2 as precursor and [C$_4$mim][NTf$_2$] as IL. a) sample before reaction; b) sample after reaction.

In summary, dissolution of the Ru precursor and PPh$_3$ ligand in toluene is necessary for the formation of the complex that catalyses CO$_2$ conversion into methanol. However, an IL medium was required for the conversion to occur, as when using toluene as solvent, toluene hydrogenation occurs instead. Reaction selectivity changes towards methane when the complex is not formed. This occurrence is often associated with the presence of a black final reaction mixture and black precipitate. Overall, increasing the ratio of H$_2$ in the gas mixture increases reactivity of the system. Reaction yield is enhanced when using [C$_8$mim][NTf$_2$] instead of [C$_4$mim][NTf$_2$]. The presence of PPh$_3$ appears to inhibit CO$_2$ conversion to methane.

Literature research led us to the work of Dupont's group [85,96–98], in particular to a paper where Ru(cod)methylallyl$_2$ was used to form Ru(0) nanoparticles in IL media, which were applied as a catalyst for the hydrogenation of arenes [67]. The similarities of the procedure and the black appearance of the reaction samples after reaction led to the conclusion that Ru(0) nanoparticles were formed during reaction and stabilized by the IL. This Ru(0) NPs catalysed CO$_2$ methanation.

After reaching these conclusions, which, as far as we know, had never been reported before, the investigation of this thesis focused on the study of CO$_2$ hydrogenation towards methane by IL immobilised Ru nanoparticles. The main reasons for this choice was the fact that methane resulted of a further reduction of CO$_2$ and could be applied in Power-to-gas technology (see **section 1.5**).

Since methane was found only as traces in the introductory work, the first step on this investigation was to improve CH$_4$ production. In **subchapter 3.2**, the set of chosen conditions studied in order to optimize the reaction are described. Different Ru catalyst precursors were tested, and their amounts were optimized. The effect of reaction temperature and reaction duration was studied, but always keeping in mind that reaction temperatures as low as possible were

preferable. Keeping the same total pressure, the pressure ratio of the reactants was also studied. After this study, "optimal reaction conditions" (the set of the best studied conditions) and "standard reaction condition" (the set of conditions determined as standard for comparison in further sections of the work) were defined. During all thesis work, reaction results were evaluated and compared using reaction yield as the main parameter, see **section 2.3.2**.

Chronologically, catalyst characterization took place at the same time as optimization. **Subchapter 3.3** displays the results from different analytical methods used to confirm the presence of Ru(0) NPs in the reactional mixture.

After standard reaction conditions were defined, additional parameters were studied in the attempt to improve and better understand the process. A different reactor with improved stirring was used, NPs prepared before reaction were tested, the effect of water presence was studied. These results are presented in **subchapter 3.4**.

 Subchapter 3.5 describes how around 20 different ILs were checked in order to study their effect on the reaction. In this study it was attempted to relate solubility of carbon dioxide in the ionic liquid with reaction yields, IL structure with NP size and stability and how it affects reaction activity and selectivity. This subchapter was divided in 2 main sections. In **section 3.5.1**, the effect of the cation was studied. Mainly imidazolium cations where used and the study focused on the effect of the length of the cation side chain and the protection of the cation acidic proton. In **section 3.5.2**, the effect of the anion was studied. Anions with different characteristics and structures where tested and compared among them, fluorinated, non-fluorinated, triflide, carboxylate and sulfonate-based.

On **subchapter 3.6**, studies of the reutilization of the NP/IL system are presented. Two recyclability tests were made, using the commercially used IL and the synthesised IL that provided the best results. In both tests, the system was reused six times.

The final subchapter, **3.7**, describes the experimental work done before the main research of this thesis. It comprises the first exploratory work using commercial catalyst pellets of noble metals in alumina while testing functionality performance of the assembled apparatus and sample recovery methods.

3.2 OPTIMIZATION REACTIONS

Optimization was conducted by studying the effect of different reaction conditions, mainly: catalytic precursor and catalyst amount, temperature of reaction, time of reaction and gas ratio. Tests were conducted using $[C_4mim][Ntf_2]$ and $[C_8mim][NTf_2]$ as liquid phase.

The experiments are not chronologically ordered, but subject ordered, meaning that reaction performance may fluctuate during this chapter. Also, some experiments may have been used to study more than one condition, meaning that the same sample may be mentioned in different sections.

After this study, standard reaction conditions were established for future experiments.

3.2.1 CATALYST

Different Ru precursors were tested. Reaction results and related information can be found in Table 3.3. From the tested precursors, Ru(cod)methylallyl$_2$ achieved the best results. This precursor was kept for the following reactions.

Table 3.3. Conditions and results of the study on the effect of the catalyst on CO_2 methanation.[a]

Entry	Catalyst	Ionic Liquid	Catalyst (μmol)	Temp. (°C)	CH$_4$ yield (%)	TON[b]	CO$_2$ Conv. (%)
NP00	-	$[C_4mim][NTf_2]$	-	140	0.0	0.0	0.0
NP01	$[Ru(cod)Cl_2]_n$	$[C_4mim][NTf_2]$	53	140	0.0	0.0	0.0
NP02	$RuCl_3$	$[C_8mim][NTf_2]$	43	140	0.0	0.0	0.0
NP03	$[Ru(\rho\text{-cymene})Cl_2]_2$	$[C_8mim][NTf_2]$	29	140	3.7	14.3	0.7
NP04	Ru(cod)methylallyl$_2$	$[C_8mim][NTf_2]$	25	140	8.6	35.2	2.1
NP05	Ru(acac)$_3$	$[C_8mim][NTf_2]$	25	150	0.2	0.7	< 0.1

[a] *conditions: 1 cm^3 of solvent; time = 24 h; Pt = 80 bar 40ºC; H$_2$:CO$_2$ pressure ratio of 1:1.*
[b] *mol CH$_4$. mol^{-1} cat.*

Reaction with different amounts of Ru(cod)methylallyl$_2$ added to the IL were conducted in order to study their effect in the reaction yield. Experimental conditions and results can be found on Table 3.4 and Figure 3.5.

Table 3.4. Conditions and results of the on study of the amount of Ru precursor in CO_2 methanation.[a]

Entry	Catalyst (µmol)	Temp. (°C)	CH_4 yield (%)	TON^{b}	CO_2 conv. (%)
NP06	25	150	14.0	64.2	3.3
NP07	75	150	39.9	62.3	7.7
NP08	100	150	46.4	54.5	6.8
NP09	110	150	64.4	67.3	13.0
NP10	125	150	53.4	49.7	10.9
NP11[c]	223	150	45.1	22.1	9.6

[a] conditions: 1 cm³ of [C₈mim][NTf₂]t; time = 24 h; Pt = 80 bar at 40°C .;
H₂:CO₂ pressure ratio of 1:1;catalytic precursor: Ru(cod)methylallyl₂
[b] mol CH₄ . mol⁻¹ cat.
[c] time = 48 h

Reaction yield increases with the amount of added precursor until a maximum of 110 µmol, which is the equivalent of 35 mg. After this point, reaction performance lowers. This could be caused by nanoparticle aggregation associated with the increase of precursor concentration in the reactional mixture. This effect is also reflected in a decrease of TON values, visible on the figure below.
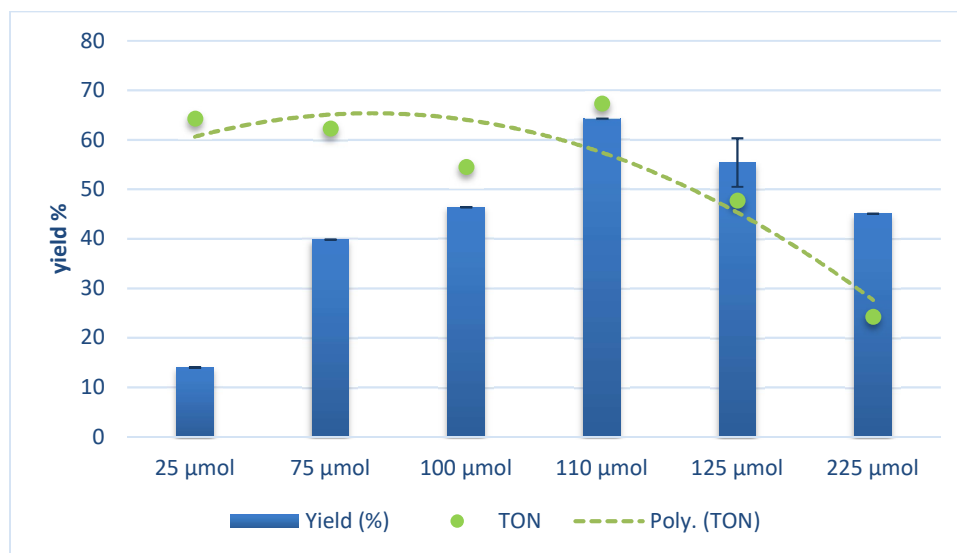
Figure 3.5. Effect of the amount of Ru precursor in CO_2 methanation yield at 150 °C using [C₈mim][NTf₂] as solvent.

Although entry **NP09** obtained the best result, this experimental point was chronologically one of the last reactions performed, therefore, standard reactions in this work use 125 µmol of precursor.

In Figure 3.5, the error bar at 125 μmol was calculated from 3 replicated results at the same conditions (see Table 3.5 for this reactions results). The average value calculated for this point was 55.4% of yield and standard deviation was used to determine the associated error, σ = ±4.9. In Table 3.4, this point was represented by sample **NP10**, the experimental median value.

Table 3.5. Summary of reaction results of CO_2 methanation using the same conditions for error determination. [a]

Entry	CH$_4$ yield (%)	TON[b]	CO$_2$ conv.(%)
NP10	53.4	49.7	10.9
NP12	50.7	47.7	11.8
CR01	62.2	55.8	13.3

[a] conditions: 1 cm³ of [C$_8$mim][NTf$_2$]t; time = 24 h; Pt = 80 bar at 40ºC ; H$_2$:CO$_2$ pressure ratio of 1:1; catalytic precursor:125μmol of Ru(cod)methylallyl$_2$; Temperature of reaction= 150℃.
[b] mol CH$_4$. mol^{-1} cat.

3.2.2 TEMPERATURE

As mentioned in the introduction, most of the catalytic CO_2 methanation reactions reported in the literature operate at temperatures above 200℃. However, this is a highly exothermic process whose equilibrium constant and yield decreases significantly with increasing temperature. Therefore, obtaining high reaction yields at temperature below this mark would be a significant improvement of the methanation process. Experimental tests were focused on conducting the reaction at low temperature levels and finding the lowest point where reaction still occurred. We had enough experimental points to study the effect of temperature for both reaction when using 25 μmol and 125 μmol of precursor. These results are presented in Table 3.6.

Table 3.6. Conditions and results of the study on the effect of the reaction temperature in CO_2 methanation.

Entry	Catalyst (μmol)	Temp. (°C)	CH₄ yield (%)	TON[b]	CO₂ conv. (%)
NP13	25	100	0.0	0.0	0.0
NP14	25	120	3.6	16.6	0.8
NP04	25	140	8.6	35.2	2.1
NP06	25	150	14.0	64.2	3.3
NP15	125	120	0.0	0.0	0.0
NP16	125	140	38.2	37.1	10.1
NP10	125	150	53.4	49.7	10.9

[a] conditions: 1 cm³ of [C₈mim][NTf₂]t; time = 24 h; Pt = 80 bar at 40ºC .; H₂:CO₂ pressure ratio of 1:1;
[b] mol CH₄ . mol⁻¹ cat.

Both reaction results reveal that reaction yield after 24 h greatly improves with increase of temperature. This means that the kinetics of the reaction (and not Thermodynamics) control the yield at lower temperatures, opening the field for improved catalysis. At 100 °C or below, the reaction does not occur (entry **NP12**). While it was possible to convert CO_2 at 120 °C when using 25 μmol (entry **NP13**) of precursor, this was not possible when using more catalyst (entry **NP14**). Considerable yields can be already obtained at 150 °C (entry **NP10**).

Figure 3.6 gives a graphical representation of the temperature dependence of reaction yields, when 25 μmol of precursor were used.
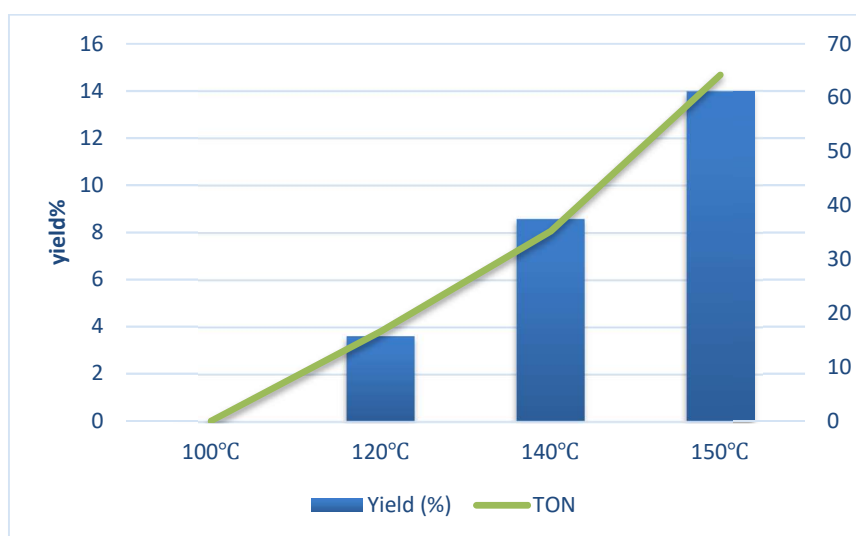
Figure 3.6. Effect of reaction temperature in CO_2 methanation yield using 25 μmol of Ru(cod)methylallyl2 as precursor and [C₈mim][NTf₂] as solvent.

3.2.3 TIME OF REACTION

Experiments conducted during 12h, 24h and 48h confirm that increasing the duration of the reaction enhances reaction yield, as shown in Table 3.7**Error! Not a valid bookmark self-reference.**.

Table 3.7. Conditions and results of the study on the effect of the reaction time in CO_2 methanation.[a]

Entry	Temp (°C)	Time (h)	CH_4 yield (%)	TON[b]	CO_2 conv. (%)
NP17	140	12	0.3	2.2	0.2
NP18	140	24	1.4	8.87	0.6
NP19	140	48	3.5	26.3	1.2

[a] *conditions: 1 cm³ of [C₄mim][NTf₂]t; Pt = 80 bar at 40°C; H₂:CO₂ pressure ratio of 3:1; Ru(cod)methylallyl₂ = 25µmol.*
[b] *mol CH₄. mol⁻¹ cat.*

Since the reaction is under kinetic limitations, increasing its duration increased considerable the yield obtained after 48h of reaction. However, test studies were kept at 24h to better adjust to laboratory schedule and maximize the number of reactions performed during the work.

3.2.4 PRESSURE GAS RATIO

The ratio of the reactants can influence in the reaction results. It is generally agreed that a $H_2:CO_2$ mole ratio between 3:1 and 4:1 provide better methane selectivity an yield [42]

Due to safety precautions, experimental studies began with low H_2 concentration in the system that increased over time. However, during these studies H_2 was always kept as the limiting reactant. The reactant ratios studied were 1:3, 1:1 and 3:1 $H_2:CO_2$ ratio. These are partial pressure ratios. Due to CO_2 compressibility the molar fraction of CO_2 in the mixture is higher than its partial pressure (see **section 2.3**). Data related to this study can be found in Table 3.8.

Table 3.8. Conditions and results of the study on the effect of reactant pressure gas ratio in CO_2 methanation.[a]

Entry	Catalyst (µmol)	Ionic liquid	Temp. (°C)	$H_2:CO_2$ ratio	CH_4 yield (%)	TON[b]	CO_2 conv. (%)
NP20[c]	25	[C₄mim][NTf₂]	140	1:3	U.C	U.C	U.C
NP21	25	[C₄mim][NTf₂]	140	1:1	2.17	8.9	0.4
NP18	25	[C₄mim][NTf₂]	140	3:1	1.39	8.9	0.6
NP04	25	[C₈mim][NTf₂]	140	1:1	8.6	35.2	2.1
NP22	25	[C₈mim][NTf₂]	140	3:1	4.0	27.8	1.9
NP10	125	[C₈mim][NTf₂]	150	1:1	53.4	49.7	10.9
NP23	125	[C₈mim][NTf₂]	150	3:1	47.5	59.4	24.6

[a] conditions: 1 cm³ of IL; time = 24 h; Temp = 150 °C; Pt = 80 bar at 40°C; $H_2:CO_2$ pressure ratio of 1:1;
[b] mol CH_4. mol⁻¹ cat.
[c] sample NP20 = sample HC11
UC: unable to calculate

Sample **NP20** is a renamed entry of sample **HC11** presented in **section 3.1**. Results of this entry are not provided in Table 3.8 because the method of reactants addition differs from the method developed to calculate de correct amount reactants. However, we can state that only traces of CH_4 were produced due to the size of the GC peak in GC analysis. The amount of methane produced in reaction **NP20** is much lower than what was produced in **NP21** and **NP18**, therefore a H2:CO_2 pressure ratio 1:3 is the least desirable for the reaction.

Since CO_2 is the reactant in excess, adding less of this compound increases CO_2 conversion values. Comparing **NP20** and **NP18** results we conclude that 1:1 pressure ratio provides better yield results. This was a surprising result, since a 3:1 ratio has a reactant proportion closer to the reaction stoichiometry. To confirm such results, another test was performed at different reaction conditions, entry **NP10** and **NP21**. Again 1:1 ratio provided lower CO_2 conversion, but higher yield.

CO_2 high solubility in the IL facilitates H_2 dissolution. We propose that a higher partial pressure of CO_2 will increase H_2 dissolution in the reaction media and therefore improve reaction results.

3.2.5 SUMMARY

Reaction optimization allowed to improve reaction results from initial trace amounts of methane, (entry **NP20**, **NP05** or **NP17**) up to a final yield of 64.4%, entry **NP09**. This result was obtained using 110 μmol of Ru(cod)methylallyl$_2$ as precursor, in [C$_8$mim][NTf$_2$] at 150 ℃ for 24h of reaction with a pressure ratio of 1:1 of reactants. This result could be further improved if using the set of the best reaction conditions tested: 110 μmol of Ru(cod)methylallyl$_2$, at 150 ℃ for 48h of reaction with a pressure ratio of 1:1.

After optimization, we defined Standard Reaction Conditions to be applied in future reactions in order to improve the method of comparison. Standard Reaction Conditions were defined as: 125 μmol of Ru(cod)methylallyl$_2$, at 150 ℃ for 24h of reaction with a pressure ratio of 1:1. They are not the best reaction conditions testes due to the aspects described in catalyst and time of reaction section, see **section 3.2.1** and **section 3.2.3**.

During this optimization process both [C$_4$mim][NTf$_2$] and [C$_8$mim][NTf$_2$] ILs were tested. As expected reaction results differ depending on the IL used as solvent. Further investigation on this subject will be reported in subchapter 3.5.

3.3 CATALYST IDENTIFICATION AND CHARACTERIZATION

3.3.1 UV/VIS STUDIES

According to literature, Ru(0) nanoparticle formation from sonification of an aqueous solution containing $RuCl_3$, SDS, $HClO_4$ and propanol can be identified by UV-vis [99]. Reduction proceeds sequentially from Ru(III) to Ru(II) to Ru(0), it occurs slowly and it is characterized by the gradual disappearance of bands situated at 560, 450 and 400 nm. Gupta et all [100] also state that Ru^{3+} ions present a peak at 383 nm, which disappears with the reduction of $RuCl_3$.

To support the theory that methane formation is catalysed by Ru(0), a series of UV-vis spectra of prepared samples of Ru(cod)methylallyl$_2$ in ILs was taken. Experiments were performed for both [C$_4$mim][NTf$_2$] and [C$_8$mim][NTf$_2$] ILs. A sample of each IL, diluted 1:200 in acetonitrile, was analysed and used as baseline for further analyses. Initially, blank samples, consisting in a mixture of IL and Ru precursor without further treatment, were analysed. Samples made at different time of sample preparation were analysed: **B1** corresponds to a 1 hour old sample, **B2** corresponds to a 24 hour old one, **B3** to 48 hours, and **B4** to a 1 week old sample. No hydrogen was admitted in these samples.

Figure 3.7. Picture of samples **B1** (Ru(cod)methyallyl$_2$ in [C$_4$mim][NTf$_2$], freshly prepared) and **B4** (Ru(cod)methyallyl$_2$ in [C$_4$mim][NTf$_2$], 2 days old).

UV/vis spectra of blank samples of both ILs present a peak at 240 nm that slowly disappears along with time. The samples also turned black over time without any kind of treatment.
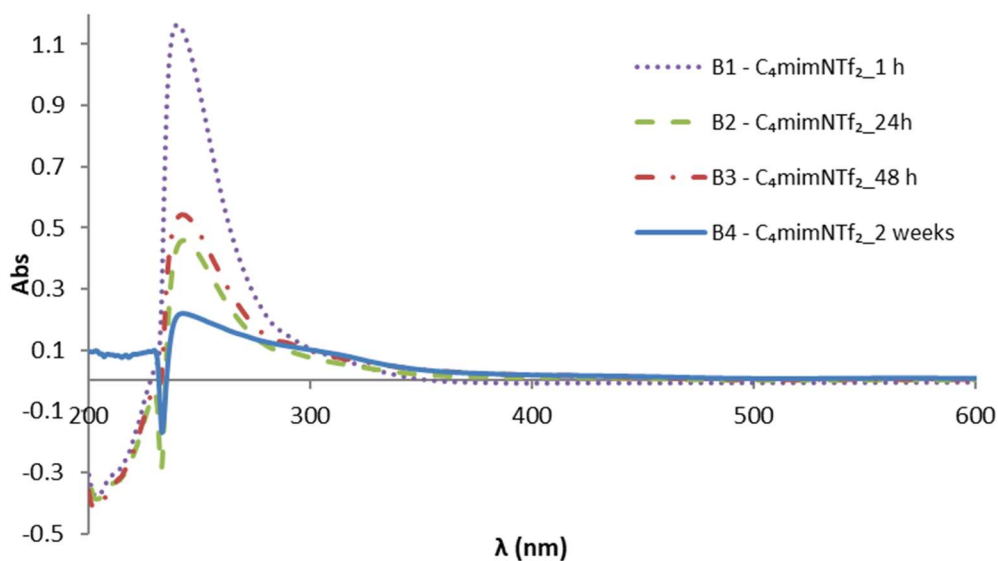
Figure 3.8. UV/vis spectra of blank samples along time in [C$_4$mim][NTf$_2$].
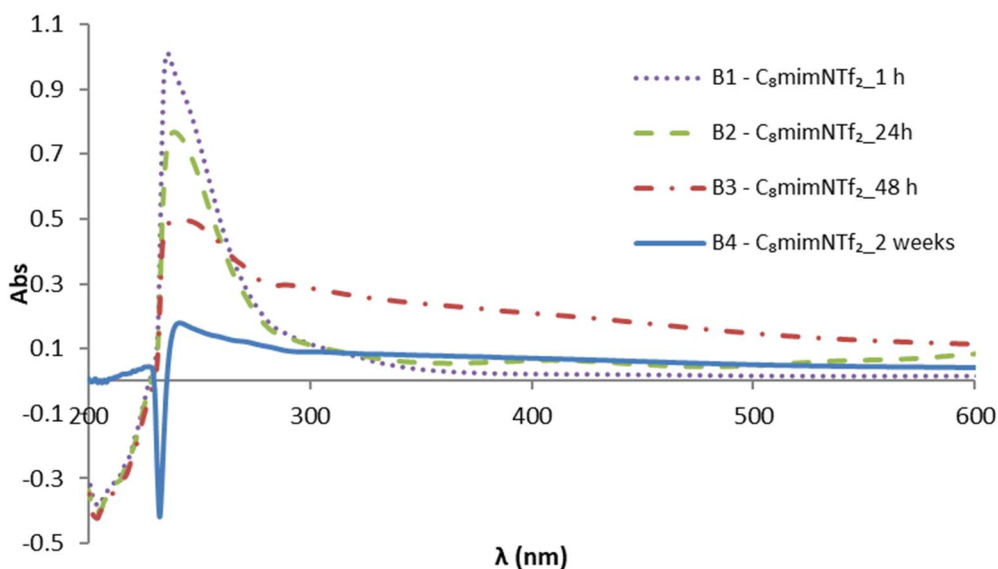
Figure 3.9. UV/vis spectra of blank samples of in [C$_8$mim][NTf$_2$]

Although, no reduction agent was added to the blank samples they were reduced to Ru(0) overtime. The reduction from Ru(II) into Ru(0) is described by the gradual disappearance of the band at 240 nm observed in Figure 3.8 and Figure 3.9. According to literature [85], the [NTf$_2$] anion in imidazolium ionic liquids can act like a nucleophile attacking the allylic-ligand of Ru(cod)methylallyl$_2$ causing decomposition of the IL and reduction of the Ru complex that generate the MNPs.

65

Subsequently we analysed samples that were reduced according to the experimental procedure described by Dupont et al.,[67] where Ru nanoparticles were generated. The Ru complex and IL were mixed at room temperature for an hour. The mixture was heated to 50 °C, and 4 bar of H_2 were admitted to the system. Three tests with different stirring times were carried out, namely: 1 hour (samples designated as **C1** and **D1**), 7 hours (samples designated as **C2** and **D2**) and 18 hours (samples designated as **C3** and **D3**).
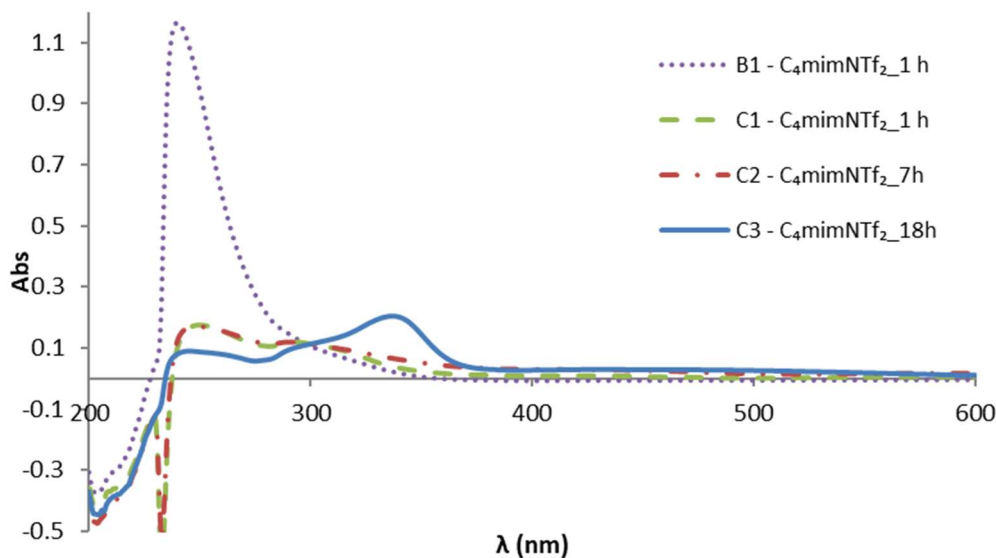
Figure 3.10. UV/vis spectra of samples of Ru nanoparticles reduced at 4 bar of H_2 and 50°C in [C$_4$mim][NTf$_2$] with different times of reduction.

UV/vis spectra of the reduced samples seen in Figure 3.10 and Figure 3.11 show the same behavior described by the blank samples over time, where the band at 240 nm gradually disappears, thus confirming that the disappearance of this band describes the reduction of Ru(II) into Ru(0). This decrease is, however much more pronounced since using H_2 as a reducing agent causes the process to occur much faster.
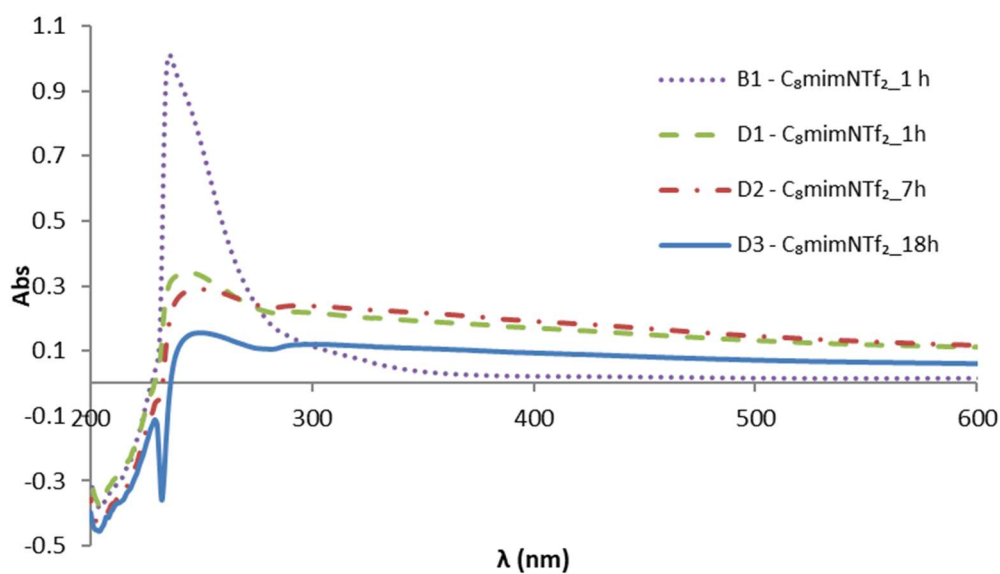
Figure 3.11. UV/vis spectra of samples of Ru nanoparticles reduced at 4 bar of H_2 and 50°C in [C_8mim][NTf$_2$] with different times of reduction.

The previous experiment was again repeated for a H_2 total pressure of 60 bar. Sample where the system was stirrer for 1 hour was designated as **C4** and **D4**, 7 hours was designated as **C5** and **D5** and 18 hours as **C6** and **D6**.
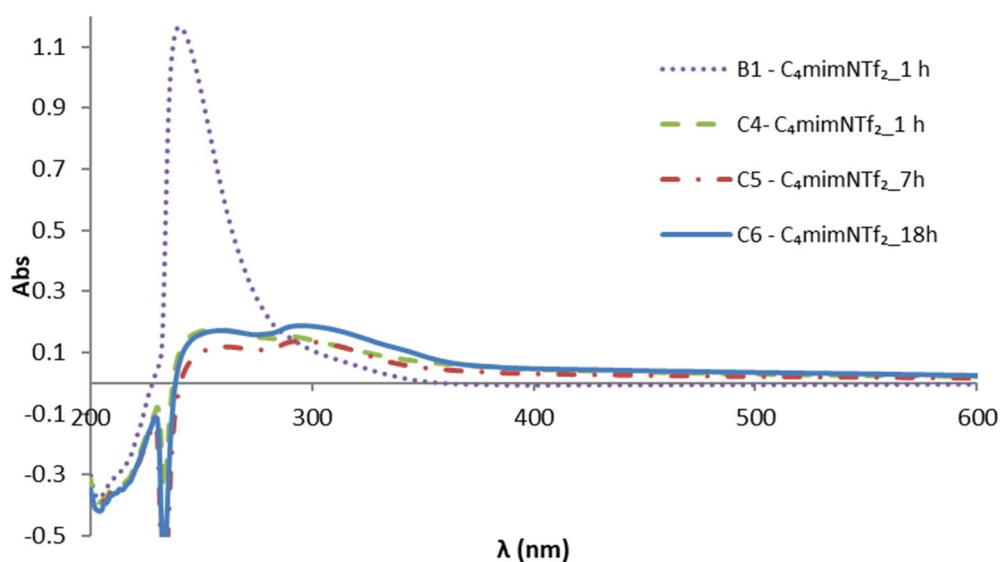
Figure 3.12. UV/vis spectra of samples of Ru nanoparticles reduced at 60 bar of H_2 and 50°C in [C_4mim][NTf$_2$] with different times of reduction.

In the [C_4mim][NTf$_2$] system 1 h is enough to completely reduce Ru.
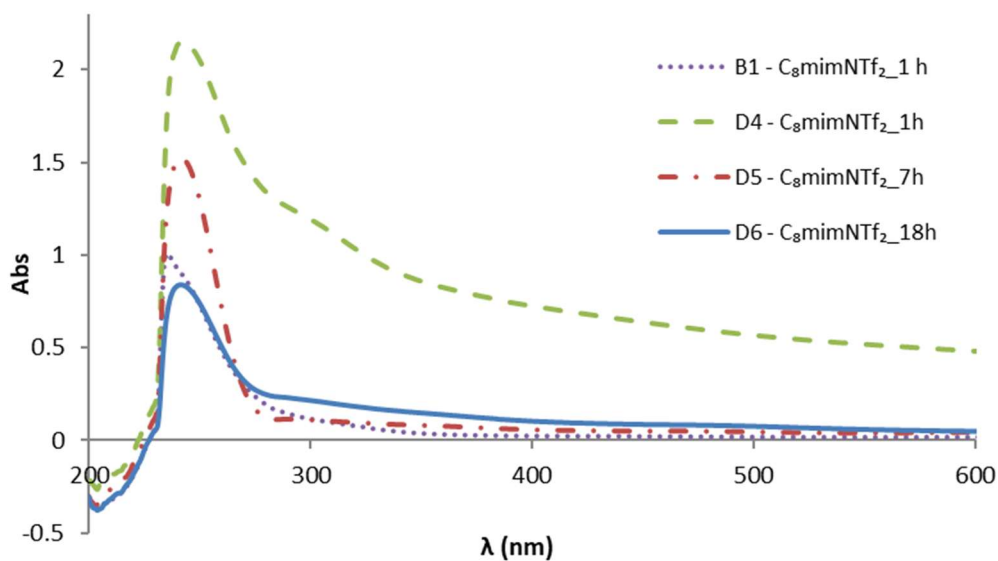
Figure 3.13. UV/vis spectra of samples of Ru nanoparticles reduced at 60 bar of H_2 and 50°C in $[C_8mim][NTf_2]$ with different times of reduction.

The $[C_8mim][Ntf_2]$ system, Figure 3.13, shows samples **D4** and **D5** with larger peak area than the blank sample. This could be explained by a dilution error, since the peaks areas keep decreasing over time, or by the production of a by-product within the same spectrum absorbance region, which slowly disappears over time.
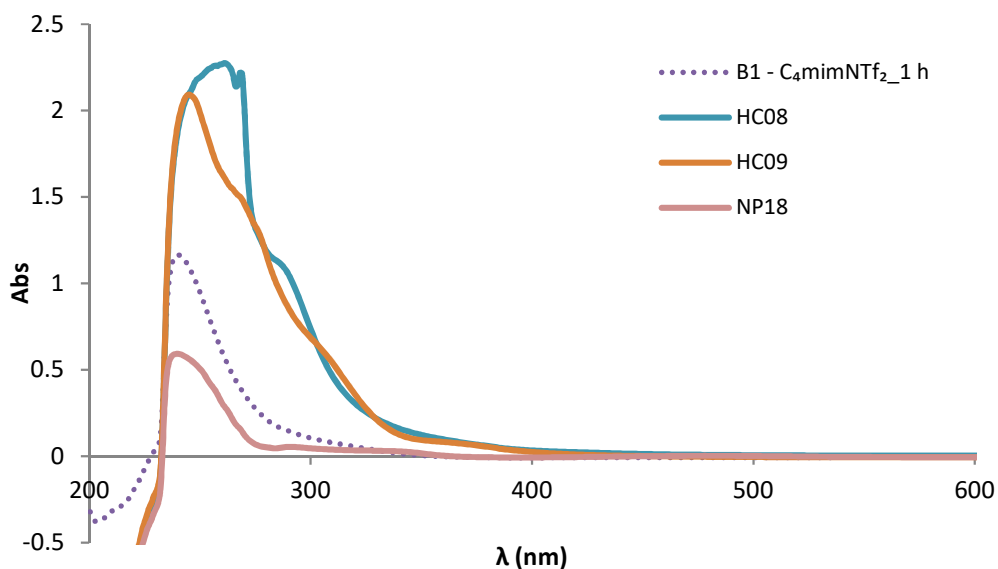
Figure 3.14. Comparison between UV/vis spectra of blank sample and reaction samples in $[C_4mim][NTf_2]$.

UV/vis analyses were made to some reaction samples, some previously described, others described in the following subchapter.

Samples **HC08** and **HC09** were analysed. They presented a broad band with an absorbance value greatly above blank value. This was mainly caused by the presence of solvents. Band cut-off values for the solvents were 270 nm for toluene and 235 nm for DCM [101].

Sample **NP19**, Table 3.7 ,correspond to a reaction where Ru(0) nanoparticles were supposed to be formed and generated methane in [C$_4$mim][NTf$_2$]. The area of the absorbance band is lower than **B1** blank, however higher than most of test samples where Ru reduction occurs (eg. **B4** or **C3**). This can be caused by a partial reduction of Ru or the production of by-product in the IL.

Sample **NP22** and **NP13** correspond to reactions where Ru(0) nanoparticles were supposed to be formed and generate methane in [C$_8$mim][NTf$_2$] IL Sample **NP22** generates methane and **NP13** doesn't due to temperature of reaction. Like UV/vis spectra presented in, Figure 3.13 presented in both samples uv/vis spectra presented a band larger than the blank sample.
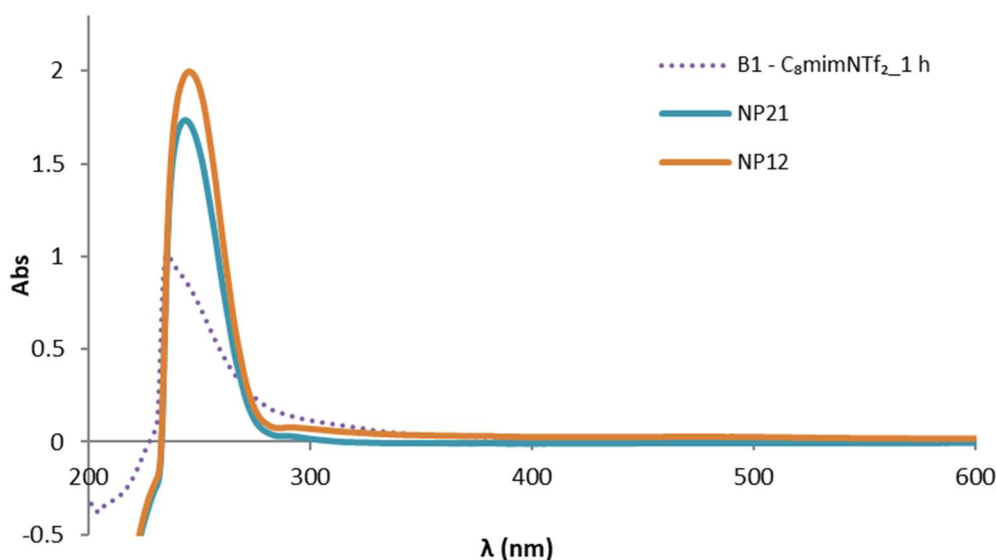
Figure 3.15. Comparison between UV/vis spectra of blank sample and reaction samples in [C$_8$mim][NTf$_2$].

3.3.2 DLS

In order to verify if the Ru(0) is present in the form of nanoparticles, particle size must be studied. The first attempts of size characterization of the Ru particles were made by dynamic light scattering, (DLS). However, after many attempts there was no positive feedback from this analysis, since most results were non-coherent or unreproducible. These problems could be related with a very heterogenous mixture regarding particle size or particle agglomeration due to the use of solvent necessary to perform the analysis.

3.3.3 MORPHOLOGY

Although, morpholi G3 equipment would not be able to identify particles below 5 μm, a reaction sample was examined to get a better insight of the mixture formed during reaction. Images of sample **NP07**, resulting from a reaction that took place in [C$_8$mim][NTf$_2$] with 75 μmol of Ru(cod)methylallyl$_2$, at 150 °C for 24 h are presented in Figure 3.16. Morphology images allow us to see a wide range of size and shapes of particles that appear to be aggregates of smaller particles. Some appeared to gather in the shape of coiled strings. Overall the particle size in the sample appeared to be extremely heterogeneous.
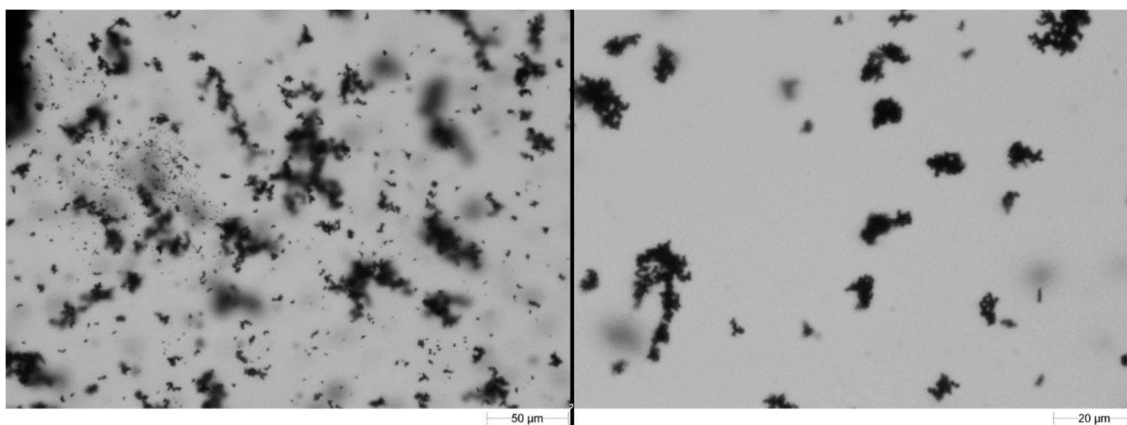
Figure 3.16. Morphologi G3 images of sample **NP07** reaction mixture, 75 μmol of Ru(cod)methuallyl$_2$ in [C$_8$mim][NTf2] at 150 °C for 24h with a pressure ratio of 1:1 of H$_2$:CO$_2$.

3.3.4 TEM

Nanoparticle identification and characterization was finally performed by transmission electron microscopy. Figure 3.17 presents micrographs of several areas of the first sample analysed by transmission electron microscopy (TEM), sample **NB08,** corresponding to a reaction that took place in [C_8mim][NTf$_2$] with 100 μmol of Ru(cod)methylallyl$_2$, at 150 °C for 24 h. Element energy dispersive spectroscopy (EDS) confirmed that the observed nanoparticles to be made of metallic Ru. The different images show areas where NPs were found aggregated and areas where they were scattered and stabilized. Histogram and size distribution of nanoparticles generated in [C_8mim][NTF$_2$] can also be found in the figure bellow. NPs presented an average particle size of 2.5 nm, with a standard deviation of 0.5, falling in the same size range as the nanoparticles previously described by Dupont and co-workers [67].
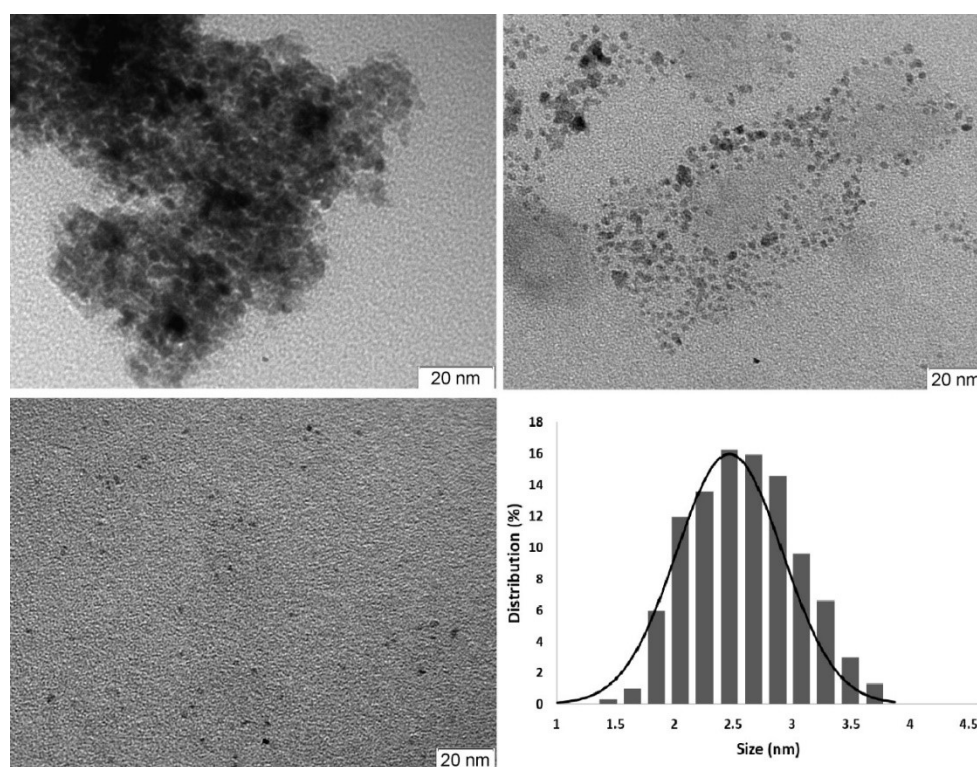
Figure 3.17. TEM micrograms and histograms showing the size distribution of Ru(0) NPs generated with 100 μmol of Ru(cod)methuallyl$_2$ in [C_8mim][NTf2] at 150 °C for 24h with a pressure ratio of 1:1 of H$_2$:CO$_2$. , sample **NP08**.

In conclusion, by using UV/Vis and TEM analysis it was possible to confirm the formation of Ru(0) NPs during CO2 methanation.

3.4 Additional Studies

3.4.1 Stirring

During most of the reaction processes described here, stirring of the reaction mixtures was essentially carried out by a 2 mm PTFE stirring bar added to the vial containing the IL and the catalyst. This magnetic bar was moved by a magnetic hot plate placed under the oil bath. During reactions, it was not possible to verify stirring velocity, since reactor did not possess a view cell. It was hypothesised that better stirring might improve mass transfer and therefore provide better results. In order to test this hypothesis, two reactions at the same condition were conducted, one in the usual reactor (defined here as reactor 1), and another in a Parr reactor with mechanically actuated magnetically coupled stirring and gas entrainment impellers to improve gas dispersion into the liquid system (defined here as reactor 2). The Parr reactor specifications and calibration can be found on experimental section, **section 2.3.3** above. Reaction conditions and results can be found below in Table 3.9.

Table 3.9. Conditions and results of the study on the effect of stirring in CO_2 methanation.[a]

Entry	Reactor	Ionic liquid	CH_4 yield (%)	TON[b]	CO_2 conv. (%)
NP24	Reactor 1	[C$_8$mim][OTf]	58.7	53.2	12.5
NP25	Reactor 2	[C$_8$mim][OTf]	61.0	57.5	11.5

[a] conditions: 1 cm³ of IL, Standard Reaction Conditions.
[b] mol CH_4 . mol^{-1} cat.

Reactions were executed using Standard Reaction Conditions and [C$_8$mim][OTf] as ionic liquid. The results provided by Reactor 2 were marginally better that by Reactor 1, possibly falling into error range. Therefore, we concluded that better mixing does not improve the results of the methanation reaction.

3.4.2 Water Content

During the progress of the experimental work, some reactions did not convert any CO_2. Some example can be found in Table 3.10.

Table 3.10. Examples of reaction conditions of CO_2 methanation reactions where conversion did not occur.[a]

Entry	Catalyst (μmol)	Ionic liquid	Temp. (°C)	H$_2$:CO$_2$ ratio
NP26	126	[C$_4$mim][Ntf$_2$]	150	1:1
NP27	75	[C$_8$mim][Ntf$_2$]	150	1:1
NP28	62	[C$_8$mim][Ntf$_2$]	150	1:1

[a] *conditions: 1 cm^3 of IL; Pt = 80 bar at 40ºC.*
[b] *mol CH$_4$. mol^{-1} cat.*

It was noted that these experiments had one factor in common, the IL was overly dried under vacuum before each reaction.

To study the effect of the IL water content in the CO_2 hydrogenation we compared reactions where [C$_8$mim][NTf$_2$] was used as purchased (entry **NP29**, 1500 ppm) and used after thoroughly dried by vacuum (entry **NP30**, <100 ppm). Interestingly, no conversion of CO_2 was observed when using the dried IL which leads us to conclude that not only the presence of water promotes the reaction but is also crucial for it to start. Salas et. Al [102] hypothesized that, like for a homogeneous catalyst, the activity of Ru(0) NPs under a 3 nm size is dependant of the nature of ligands, increasing in the presence of σ-donors like water or decreasing in the presence of π-acceptors, like phosphines.

Table 3.11. Conditions and results of the study on the effect of water content in CO_2 methanation.[a]

Entry	Water content (ppm)	Ionic liquid	CH$_4$ yield (%)	TON[b]	CO$_2$ conv. (%)
NP29	1480	[C$_8$mim][NTf$_2$]	61.8	55.8	12.8
NP30	102	[C$_8$mim][NTf$_2$]	0.0	0.0	0.0

[a] *conditions: 1 cm^3 of IL; Standard Reaction Conditions.*
[b] *mol CH$_4$. mol^{-1} cat.*

3.4.3 NPS SYNTHESIS

During the course of the work, Ru(0) NPs that catalysed the reaction were formed *in situ*, as the reaction took place. A couple of tests were done to verify how synthesizing the NPs before reaction would affect reaction results. For this test, two reactions were carried out, entry **NP31,**

with 25 μmol of catalyst, and entry **NP32**, with 125 μmol. Each reaction result was compared with its equivalent reaction with *in-situ* catalyst generation in Table 3.12. Catalyst synthesis method can be found in the experimental part, **section 2.2.6**.

Table 3.12. Conditions and results of the study on the effect of generating Ru(0) NPs prior to reaction.[a]

Entry	Catalyst (μmol)	Time (h)	Temp. (ºC)	CH$_4$ yield (%)	TON[b]	CO$_2$ conv. (%)
NP04	25	24	140	8.6	35.2	2.1
NP31	25	18 + 24[c]	140	4.3	18.7	0.9
NP16	125	24	140	38.2	37.1	10.1
NP32	124	18 + 24[c]	140	18.6	17.2	2.2

[a] *conditions: 1 cm^3 of [C$_8$mim][NTf$_2$]; Pt = 80 bar at 40ºC; H$_2$:CO$_2$ pressure ratio of 1:1.*
[b] *mol CH$_4$. mol^{-1} cat.*
[c] *18h of NPs formation + 24h of reaction.*

After comparing results between entries **NP04** and **NP31** and between entries **NP16** and **NP32** we can see that in both cases the catalyst activity decreases to half of its value when synthesizing the NPs prior to reaction. This decrease in the catalyst activity could be explained by the fact that the previously synthesised NPs are formed before the NPs generated in-situ therefore they had more time to start deactivating. Previously synthesised NPs are also submitted to more conditions changes that in-situ NPs which could also lead to aggregation.

3.5 STUDY OF THE EFFECT OF DIFFERENT IONIC LIQUIDS ON REACTION YIELD

Ionic liquids possess unique properties that can be tuned for different purposes, depending on the cation and anion in its composition. To design a task-specific IL for CO_2 methanation by Ru(0) NPs it is necessary to find what are the ions that provide the best results and the reason why they improve the reaction. Since transfer of reactants to the surface of the catalyst might be the limiting step of the reaction, studies were initially focused on the possible effect of CO_2 solubility in reaction performance. The study was divided in the separate effects of the cation and of the anion. Unless stated otherwise, all testes were executed using Standard Reaction Conditions determined in the previous subchapter.

For cations, mainly imidazolium-based ILs were chosen, for two reasons: (1) they have been widely described for the preparation and stabilization of several metal nanoparticles [79] and (2) there are CO_2 solubility data available. For anions, mainly fluorinated based ones were chosen for two reasons: (1) according to literature [103] fluorinated ILs have been considered to have high CO_2 solubility and (2) due to the availability of CO_2 solubility data.
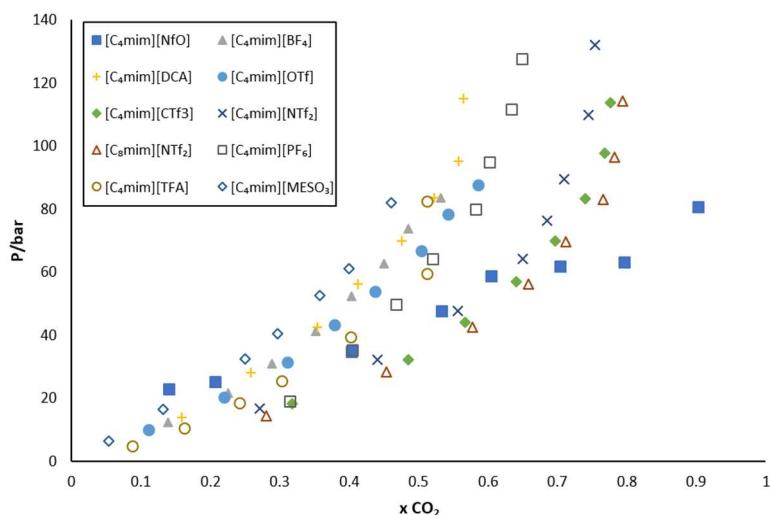

Figure 3.18. Solubility of CO_2 in [C_8mim][NTf$_2$] and C$_4$mim based ionic liquid with different anions at 40 °C: [NfO];[104] [DCA], [CTf3], [NTf2], [BF4], [OTf] and [PF6];[91] [TFA][105] and [MeSO$_3$].[106]

Although not enough data on CO_2 solubility in ILs at 150°C were found, we retrieved literature data of most of the used ILs at 40°C. These data can be found in Figure 3.18. According to it, the solubility of the CO_2 in the IL with [C_4mim] cation follows this order: [MeSO$_3$] < [DCA] ~ [BF$_4$]

< [OTF] < [TFA] < [PF$_6$] < [NTf$_2$] < [CTf$_3$] < [NfO].[91,104–106] Regarding the imidazolium cation, solubility slightly increases with a longer alkyl side chain.

3.5.1 CATION EFFECT

Alkyl chain length

Obtaining imidazolium ILs with different length of the alkyl side chain is a fairly easy process. Furthermore, it was noticed at the beginning of these studies that [C$_8$mim][Ntf$_2$] performed better then [C$_4$mim][NTf$_2$].

For this study we compared the results of methanation reactions using [C$_n$mim][NTf$_2$] ILs where n = 2,4,8 and 10. Reaction results can be found in Figure 3.19 or in Table 3.13 with detailed information.

Table 3.13. Conditions and results of the study on the effect of size of the alkyl size chain of the cation of the IL used as solvent for CO$_2$ methanation. [a]

Entry	Ionic liquid	CH$_4$ yield (%)	TON[b]	CO$_2$ conv. (%)
NP33	[C$_2$mim][NTf$_2$]	25.6	24.0	4.9
NP34	[C$_4$mim][NTf$_2$]	24.1	49.9	5.14
NP29	[C$_8$mim][NTf$_2$]	61.8	55.8	12.8
NP35	[C$_{10}$mim][NTf$_2$]	67.5	60.5	14.4

[a] *conditions: 1 cm³ of IL; Standard Reaction Conditions.*
[b] *mol CH$_4$. mol^{-1} cat.*

Reaction results generally show that a longer alkyl chain enhances methanation performance. Although this improvement is not seen between the shortest chains (from entry **NP33** to **NP34**), it can be seen on the remaining ones, specially between **NP34** and **NP29**. Furthermore, whenever possible, the anion effect studies were done using both, [C$_4$mim] and [C$_8$mim] as cations, to keep comparing the effect of the side chain of the imidazolium cation. When methanation occurred, the best results were always obtained with [C$_8$mim] based ILs with exception of one sample, see Table 3.16.
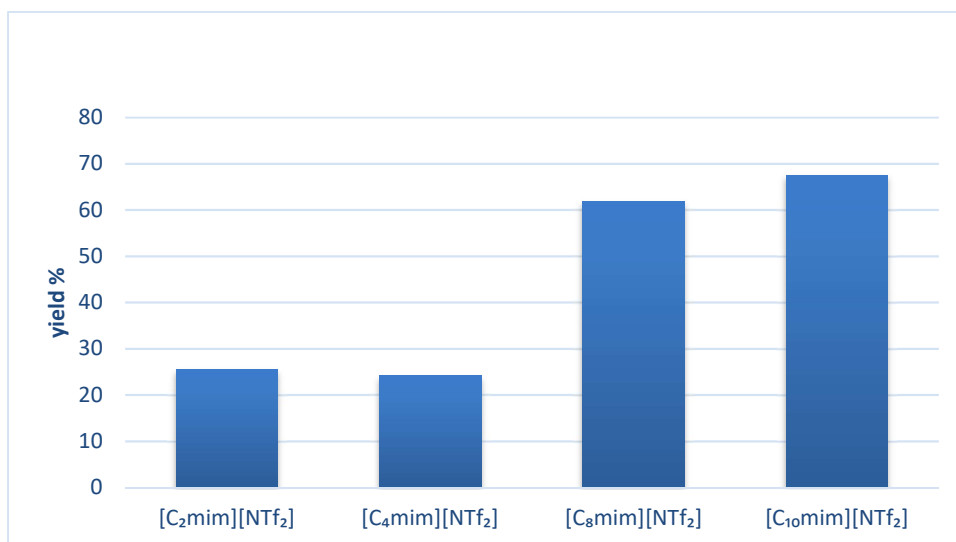
Figure 3.19. Effect of the size of the alkyl size chain of the cation of the IL used as solvent for CO_2 methanation.

Solubility of CO_2 in these ionic liquids increase with the length of the alkyl chain[107] which can benefit the reaction performance. Nanoparticle size and stability can also be involved in the results. When the IL has a long alkyl side chain, a steric effect occurs. The cation that are attracted near NPs surface provide steric forces stretching out their bulky side-chains, thus hindering the nanoparticles from approaching each other [108]. TEM analysis were performed to entry **NP34** sample ([C_4mim][NTf_2]), and entry **NP29** sample ([C_4mim][NTf_2]). When comparing **NP34** images (Figure 3.20) and **NP29** images (Figure 3.17) it can be seen that in both ILs some degree of aggregation has occurred, probably due to reaction conditions or reaction itself, although, aggregates in [C_4mim][NTf_2] sample are visible denser and in higher amount.
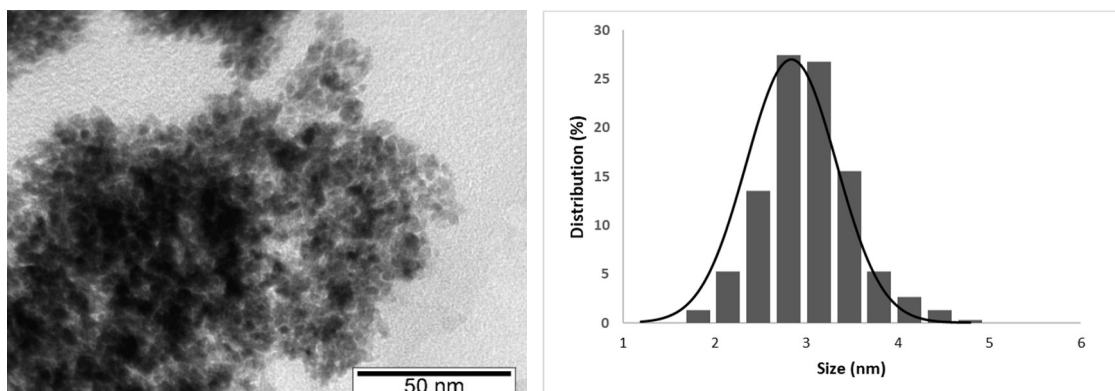

Figure 3.20. TEM micrograph and histogram showing the size distribution of Ru NPs generated in [C_4mim][NTf_2].

Santini's group [102] identified a relationship between length of the alkyl chain of [C$_n$mim] based ILs and Ru NP size. NPs size is influenced by the volume of the polar and non-polar domains in the ionic liquid and the preferential solubility of the metallic precursor to these domains. IL's non-polar regions are composed by the alkyl chains [109] In our case, Ru(cod)methylallyl$_2$ is soluble in water. Due to its affinity to the polar regions, longer alkyl chains increase the volume of the non-polar regions and thus decreasing the NPs size. Entry **NP34** NPs mean size is 2.5 nm with a σ of 0.5; entry **NP29** NPs mean size is 2.8 nm with a σ of 0.5. Effectively, analysis results correspond to what was expected, however with such high standard deviation, we can say that the obtained value fall in the same range and cannot confirm that such size difference can have an actual effect on the final reaction yield.

Imidazolium's ring C2 protection

The ring of the imidazolium cation is a planar pentagon. The hydrogen atom attached to the C2 position of the ring is very acidic (i.e., it has a relatively large positive charge). This allows better dissolution of the CO_2 in the IL via hydrogen bond. According to molecular simulations, replacing the proton in the C2 position with a methyl group would slightly decrease de CO_2 solubility of the Ionic liquid [19]. Since CO_2 solubility can influence the reaction results it is interesting to study the effect of the protection of the C2 position by a methyl group. To study this, results from CO_2 methanation with [C$_4$mim][NTf$_2$], entry **NP32**, and [C$_4$dmim][NTf$_2$], entry **NP36**, were compared. A drop in CO_2 solubility would anticipate lower reaction yields, however, against what was initially expected, the replacement of the proton for a methyl group greatly improved the yield of the reaction, Table 3.14.

Table 3.14. Conditions and results of the study on the effect of protecting the C2 position of the cation's imidazolium ring with a methyl group of the IL used as solvent for CO_2 methanation. [a]

Entry	Ionic liquid	CH$_4$ yield (%)	TON[b]	CO$_2$ conv. (%)	Ru NPs size (nm)[c]
NP32	[C$_4$mim][NTf$_2$]	24.1	49.9	5.14	2.8 (±0.5)
NP36	[C$_4$dmim][NTf$_2$]	58.4	53.2	12.2	2.2 (±0.3)

[a] *conditions: 1 cm^3 of IL; Standard Reaction Conditions.*
[b] *mol CH$_4$. mol^{-1} cat.*
[c] *values in parenthesis: standard deviation, σ*

This was a very interesting result since Luska et all [110] compared the hydrogenation of cyclohexane with Ru NPs formed in the same ILs with the same precursor and obtained opposite results. In that case it was proposed that the nanoparticles were more stable with [C4mim] based IL due to is lower degree of ionicity and the potential formation of C2-carbene (NHC) stabilizing species that would provide a more stable molecular arrangement of the IL. We propose that in the case of CO_2 methanation the presence of CO_2 at high conditions of pressure and temperature could create interactions between CO_2 and the carbene species that will not only decrease the reaction performance, but also cause a disruption of the molecular arrangement greater than the provoked by the C2-methylation.
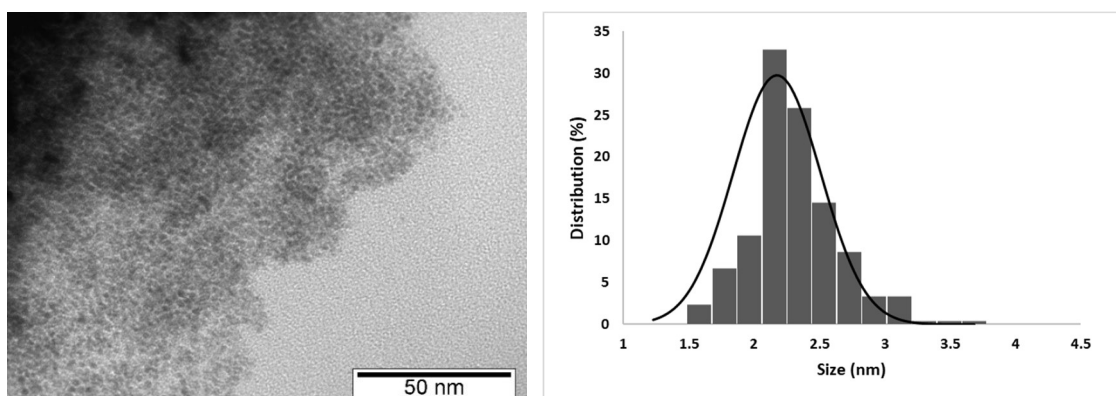

Figure 3.21. TEM micrograph and histogram showing the size distribution of Ru NPs generated in [C4dmim][NTf2], sample **NP36**.

Experimentally, TEM, analysis to the [C4mim][NTF2] and [C4dmim][NTf2] after ILs also contradict the results obtained in the literature. According to Luska et al[110], after reaction NPs in [C4mim][NTf2] and [C4dmim][NTf2] mean size was 1.9 (±0.4) and 2.6 (±0.6) respectively. Our results reveal NPs in [C4dmim] IL to be smaller than NPs in [C4mim] IL, although, both values fall in the same range size. More importantly, it is fairly noticeable in TEM micrographs provided for both NPs, Figure 3.20 and Figure 3.21, that NPs stabilized in [C4dmim][NTf2] are much more spaced apart between each other and present less and smaller aggregates than NPs stabilized in [C4mim][NTf2]. In our case [C4dmim][NTf2] is the system containing the most stabilized NPs and providing better results.

Luska ell all [110] also reported two theories that would provide different stabilization results: DLVO theory, where NP stabilization is influenced by the layer of anionic species surrounding the metal surface, and an increase in iconicity would increase the IL anion availability and provide better NP stabilization; and the stabilization mechanism proposed by Dupont and co-worker that states where NP stabilization is influenced by the formation of anionic aggregates close to the

metal surface,$[(DAI)_{x-n}(X)_x]^{n-}$, that are stabilized by the partial positively charged metal, and a decrease in iconicity would increase the interaction between the IL and this aggregates and provide better NP stabilization. To better understand how these mechanisms would influence NP stabilization in the current reactions an exhaustive study on the matter would be required.

Other cations

During anion effect study, [NfO] base ILs were tested. Before synthetizing an imidazolium base IL for the study, $[C_2C_1py][NfO]$, a commercially available IL was tested as solvent. This result is compared with the results obtained with the imidazolium based ILs in Table 3.15.

Table 3.15. Comparison of CO_2 methanation results obtained for IL containing the same anion, [NfO], for imidazolium and pyridinium based ILs.[a]

Entry	Ionic liquid	CH$_4$ yield (%)	TON[b]	CO$_2$ conv. (%)
NP43	$[C_4mim][NfO]$	54.0	49.0	11.2.
NP44	$[C_8mim][NfO]$	84.4	78.0	18.0
NP37	$[C_2C_1py][NfO]$	64.8	60.0	12.5

[a] *conditions: 1 cm^3 of IL; Standard Reaction Conditions.*
[b] *mol CH$_4$. mol^{-1} cat.*

While using $[C_2C_1py][NfO]$, 1-ethyl-3-methylpyridinium nonaflate, provided better results that $[C_4mim][NfO]$ it was not as efficient as $[C_8mim][NfO]$. However, it is to be noticed that the pyridinium cation used has an ethyl group as alkyl side chain, while it is being compared with cations with longer alkyl chains. As stated previously in this subchapter, longer alkyl side chains in cations provide better NPs stability, thus improving reaction performance. We can assume that an IL with a butyl or octyl side chain could provide even better results. Therefore, ILs with pyridinium based cations have an interesting potential for future investigation.

3.5.2 ANION EFFECT

Hydrogenation reactions were executed with imidazolium ILs and the following anions: dycianoamide ([DCA]), mesylate ([MeSO$_3$]), trifluoroacetate ([TFA]), hexafluorophosphate ([PF$_6$]), tetrafluoroborate ([BF$_4$]), Triflate ([OTf]), bis(trifluoromethylsulfonyl)imide ([NTf$_2$]), trisfluoromethanesulfonyl)imide ([CTf$_3$]) and perfluorobutanesulfonate ([NfO]). All anions were tested with both [C$_4$mim] and [C$_8$mim] cations with exception of [DCA] and [BF$_4$], where only [C$_4$mim] was tested. Reaction results can be seen in Table 3.16.

Table 3.16. Reaction and NPs characterization results for the study of the anion effect in the hydrogenation of CO$_2$ in Ru(0) NPs. [a]

Entry	Ionic Liquid	CH$_4$ yield (%)	CO yield (%)	TON[b]	CO$_2$ conv. (%)	Ru NPs size (nm)[c]
NP34	[C$_4$mim][NTf$_2$]	24.1	0.0	22.2	5.1	2.8 (±0.5)
NP29	[C$_8$mim][NTf$_2$]	61.8	0.0	55.8	12.8	2.5 (±0.5)
NP38	[C$_4$mim][DCA]	0.0	0.0	0.0	0.0	-
NP39	[C$_8$mim][BF$_4$]	43.7	0.0	41.8	10.4	-
NP40	[C$_8$mim][PF$_6$]	1.8	traces	1.67	0.3	-
NP41	[C$_4$mim][OTf]	46.0	0.0	42.3	10.5	-
NP42	[C$_8$mim][OTf]	58.6	0.0	56.3	12.0	-
NP43	[C$_4$mim][NfO]	54.0	0.0	49.1	11.2	-
NP44	[C$_8$mim][NfO]	84.4	0.0	78.0	18.0	2.4 (±0.5)
NP45	[C$_4$mim][CTf$_3$]	7.6	0.0	7.9	1.4	-
NP46	[C$_8$mim][CTf$_3$]	19.9	0.0	18.0	4.1	2.7 (±0.5)
NP47	[C$_4$mim][MeSO$_3$]	0.0	2.1	7.6	< 0.1	-
NP48	[C$_8$mim][MeSO$_3$]	0.0	7.5	27.8	< 0.1	2.9 (±1.0)
NP49	[C$_4$mim][TFA]	0.0	5.0	17.9	< 0.1	-
NP50	[C$_8$mim][TFA]	0.0	3.2	11.7	< 0.1	2.9 (±0.7)
NP51	[C$_4$mim][PFO]	60.7	0.0	53.8	11.0	-
NP52	[C$_8$mim][PFO]	50.0	0.0	45.9	10.2	1.6 (±0.2)

[a] conditions: 1 cm^3 of IL; Standard Reaction Conditions.
[b] mol CH$_4$. mol^{-1} cat.
[c] values in parenthesis: standard deviation, σ.

Entries **NP34** and **NP29** used [C$_4$mim][NTf$_2$] and [C$_8$mim][NTf$_2$] as solvent medium respectively. This ILs have been used since the beginning of the work and have been established as standard

for results comparison. They have been chosen due to the anion low coordination, their high thermal stability and high CO_2 solubility. After reaction both samples present as a black suspension with some precipitate in the bottom of the flask. This appearance was caused by the formation of Ru NPs (see Figure 3.20 for $[C_4mim][NTf_2]$ and Figure 3.17 for $[C_8mim][NTf_2]$) in situ. These reactions produced a considerable amount of methane. Entries **NP34** and **NP29** produced 24.1% and 61.8% of yield respectively.

Entry **NP38** used $[C_4mim][DCA]$ as solvent medium. CO_2 hydrogenation reaction did not occur. After the test the reactional mixture presented a brown yellowish colour and foamy appearance, see Figure 3.22. It is assumed that the strong coordinating nature of this anion prevented the reduction of metal precursor. [85]

Figure 3.22. Photographs of sample **NP38** after reaction.

Entry **NP39** used $[C_8mim][BF_4]$ as solvent medium. After reaction, IL sample presented the same appearance of most samples, black suspension with some precipitate at the bottom. No TEM analysis were made to this sample. Results were below par (yield of 43.7%) when compared with standard reaction, **NP29**. These results were in accordance with the expected, since this anion smaller volume and higher coordination anion provides lower NPs stabilization.

Entry **NP40** used $[C_8mim][PF_6]$ as solvent medium. This IL was tested to be compared with $[BF_4]$. As a least coordinate bulkier anion and providing better CO_2 solubility it was expected better reaction results. However, reaction condition caused this IL to degrade. Because of this, no more experiments were attempted with this IL. This reaction was only worth mentioning since it was the only reaction where both methane and CO (although in trace quantity) where produced at the

same time. After reaction, the mixture looked solidified with black precipitate imbued in it. TON and CO_2 conversion was only calculated from CH_4 data, since CO produced was not quantified, only identified.

Figure 3.23. Photographs of sample **NP40** after reaction.

Entries **NP41** and **NP42** used [C_4mim][OTf] and [C_8mim][OTf] as solvent medium respectively. After reaction samples presented typical black suspension appearance. When compared to standard reactions, reaction **NP41** produced more methane, while **NP42** results fell in the same range as their [NTf_2] counterparts. This was an interesting result since the anion [OTf] has a smaller molecular volume and less CO_2 affinity. Sample **NP42** was treated for TEM analysis with a different method, which left only a residual number of scattered NPs to be analysed, see Figure 3.24. There were no aggregates because they were eliminated in the analysis process and there was not enough NP quantity to correctly assess the mean size and distribution. The mean size of the visible group (≈20 particles) was calculated as 2.6 nm, an estimate that is in the same range as the standard samples.
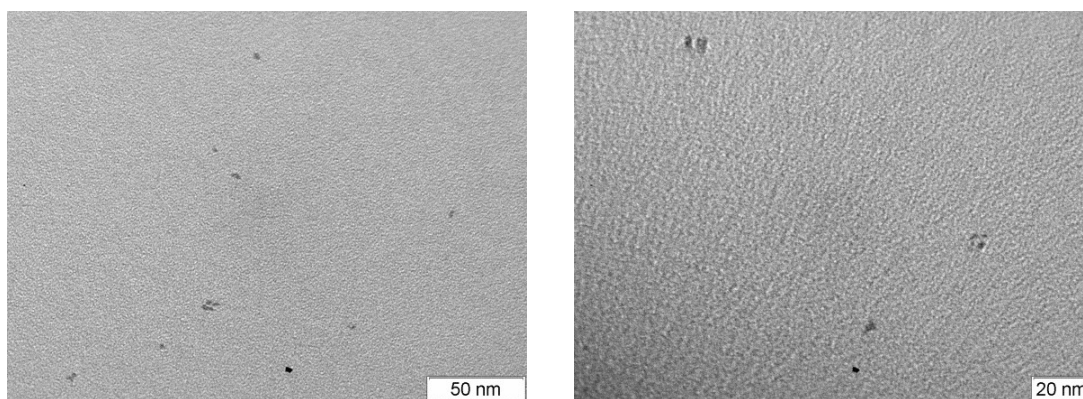
Figure 3.24. TEM images of Ru NPs generated in [C_8mim][OTf], sample **NP42**.

Entries **NP43** and **NP44** used [C$_4$mim][NfO] and [C$_8$mim][NfO] as solvent medium respectively. After reaction samples presented typical black suspension appearance. Both reactions performed better when compared to standard reactions. Sample **NP43** yield is more than the double of standard reaction and **NP44** achieved the best result during all work with a final yield of 84.4%. From the data recovered [NfO] anion provides the highest values of CO_2 solubility.

TEM analysis (see Figure 3.25) were conducted to sample **NP44**, showed regions with both aggregates and scattered nanoparticles. Overall, in this IL nanoparticles are more spaced apart when compared to standard sample (see Figure 3.17). NP mean size is slightly smaller but falls in the same range as NPs of standard sample. This anion provides higher CO_2 solubility and has a larger molecular volume with more fluorine atoms in its structures, overall explaining results obtained.
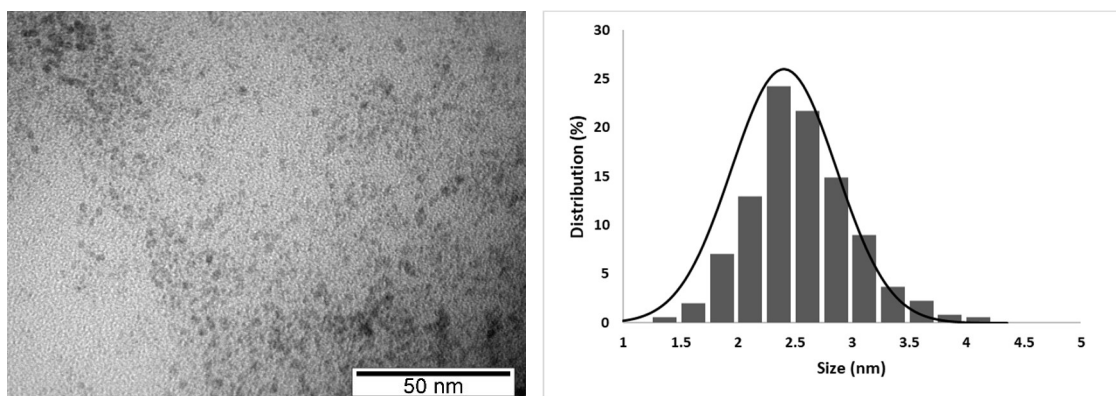
Figure 3.25. TEM micrograph and histogram showing the normal size distribution of Ru NPs generated in [C$_8$mim][NfO], sample **NP44**.

Entries **NP45** and **NP46** used [C$_4$mim][CTf$_3$] and [C$_8$mim][CTf$_3$] as solvent medium respectively. After reaction samples presented typical black suspension appearance. This ILs were synthesised and used because the [CTf$_3$] anion has a very large volume, and the same amount of fluorine atoms as [NfO] anion. Solubility of CO_2 in [CTf$_3$] based ILs, studied by Brennecke's group, is higher that [NTf$_2$]. Interestingly, reaction results reveal yields of 7.6% and 19.9% for sample **NP45** and **NP46** respectively. This were among the lowest methane yield results obtained. TEM analysis (see Figure 3.26) were conducted to sample **NP46**, most of the NPs in the sample were sintered. The anion [CTf$_3$] did not provide the necessary stabilization. This shows that capacity of the IL to form and stabilize NPs is more relevant to the performance of reaction than its capacity to solubilize CO_2. NP mean size is slightly larger but falls in the same range as NPs in the standard sample, showing that NPs size may also not be as relevant. We propose that the presence and size of the fluorinated side chain of the anion is will greatly influence NP stabilization in the IL.

84
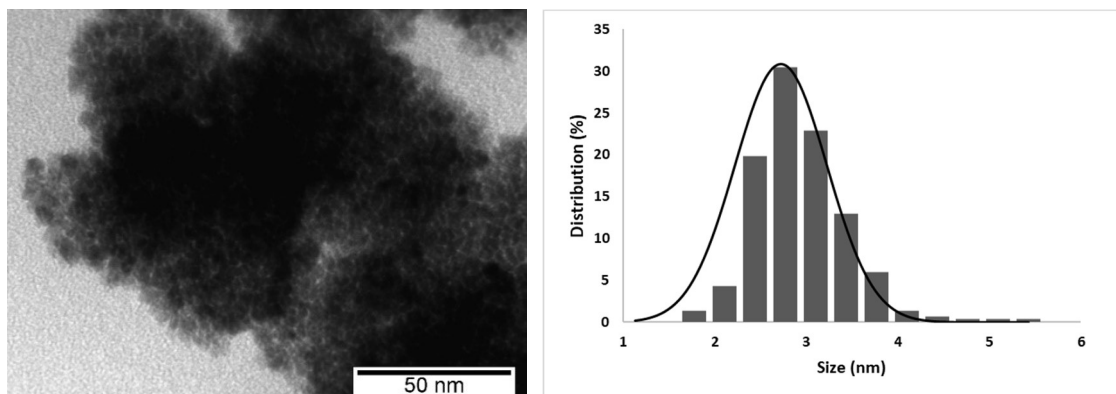
Figure 3.26. TEM and histogram showing the size distribution of Ru NPs generated in [C$_8$mim][CTf$_3$], sample **NP46**.

Entries **NP47** and **NP48** used [C$_4$mim][MeSO$_3$] and [C$_8$mim][MeSO$_3$] as solvent medium respectively. Entries **NP49** and **NP50** used [C$_4$mim][TFA] and [C$_8$mim][TFA] as solvent medium respectively. After reaction samples presented a black colour with a yellowish tonality. Instead of producing methane, CO$_2$ hydrogenation in this ILs produced a small amount of carbon monoxide (2-8%). Carbon monoxide was identified by GC, see Figure 3.27 as example of sample NP47. The remaining GCs can be found in Appendix E. CO is commonly considered an intermediate product according to one of the most accepted mechanisms for CO$_2$ methanation [42]. The tested ILs changed reaction selectivity towards the intermediate product. It was not possible to detect a pattern between reaction yield and the ions of the ILs used.
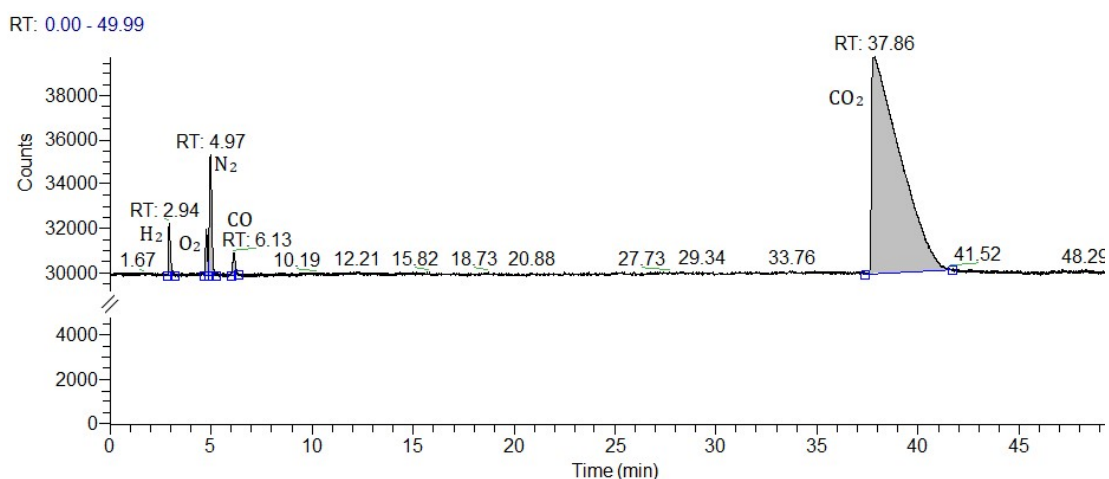
Figure 3.27. Gas Chromatograph of gas sample taken from CO$_2$ hydrogenation in Ru NPs/[C$_4$mim][MeSO$_3$]. Peaks observed: H$_2$, RT=2.94 min.; O$_2$ (traces), RT=4.77 min.; N$_2$ (traces), RT=4.97 min.; CO, RT=6.13 min.; CO$_2$, RT=37.86 min.

TEM analysis were conducted to sample NP48 (see Figure 3.28) and NP50 (Figure 3.29).

Interestingly, NPs in [C$_8$mim][MeSO$_3$] sample present two distinct sizes: smaller NPs within the same size range as other NPs samples, and larger samples near 5 nm size. This is possible to be observed in TEM micrographs and in the histogram that presents a bimodal distribution instead of a normal distribution. Apart from size distribution it was also visible by TEM analysis that NPs were found in less amount and very spaced apart from each other. No aggregation was visible.
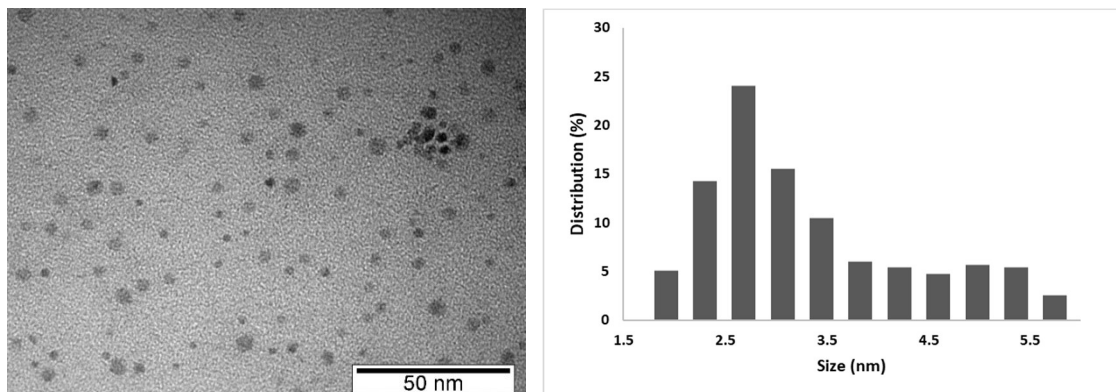
Figure 3.28. TEM micrograph and histogram of Ru NPs generated in [C$_8$mim][MeSO$_3$], sample **NP48**.

From TEM analysis to Ru NPs generated in [C$_8$mim][TFA] it is possible to see the formation small aggregates where the NPs are visibly spaced apart. NP mean size is larger that but also falls in the same range as NPs in the standard sample.
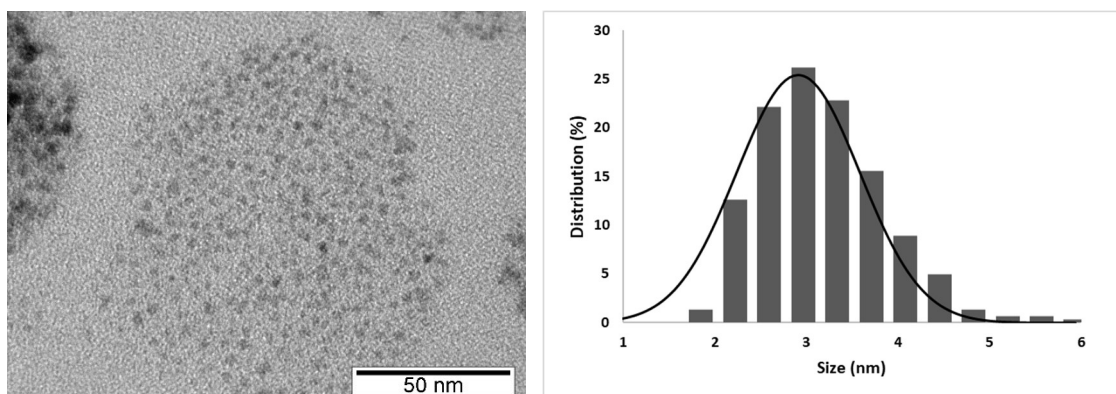
Figure 3.29. TEM micrograph and histogram showing the size distribution of Ru NPs generated in [C$_8$mim][TFA], sample **NP50**.

Overall NPs where CO is formed instead of methane are more dispersed then NPs that catalysed CO$_2$ methanation.

Initially, these anions were tested to study the influence of the sulfonate group (comparing results between [OTf] and [TFA]) and fluorine presence in the anion (comparing results between [OTf]

86

and [MeSO₃]). In both cases there was selectivity changed from methane ([OTf]) to CO ([TFA] and [MeSO₃]), but further studies should be done to confirm that this effect is caused by the absence of this groups. Like what happened with [DCA], the strong coordination of this anions could be preventing the formation of most Ru NPs and reducing the catalyst activity towards the formation of small amounts of the intermediate product. CO_2 methanation can also be inhibited by the presence of CO itself [111].

Entries **NP51** and **NP52** used [C₄mim][PFO] and [C₈mim][PFO] as solvent medium respectively. The results from this ILs was quite interesting. Entry NP51 provided the best methane yield ever obtained with a [C₄mim] based IL, 60.7%. **NP52** results, however, were below expectations, and the reaction with [C₈mim] based IL preformed worse than [C₄mim] based IL. No solubility data was found for this ILs since there was no existing literature information regarding this ILs.

TEM analysis were conducted to sample **NP52** (see Figure 3.30). No aggregation was found in all the analysed sample. NPs were smallest analysed in this work, 1.6 nm the and uniformly scattered among each other. Overall the IL appeared to be highly stabilized, which is accordance with the theory that a longer fluorinated side chain in the anion promotes NPs stabilization.
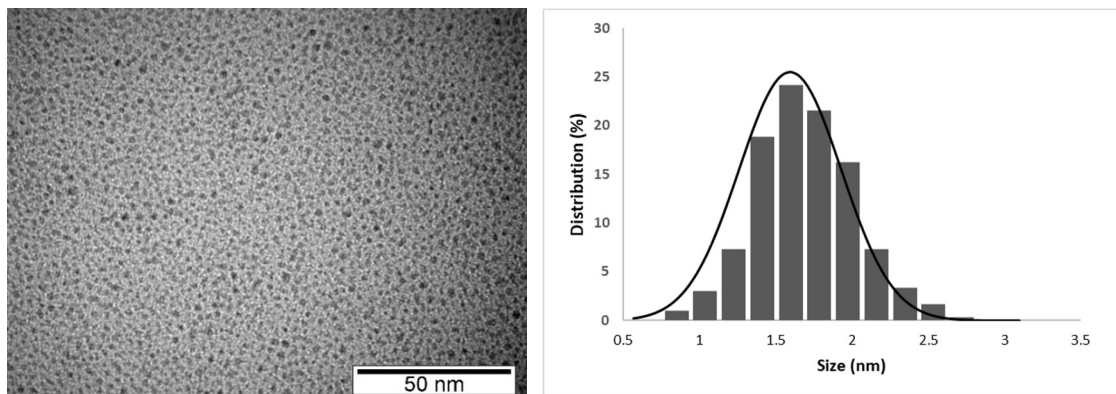
Figure 3.30. TEM micrograph and histogram showing the size distribution of Ru NPs generated in [C₈mim][PFO], sample **NP52**.

The low yield could be realated to the following facts: (1) [C₈mim][PFO] presented itself as a solid at the condition of admitance of the rectants in the apparatus. (2) Although possessing the longest chain and most stable nanoparticles [PFO] does not sulfonate group in its composition. The lack of this grop could affect the reaction outcame. (3) We also propose that when nanoparticles are too dispersed, (eg. [C₈mim][MeSO₃]) the system may be overstabilized, the interaction between the IL and the NPs strong enough that the reactants to interact with the surface

of the catalyst thus decreasing overall activity. (4) NPs mean size is smallest, being slightly out of size range. This may affect the reaction but there is not a mean of comparison since all other NPs are in the same size range among them. To understand what factor causes this, further investigation should be made.

3.6 Catalyst Recycling

The last step after improving reaction results was to test the capacity of the system (IL + catalyst) to be reutilized several times. Being able to reutilize this system would reduce the amount of catalyst and solvent necessary for a set of reactions and allow a future conversion of this batch process into a continuous process.

During reaction optimization, to assess the potential of catalyst reutilization sample **NP04** (see **section 3.2.1**) was reutilized. This experiment was conducted 20 days after the first reaction took place. A small drop from 8.6% to 7.3% yield was registered. The positive feedback of the results prompted the recyclability study.

The main catalyst recyclability study consisted in the realization of a set catalytic reactions using the established standard reaction conditions followed by gas analysis, depressurization, and another reaction at the same conditions. The process was repeated 6 times. During each reaction vacuum was submitted to the reactor and stirring was kept on avoiding aggregation. The reactor was kept closed during all process. A detailed description of the process can be found in the experimental section. A total of two studies were performed, one with $[C_8mim][NTf_2]$ and other with $[C_8mim][NfO]$.

3.6.1 1ST Reutilization Test

The first study used $[C_8mim][NTf_2]$, the commercially acquired IL that provided best results for CO_2 methanation results. Table 3.17 and Figure 3.31 provide relevant information on conditions and results of this study.

Table 3.17. Conditions and results of the study on catalyst recyclability of CO_2 methanation with Ru(0) NPs in [C_8mim][NTf$_2$]. [a]

Entry	P'$_{H_2}$ (bar)	Pt (bar)[b]	CH$_4$ yield (%)	TON[b]	CO$_2$ conv. (%)
CR01	42.0	119.7	62.2	55.8	13.3
CR02	42.2	121.8	60.9	54.8	13.15
CR03	42.0	127.7	40.5	36.3	8.7
CR04	42.1	137.5	40.1	36.0	7.6
CR05	41.9	122.9	53.6	47.9	11.4
CR06	41.8	131.2	42.1	39.5	8.6

[a] *conditions: 1 cm^3 of [C$_8$mim][NTf$_2$]; Standard Reaction Conditions.*
[b] *Total pressure at 150°C*
[c] *mol CH$_4$. mol^{-1} cat.*
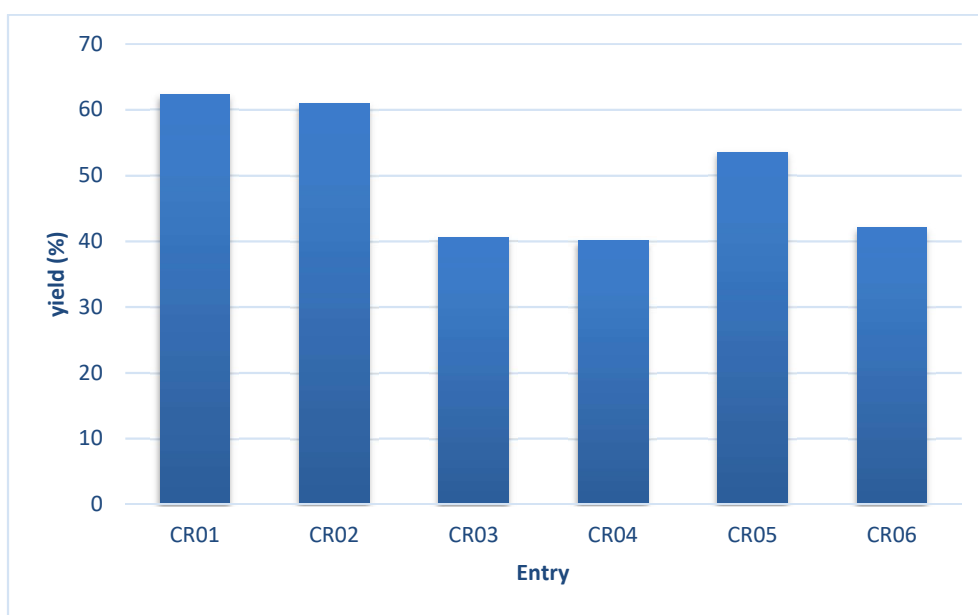
Figure 3.31. CO_2 methanation yield of the recyclability study for Ru(0) NPs in [C_8mim][NTf$_2$] system.

It is possible to verify that in general the yield slightly decreased over time. Overall a 20% decrease in yield was verified. An exception can be found at entry **CR05** where yield of reaction increased. To better understand this discrepancy, we provide Figure 3.32 where reaction results are displayed over time.

This graphic reveals a period of inactivity of 3 days where reactions did not take place between **CR02** and **CR03** and between **CR04** and **CR05**. This inactivity corresponds to weekend time when reaction and analysis could not be performed. It's also after these periods of inactivity that results deviate the most from the previous one leading us to believe that these facts could be related. Over time the nanoparticles in the system have tendency to aggregate, this can explain the regular decrease of activity during time and the great drop after a 3 day of inactivity after **CR02**. However, not the increase at **CR05**.
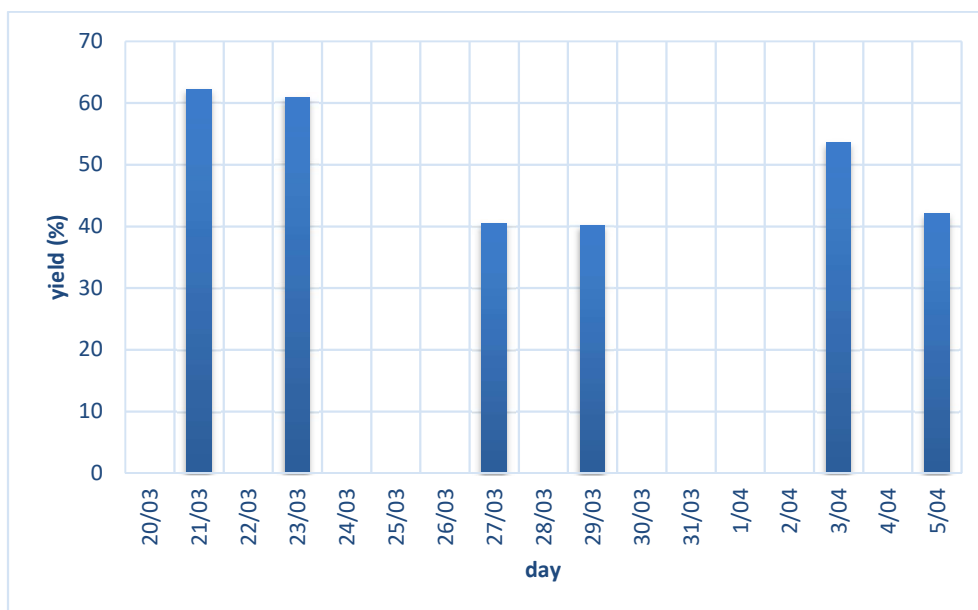
Figure 3.32. Time-line of the recyclability study for the Ru(0) NPs in [C$_8$mim][NTf$_2$] system.

During this test it was noticed irregular values when vacuum was submitted to the system between reactions. It was later confirmed that the tubing between the reactor and the vacuum pump was clocking. The objective of the vacuum was to eliminate part of the water produced during reaction. Although it has been shown that water is necessary to start the reaction and explained that small amount of water improve the reaction, water is still a product of reaction. In substantial amounts it will decrease the systems catalytic activity. A deficient vacuum application could cause the amount of water before each reaction to be irregular causing the irregular results obtained during the test. It was also noticed that the total pressure at 150 °C before reaction takes place reactions was the highest when the yield achieved was the lowest. However, amount of gas initially admitted in the reactor. This pressure increase can be a sign of water accumulation in the system.

After the experiment the sample was taken from the reactor. Two distinct phases, with apparently the same volume were seen in the vial: A top phase consisting mainly of water and a bottom phase with the IL with a large amount of black precipitated in the bottom, supporting both theories.

3.6.2 2ND REUTILIZATION TEST

The second reutilization test used the Ru(0) generated in situ in [C$_8$mim][NfO], the system that provided the best methanation results. In order to provide more consisting results, the following measures took place: Inactivity times were reduced to a 2 day stop between **CR09** and **CR10**. Reactor connection to the vacuum pump was replaced. The period the system was subjected to vacuum was controlled to be precisely 5 min. before each reaction and 30 min. after each reaction. Test results can be found in Table 3.18 and Figure 3.33.

Table 3.18. Conditions and results of the study on catalyst recyclability of CO$_2$ methanation with Ru(0) NPs in [C$_8$mim][NFO].[a]

Entry	P'$_{H2}$ (bar)	Pt (bar)[b]	CH$_4$ yield (%)	TON[c]	CO$_2$ conv. (%)
CR07	42.3	127.9	80.2	72.5	14.7
CR08	42.3	124.9	75.3	68.2	14.5
CR09	42.1	127.9	72.5	65.3	13.7
CR10	42.3	122.5	67.7	63.5	13.8
CR11	42.2	120.8	60.2	54.4	12.4
CR12	42.4	119.0	UC	UC	UC

[a] conditions: 1 cm^3 of [C$_8$mim][NFO]; Standard Reaction Conditions.
[b] Total pressure at 150℃
[c] mol CH$_4$. mol^{-1} cat.
UC: unable to calculate.

During reaction **CR12** a leak was found in the system invalidating the precision of results obtained by GC. For this reason, values of **CR12** were not taken in account, nonetheless a considerable concentration of methane was still detected.
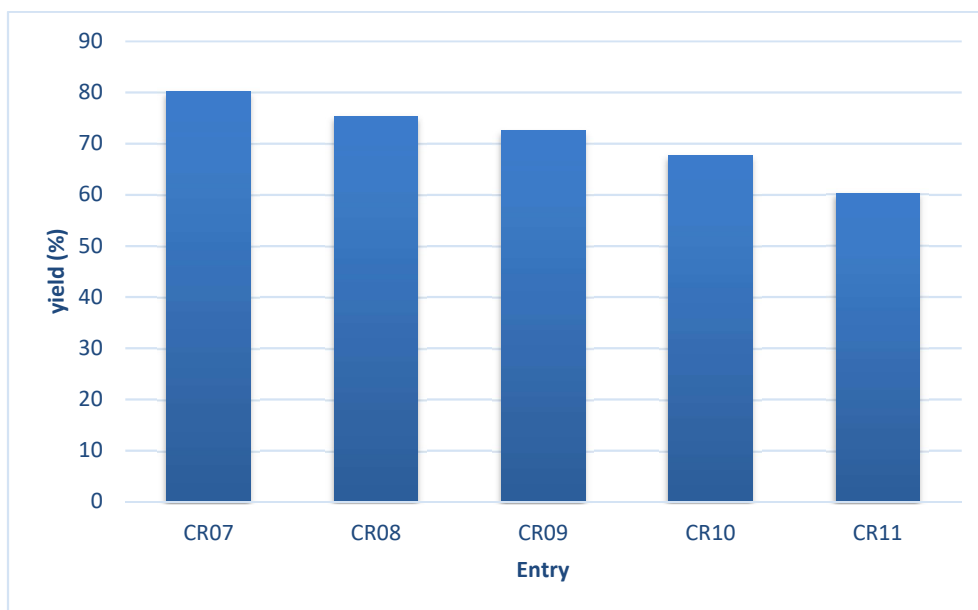
Figure 3.33. CO_2 methanation yield of the recyclability study for the Ru(0) NPs in [C$_8$mim][NfO] system.

As expected, the initial yield of this experiment reaches up to 80% of yield, similar to the result obtained with sample **NP44** during IL study. Measures applied for this test had a positive feedback since the catalytic activity decreases after each reaction at a slow and steady pace. Overall a 20% decrease in yield was verified after 5 reaction which is a slightly more accentuated overall decreased when compared with the same decrease after 6 reactions with [C$_8$mim][NTf$_2$]. Nevertheless, the yield achieved after 5 cycles of reaction with [C$_8$mim][NfO] is comparable with the yield obtained in the first reaction with [C$_8$mim][NTf$_2$]. After 168h of the first use corresponding of a total of 120h of reaction the catalyst was still active. Apart from vacuum, no other treatment was applied to the system between reactions.

After the experiment the sample was taken from the reactor. Instead of two phases, the black liquid was found scatter around the walls of the vial and the reactor, probably caused by the several changes of pressure during the process. This sample was analysed by TEM and compared with TEM of sample **NP44**.
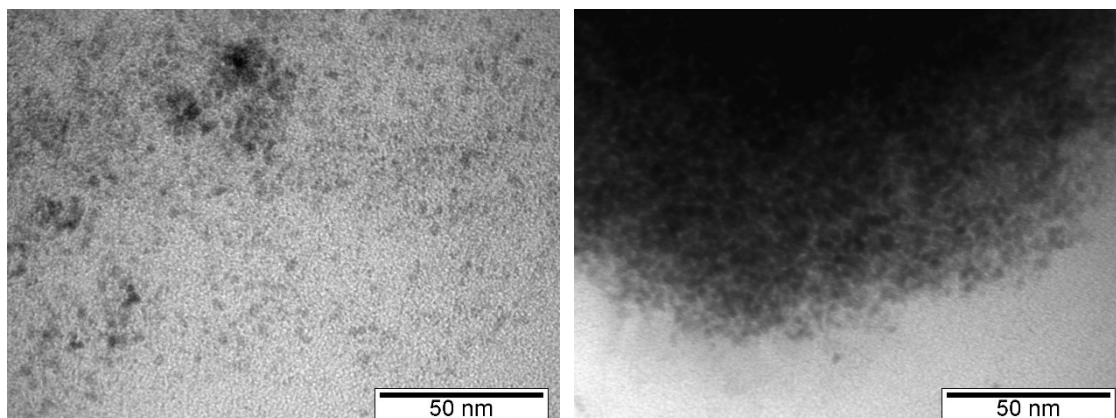
Figure 3.34. TEM micrographs of sample **NP52** at the right (Ru NPs in [C$_8$mim][NfO] after one reaction) and sample **CR12** in the right (Ru NPs in [C$_8$mim][NfO] after 6 hydrogenation cycles).

No considerable change was noted in size distribution, average NPs size was kept at 2.4 nm and standard deviation slightly increased from 0.5 to 0.6. TEM revealed more areas with aggregates in comparison to as it can be seen in Figure 3.34. This is probably the main cause for catalytic activity decrease. Further investigation should be considered in order to improve NPs stabilization during reaction. This investigation could allow the method to be developed into a larger scale continuous flow process.
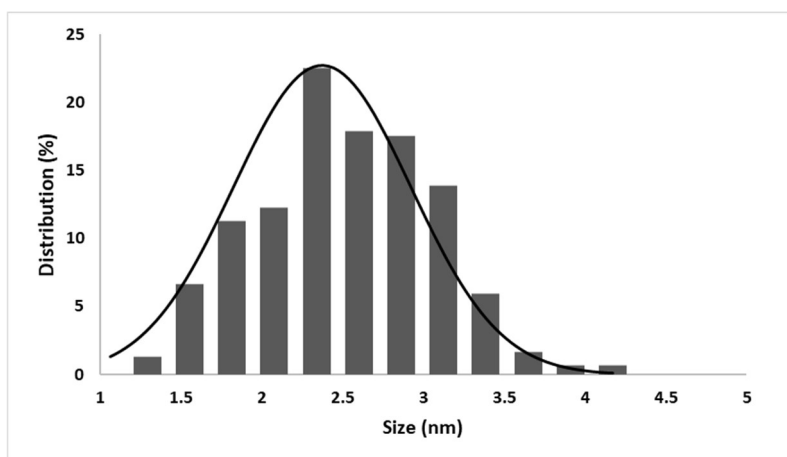
Figure 3.35. Histogram showing the size distribution of Ru NPs generated in [C$_8$mim][NfO] after being reused after 6 hydrogenation cycles, sample **CR12**.

3.7 SCREENING TESTS

In this section follows the necessary experimental work that took place before investigations main work.

Laboratory investigation started with screening tests in the assembled apparatus. The main purpose was to: (1) test the proper functioning of the apparatus and product detection methods, (2) start the exploratory work on CO_2 reduction. These preliminary tests consisted in the hydrogenation of CO_2 using commercially available heterogeneous catalysts of different metal basis. Due to their high catalytic activity, noble metal-based catalysts were chosen, namely, Ru, Rh and Pd supported in alumina. For safety reasons, the initial tests were performed with low amount of H_2.

After the catalytic tests a sample of the gas phase was analysed by gas chromatography, then, the reactor was opened. Inside the catalyst appeared to be dry. Some catalyst pellets were found destroyed, caused by reaction stirring. Gas analysis detected the presence of the reactants, and in some cases, methane.

Figure 3.36 and Figure 3.37, displayed below, show the chromatograms of the sample with highest methane peak as an example of what was obtained after GC analysis. The remaining chromatograms where methane was detected can be found in Appendix D. Method 1 of CG analysis (described on **section 2.2.7**) was used, and two channels are presented.
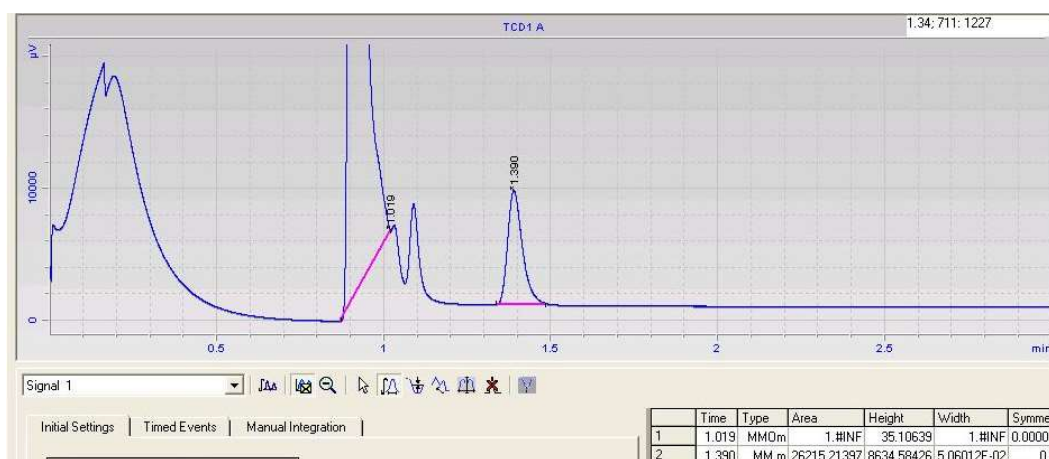
Figure 3.36. Chromatogram of entry ST11 provided by channel 1, method 1. 1st peak corresponds to H_2, 2nd peak corresponds to CH_4.
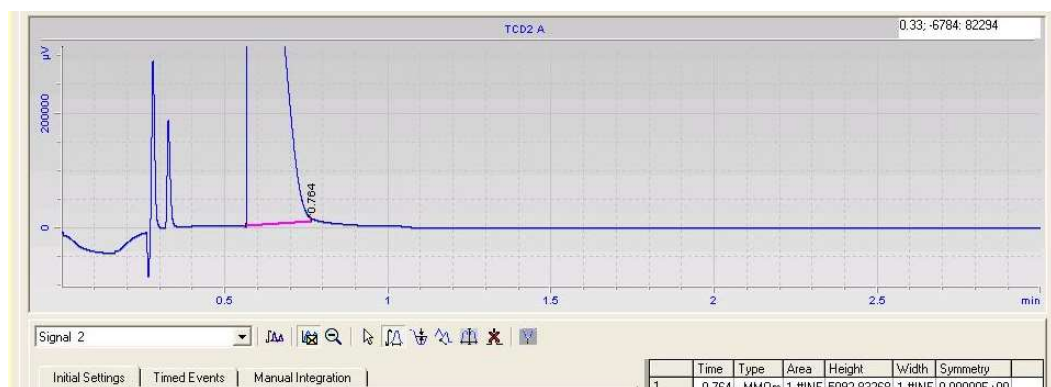
Figure 3.37. Chromatogram of entry ST11 provided by channel 2, method 1. 1st peak corresponds to CO_2.

Tested conditions and reaction results are summarised in Table 3.19. Gas ratio presented in the table is referent to pressure and not to molar fraction of the compounds. As mentioned before, for safety reasons, the initial $H_2:CO_2$ ratio tested is lower than the stoichiometrically required, independently of the product obtained. Another safety measure taken, was the fact that, with a 1:3 ratio, CO_2 was added fractionally to the reactor: 20 bar of CO_2, followed by 20 bar of H_2 and another 40 bar of CO_2. Together with the fact that the gases were added to the reactor at room temperature did not allow a precise calculation of the reaction yield. Since reaction conditions are the same in most of the catalytic tests, the peak area of the produced methane can be initially used as a parameter to compare the efficiency of the reaction.

Observing catalytic tests, **ST01**, **ST02** and **ST03** we can conclude that commercial Ru/Al_2O_3 (0.5 wt.%) and Pd/Al_2O_3 (0.5 wt.%) are able to produce methane at reaction conditions. Reaction selectivity was 100%. Ru and Rh supported catalysts are known to be most active and selective catalysts for CO_2 methanation [112]. However, unlike expected, Rh/Al_2O_3 (0.5 wt.%), did not catalysed the reaction. Ru catalyst was more active than Pd.

In the attempt of improving the results, some reaction conditions were modified: time of reaction was increased to 72 h and $H_2:CO_2$ ratio was changed to 1:1. Higher time of reaction was attempted at **ST04** and **ST08**, but no improvement was observed in either case. H_2 ratio in the reactor was increased when using Ru catalyst, entry, **ST11**. The amount of methane produced has greatly increased in this condition. For this reason, this same condition was attempted with Rh catalyst, however, still no reaction occurred, entry **ST12**.

96

Table 3.19. Conditions and GC results of screening tests.[a]

Entry	Catalyst	Time	$H_2:CO_2$ ratio	EZ bath	GC peak area of CH_4
ST01	Rh/Al_2O_3	24 h	1:3	N_2+ salt + ice	–
ST02	Ru/Al_2O_3	24 h	1:3	N_2+ salt + ice	11596
ST03	Pd/Al_2O_3	24 h	1:3	N_2+ salt + ice	2835
ST04	Pd/Al_2O_3	72 h	1:3	N_2+ salt + ice	2473
ST05	IL coated Rh/Al_2O_3	24 h	1:3	N_2+ salt + ice	–
ST06	IL coated Ru/Al_2O_3	24 h	1:3	N_2+ salt + ice	–
ST07	IL coated Pd/Al_2O_3	24 h	1:3	N_2+ salt + ice	–
ST08	IL coated Pd/Al_2O_3	72 h	1:3	N_2+ salt + ice	–
ST09	Ru/Al_2O_3	24 h	1:3	ice	7764
ST10	Ru/Al_2O_3	24 h	1:3	none	4729
ST11	Ru/Al_2O_3	24 h	1:1	none	26215
ST12	Rh/Al_2O_3	24 h	1:1	none	–
ST13	IL coated Ru/Al_2O_3	24 h	1:1	none	4993

[a] *conditions: 1g of catalyst (~50 μmol of metal), T=140 °C, Pt = 80 bar at room temp.*

Another objective of this tests was to obtain a preliminary assessment of whether the use of ionic liquids as solvents or as catalyst modifiers could prove beneficial to this reaction. For this reason, the same reactions were executed using solid catalysts with the ionic liquid layer (SCIL). Catalyst pellets were impregnated with [C_4mim][BF_4] by incipient wetness method. Entries **ST05**, **ST06** and **ST07** tested the three-different impregnated catalyst. No reaction took place with any of this coated catalyst. Taking in account the improvement verified when gas ratio was 1:1, the same reaction conditions where attempted with coated Ru/Al_2O_3, **ST13**. Methane was produced in smaller amounts compared to the IL-free catalyst. In conclusion, coating the catalyst with IL did not change the reaction selectivity and decreased the catalyst activity.

During depressurization process, the expansion vessel was immersed in a cryogenic bath, initially composed by N_2, salt and ice. The initial idea was to liquify some of the CO_2 in the vessel decreasing the concentration of CO_2 in the gas phase and increasing methane concentration. This method would allow us to detect products by GC even if produced in trace amount. Technically, the expansion vessel used was too large to allow CO_2 condensation. After depressurization to the

expansion vessel, the pressure would drop from 75-85 bar to 2-4 bar. However, it was possible to see that temperature change in the expansion vessel bath changed the methane concentration detected by the GC in the desired away. This reaction was attempted, and gas sample was capture, in three diverse ways: while the expansion vessel was in the N_2 + salt + ice cryogenic bath, **ST02**, in an ice bath, **ST09**, and at room temperature **ST10**. The colder the bath, the higher were the values of methane detected. Having equilibrium between in all system means that the methane concentration inside the reactor is the same inside the expansion vessel, when the expansion vessel is colder the apparatus is not in equilibrium and the values provided are enhanced. Since it was possible to capture and identify methane when the reaction system is at the same temperature, we concluded that no cooling bath should be used when attempting to quantify the produced methane.

Chapter 4 – CONCLUSIONS AND FUTURE PERSPECTIVES

This work aimed to develop a new process of conversion of carbon dioxide into fuels, implementing ionic liquids.

Initially two methods where approached: (1) using a Ru organometallic precursor, Ru(cod)methyallyl$_2$, and a phosphine ligand, (triphenylphosphine) to form a complex that catalysed the reaction in IL, and (2) using the same precursor without the ligand as catalyst in the same reaction in IL. While the first method generated traces of methanol, on the second method reaction selectivity changes and traces of methane were formed.

This thesis focused mainly the method to produce methane, since the use of this compound as a fuel is preferential do to the already implemented infrastructures of natural gas distribution.

Through analytical methods it was confirmed that, during reaction (*in-situ*), the Ru precursor was reduced into Ru(0) NPs with a mean size raging 1.6–2-9 nm. This NPs were stabilized in IL due to this solvent steric and electrostatic properties, and capable of converting CO_2 into methane with a 100% selectivity.

Initially only traces of methane were detected, but after some initial optimization higher reaction yields were obtained. Best reaction result during optimization tests was 64.4% of yield with the following conditions: Reaction temperature of 150°C, duration of 24h, total initial pressure of 80 bar (40 bar admission of both reactants), using 35 mg of Ru(cod)methylallyl$_2$ as precursor and 1 mL [C$_8$mim][NTf$_2$] IL as solvent. The reaction temperatures achieved during this work were very low compared with most CO_2 methanation processes.

During this study we were also able to conclude that hydrogenation is favoured when the nanoparticles are synthesized in-situ. Although it is a product of reaction the presence of small amount of water is required to start the reaction.

Tests were performed with various ILs and [C$_8$mim][NfO] was found to be the best solvent in an efficiency of 84.4%. During the tests with imidazolium-based cations it was concluded that longer side alkyl chains benefits the reaction results. Improvement was also noticed when using [C$_4$dmim][NTF$_2$], were the proton in position C2 of the imidazolium ring was replaced by a methyl group. Among the several anions tested the ones with longer fluorinated side chain provided higher NPs stability and reaction yields. Reaction selectivity changed with [MeSO$_3$] and

[TFA] anions. In these cases, cation-anion interactions are stronger and CO, an intermediate product, in generated instead of CH_4.

Overall, we conclude that the capacity of the IL to form and stabilize NPs is more relevant to the performance of reaction than its capacity to solubilize CO_2. NPs size was considered not relevant since most of the nanoparticles were within the same size range.

The recycling tests performed show that it is possible to reutilize the NPs/ILs system, however, a constant slight catalyst deactivation is present after each reaction. After 5 reutilization cycles catalyst activity decreases around 20%, a total of 120h of reaction. This deactivation was mainly caused by the aggregation of nanoparticles and accumulation of water in the system, factors that can still be improved.

Regarding future work, investigation to improve the process can still be made through a wide myriad of approaches:

New cations can be tested, such as guanidinium, ammonium or pyridinium, based ILs. Some of our tests already concluded that pyridinium based ILs to be very promising.

Being a noble metal, Ru is very expensive. The process can become economically more viable if a cheaper metal is used as catalyst in the reaction. Tests with different metallic precursor such Nickel, Iron, Copper or Zinc could be attempted. Even if some of this metallic catalyst do not catalyse the reaction or aren't as active, bimetallic systems with Ru could improve reaction performance.

Different conditions could be tested for optimization, such as testing the stoichiometric ratio of the reactants, changing the amount of IL used or the total pressure in the system. The initial quantity of water in the reactor could also be optimized to an ideal amount.

New ways of keeping the NPs stabilized for longer periods of time could be investigated such as the use of additives or methods for catalyst immobilization with supports

All this investigation allied with nowadays technology experience in CO_2 reaction in continuous flow would allow further improvement and development of this method into a larger scale process.

REFERENCES

[1] Wesselbaum, S.; Hintermair, U.; Leitner, W. Continuous-Flow Hydrogenation of Carbon Dioxide to Pure Formic Acid Using an Integrated ScCO₂ Process with Immobilized Catalyst and Base. *Angew. Chemie Int. Ed.* **2012**, *51* (34), 8585–8588.

[2] Götz, M.; Lefebvre, J.; Mörs, F.; McDaniel Koch, A.; Graf, F.; Bajohr, S.; Reimert, R.; Kolb, T. Renewable Power-to-Gas: A Technological and Economic Review. *Renew. Energy* **2016**, *85*, 1371–1390.

[3] Srivastava, V. In Situ Generation of Ru Nanoparticles to Catalyze CO₂ Hydrogenation to Formic Acid. *Catal. Letters* **2014**, *144* (10), 1745–1750.

[4] Upadhyay, P. R.; Srivastava, V. Ionic Liquid Mediated In Situ Synthesis of Ru Nanoparticles for CO₂ Hydrogenation Reaction. *Catal. Letters* **2017**, *147* (4), 1051–1060.

[5] Melo, C. I.; Szczepańska, A.; Bogel-Łukasik, E.; Nunes Da Ponte, M.; Branco, L. C. Hydrogenation of Carbon Dioxide to Methane by Ruthenium Nanoparticles in Ionic Liquid. *ChemSusChem* **2016**, *9* (10), 1081–1084.

[6] Dutcher, B.; Fan, M.; Russell, A. G. Amine-Based CO₂ Capture Capture Technology Development from the Beginning of 2013 - A Review. *ACS Appl. Mater. Interfaces* **2015**, *7* (4), 2137–2148.

[7] International Energy Agency. *CO₂ Emissions from Fuel Combustion 2017 - Highlights*; 2017; Vol. 1.

[8] Kondratenko, E. V.; Mul, G.; Baltrusaitis, J.; Larrazabal, G. O.; Perez-Ramirez, J. Status and Perspectives of CO₂ Conversion into Fuels and Chemicals by Catalytic, Photocatalytic and Electrocatalytic Processes. *Energy Environ. Sci.* **2013**, *6* (11), 3112–3135.

[9] Sanz-Pérez, E. S.; Murdock, C. R.; Didas, S. A.; Jones, C. W. Direct Capture of CO₂ from Ambient Air. *Chem. Rev.* **2016**, *116* (19), 11840–11876.

[10] US Department of Commerce, NOAA, E. S. R. L. ESRL Global Monitoring Division - Global Greenhouse Gas Reference Network https://www.esrl.noaa.gov/gmd/ccgg/trends/ (accessed Jun 18, 2018).

[11] UNFCCC. Conference of the Parties (COP). Paris Climate Change Conference-November 2015, COP 21. In *Adoption of the Paris Agreement. Proposal by the President.*; 2015; Vol. 21932, p 32.

[12] Mikkelsen, M.; Jørgensen, M.; Krebs, F. C. The Teraton Challenge. A Review of Fixation and Transformation of Carbon Dioxide. *Energy Environ. Sci.* **2010**, *3*, 43.

[13] Machado, A. S. R.; Nunes, A. V. M.; da Ponte, M. N. Carbon Dioxide Utilization-Electrochemical Reduction to Fuels and Synthesis of Polycarbonates. *J. Supercrit. Fluids* **2017**, No. December, 0–1.

[14] Tan, Y.; Nookuea, W.; Li, H.; Thorin, E.; Yan, J. Property Impacts on Carbon Capture and Storage (CCS) Processes: A Review. *Energy Convers. Manag.* **2016**, *118*, 204–222.

[15] Lip, W.; Shiun, J.; Hashim, H.; Azri, A.; Shin, W. Review of Pre-Combustion Capture and Ionic Liquid in Carbon Capture and Storage. *Appl. Energy* **2016**, *183*, 1633–1663.

[16] Songolzadeh, M.; Soleimani, M.; Takht Ravanchi, M.; Songolzadeh, R. Carbon Dioxide

Separation from Flue Gases: A Technological Review Emphasizing Reduction in Greenhouse Gas Emissions. *ScientificWorldJournal.* **2014**, *2014* (Figure 1), 828131.

[17]   Leung, D. Y. C.; Caramanna, G.; Maroto-Valer, M. M. An Overview of Current Status of Carbon Dioxide Capture and Storage Technologies. *Renew. Sustain. Energy Rev.* **2014**, *39*, 426–443.

[18]   Blomen, E.; Hendriks, C.; Neele, F. Capture Technologies: Improvements and Promising Developments. *Energy Procedia* **2009**, *1* (1), 1505–1512.

[19]   Ramdin, M.; Loos, T. W. de; Vlugt, T. J. H. State-of-the-Art of CO_2 Capture with Ionic Liquids. *Ind. Eng. Chem. Res.* **2012**, *51* (24), 8149–8177.

[20]   Shiflett, M. B.; Drew, D. W.; Cantini, R. a.; Yokozeki, a. Carbon Dioxide Capture Using Ionic Liquid 1-Butyl-3-Methylimidazolium Acetate. *Energy & Fuels* **2010**, *24* (10), 5781–5789.

[21]   Tomé, L. C.; Marrucho, I. M. Ionic Liquid-Based Materials: A Platform to Design Engineered CO_2 Separation Membranes. *Chem. Soc. Rev.* **2016**, *45* (10), 2785–2824.

[22]   Zeng, S.; Zhang, X.; Bai, L.; Zhang, X.; Wang, H.; Wang, J.; Bao, D.; Li, M.; Liu, X.; Zhang, S. Ionic-Liquid-Based CO_2 Capture Systems: Structure, Interaction and Process. *Chem. Rev.* **2017**, *117* (14), 9625–9673.

[23]   Perejón, A.; Romeo, L. M.; Lara, Y.; Lisbona, P.; Martínez, A.; Valverde, J. M. The Calcium-Looping Technology for CO_2 Capture: On the Important Roles of Energy Integration and Sorbent Behavior. *Appl. Energy* **2016**, *162*, 787–807.

[24]   Sridhar, N.; Hill, D. *Carbon Dioxide Utilization. Electrochemical Conversion of CO_2 - Opportunities and Challenges*; 2011.

[25]   Al-Mamoori, A.; Krishnamurthy, A.; Rownaghi, A. A.; Rezaei, F. Carbon Capture and Utilization Update. *Energy Technol.* **2017**, *5* (6), 834–849.

[26]   Federsel, C.; Jackstell, R.; Beller, M. State-of-the-Art Catalysts for Hydrogenation of Carbon Dioxide. *Angew. Chem. Int. Ed. Engl.* **2010**, *49* (36), 6254–6257.

[27]   Peng, G.; Sibener, S. J.; Schatz, G. C.; Ceyer, S. T.; Mavrikakis, M. CO_2 Hydrogenation to Formic Acid on Ni (111). **2012**, No. 111, 3001–3006.

[28]   Bratt, D. *Catalytic CO_2 Hydrogenation - Literature Review : Technology Development since 2014*; 2016.

[29]   Behr, A.; Nowakowski, K. *Catalytic Hydrogenation of Carbon Dioxide to Formic Acid*, 1st ed.; Elsevier Inc., 2014; Vol. 66.

[30]   Zhang, W.; Wang, S.; Zhao, Y.; Ma, X. Hydrogenation of CO_2 to Formic Acid Catalyzed by Heterogeneous Ru-PPh$_3$/Al$_2$O$_3$ Catalysts. *Fuel Process. Technol.* **2018**, *178* (February), 98–103.

[31]   Le, Y.; Zhong, H.; Yang, Y.; He, R.; Yao, G.; Jin, F. Mechanism Study of Reduction of CO_2 into Formic Acid by In-Situ Hydrogen Produced from Water Splitting with Zn: Zn/ZnO Interface Autocatalytic Role. *J. Energy Chem.* **2017**, *26* (5), 936–941.

[32]   Montandon-Clerc, M.; Laurenczy, G. Additive Free, Room Temperature Direct Homogeneous Catalytic Carbon Dioxide Hydrogenation in Aqueous Solution Using an

Iron(II) Phosphine Catalyst. *J. Catal.* **2018**, *362*, 78–84.

[33]   Olah, G. A. Beyond Oil and Gas: The Methanol Economy. *Angew. Chemie Int. Ed.* **2005**, *44* (18), 2636–2639.

[34]   Bozzano, G.; Manenti, F. Efficient Methanol Synthesis: Perspectives, Technologies and Optimization Strategies. *Prog. Energy Combust. Sci.* **2016**, *56*, 71–105.

[35]   Wang, W.; Wang, S.; Ma, X.; Gong, J. Recent Advances in Catalytic Hydrogenation of Carbon Dioxide. *Chem. Soc. Rev.* **2011**, *40* (7), 3703–3727.

[36]   Kar, S.; Kothandaraman, J.; Goeppert, A.; Prakash, G. K. S. Advances in Catalytic Homogeneous Hydrogenation of Carbon Dioxide to Methanol. *J. CO_2 Util.* **2018**, *23* (December 2017), 212–218.

[37]   Bailera, M.; Lisbona, P.; Romeo, L. M.; Espatolero, S. Power to Gas Projects Review: Lab, Pilot and Demo Plants for Storing Renewable Energy and CO_2. *Renew. Sustain. Energy Rev.* **2017**, *69* (October 2016), 292–312.

[38]   Ghaib, K.; Ben-Fares, F. Z. Power-to-Methane: A State-of-the-Art Review. *Renew. Sustain. Energy Rev.* **2018**, *81* (June 2017), 433–446.

[39]   Renewable energy generated 104% of Portugal's electricity consumption in March | The Independent   https://www.independent.co.uk/news/world/europe/portugal-renewable-energy-generated-electricity-consumption-march-greenhouse-gas-environment-a8289656.html (accessed Jun 19, 2018).

[40]   Portugal breaks 100% renewables mark but remains isolated – EURACTIV.com https://www.euractiv.com/section/energy/news/portugal-breaks-100-renewables-mark-but-remains-isolated/ (accessed Jun 19, 2018).

[41]   Sabatier, P.; Senderens, J. B. New Synthesis of Methane. *Comptes Rendus l'Académie des Sci. Paris* **1902**, *134*, 1902.

[42]   Baraj, E.; Vagaský, S.; Hlinčík, T.; Ciahotný, K.; Tekáč, V. Reaction Mechanisms of Carbon Dioxide Methanation. **2016**, *70* (4), 395–403.

[43]   Kuznecova, I.; Gusca, J. Property Based Ranking of CO and CO_2 Methanation Catalysts. In *Energy Procedia*; 2017; Vol. 128, pp 255–260.

[44]   Su, X.; Xu, J.; Liang, B.; Duan, H.; Hou, B.; Huang, Y. Catalytic Carbon Dioxide Hydrogenation to Methane: A Review of Recent Studies. *J. Energy Chem.* **2016**, *25* (4), 553–565.

[45]   Frontera, P.; Macario, A.; Ferraro, M.; Antonucci, P. Supported Catalysts for CO_2 Methanation: A Review. *Catalysts* **2017**, *7* (2), 59.

[46]   Cheng, D.; Negreiros, F. R.; Aprà, E.; Fortunelli, A. Computational Approaches to the Chemical Conversion of Carbon Dioxide. *ChemSusChem* **2013**, *6* (6), 944–965.

[47]   Miao, B.; Ma, S. S. K.; Wang, X.; Su, H.; Chan, S. H. Catalysis Mechanisms of CO_2 and CO Amethanation. *Catal. Sci. Technol.* **2016**, *6* (12), 4048–4058.

[48]   Rönsch, S.; Schneider, J.; Matthischke, S.; Schlüter, M.; Götz, M.; Lefebvre, J.; Prabhakaran, P.; Bajohr, S. Review on Methanation - From Fundamentals to Current Projects. *Fuel* **2016**, *166*, 276–296.

[49]   Tada, S.; Ochieng, O. J.; Kikuchi, R.; Haneda, T.; Kameyama, H. Promotion of CO_2 Methanation Activity and CH_4 Selectivity at Low Temperatures over $Ru/CeO_2/Al_2O_3$ Catalysts. *Int. J. Hydrogen Energy* **2014**, *39* (19), 10090–10100.

[50]   Sharma, S.; Hu, Z.; Zhang, P.; McFarland, E. W.; Metiu, H. CO2methanation on Ru-Doped Ceria. *J. Catal.* **2011**, *278* (2), 297–309.

[51]   Zamani, A. H.; Ali, R.; Abu Bakar, W. A. W. Optimization of CO_2 Methanation Reaction over M*/Mn/Cu-Al_2O_3 (M*: Pd, Rh and Ru) Catalysts. *J. Ind. Eng. Chem.* **2015**, *29*, 238–248.

[52]   Brunner, G. *Gas Extraction - An Introduction to Fundamentals of Supercritical Fluids and the Application to Separation Processes*; Baumgärtel, H., Franck, E. U., Grünbein, W., Eds.; Steinkopff-Verlag Heidelberg, 1994.

[53]   Smith, R. M. Nomenclature for Supercritical Fluid Chromatography and Extraction (IUPAC Recommendations 1993). *Pure Appl. Chem.* **1993**, *65* (11), 2397–2403.

[54]   Beckman, E. J. Supercritical and Near-Critical CO2in Green Chemical Synthesis and Processing. *J. Supercrit. Fluids* **2004**, *28* (2–3), 121–191.

[55]   Paninho, A. B.; Ventura, A. L. R.; Branco, L. C.; Pombeiro, A. J. L.; da Silva, M. F. C. G.; da Ponte, M. N.; Mahmudov, K. T.; Nunes, A. V. M. CO_2 + Ionic Liquid Biphasic System for Reaction/Product Separation in the Synthesis of Cyclic Carbonates. *J. Supercrit. Fluids* **2018**, *132* (January 2017), 71–75.

[56]   Melo, C. I.; Bogel-Łukasik, R.; Gomes, M.; Bogel-Łukasik, E.; da Silva, M. G. Advantageous Heterogeneously Catalysed Hydrogenation of Carvone with Supercritical Carbon Dioxide. *Green Chem.* **2011**, *13* (10), 2825.

[57]   Yang, W.; Cheng, H.; Zhang, B.; Li, Y.; Liu, T.; Lan, M.; Yu, Y.; Zhang, C.; Lin, W.; Fujita, S.; et al. Hydrogenation of Levulinic Acid by $RuCl_2$ (PPh_3)$_3$ in Supercritical CO_2 : The Significance of Structural Changes of Ru Complexes via Interaction with CO_2. *Green Chem.* **2016**, *18* (11), 3370–3377.

[58]   Sahle-Demessie, E.; Devulapelli, V. G.; Hassan, A. A. Hydrogenation of Anthracene in Supercritical Carbon Dioxide Solvent Using Ni Supported on Hβ-Zeolite Catalyst. *Catalysts* **2012**, *2* (4), 85–100.

[59]   Ventura, S. P. M.; e Silva, F. A.; Quental, M. V.; Mondal, D.; Freire, M. G.; Coutinho, J. A. P. Ionic-Liquid-Mediated Extraction and Separation Processes for Bioactive Compounds: Past, Present, and Future Trends. *Chem. Rev.* **2017**, *117* (10), 6984–7052.

[60]   Petkovic, M.; Seddon, K. R.; Rebelo, L. P. N.; Pereira, C. S. Ionic Liquids: A Pathway to Environmental Acceptability. *Chem. Soc. Rev.* **2011**, *40* (3), 1383–1403.

[61]   Holbrey, J. D.; Rogers, R. D.; Mantz, R. A.; Trulove, P. C.; Cocalia, V. A.; Visser, A. E.; Anderson, J. L.; Anthony, J. L.; Brennecke, J. F.; Maginn, E. J.; et al. Physicochemical Properties. In *Ionic Liquids in Synthesis*; Wasserscheid, P., Welton, T., Eds.; Wiley-VCH Verlag GmbH & Co. KGaA: Germany, 2008; pp 57–174.

[62]   Melo, C. I.; Bogel-Łukasik, R.; Bogel-Łukasik, E. Combination of Supercritical Carbon Dioxide and Ionic Liquid in a Novel Assembly of Carvacrol. *J. Supercrit. Fluids* **2012**, *61*, 191–198.

[63]   Marsh, K. .; Boxall, J. .; Lichtenthaler, R. Room Temperature Ionic Liquids and Their

Mixtures—a Review. *Fluid Phase Equilib.* **2004**, *219* (1), 93–98.

[64] Ranu, B. C.; Banerjee, S. Ionic Liquid as Catalyst and Reaction Medium. The Dramatic Influence of a Task-Specific Ionic Liquid, [BmIm]OH, in Michael Addition of Active Methylene Compounds to Conjugated Ketones, Carboxylic Esters, and Nitriles. *Org. Lett.* **2005**, *7* (14), 3049–3052.

[65] Zakrzewska, M. E.; Bogel-Łukasik, E.; Bogel-Łukasik, R. Ionic Liquid-Mediated Formation of 5-Hydroxymethylfurfural-A Promising Biomass-Derived Building Block. *Chem. Rev.* **2011**, 397–417.

[66] Melo, C. I.; Rodrigues, A. I.; Ł, R. B.-; Ł, E. B.-. Outlook on the Phase Equilibria of the Innovative System of "Protected Glycerol": 1,4-Dioxaspiro[4.5]Decane-2-Methanol and Alternative Solvents. *J. Phys. Chem. A 2012,* **2012**, 1765−1773.

[67] Prechtl, M. H. G.; Scariot, M.; Scholten, J. D.; Machado, G.; Teixeira, S. R.; Dupont, J. Nanoscale Ru(0) Particles: Arene Hydrogenation Catalysts in Imidazolium Ionic Liquids. *Inorg. Chem.* **2008**, *47* (19), 8995–9001.

[68] Cabaço, M. I.; Besnard, M.; Danten, Y.; Coutinho, J. a P. Carbon Dioxide in 1-Butyl-3-Methylimidazolium Acetate. I. Unusual Solubility Investigated by Raman Spectroscopy and DFT Calculations. *J. Phys. Chem. A* **2012**, *116* (6), 1605–1620.

[69] Gurkan, B. E.; de la Fuente, J. C.; Mindrup, E. M.; Ficke, L. E.; Goodrich, B. F.; Price, E. a; Schneider, W. F.; Brennecke, J. F. Equimolar CO_2 Absorption by Anion-Functionalized Ionic Liquids. *J. Am. Chem. Soc.* **2010**, *132* (7), 2116–2117.

[70] Carvalho, P. J.; Coutinho, J. a. P. The Polarity Effect upon the Methane Solubility in Ionic Liquids: A Contribution for the Design of Ionic Liquids for Enhanced CO_2/CH_4 and H_2S/CH_4 Selectivities. *Energy Environ. Sci.* **2011**, *4* (11), 4614.

[71] Zulfiqar, S.; Sarwar, M. I.; Mecerreyes, D. Polymeric Ionic Liquids for CO_2 Capture and Separation: Potential, Progress and Challenges. *Polym. Chem.* **2015**, *6* (36), 6435–6451.

[72] Blanchard, L. A.; Hancu, D.; Beckman, E. J.; Brennecke, J. F. Green Processing Using Ionic Liquids and CO_2. *Nature* **1999**, *399* (6731), 28–29.

[73] Papaiconomou, N.; Yakelis, N.; Salminen, J.; Bergman, R.; Prausnitz, J. M. Synthesis and Properties of Seven Ionic Liquids Containing 1-Methyl-3-Octylimidazolium or 1-Butyl-4-Methylpyridinium Cations. *J. Chem. Eng. Data* **2006**, *51* (4), 1389–1393.

[74] Bogel-Łukasik, E.; Santos, S.; Bogel-Łukasik, R.; Nunes da Ponte, M. Selectivity Enhancement in the Catalytic Heterogeneous Hydrogenation of Limonene in Supercritical Carbon Dioxide by an Ionic Liquid. *J. Supercrit. Fluids* **2010**, *54* (2), 210–217.

[75] Liu, F.; Abrams, M. B.; Baker, R. T.; Tumas, W. Phase-Separable Catalysis Using Room Temperature Ionic Liquids and Supercritical Carbon Dioxide. *Chem. Commun.* **2001**, No. 5, 433–434.

[76] Lopez-Serrano, A.; Olivas, R. M.; Landaluze, J. S.; Camara, C. Nanoparticles: A Global Vision. Characterization, Separation, and Quantification Methods. Potential Environmental and Health Impact. *Anal. Methods* **2014**, *6*, 38–56.

[77] Gual, A.; Godard, C.; Castillón, S.; Curulla-Ferré, D.; Claver, C. Colloidal Ru, Co and Fe-Nanoparticles. Synthesis and Application as Nanocatalysts in the Fischer–Tropsch Process. *Catal. Today* **2012**, *183* (1), 154–171.

[78] Luska, K. L.; Moores, A. Functionalized Ionic Liquids for the Synthesis of Metal Nanoparticles and Their Application in Catalysis. *ChemCatChem* **2012**, *4* (10), 1534–1546.

[79] Dupont, J.; Kollár, L. Ionic Liquids (ILs) in Organometallic Catalysis. *Top. Organomet. Chem.* **2015**, *51*.

[80] Dupont, J.; Fonseca, G. S.; Umpierre, A. P.; Fichtner, P. F. P.; Teixeira, S. R. Transition-Metal Nanoparticles in Imidazolium Ionic Liquids: Recycable Catalysts for Biphasic Hydrogenation Reactions. *J. Am. Chem. Soc.* **2002**, *124* (16), 4228–4229.

[81] Patzke, G. R.; Zhou, Y.; Kontic, R.; Conrad, F. Oxide Nanomaterials: Synthetic Developments, Mechanistic Studies, and Technological Innovations. *Angew. Chemie - Int. Ed.* **2011**, *50* (4), 826–859.

[82] Salas, G.; Podgoršek, A.; Campbell, P. S.; Santini, C. C.; Pádua, A. a H.; Costa Gomes, M. F.; Philippot, K.; Chaudret, B.; Turmine, M. Ruthenium Nanoparticles in Ionic Liquids: Structural and Stability Effects of Polar Solutes. *Phys. Chem. Chem. Phys.* **2011**, *13* (30), 13527–13536.

[83] Dupont, J.; Scholten, J. D. On the Structural and Surface Properties of Transition-Metal Nanoparticles in Ionic Liquids. *Chem. Soc. Rev.* **2010**, *39*, 1780–1804.

[84] Gutel, T.; Garcia-Antõn, J.; Pelzer, K.; Philippot, K.; Santini, C. C.; Chauvin, Y.; Chaudret, B.; Basset, J.-M. Influence of the Self-Organization of Ionic Liquids on the Size of Ruthenium Nanoparticles: Effect of the Temperature and Stirring. *J. Mater. Chem.* **2007**, *17* (31), 3290–3292.

[85] Prechtl, M. H. G.; Campbell, P. S.; Scholten, J. D.; Fraser, G. B.; Machado, G.; Santini, C. C.; Dupont, J.; Chauvin, Y. Imidazolium Ionic Liquids as Promoters and Stabilising Agents for the Preparation of Metal(0) Nanoparticles by Reduction and Decomposition of Organometallic Complexes. *Nanoscale* **2010**, *2* (12), 2601–2606.

[86] National Institute of Standards and Thecnology, U. Thermophysical Properties of Fluid Systems http://webbook.nist.gov/chemistry/fluid/ (accessed Mar 8, 2018).

[87] Leachman, J. W.; Jacobsen, R. T.; Penoncello, S. G.; Lemmon, E. W. Fundamental Equations of State for Parahydrogen, Normal Hydrogen, and Orthohydrogen. *J. Phys. Chem. Ref. Data* **2009**, *38* (3), 721–748.

[88] Giancoli, D. C. *Physics : Principles with Applications*; Prentice Hall, 1998.

[89] Span, R.; Wagner, W. A New Equation of State for Carbon Dioxide Covering the Fluid Region from the Triple-Point Temperature to 1100 K at Pressures up to 800 MPa. *J. Phys. Chem. Ref. Data* **1996**, *25* (6), 1509–1596.

[90] Ababio, B. D.; McElroy, P. J. (Pressure, Amount-of-Substance Density, Temperature) of $\{(1-x)CO_2+xH_2\}$ Using a Direct Method. *J. Chem. Thermodyn.* **1993**, *25* (12), 1495–1501.

[91] Aki, S. N. V. K.; Mellein, B. R.; Saurer, E. M.; Brennecke, J. F. High-Pressure Phase Behavior of Carbon Dioxide with Imidazolium-Based Ionic Liquids. *J. Phys. Chem. B* **2004**, *108* (52), 20355–20365.

[92] Thermodynamics, J. C.; Tariq, M.; Forte, P. A. S.; Gomes, M. F. C.; Lopes, J. N. C.; Rebelo, L. P. N. Densities and Refractive Indices of Imidazolium- and Phosphonium-Based Ionic Liquids : Effect of Temperature , Alkyl Chain Length , and Anion. *J. Chem.*

Thermodyn. **2009**, *41* (6), 790–798.

[93] Wesselbaum, S.; Vom Stein, T.; Klankermayer, J.; Leitner, W. Hydrogenation of Carbon Dioxide to Methanol by Using a Homogeneous Ruthenium-Phosphine Catalyst. *Angew. Chemie Int. Ed.* **2012**, *51* (30), 7499–7502.

[94] Pardal, T.; Messias, S.; Sousa, M.; Machado, A. S. R.; Rangel, C. M.; Nunes, D.; Pinto, J. V.; Martins, R.; Da Ponte, M. N. Syngas Production by Electrochemical CO_2 Reduction in an Ionic Liquid Based-Electrolyte. *J. CO_2 Util.* **2017**, *18*, 62–72.

[95] Gottlieb, H. E.; Kotlyar, V.; Nudelman, A. NMR Chemical Shifts of Common Laboratory Solvents as Trace Impurities In the Course of the Routine Use of NMR as an Aid for Organic Chemistry , a Day-to-Day Problem Is the Identification of Signals Deriving from Common Contaminants Literature , but The. **1997**, *3263* (3), 7512–7515.

[96] Ali, M.; Gual, A.; Ebeling, G.; Dupont, J. Carbon Dioxide Transformation in Imidazolium Salts: Hydroaminomethylation Catalyzed by Ru-Complexes. *ChemSusChem* **2016**, *9* (16), 2129–2134.

[97] Prechtl, M. H. G.; Scholten, J. D.; Dupont, J. Tuning the Selectivity of Ruthenium Nanoscale Catalysts with Functionalised Ionic Liquids: Hydrogenation of Nitriles. *J. Mol. Catal. A Chem.* **2009**, *313*, 74–78.

[98] Scholten, J. D.; Leal, B. C.; Dupont, J. Transition Metal Nanoparticle Catalysis in Ionic Liquids. *ACS Catal.* **2012**, *2* (1), 184–200.

[99] He, Y.; Vinodgopal, K.; Ashokkumar, M.; Grieser, F. Sonochemical Synthesis of Ruthenium Nanoparticles. *Res. Chem. Intermed.* **2006**, *32* (8), 709–715.

[100] Gupta, S.; Giordano, C.; Gradzielski, M.; Mehta, S. K. Microwave-Assisted Synthesis of Small Ru Nanoparticles and Their Role in Degradation of Congo Red. *J. Colloid Interface Sci.* **2013**, *411*, 173–181.

[101] Upstone, S. Ultraviolet/Visible Light Absorption Spectrophotometry in Clinical Chemistry. *Encycl. Anal. Chem.* **2000**, 1699–1714.

[102] Salas, G.; Campbell, P. S.; Santini, C. C.; Philippot, K.; Costa Gomes, M. F.; Pádua, A. A. H. Ligand Effect on the Catalytic Activity of Ruthenium Nanoparticles in Ionic Liquids. *Dalt. Trans.* **2012**, *41* (45), 13919.

[103] Zakrzewska, M. E.; Nunes da Ponte, M. Volumetric and Phase Behaviour of Mixtures of Tetracyanoborate-Based Ionic Liquids with High Pressure Carbon Dioxide. *J. Supercrit. Fluids* **2016**, *113*, 31–38.

[104] Hong, S. K.; Park, Y.; Pore, D. M. Experimental Determination and Prediction of Phase Behavior for 1-Butyl-3-Methylimidazolium Nonafluorobutyl Sulfonate and Carbon Dioxide. **2014**, *31* (4), 1–5.

[105] Cabaço, M. I.; Besnard, M.; Danten, Y.; Coutinho, J. A. P. Solubility of CO_2 in 1-Butyl-3-Methyl-Imidazolium-Trifluoro Acetate Ionic Liquid Studied by Raman Spectroscopy and DFT Investigations. *J. Phys. Chem. B* **2011**, *115* (13), 3538–3550.

[106] Jung, Y.-H.; Jung, J.-Y.; Jin, Y.-R.; Lee, B.-C.; Baek, I.-H.; Kim, S.-H. Solubility of Carbon Dioxide in Imidazolium-Based Ionic Liquids with a Methanesulfonate Anion. *J. Chem. Eng. Data* **2012**, *57* (12), 3321–3329.

[107] Aki, S. n. v. k. S. N. V. K.; Mellein, B. R.; Saurer, E. M.; Brennecke, J. F. High-Pressure Phase Behavior of Carbon Dioxide with Imidazolium-Based Ionic Liquids, J. *J. Phys. Chem. B* **2004**, *108*, 20355–20365.

[108] He, Z.; Alexandridis, P. Nanoparticles in Ionic Liquids: Interactions and Organization. *Phys. Chem. Chem. Phys.* **2015**, *17* (28), 18238–18261.

[109] Konnerth, H.; Prechtl, M. H. G. Selective Hydrogenation of N-Heterocyclic Compounds Using Ru Nanocatalysts in Ionic Liquids. *Green Chem.* **2017**, *19* (12), 2762–2767.

[110] Luska, K. L.; Moores, A. Ruthenium Nanoparticle Catalysts Stabilized in Phosphonium and Imidazolium Ionic Liquids: Dependence of Catalyst Stability and Activity on the Ionicity of the Ionic Liquid. *Green Chem.* **2012**, *14* (6), 1736.

[111] Beuls, A.; Swalus, C.; Jacquemin, M.; Heyen, G.; Karelovic, A.; Ruiz, P. Methanation of CO_2: Further Insight into the Mechanism over $Rh/\gamma\text{-}Al_2O_3$ Catalyst. *Appl. Catal. B Environ.* **2012**, *113–114*, 2–10.

[112] Karelovic, A.; Ruiz, P. Improving the Hydrogenation Function of $Pd/\gamma\text{-}Al_2O_3$ Catalyst by $Rh/\gamma\text{-}Al_2O_3$ Addition in CO_2 Methanation at Low Temperature. *ACS Catal.* **2013**, *3* (12), 2799–2812.

Appendix A. NMR spectra of the synthesized Ionic liquids.
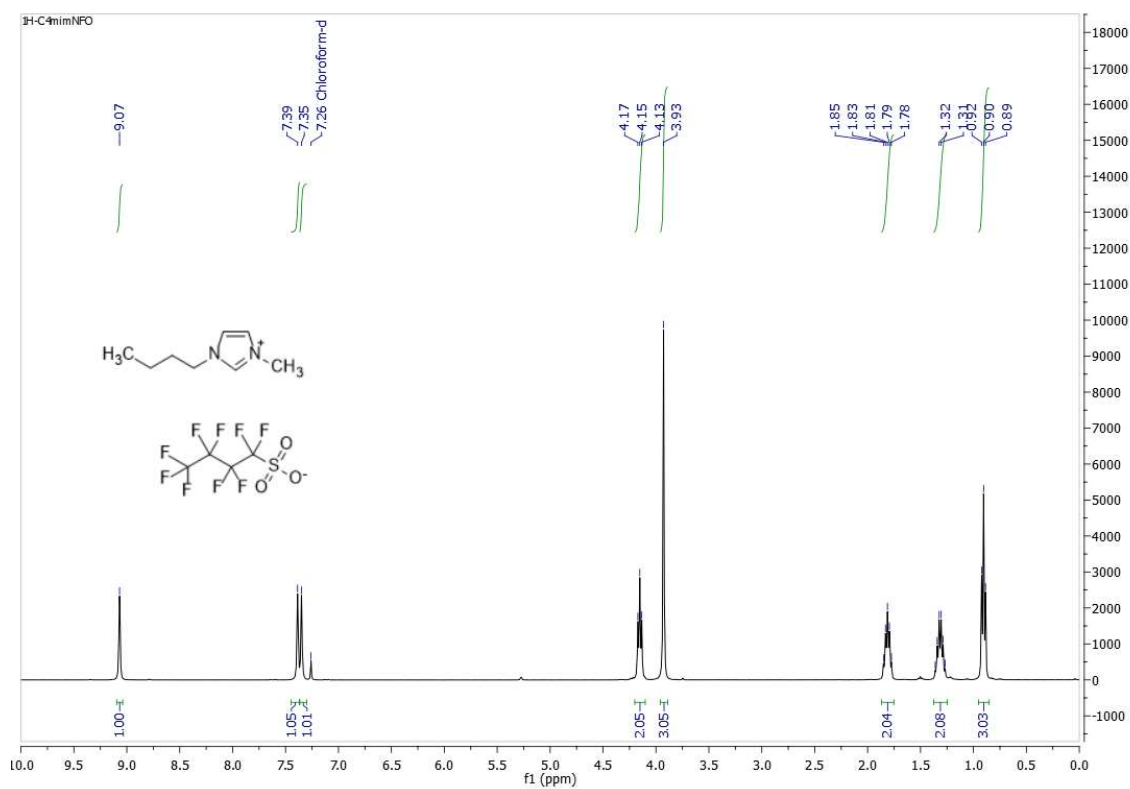
Figure A.1. ^{1}H NMR spectrum of [C$_4$mim][NfO].
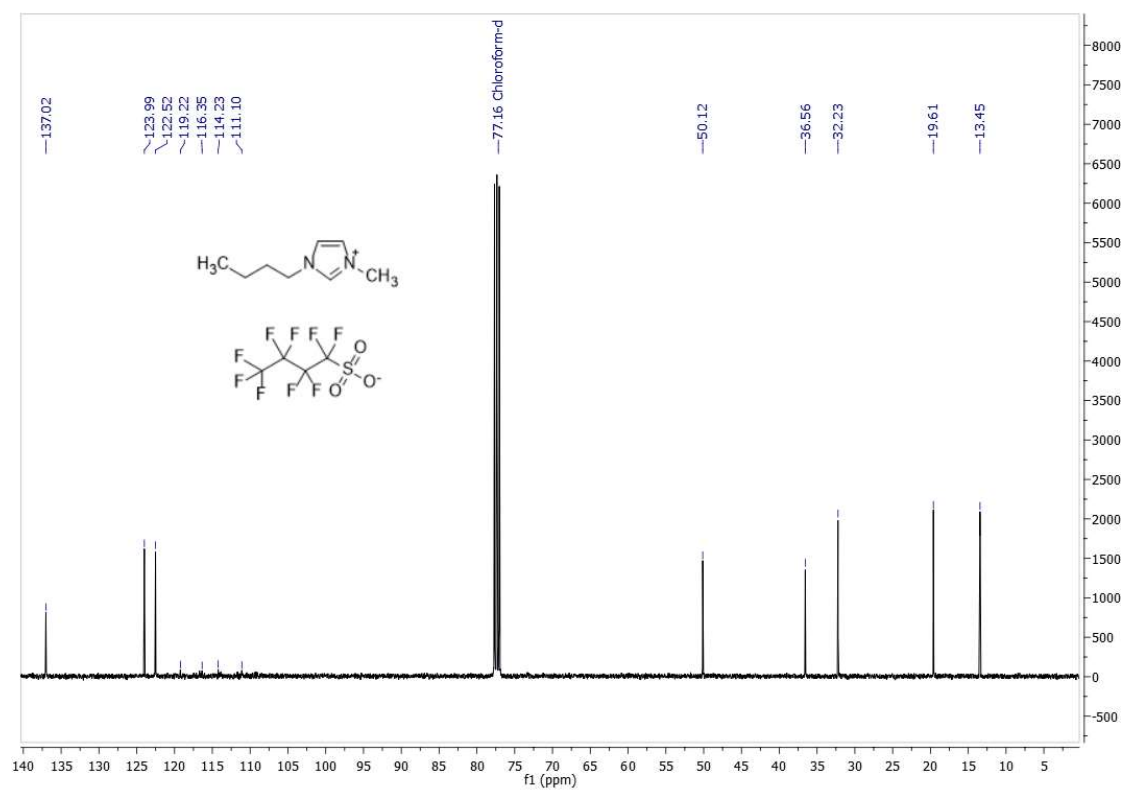
Figure A.2. ^{13}C NMR spectrum of [C$_4$mim][NfO].
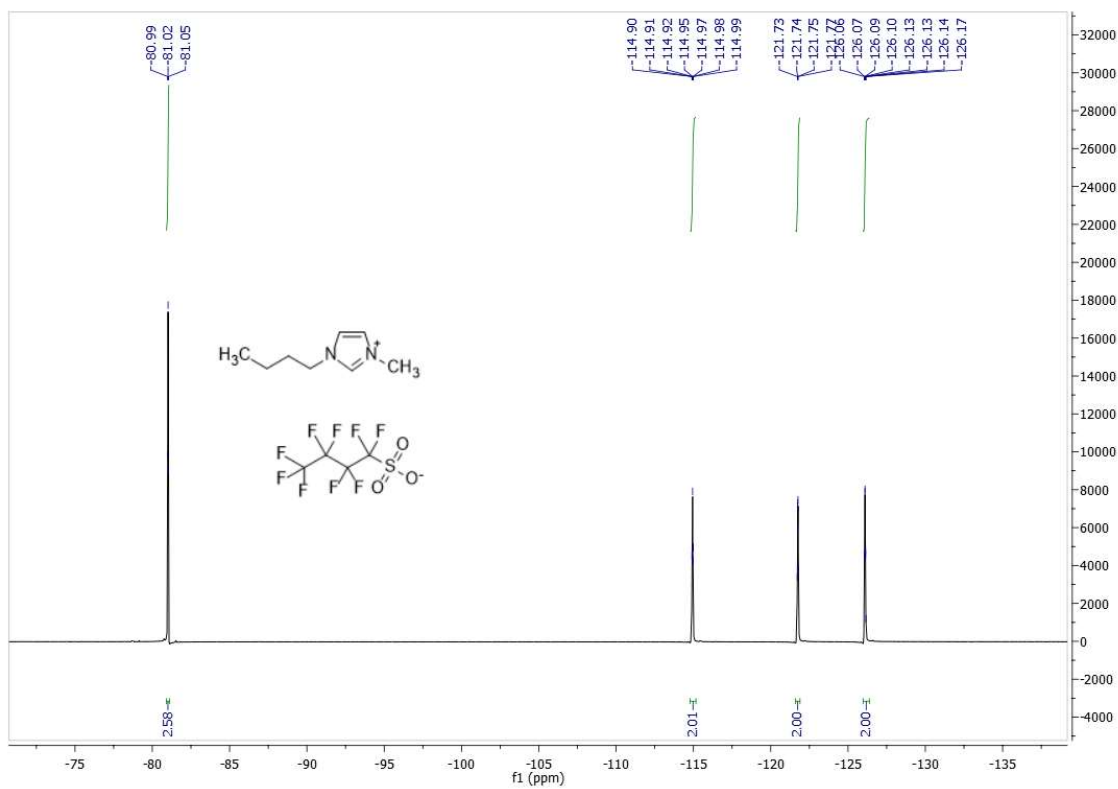
Figure A.3. ^{19}F NMR spectrum of [C$_4$mim][NfO].
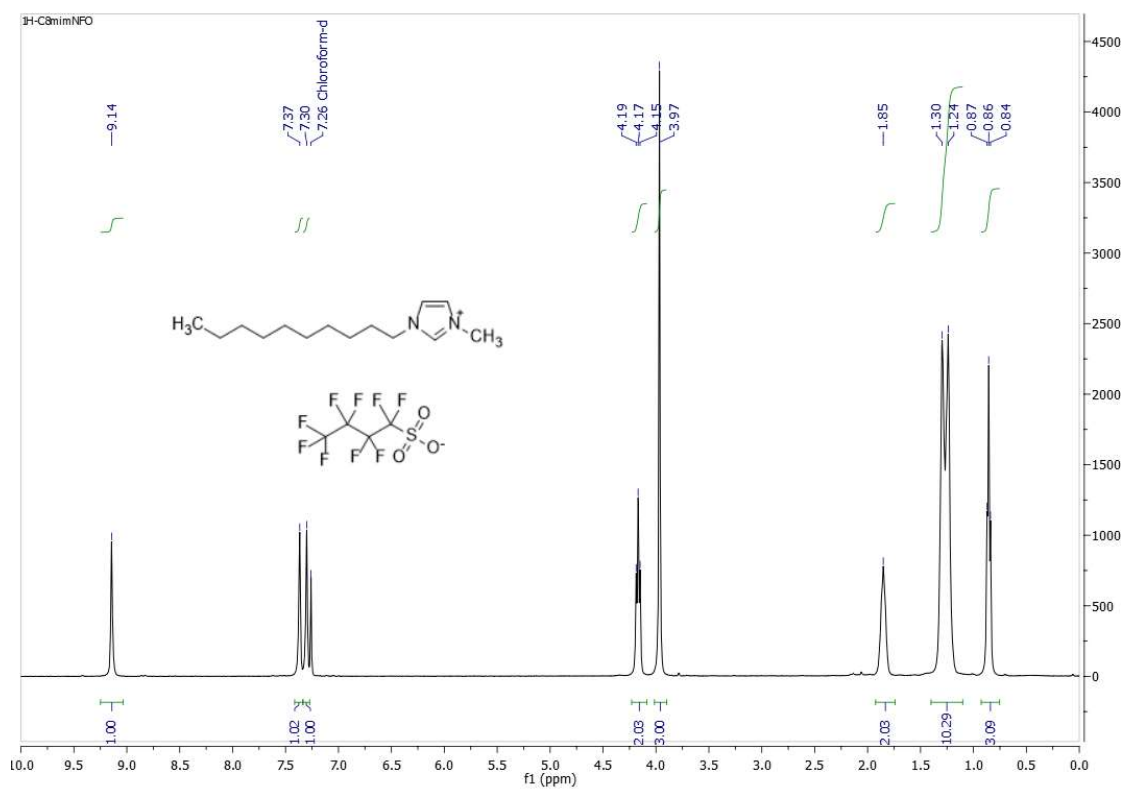
Figure A.4. ^{1}H NMR spectrum of [C$_8$mim][NfO].

110
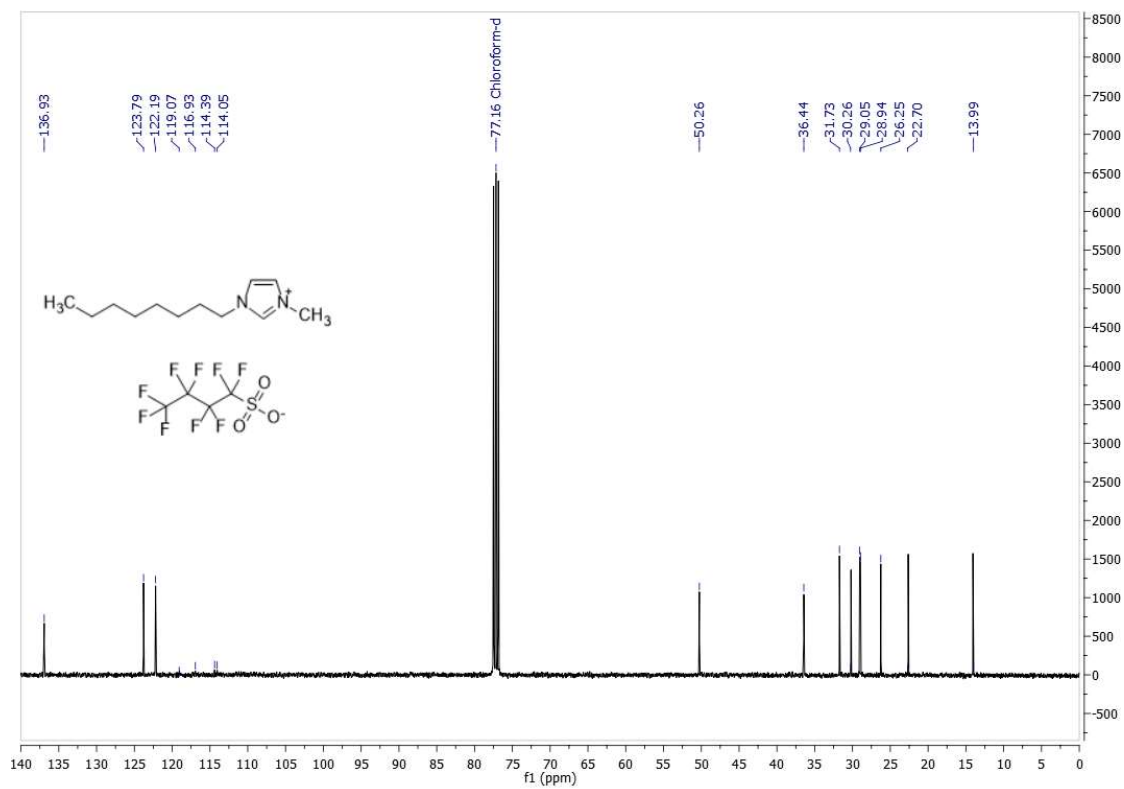
Figure A.5. ^{13}C NMR spectrum of [C$_8$mim][NfO].
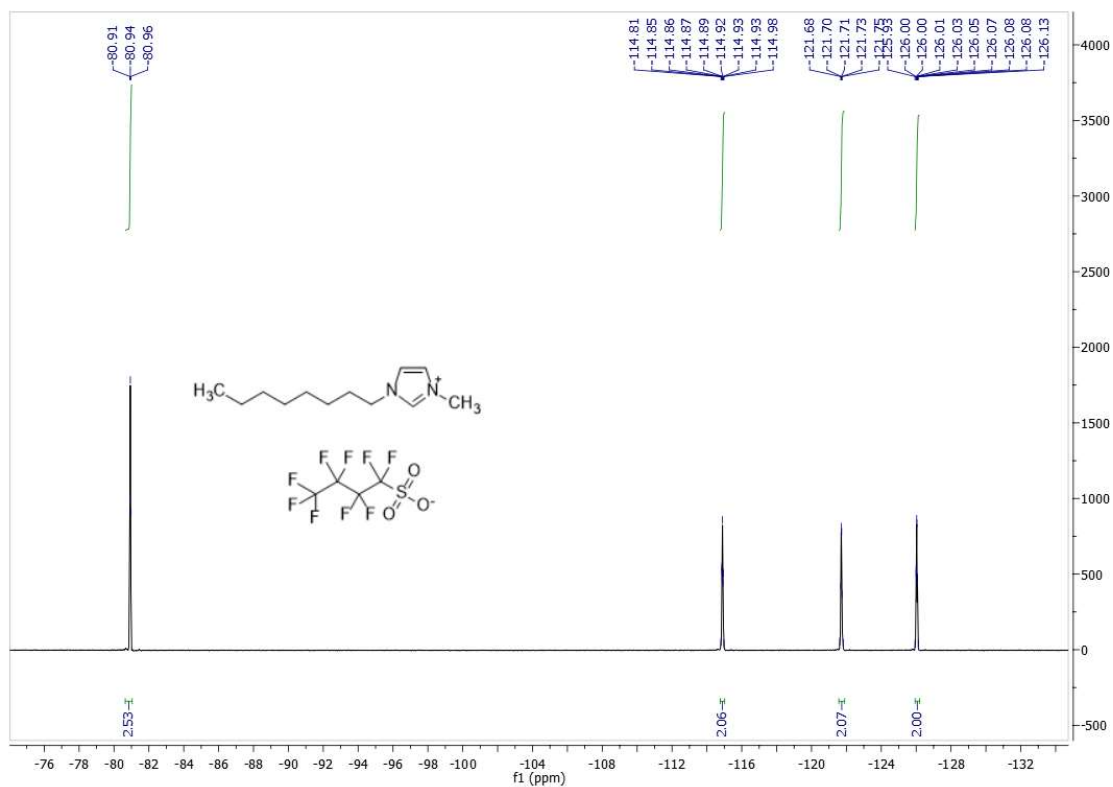
Figure A.6. ^{19}F NMR spectrum of [C$_8$mim][NfO].
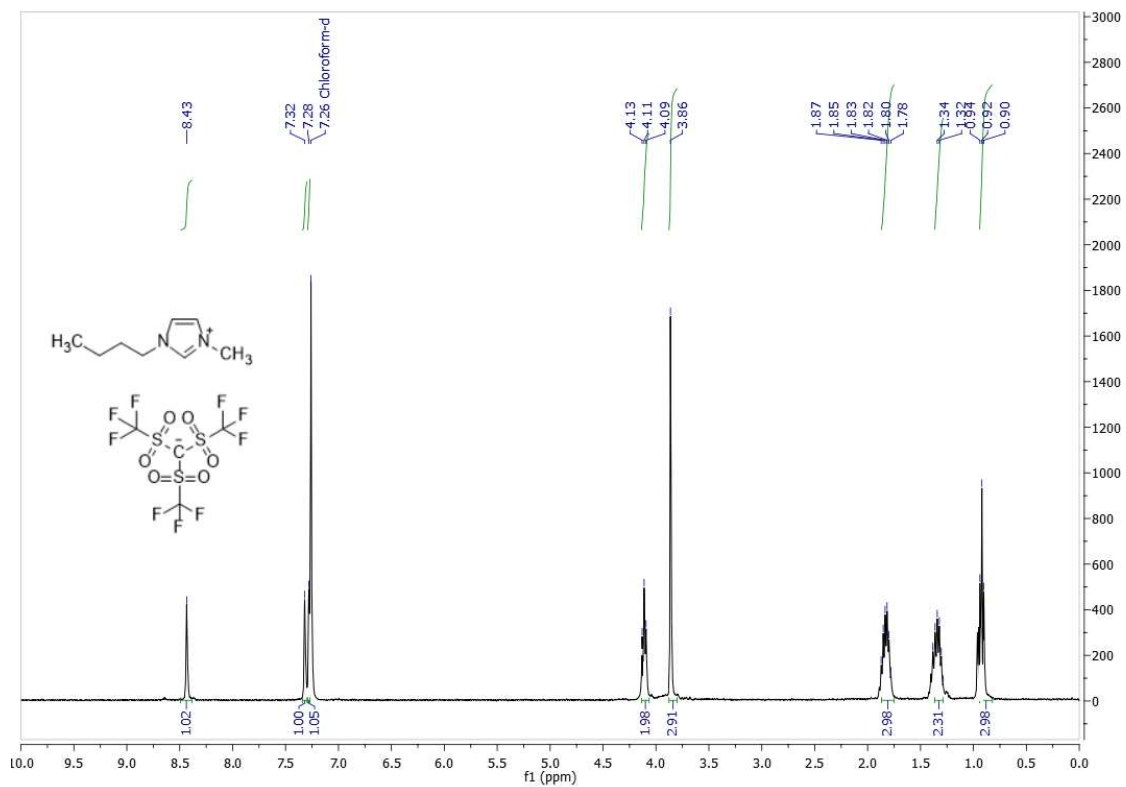
Figure A.7. ^{1}H NMR spectrum of [C$_4$mim][CTf$_3$].
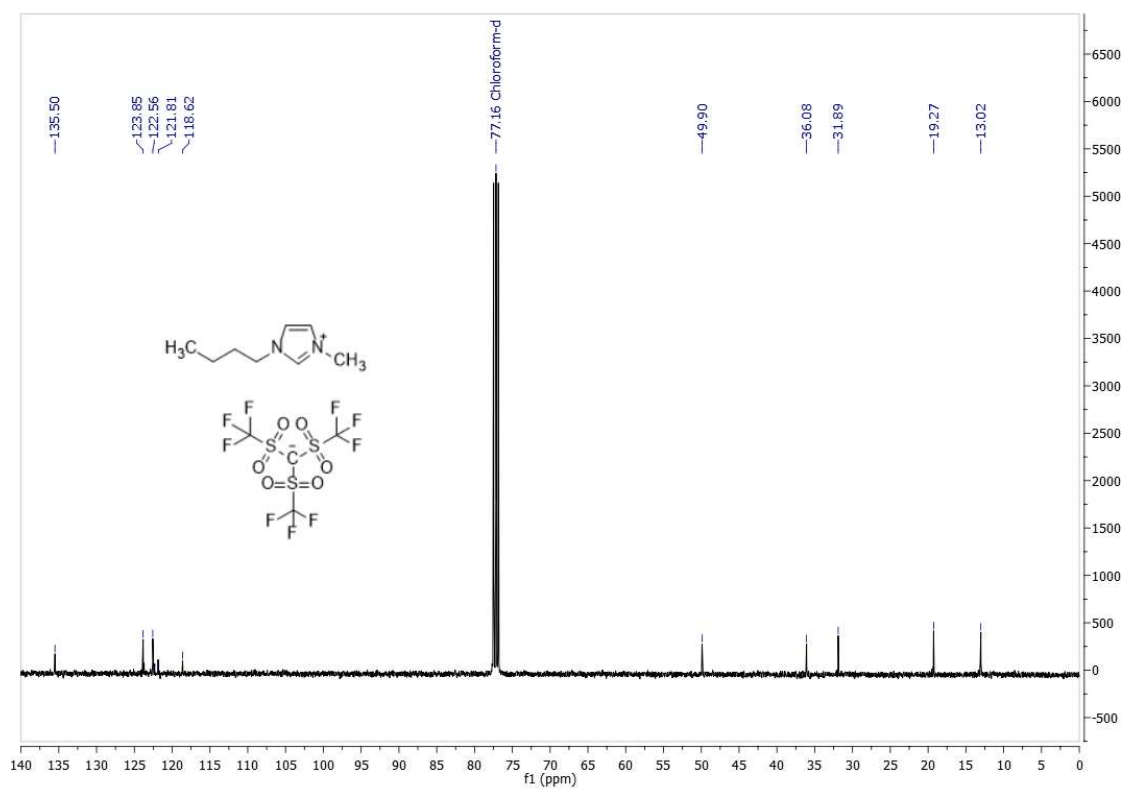
Figure A.8. ^{13}C NMR spectrum of [C$_4$mim][CTf$_3$].

112
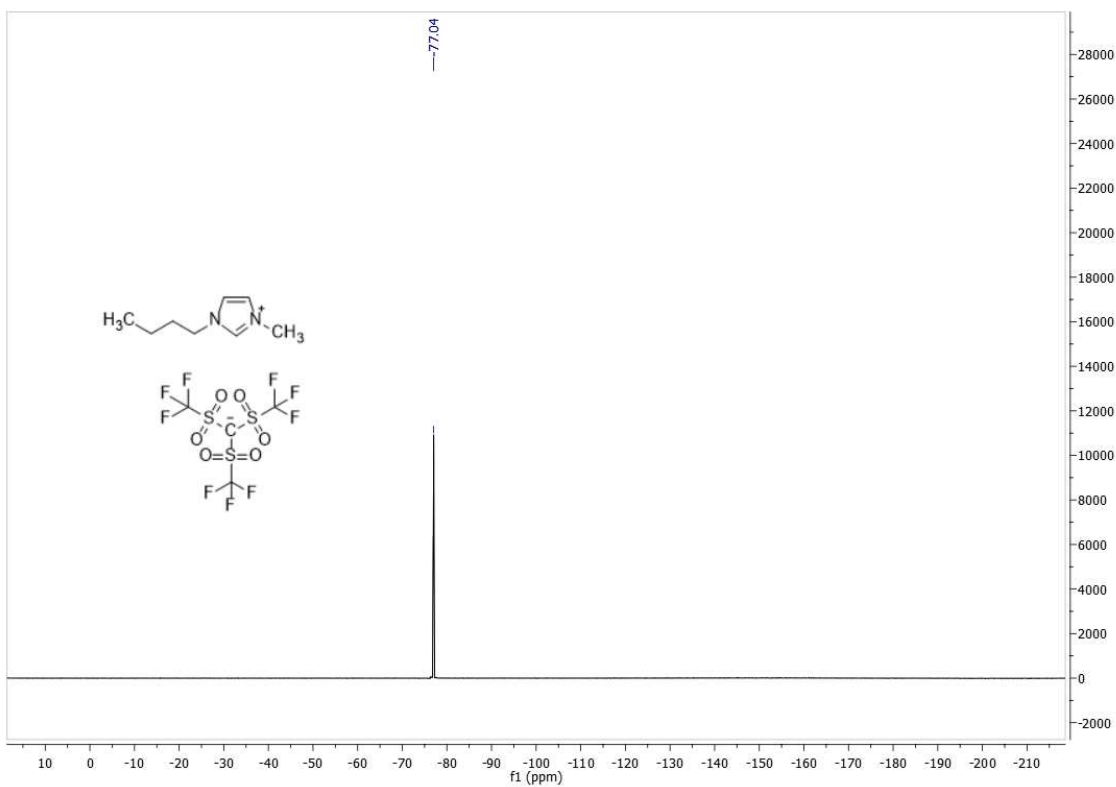
Figure A.9. ^{19}F NMR spectrum of [C$_4$mim][CTf$_3$].
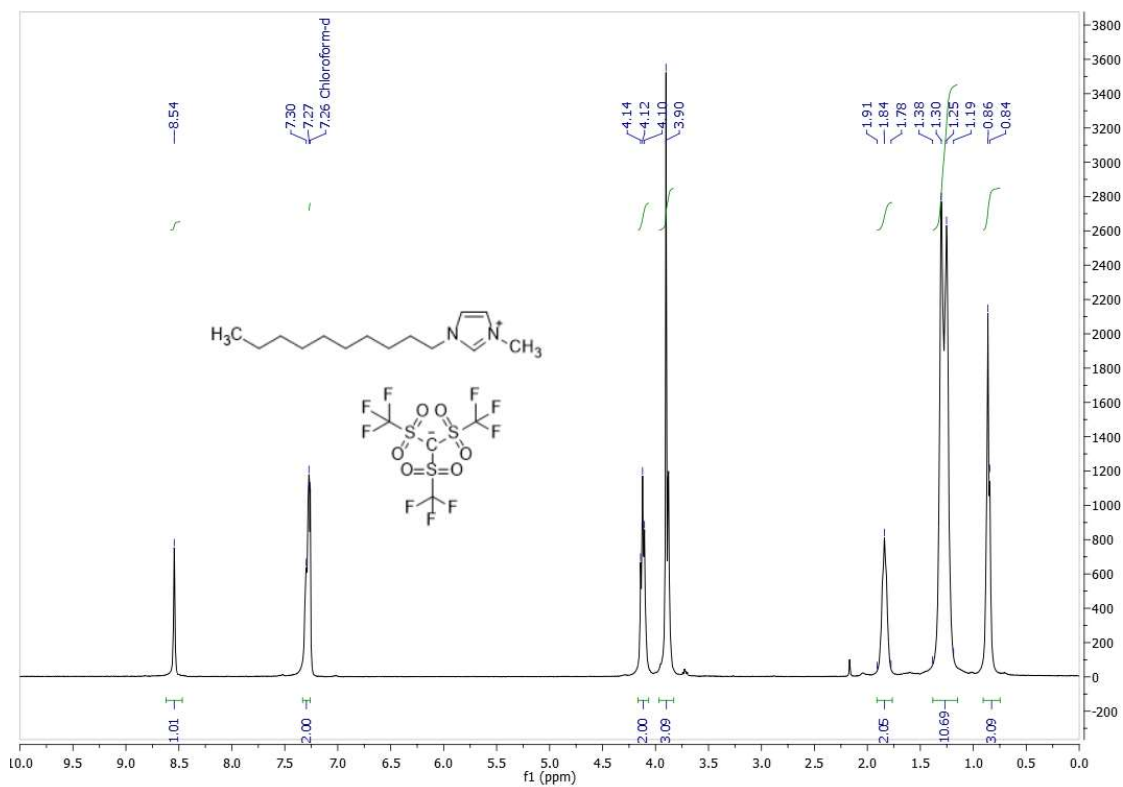
Figure A.10. ^1H NMR spectrum of [C$_8$mim][CTf$_3$].
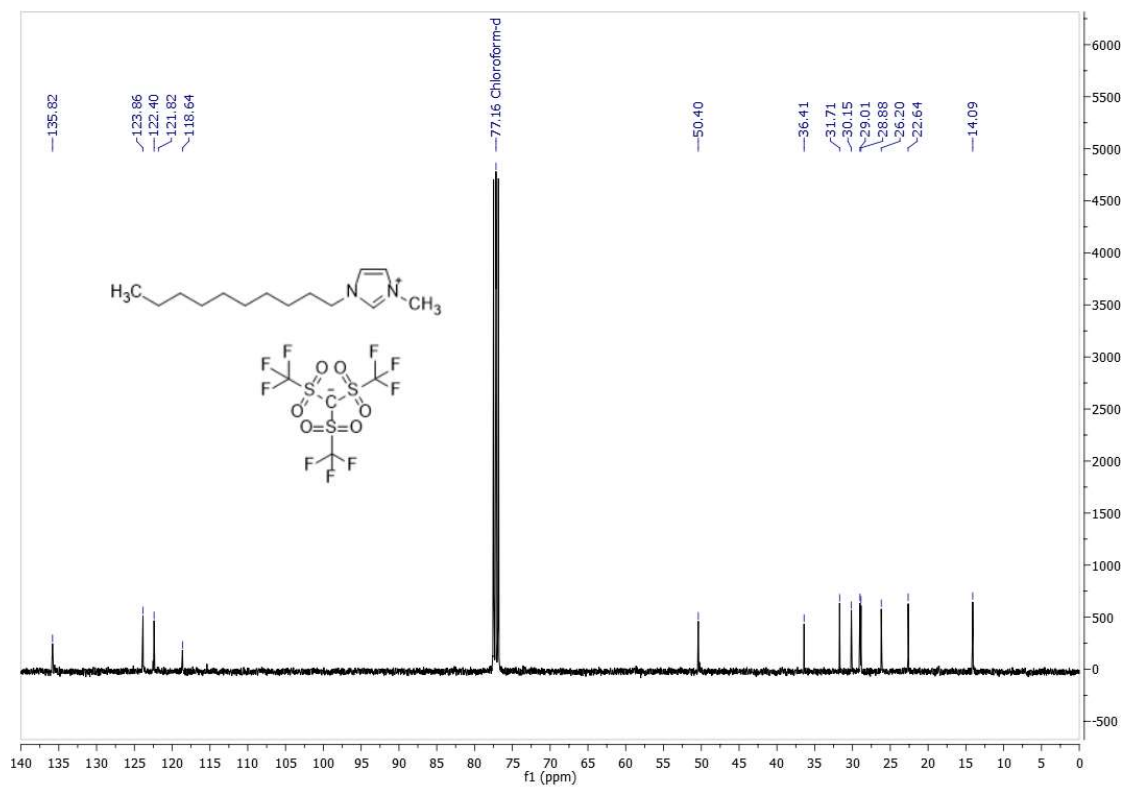
Figure A.11. ^{13}C NMR spectrum of [C$_8$mim][CTf$_3$].
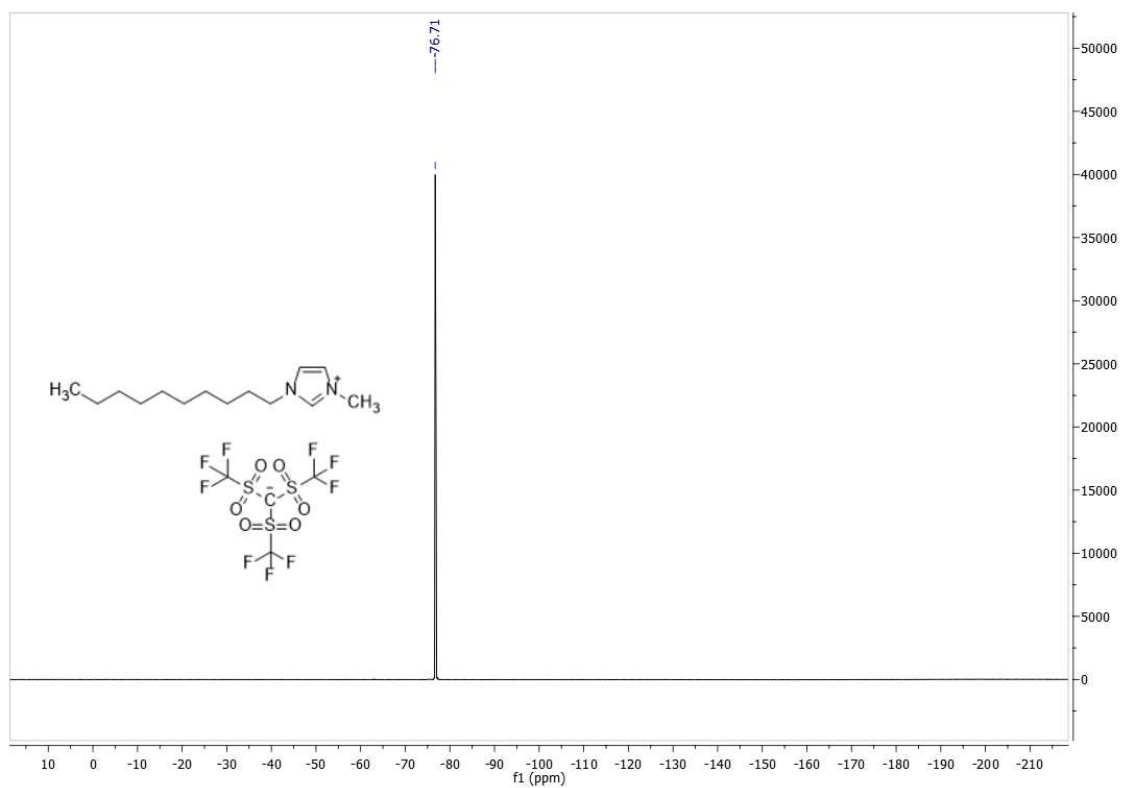
Figure A.12. ^{19}F NMR spectrum of [C$_8$mim][CTf$_3$].
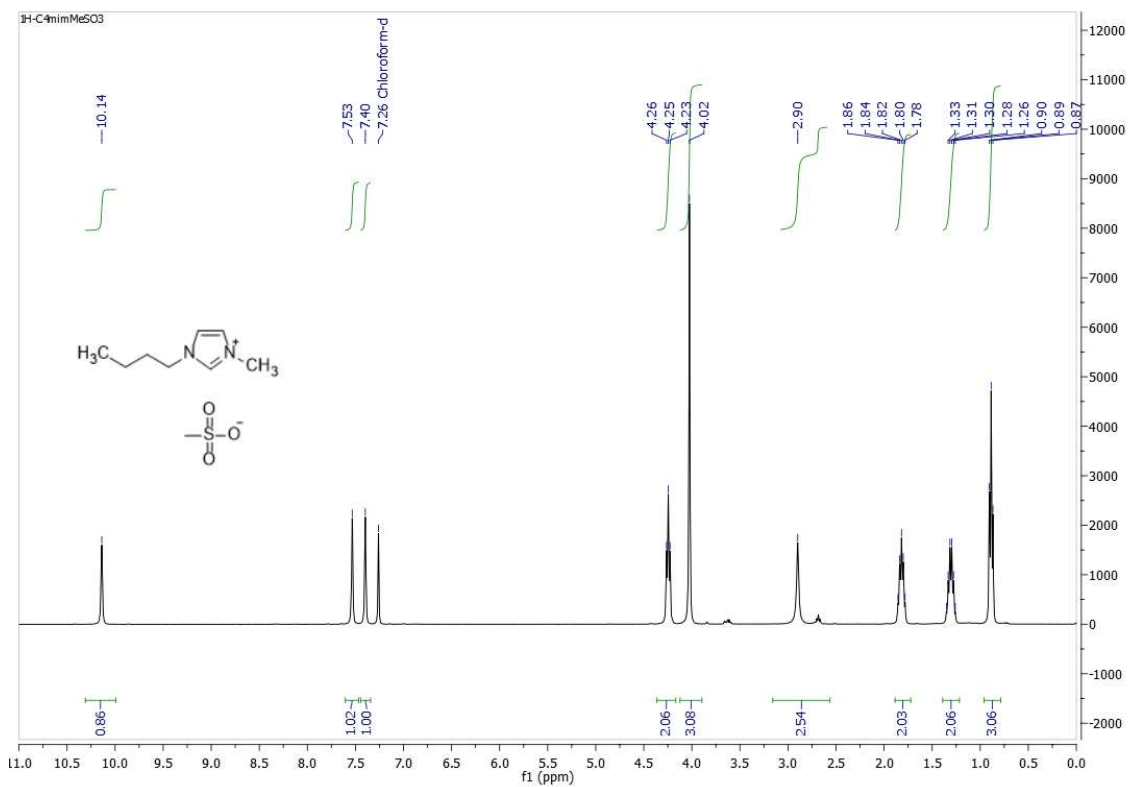
Figure A.13. ^{1}H NMR spectrum of [C$_4$mim][MeSO$_3$].
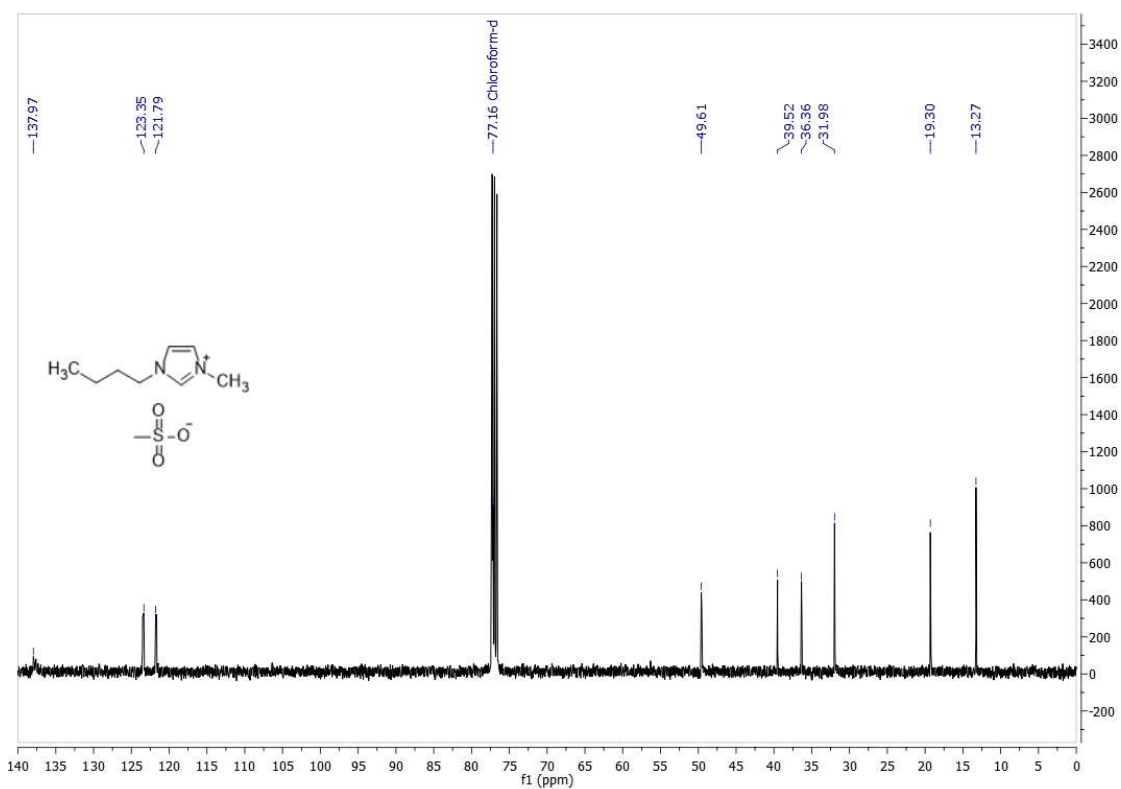
Figure A.14. ^{13}C NMR spectrum of [C$_4$mim][MeSO$_3$].
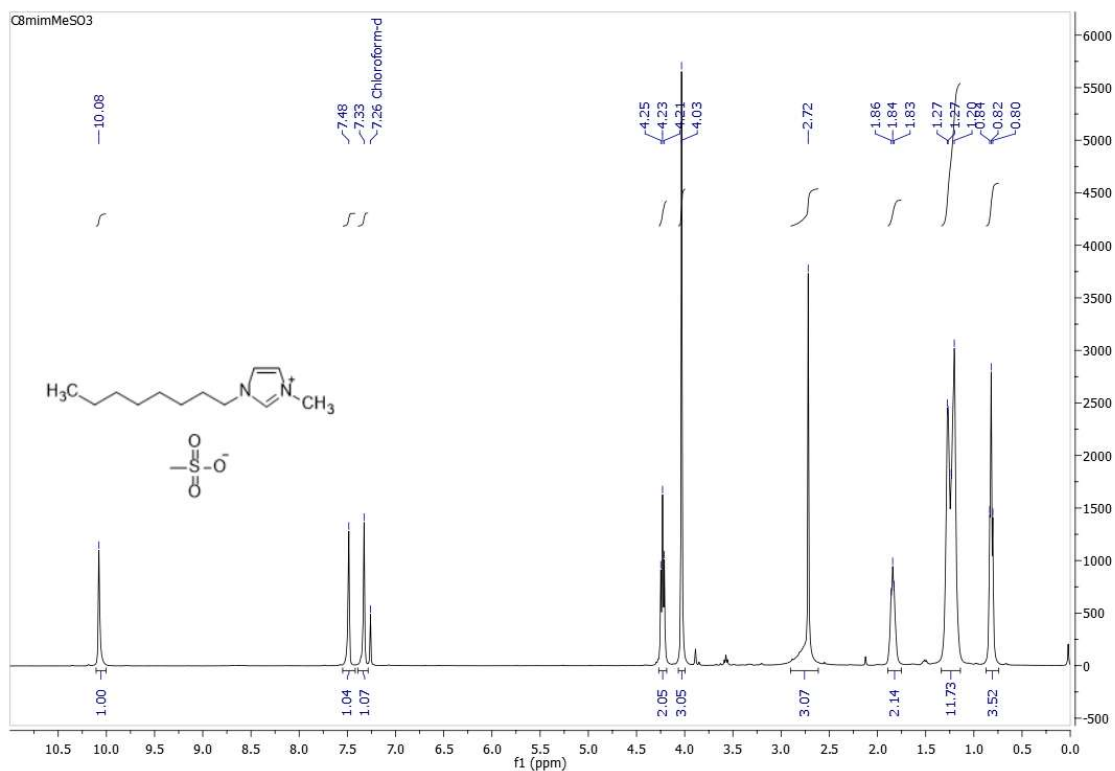
Figure A.15. ^{1}H NMR spectrum of [C$_8$mim][MeSO$_3$].
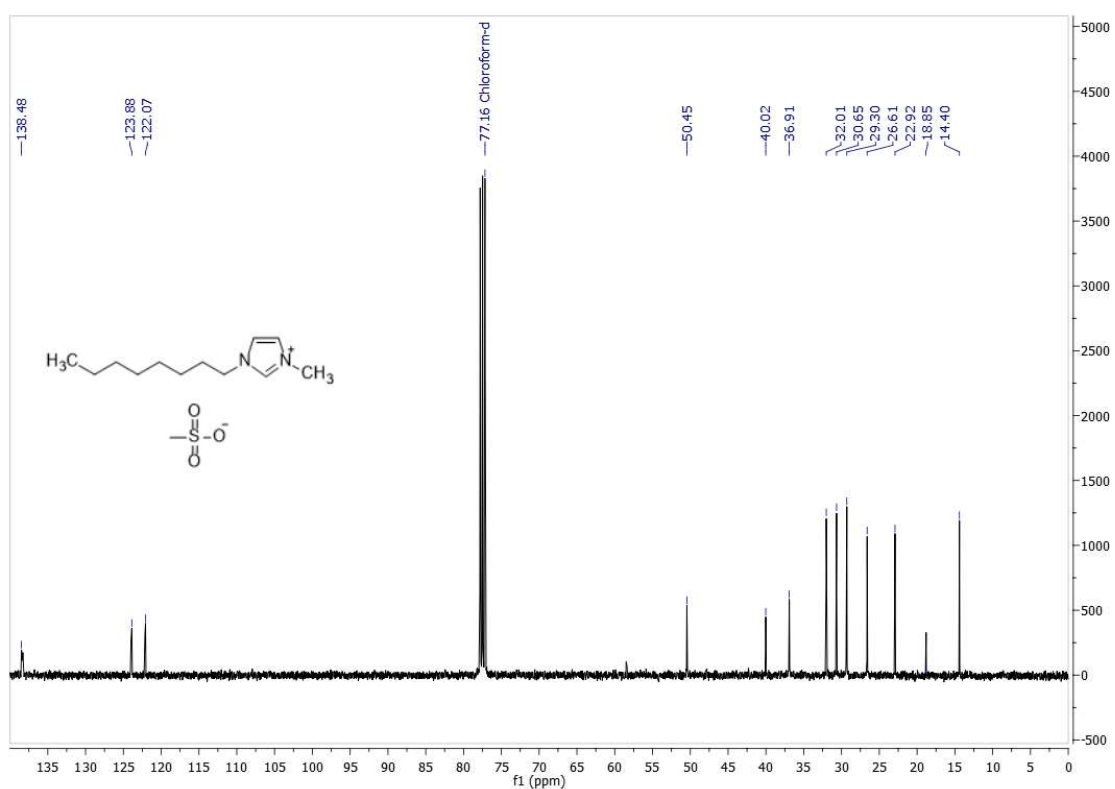
Figure A.16. ^{13}C NMR spectrum of [C$_8$mim][MeSO$_3$].

116
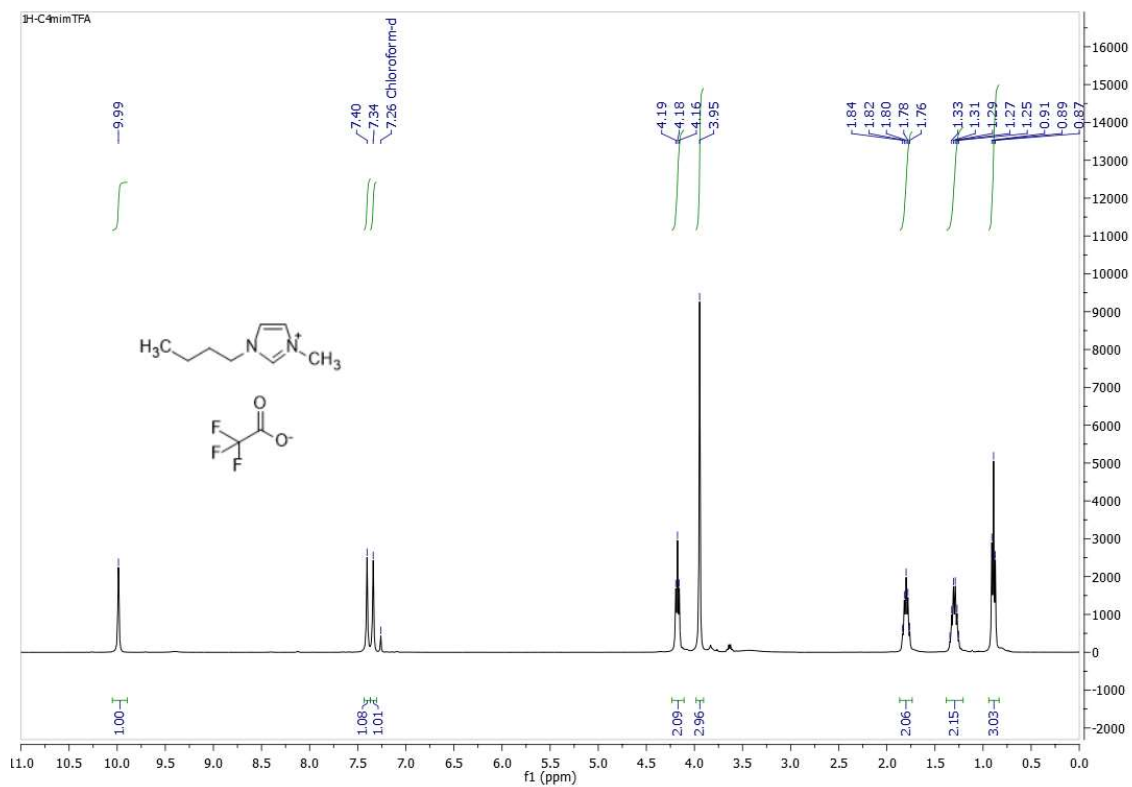
Figure A.17. ^{1}H NMR spectrum of [C$_4$mim][TFA].
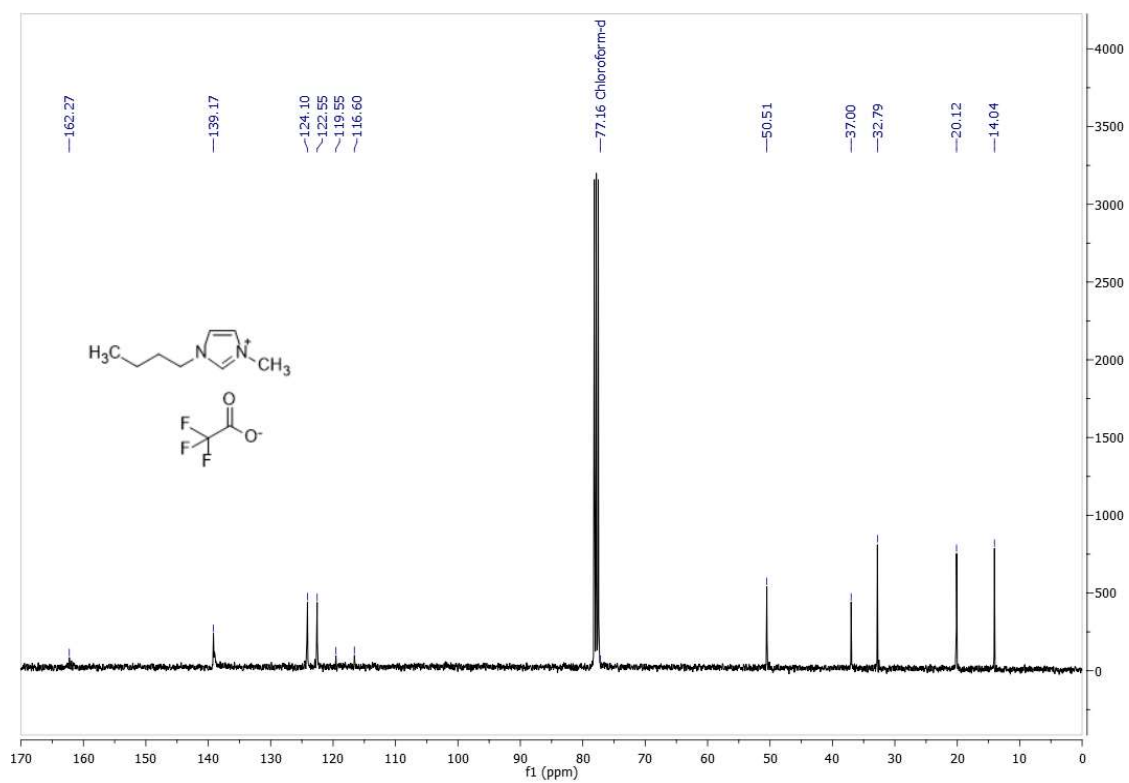
Figure A.18. ^{13}C NMR spectrum of [C$_4$mim][TFA].
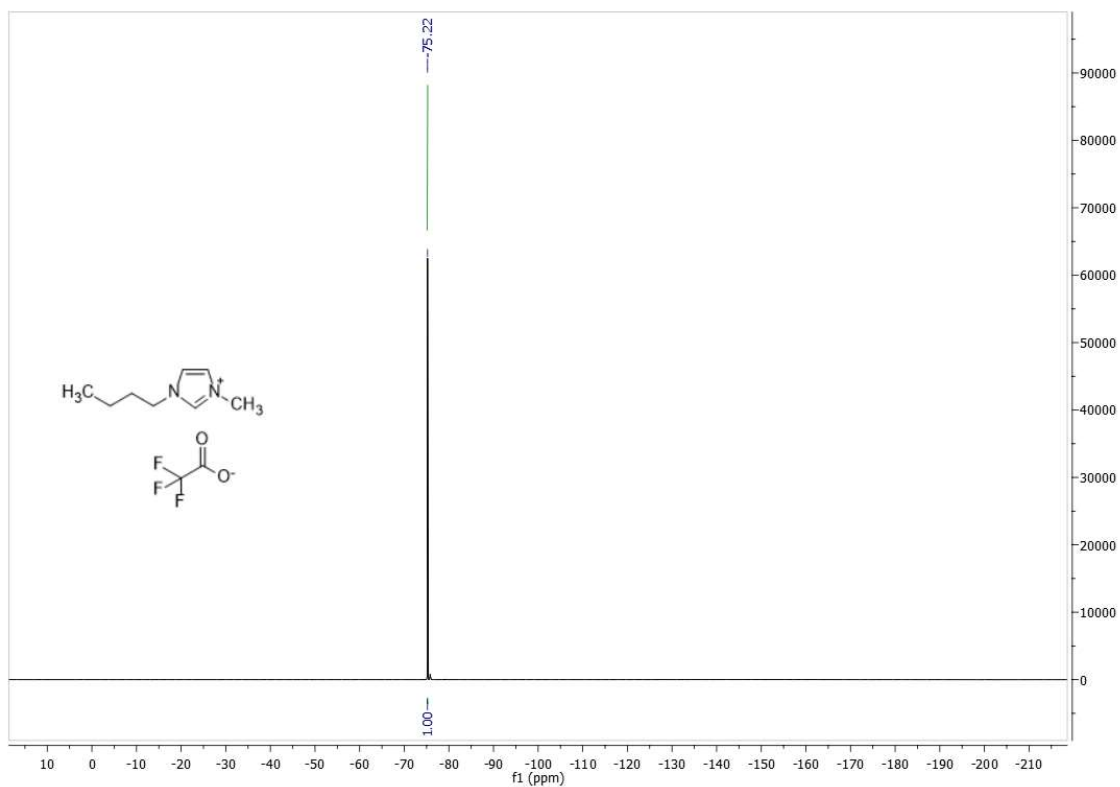
Figure A.19. ^{19}F NMR spectrum of [C$_4$mim][TFA].
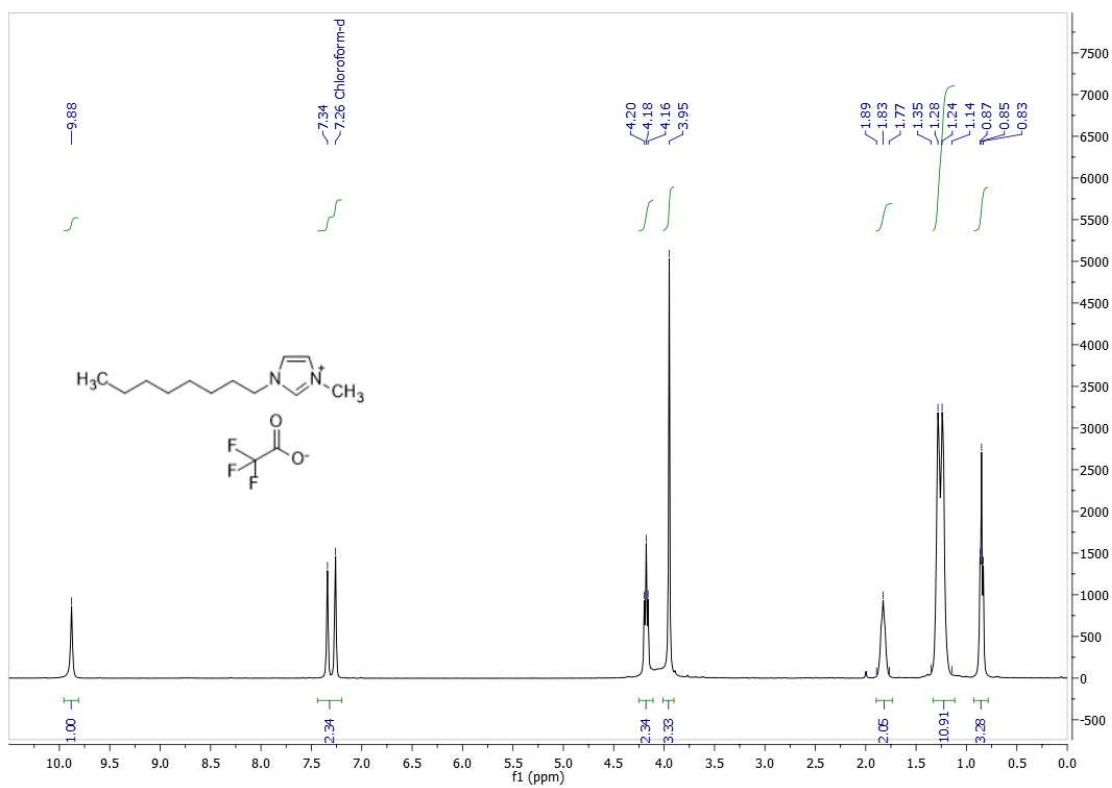
Figure A.20. ^{1}H NMR spectrum of [C$_8$mim][TFA].
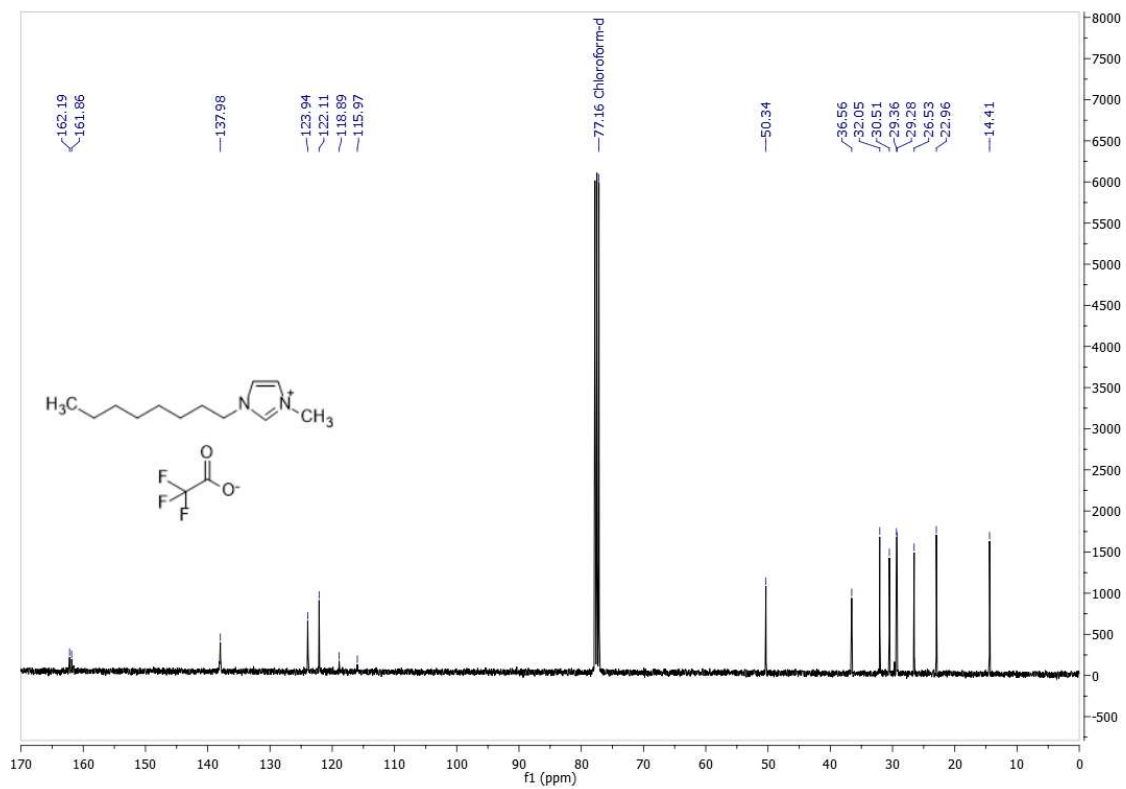
Figure A.21. ^{13}C NMR spectrum of [C$_8$mim][TFA].
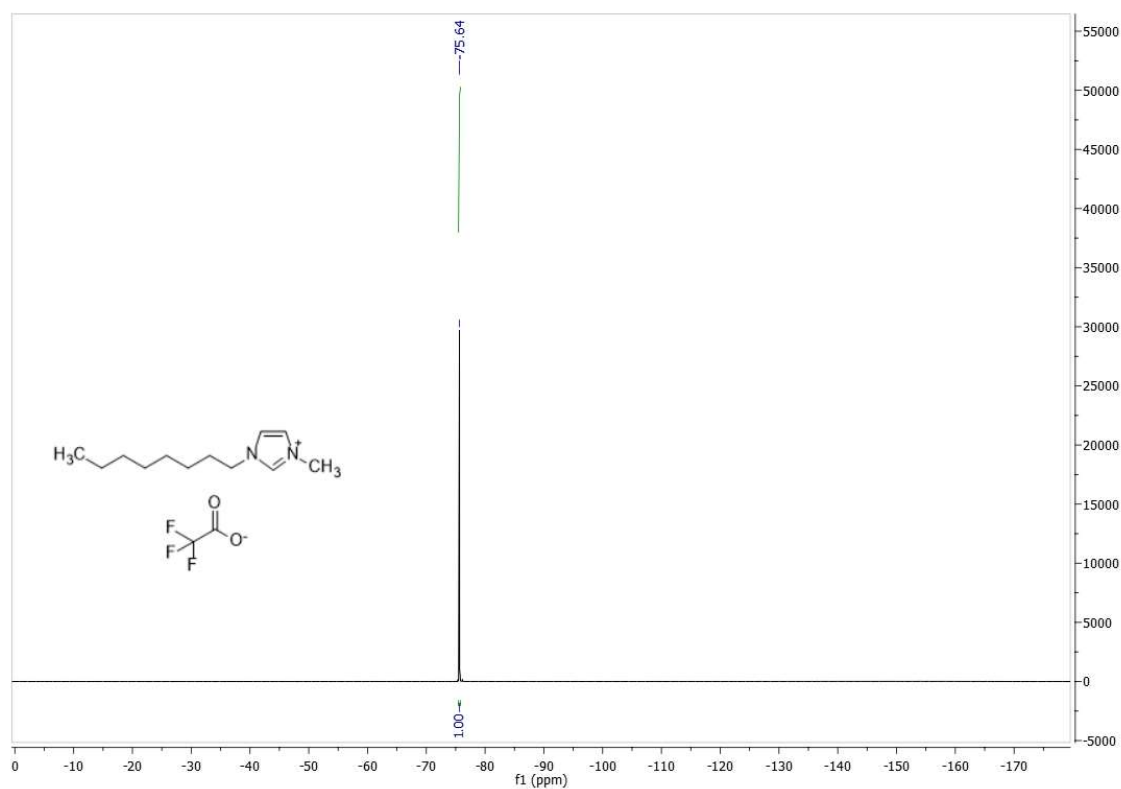
Figure A.22. ^{19}F NMR spectrum of [C$_4$mim][TFA].
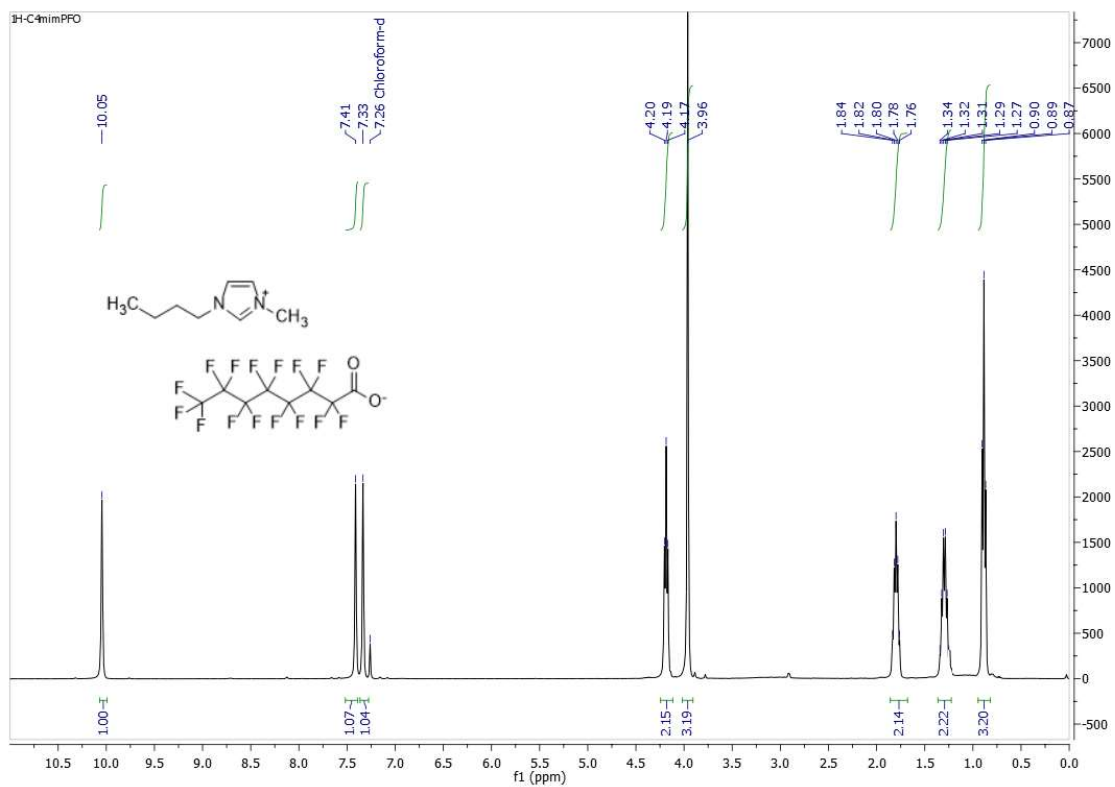
Figure A.23. ^{1}H NMR spectrum of [C$_4$mim][PFO].
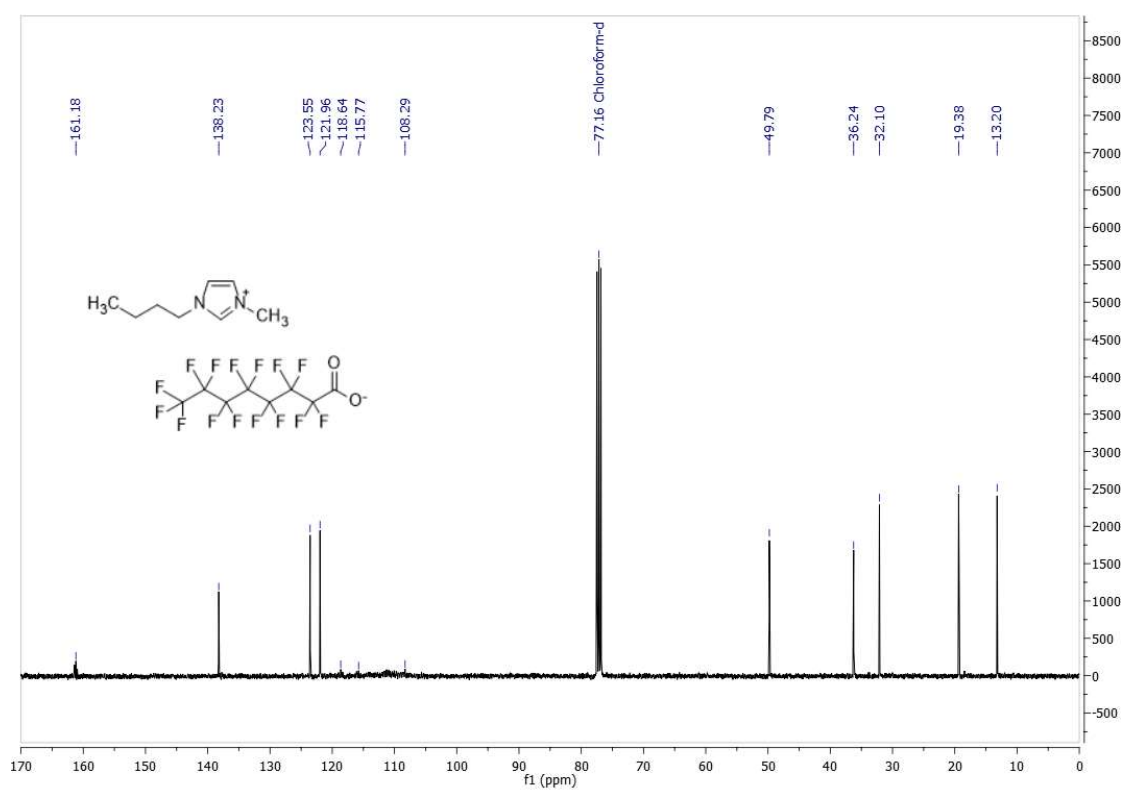
Figure A.24. ^{13}C NMR spectrum of [C$_4$mim][PFO].

120
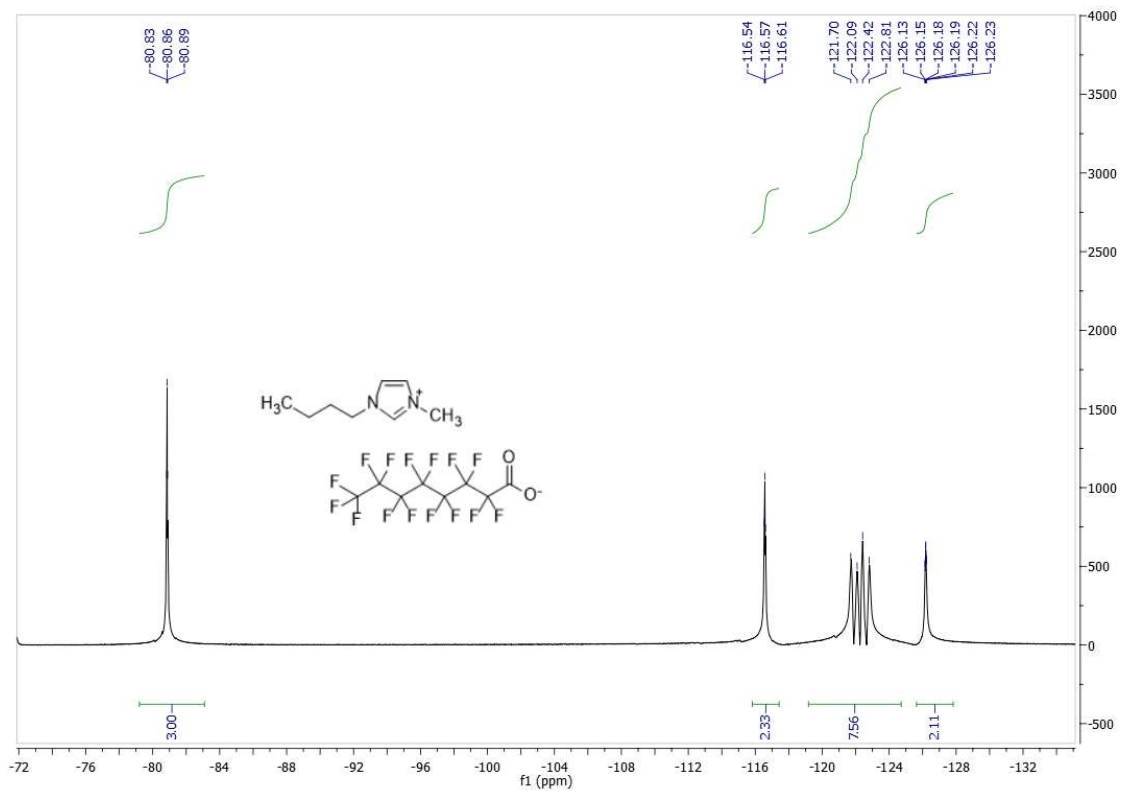
Figure A.25. ^{19}F NMR spectrum of [C$_4$mim][PFO].
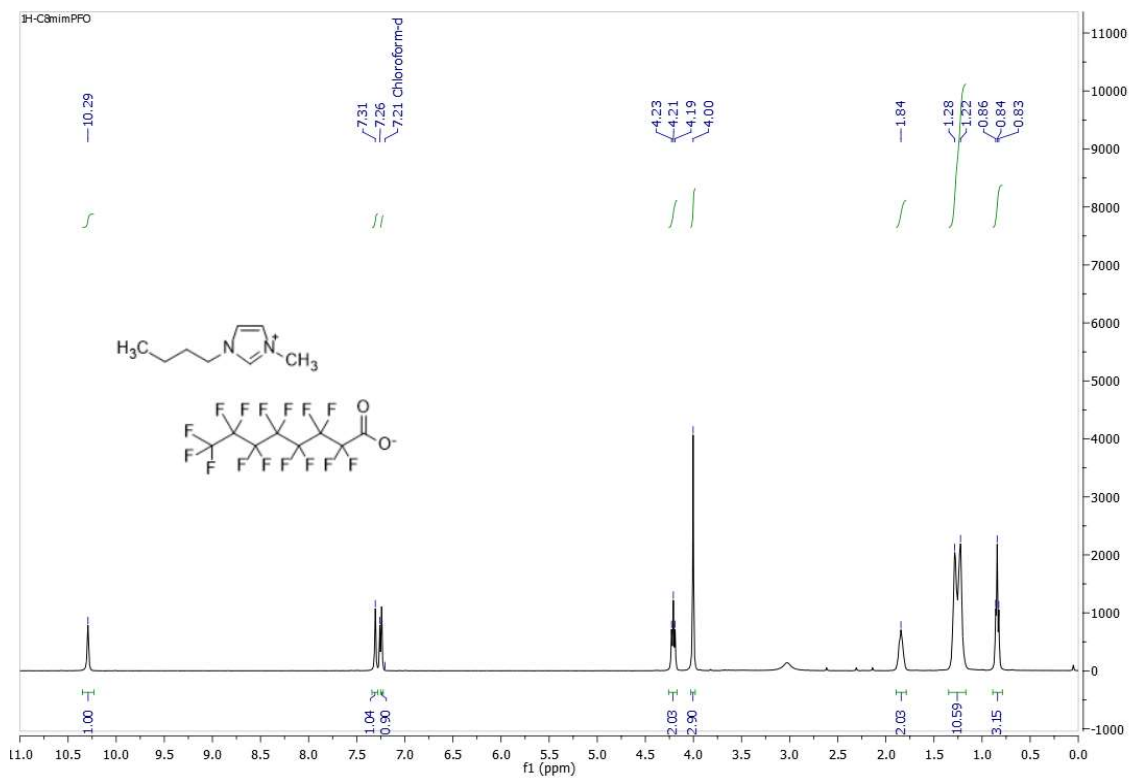
Figure A.26. ^{1}H NMR spectrum of [C$_8$mim][PFO].

121

Figure A.27. ^{13}C NMR spectrum of [C$_8$mim][PFO].

Figure A.28. ^{19}F NMR spectrum of [C$_8$mim][PFO].

Appendix B. DSC of ILs solid at room temperature
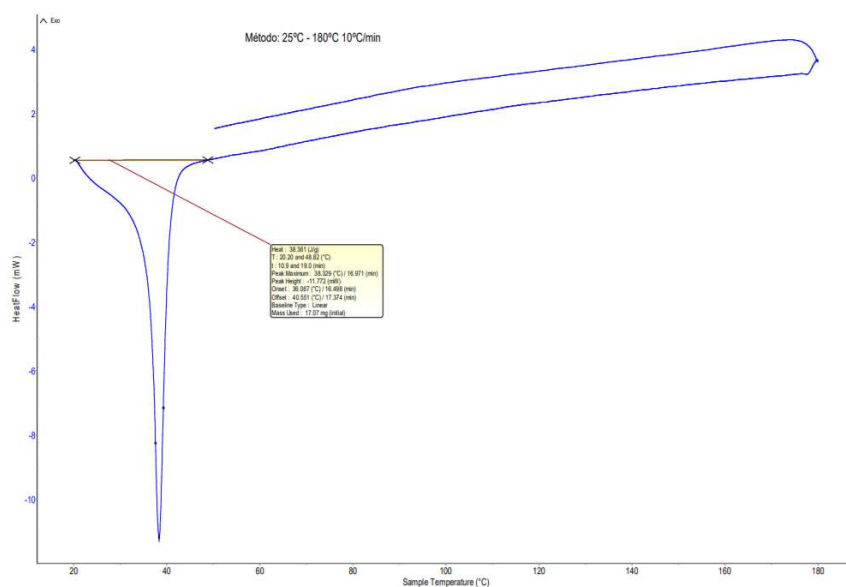
Figure B.1. DSC thermogram above room temperature of [C₈mim][NfO].
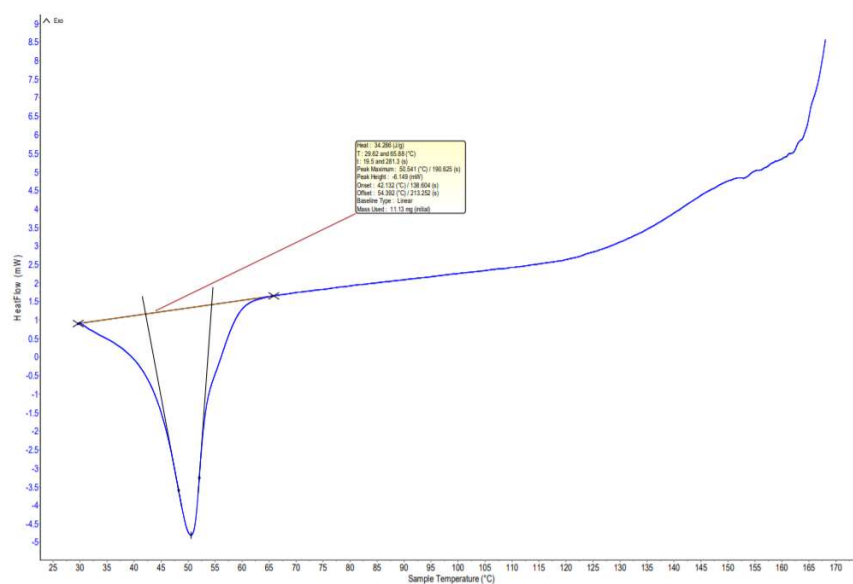
Figure B.2. DSC thermogram above room temperature of [C₈mim][NfO].

124

**Appendix C.   Calibration certified of the hydrocarbon gas mixture used
to calibrate GC-TCD of GC1**

AIR LIQUIDE

ALPHAGAZ

CERTIFICADO DE CALIBRACION/ CALIBRAÇÃO 678030

Conforme a Norma UNE-EN ISO 6141   *Página 1/1*

Tipo de mezcla/Mistura	Crystal		
Código de producto/ Produto	DR311314	*Pedido CTO Nº*	383417
Número de botella/garrafa	EF83XRK	*Número de lote*	678030
Tipo de botella/garrafa	B10	*Estado físico a 15° C*	GAS
Presión/Pressão a 15° C	151 Bar	*Racord/Grifo*	MHM
Límite de garantía	36 MESES		
Fecha de preparación/ Data de preparação	15/04/2013		
Ficha de Seguridad/Segurança	MSDSCR00016		

COMPONENTE	CONCENTRACION CONCENTRAÇÃO SOLICITADA	CONCENTRACION/ CONCENTRAÇÃO REALIZADA	INCERTIDUMBRE /INCERTEZA ABSOLUTA (*)	INCERTIDUMBRE /INCERTEZA % RELATIVA (*)
ppm CH4	2500,0	2482,1	49,60	2,00
ppm C2H4	2500,0	2647,1	52,90	2,00
ppm C2H6	2500,0	2370,7	47,40	2,00
ppm CO	2500,0	2667,8	53,40	2,00
ppm CO2	2500,0	2500,7	50,00	2,00
% HE	Q.S.	Q.S.		

(*) O cálculo de incerteza foi realizado para um intervalo de confiança de 95 % (K=2)

(*) El calculo de incertidumbre ha sido realizado para un intervalo de confianza al 95% (K=2)

Temperatura de utilización/utilização - conservación/conservação: -10 y 50 °C

Límite de utilización /utilização: 10 % DE LA CARGA/DA CARGA

Visado/Visto: Rodrigo Sagredo

*Observaciones/
Observações :*

Appendix D. Calibration curves used in GC2
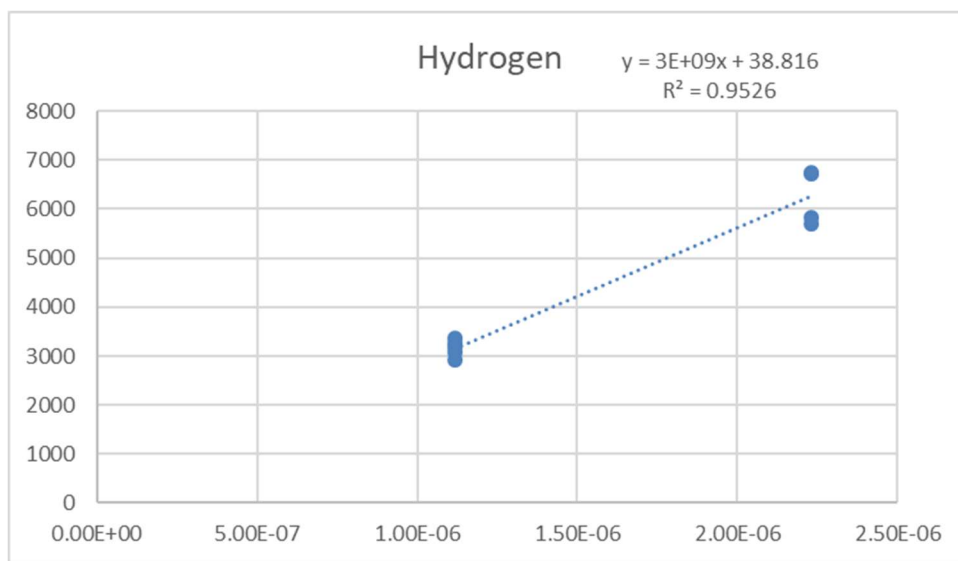
Figure D.1. Supplied Calibration curve of hydrogen gas in GC 2, y values represent peak area, x values represent amount (mol) of gas inside the sample syringe.
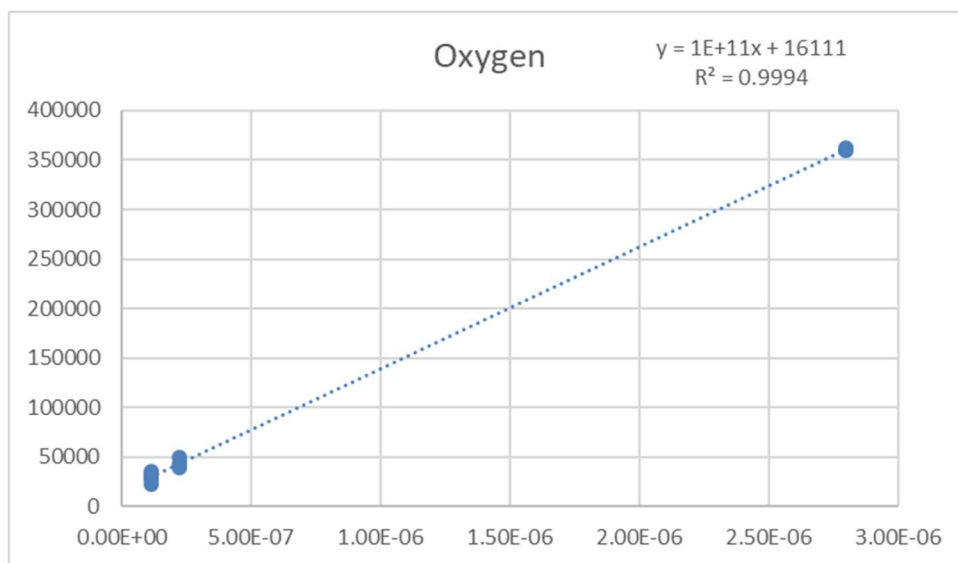
Figure D.2. Supplied Calibration curve of oxygen gas in GC 2, y values represent peak area, x values represent amount (mol) of gas inside the sample syringe.
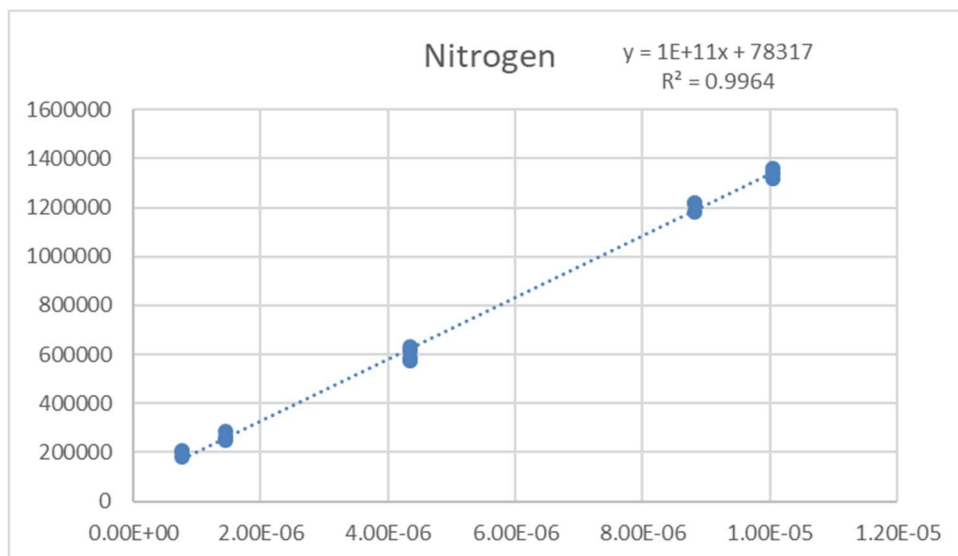
Figure D.3. Supplied Calibration curve of nitrogen gas in GC 2, y values represent peak area, x values represent amount (mol) of gas inside the sample syringe.
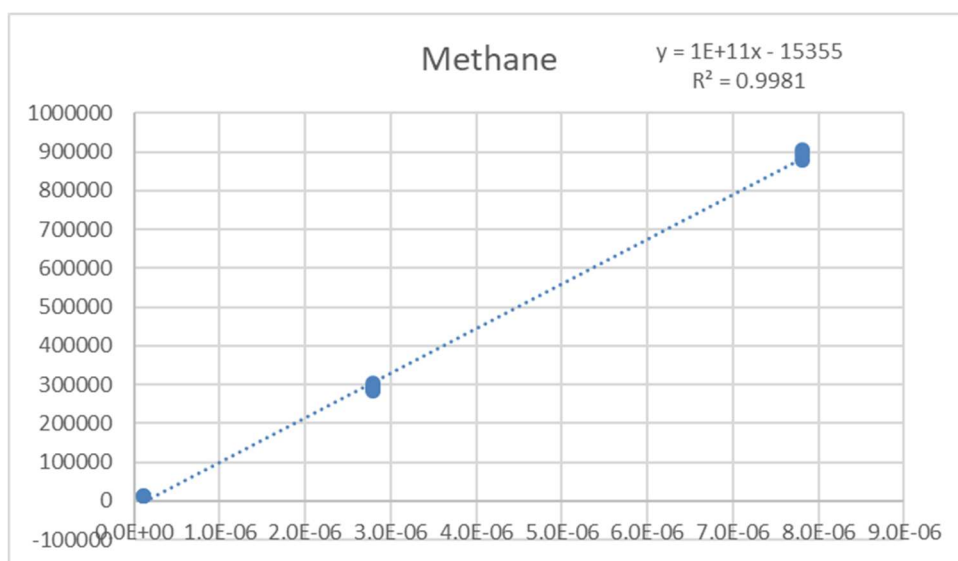
Figure D.4 Supplied Calibration curve of methane gas in GC 2, y values represent peak area, x values represent amount (mole) of gas inside the sample syringe.

128
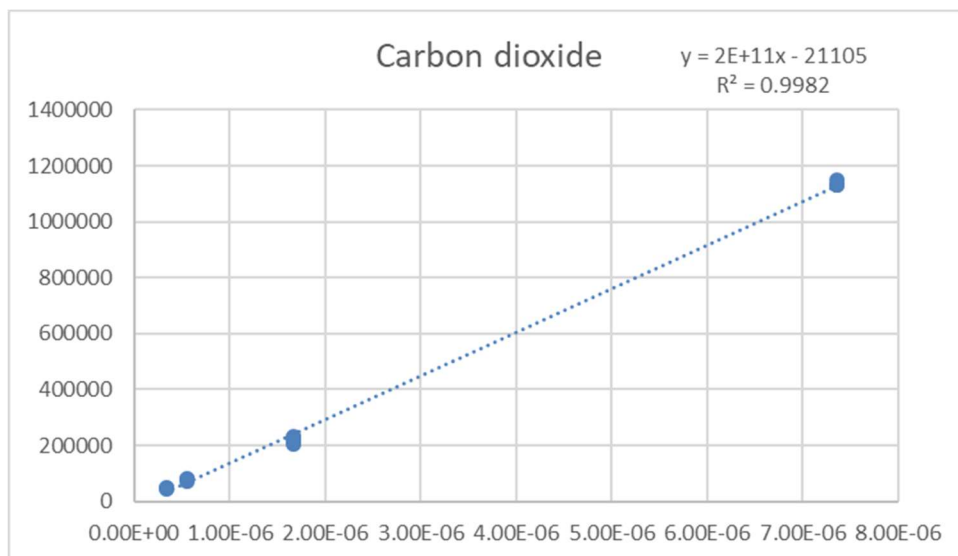
Figure D.5. Supplied Calibration curve of carbon dioxide gas in GC 2, y values represent peak area, x values represent amount (mol) of gas inside the sample syringe.
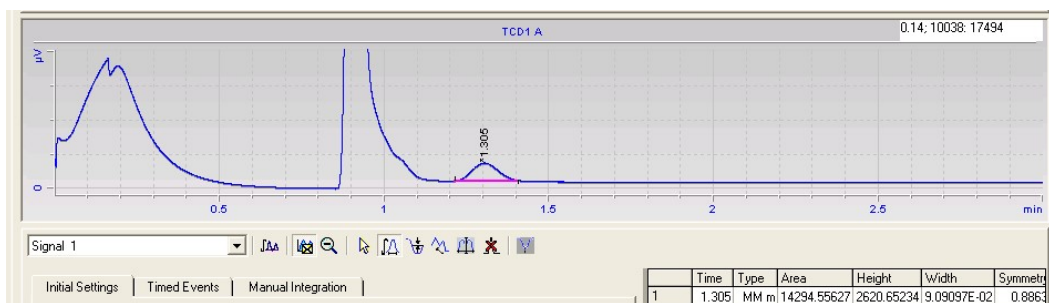
Appendix E. CG Chromatograms obtained from GCs.
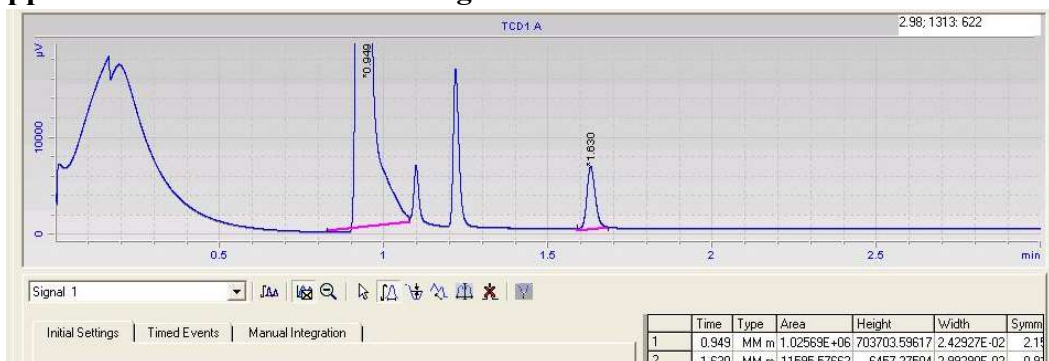
Figure E.1. Chromatogram of entry ST02 provided by channel 1.
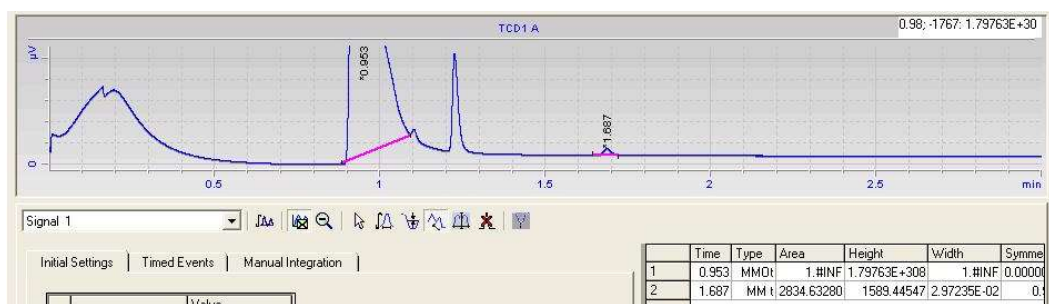
Figure E.2. Chromatogram of entry ST03 provided by channel 1.
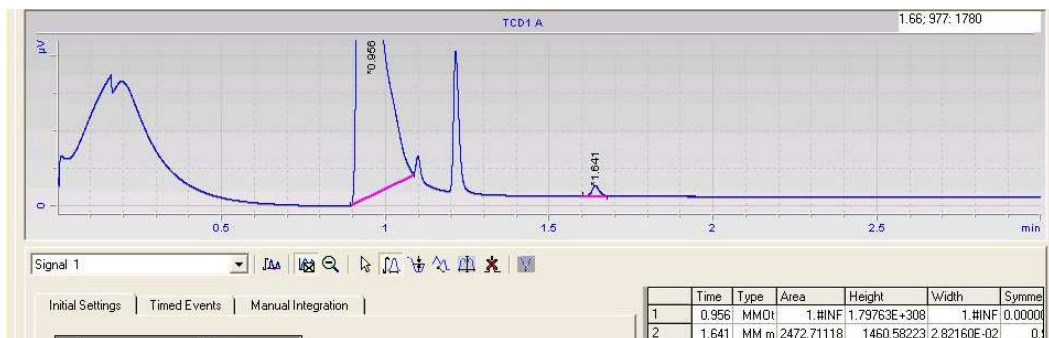
Figure E.3. Chromatogram of entry ST04 provided by channel 1.
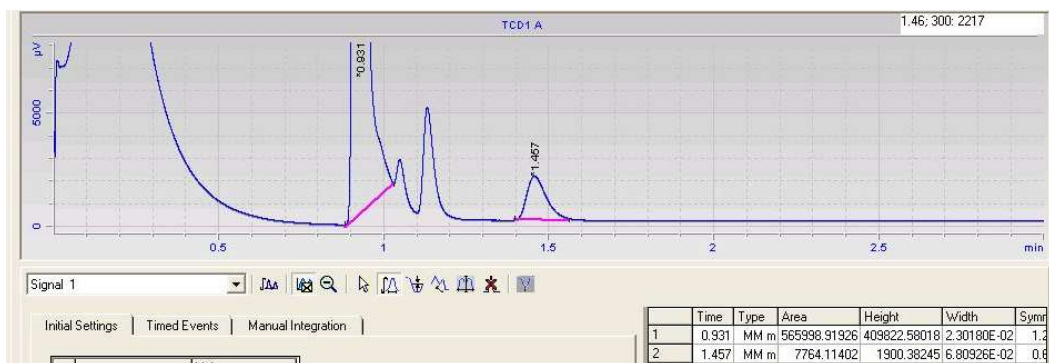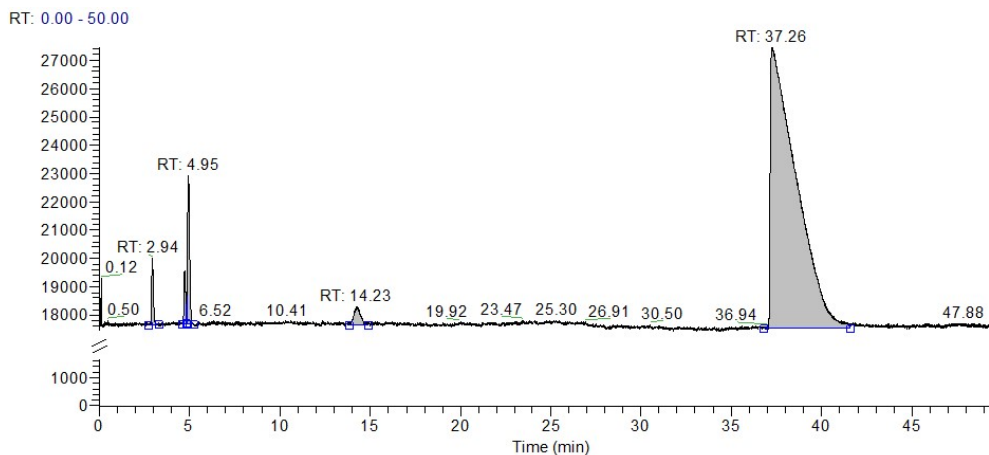

Figure E.4. Chromatogram of entry ST09 provided by channel 1.
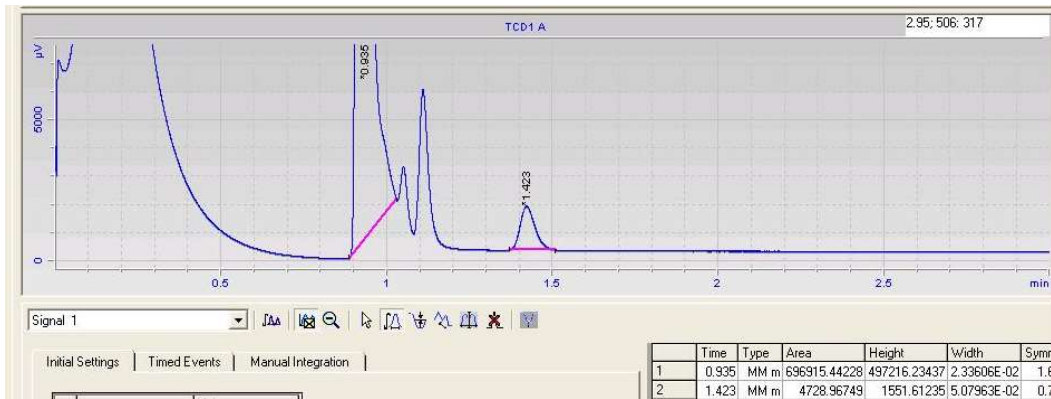
Figure E.5. Chromatogram of entry ST10 provided by channel 1.
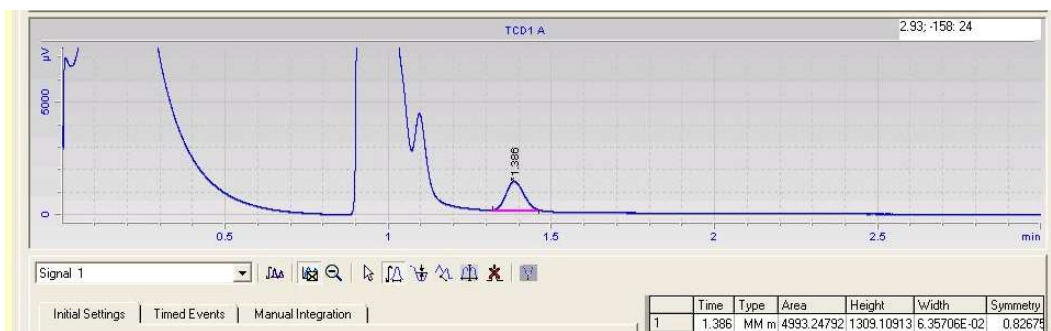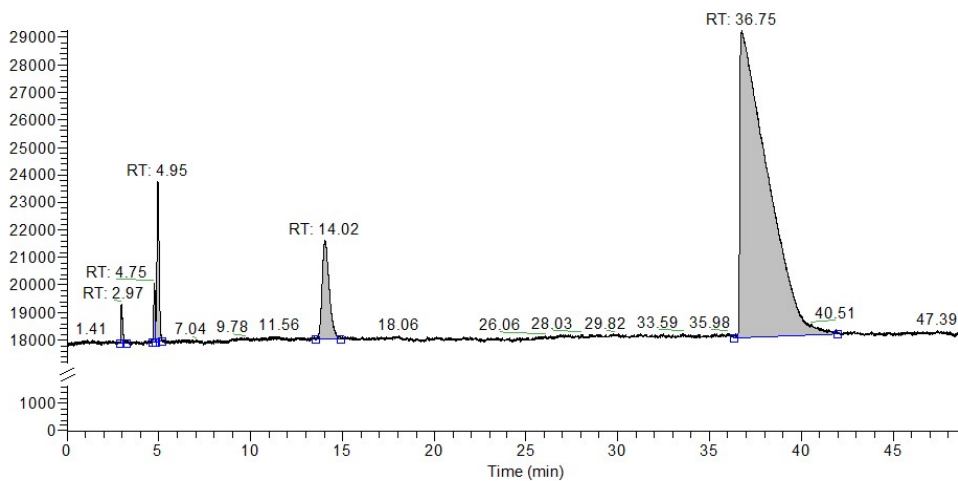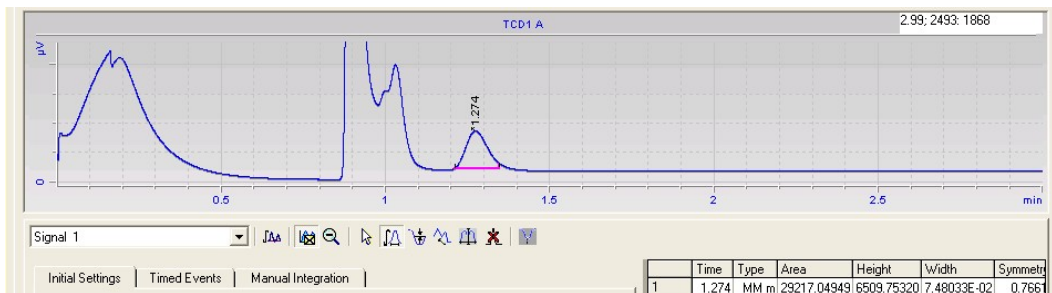

Figure E.6. Chromatogram of entry ST12 provided by channel 1.
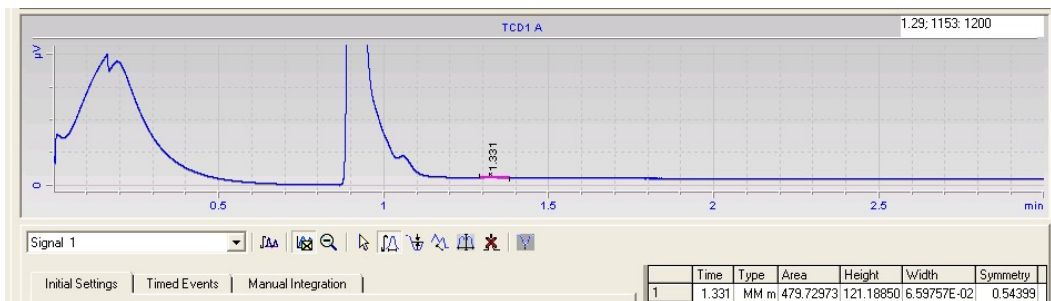
Figure E.7. Chromatogram of entry HC05 provided by channel 1.
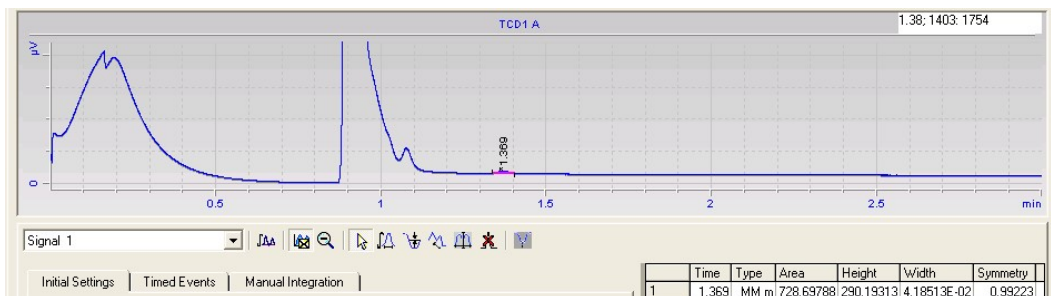
Figure E.8. Chromatogram of entry HC10 provided by channel 1.

132
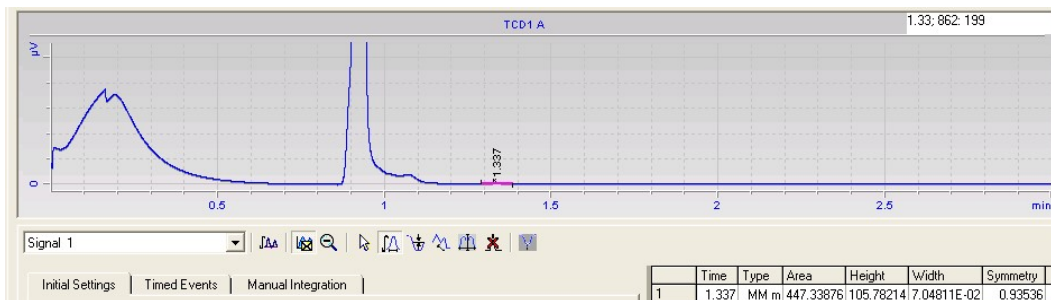
Figure E.9. Chromatogram of entry HC11 provided by channel 1.
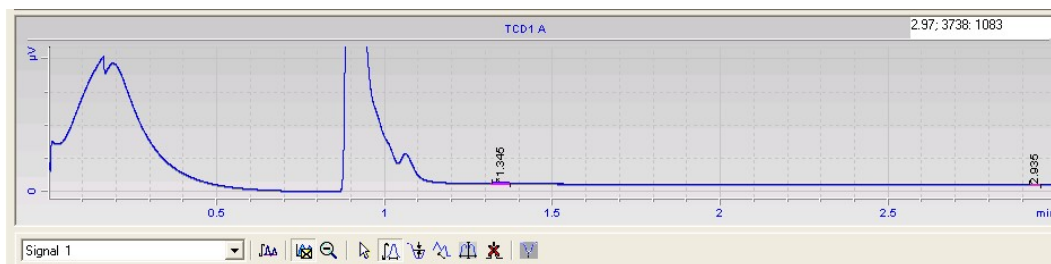
Figure E.10. Chromatogram of entry NP01 provided by channel 1
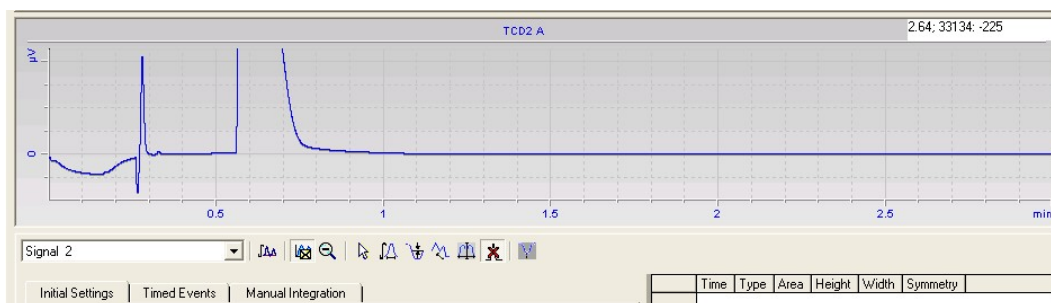
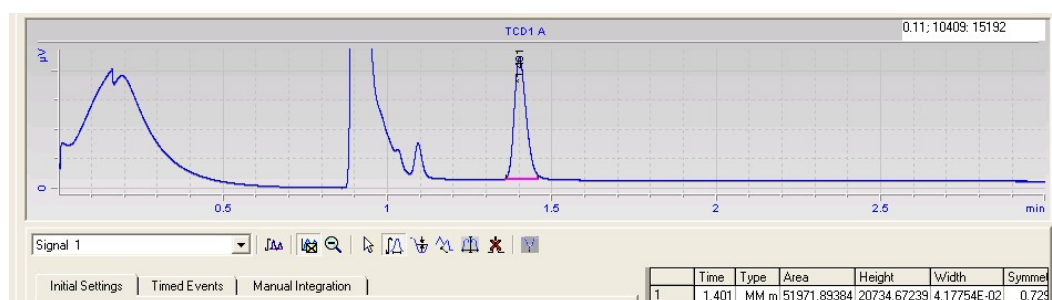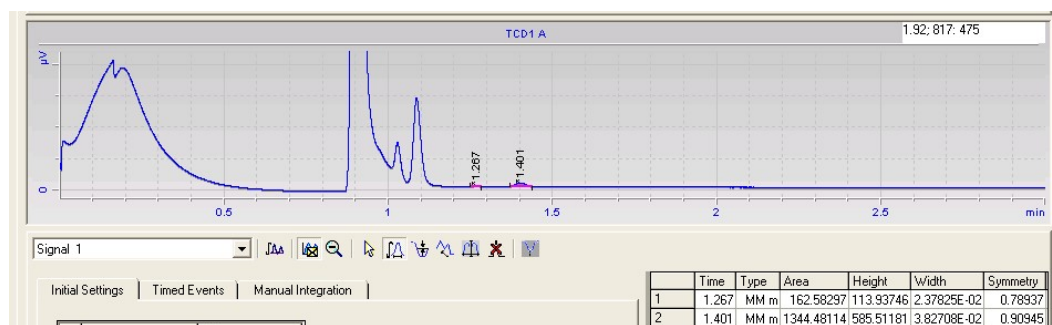Figure E.11. Chromatogram of entry CM06 provided by channel 2
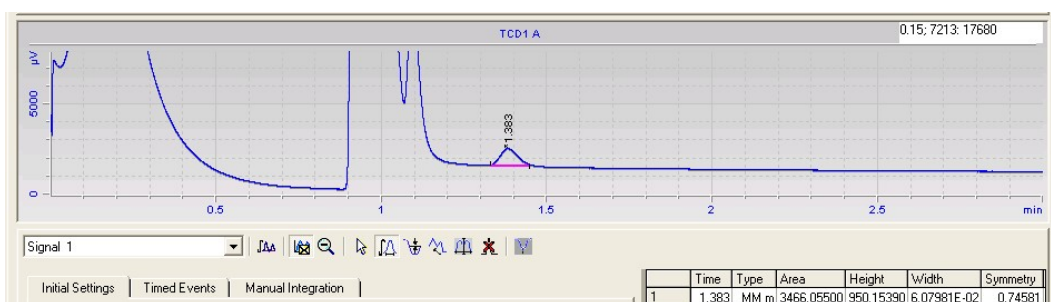
Figure E.12. Chromatogram of entry NP03 provided by channel 1.
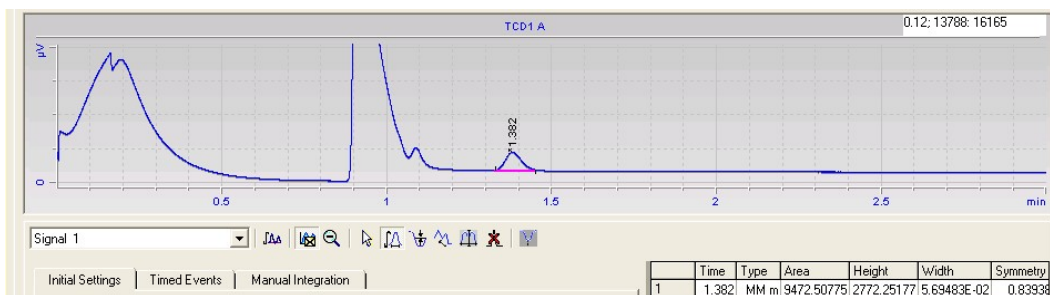
Figure E.13. Chromatogram of entry NP04 provided by channel 1.
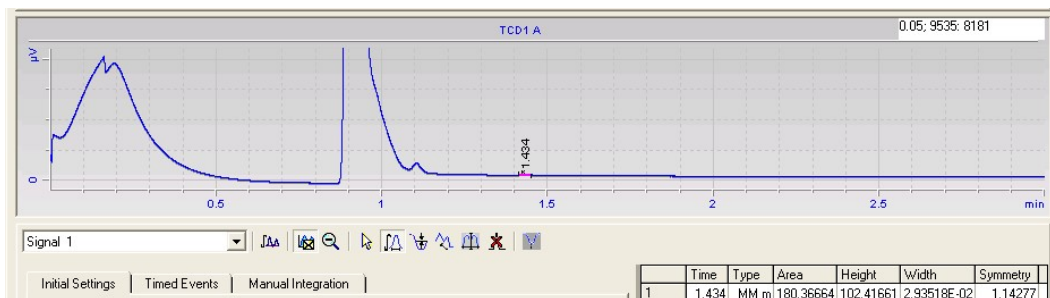
Figure E.14. Chromatogram of entry NP05 provided by channel 1.
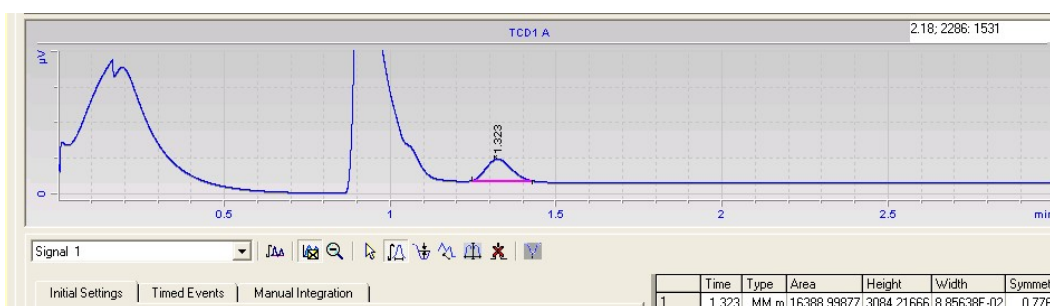
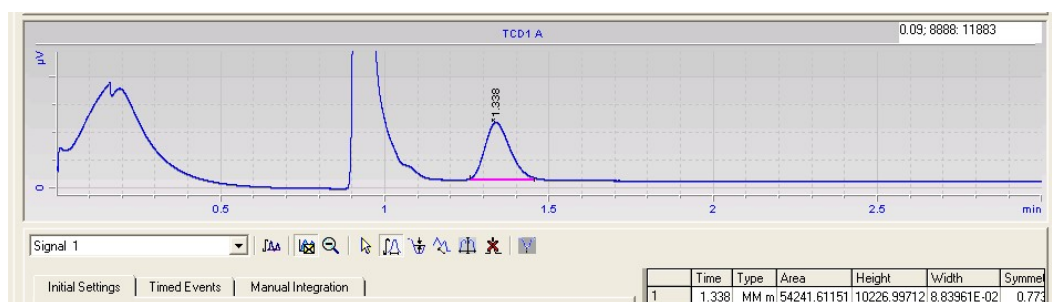Figure E.15. Chromatogram of entry NP06 provided by channel 1.
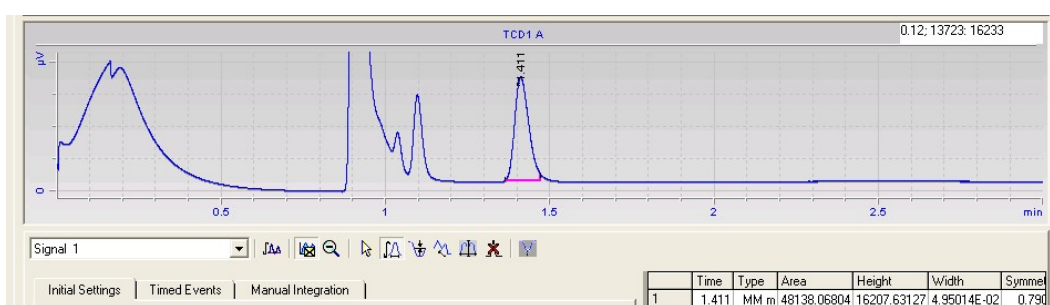
Figure E.16. Chromatogram of entry NP07 provided by channel 1.
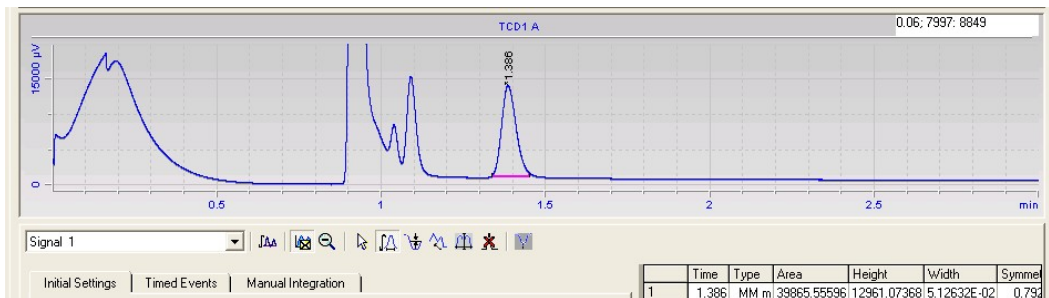
Figure E.17. Chromatogram of entry NP08 provided by channel 1.
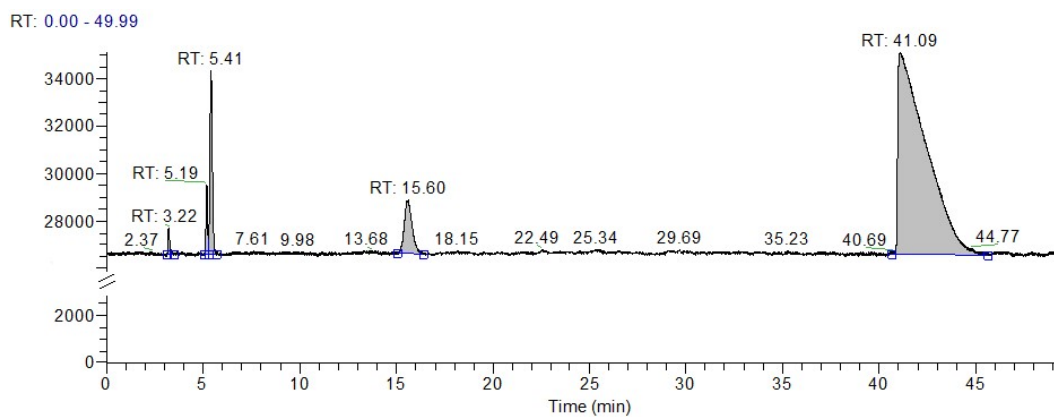
Figure E.18. Chromatogram of entry NP09.
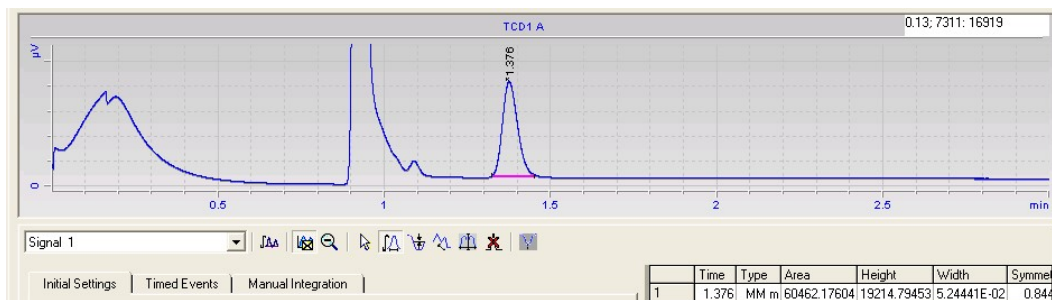
Figure E.19. Chromatogram of entry NP10 provided by channel 1.
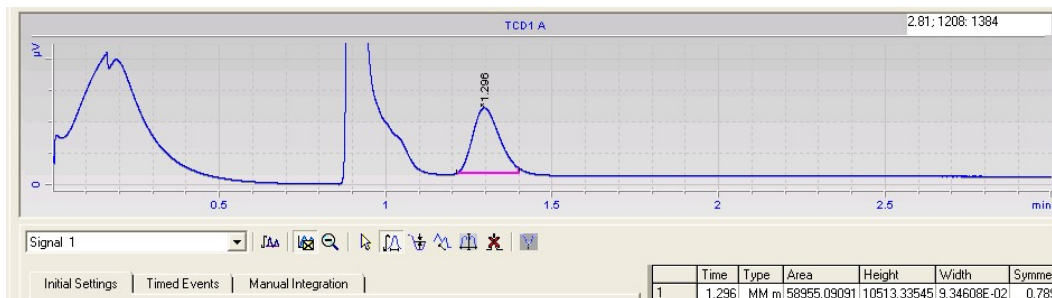
Figure E.20. Chromatogram of entry NP11 provided by channel 1.
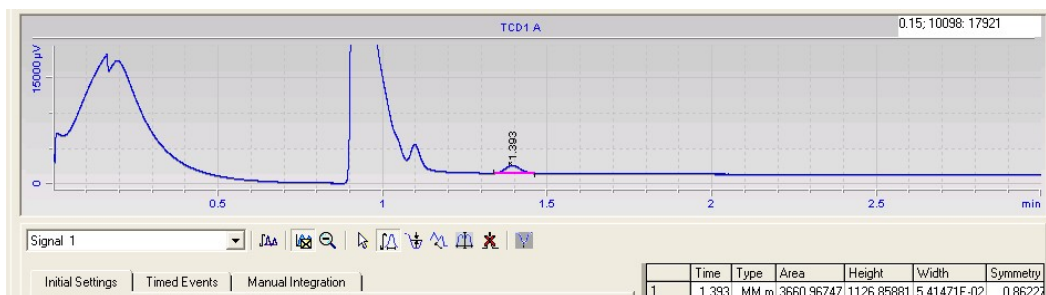
Figure E.21. Chromatogram of entry NP14 provided by channel 1.
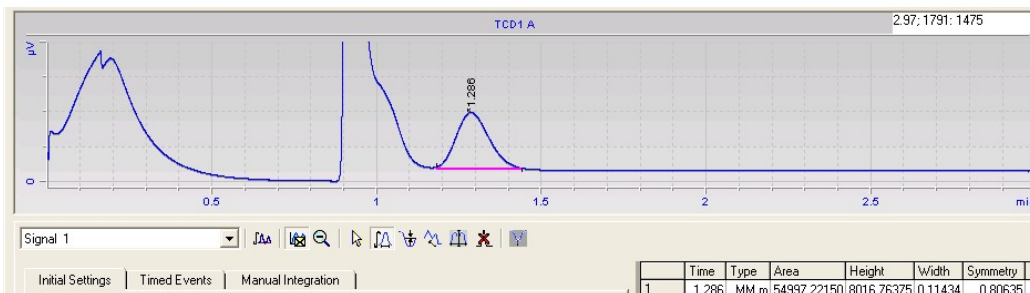
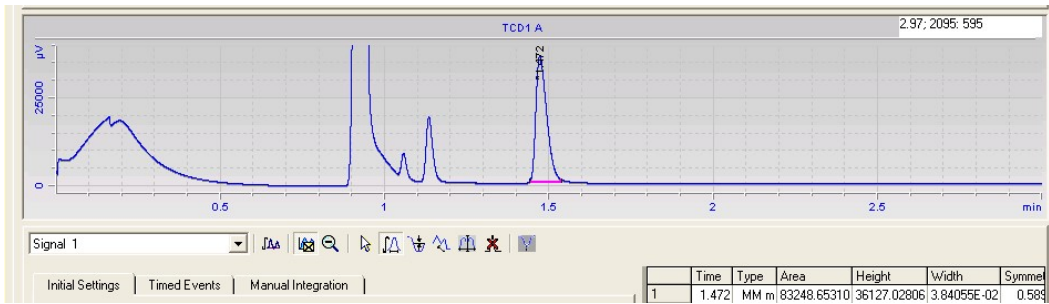Figure E.22 Chromatogram of entry NP16 provided by channel 1.
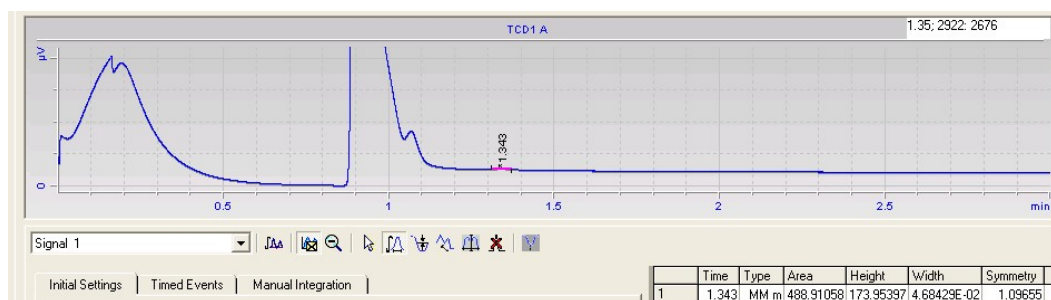
Figure E.23. Chromatogram of entry NP17 provided by channel 1.
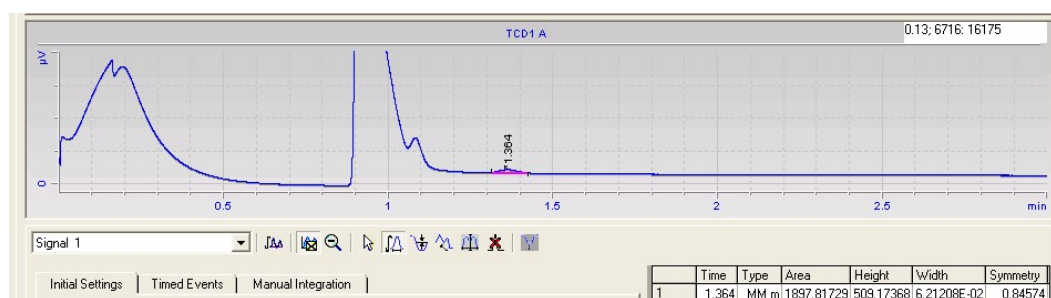
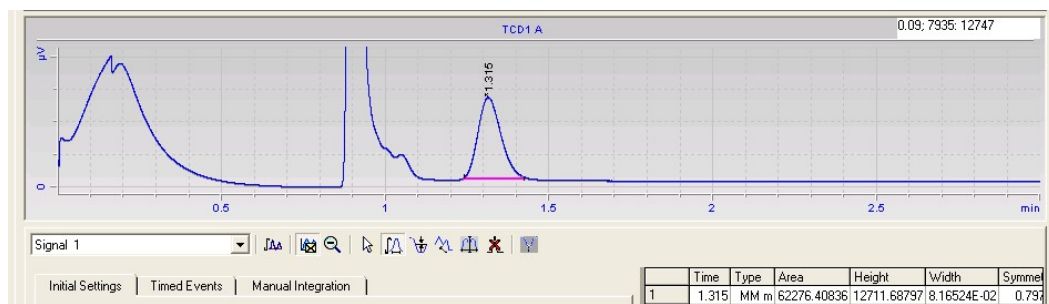Figure E.24. Chromatogram of entry NP18 provided by channel 1.
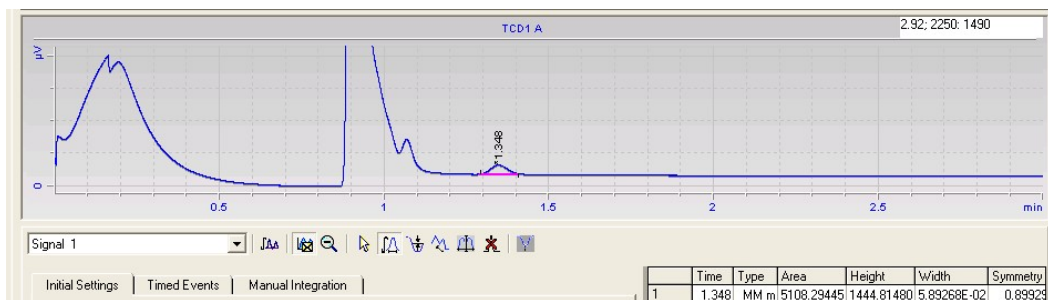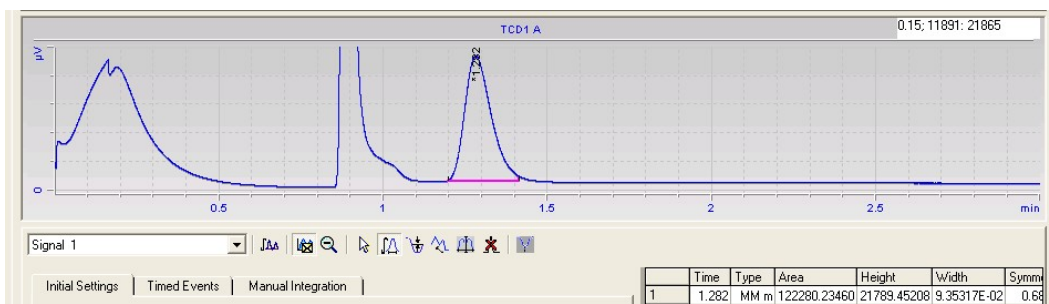
Figure E.25. Chromatogram of entry NP19 provided by channel 1.
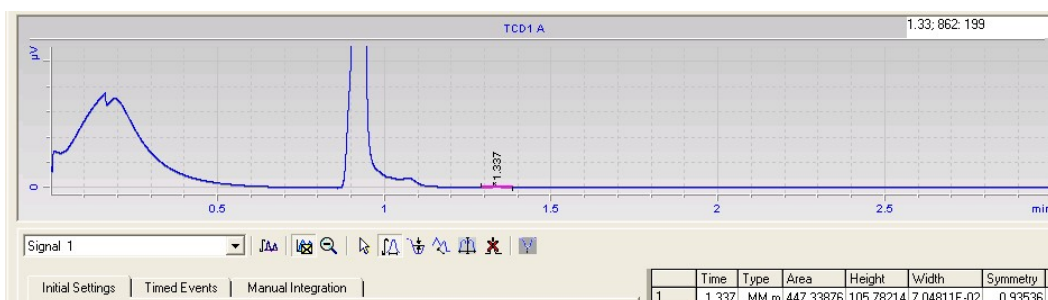
Figure E.26. Chromatogram of entry NP20 provided by channel 1.
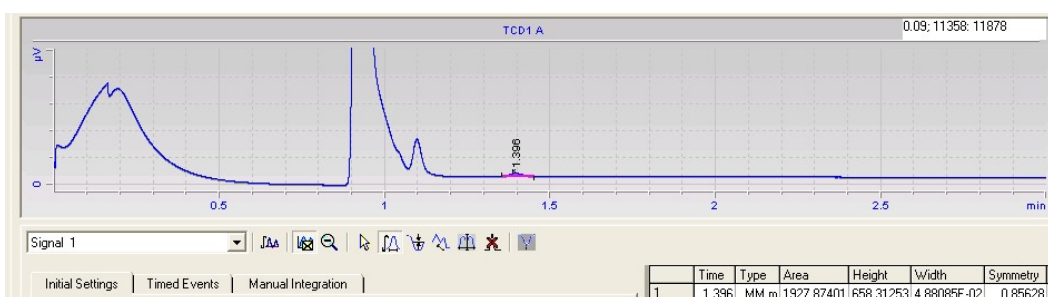
Figure E.27. Chromatogram of entry NP21 provided by channel 1.
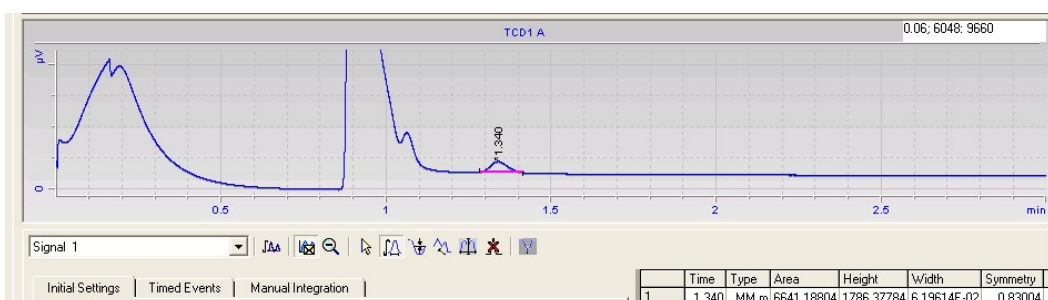
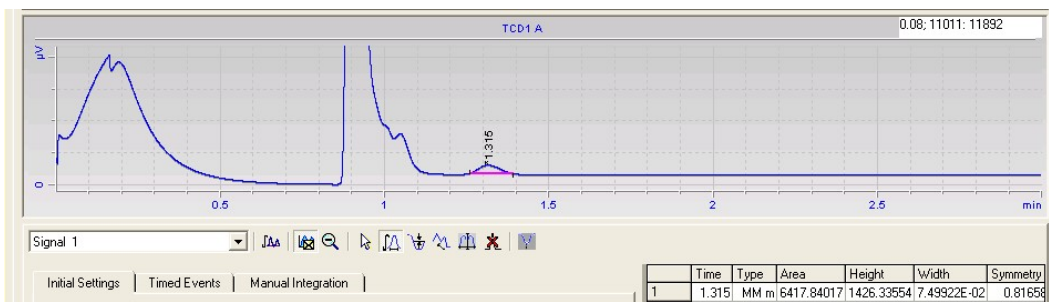Figure E.28. Chromatogram of entry NP22 provided by channel 1.

137
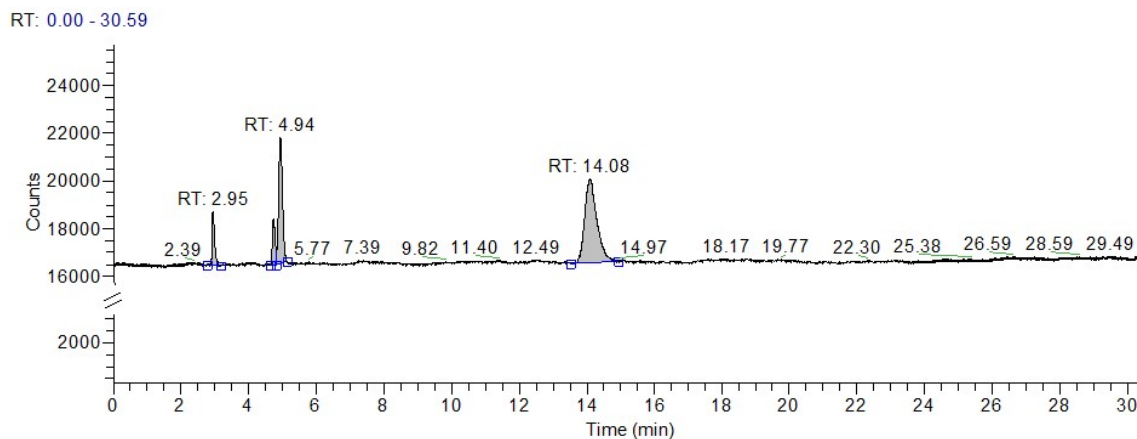
Figure E.29. Chromatogram of entry NP23.
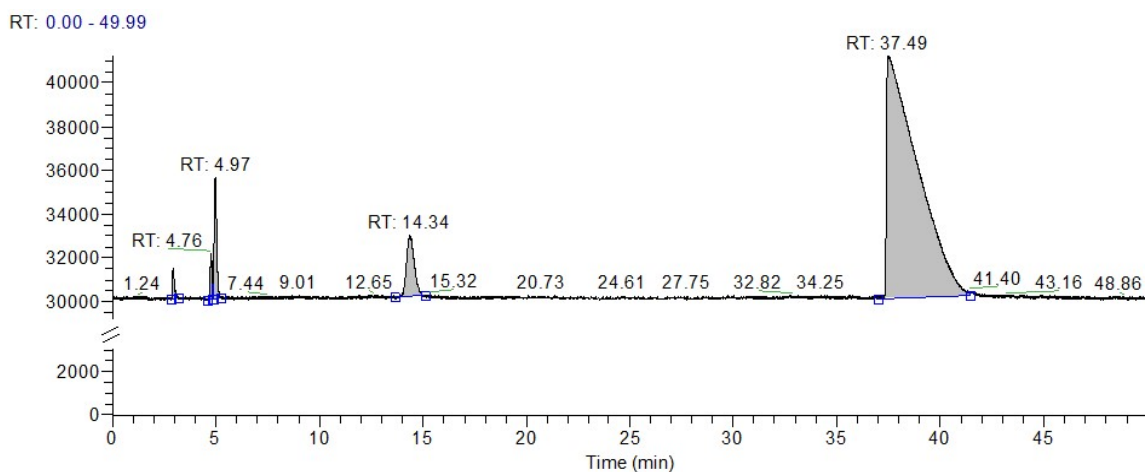
Figure E.30. Chromatogram of entry NP24.
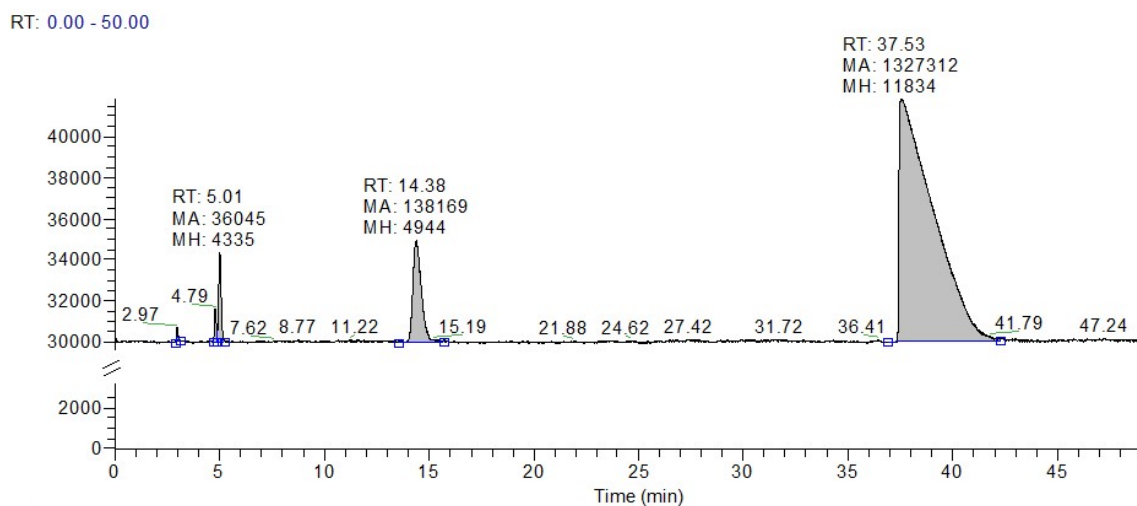
Figure E.31. Chromatogram of entry NP25.

138
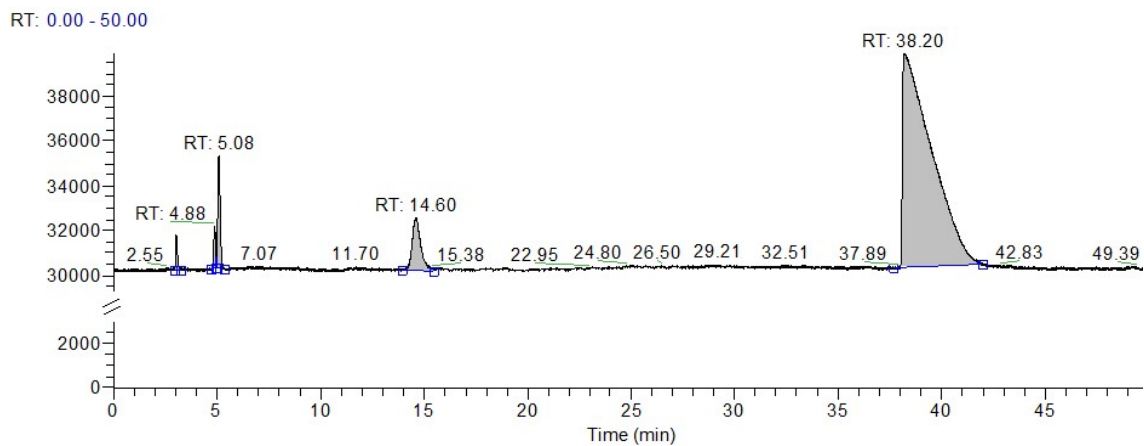
Figure E.32. Chromatogram of entry NP29.
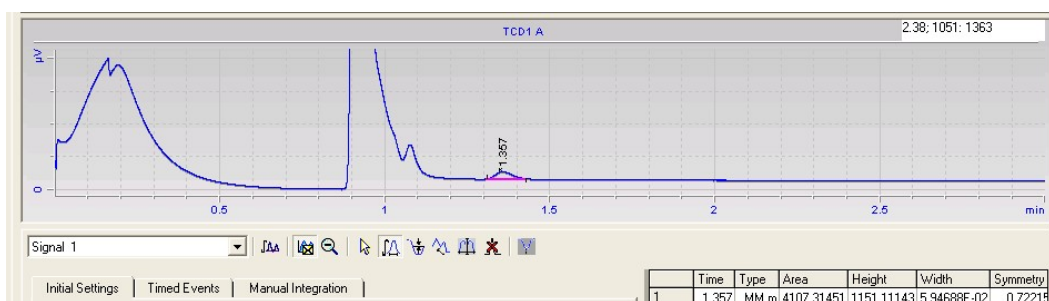
Figure E.33. Chromatogram of entry NP31 provided by channel 1

Figure E.34. Chromatogram of entry NP32 provided by channel 1
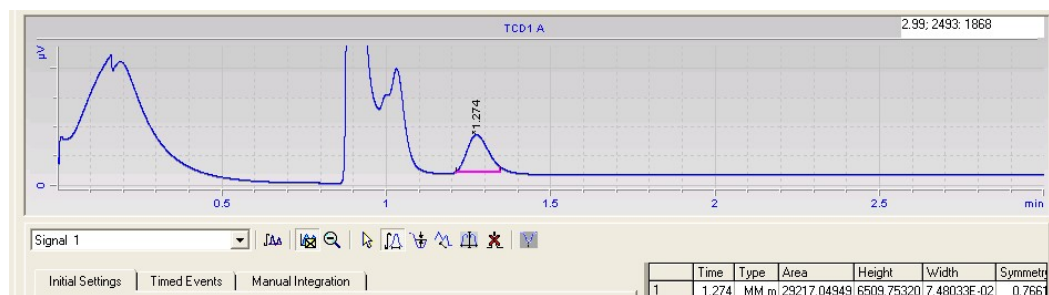
Figure E.35. Chromatogram of entry NP33 provided by channel 1.
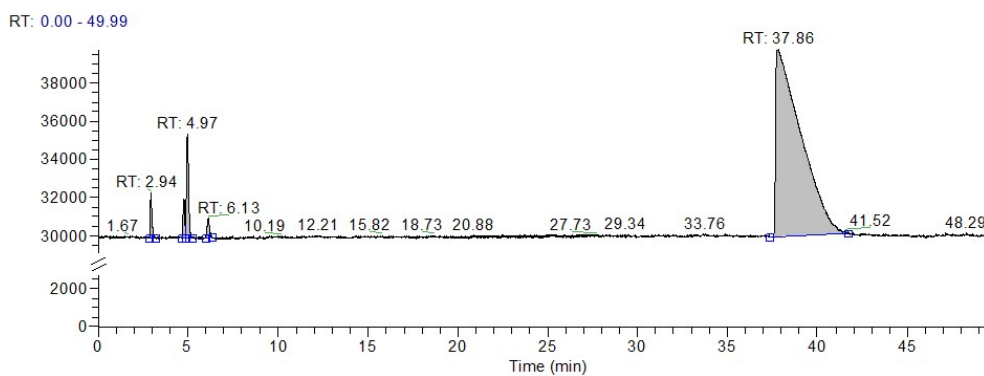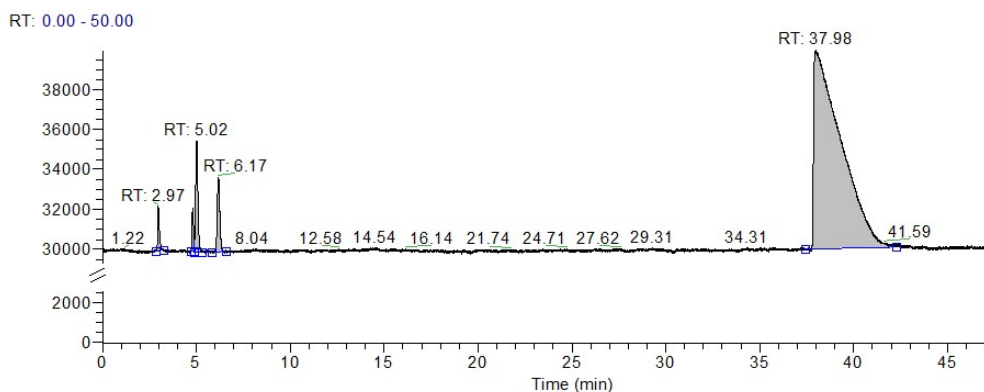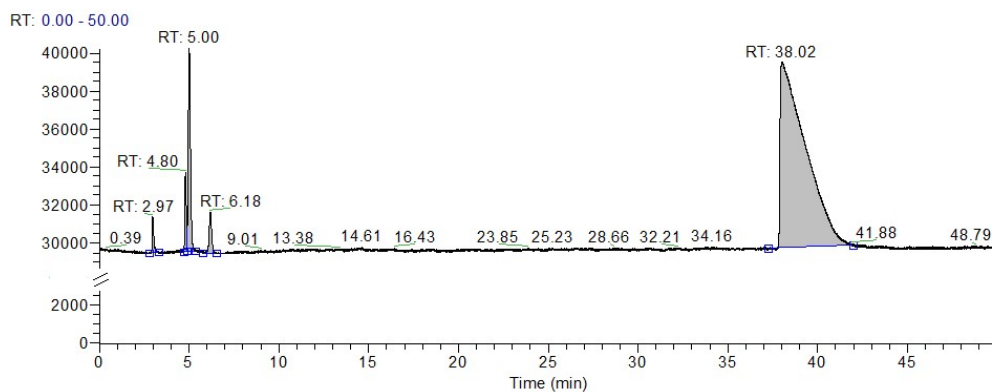
Figure E.36. Chromatogram of entry NP34.

Figure E.37 Chromatogram of entry NP35.
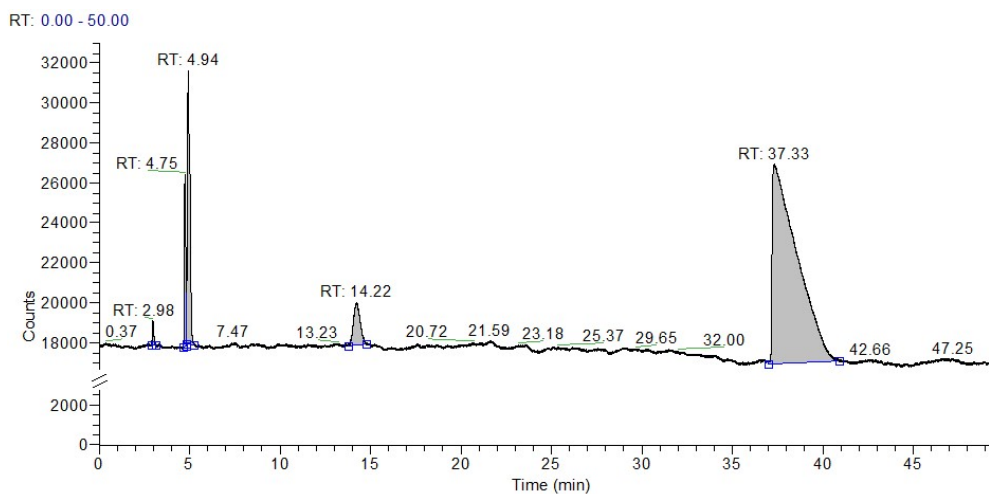
Figure E.38. Chromatogram of entry NP36.

140

Figure E.39. Chromatogram of entry NP37 provided by channel 1.

Figure E.40. Chromatogram of entry NP39 provided by channel 1.

Figure E.41. Chromatogram of entry NP40 provided by channel 1.

Figure E.42. Chromatogram of entry NP41 provided by channel 1.

Figure E.43. Chromatogram of entry NP42 provided by channel 1.

Figure E.44. Chromatogram of entry NP43 provided by channel 1.

Figure E.45. Chromatogram of entry NP44 provided by channel 1.

Figure E.46. Chromatogram of entry NP45 provided by channel 1.

142
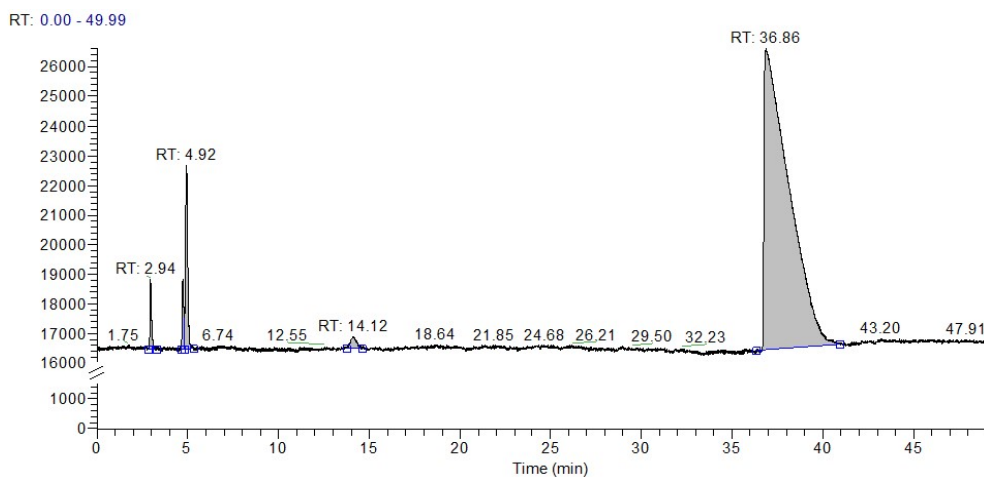
Figure E.47. Chromatogram of entry NP46.

Figure E.48. Chromatogram of entry NP47.

Figure E.49. Chromatogram of entry NP48.

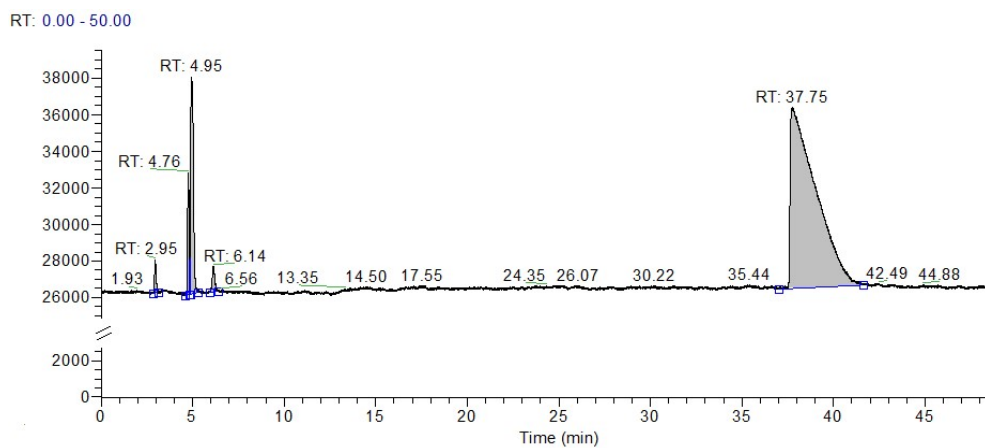Figure E.50. Chromatogram of entry NP49.

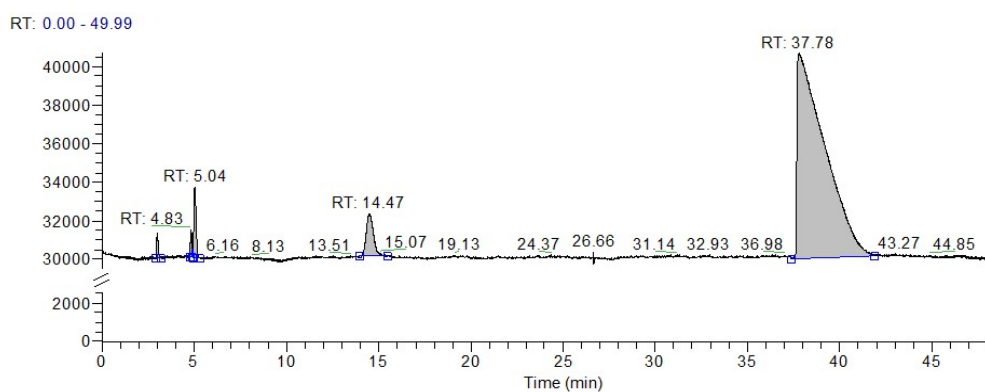Figure E.51. Chromatogram of entry NP50.

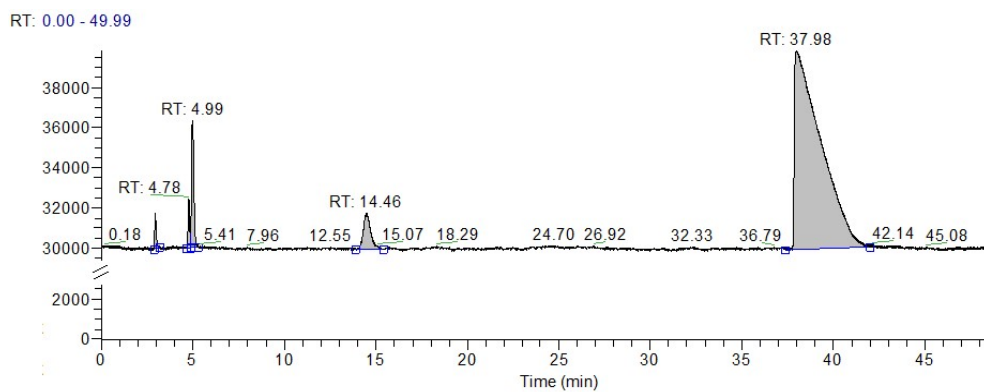Figure E.52. Chromatogram of entry NP51.
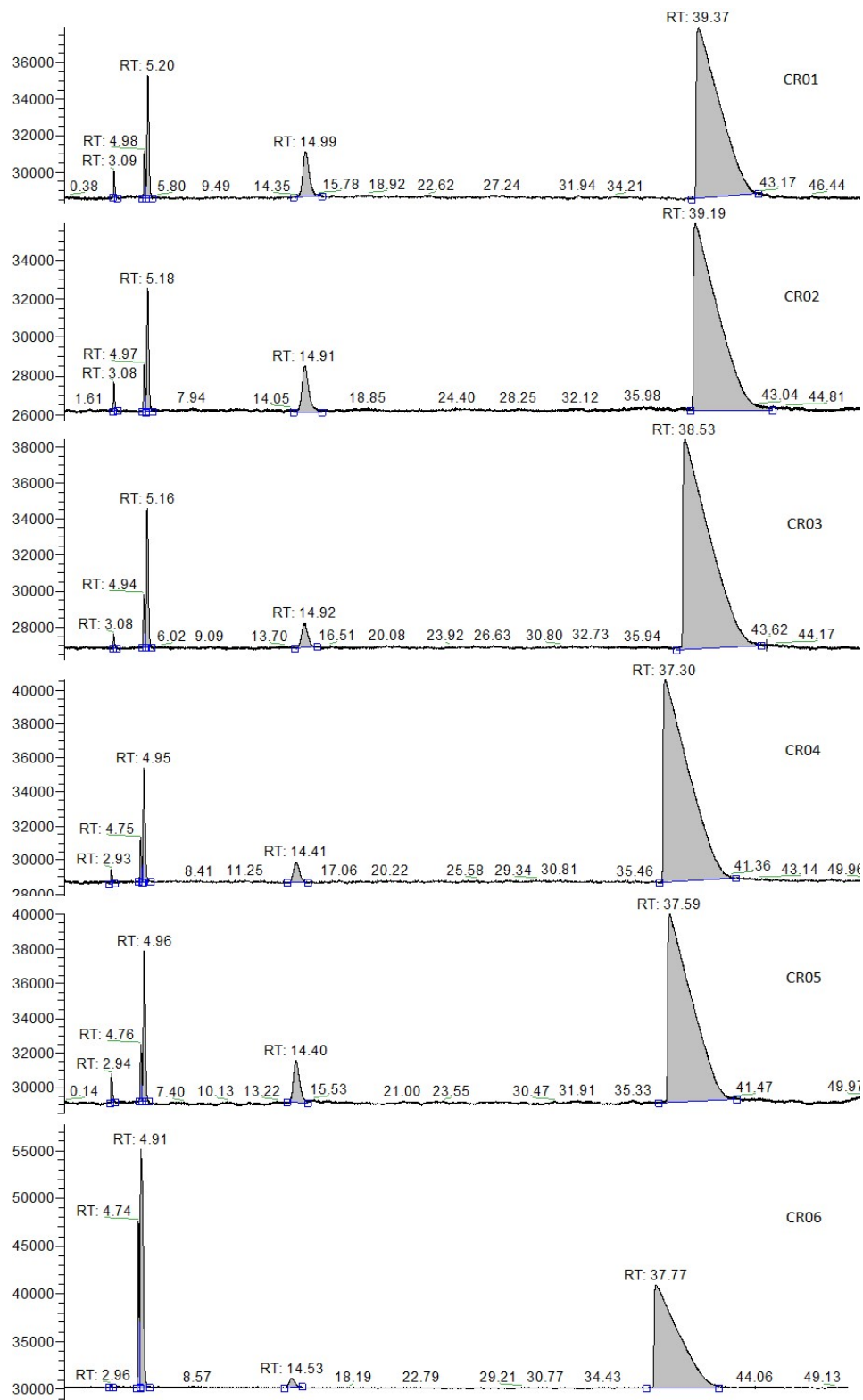
144

Figure E.53. Chromatogram of entry NP52.

Figure E.54. Chromatogram of recycling reactions using [C$_8$mim][NTf$_2$] IL. Entries CR01 to CR06.

Figure E.55. Chromatogram of recycling reactions using [C$_8$mim][NfO] IL. Entries CR07 to CR12.